Active noise control for open air live events at low frequencies

Libianchi, Pierangelo

Publication date:
2023

Document Version
Publisher's PDF, also known as Version of record

DTU Electrical and Photonics Engineering
Department of Electrical and Photonics Engineering

Active noise control for open air live events at low frequencies

Pierangelo Libianchi

Ph.D. Thesis

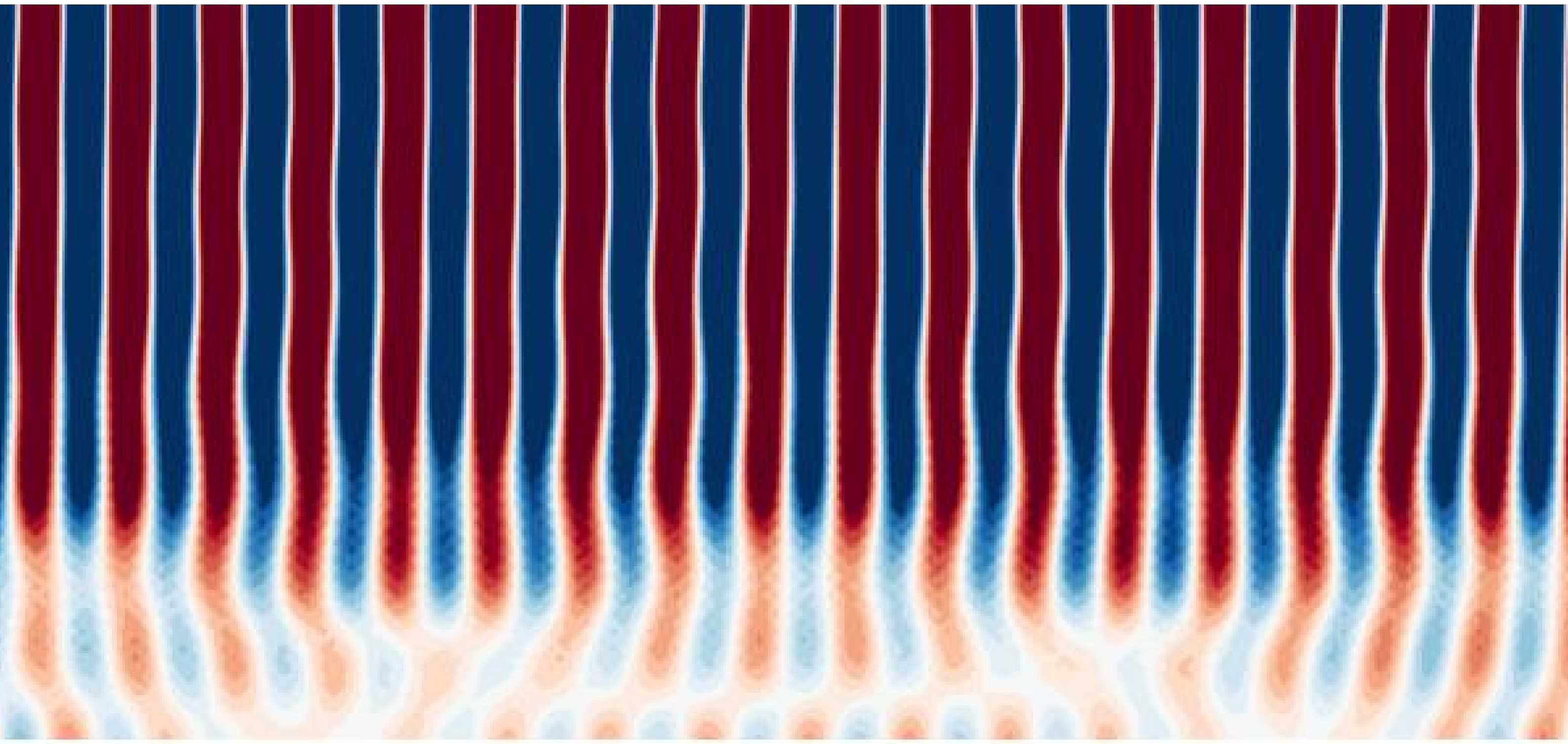

Active noise control for open air live events at low frequencies

Ph.D. Thesis
August, 2023

By
Pierangelo Libianchi

Cover photo: Real part of the sound field close to the ground in a conventionally neutral boundary layer with a strong inversion, Pierangelo Libianchi, 2022

Published by: DTU, Department of Electrical and Photonics Engineering, Ørsted Plads, Building 352, 2800 Kgs. Lyngby Denmark
www.electro.dtu.dk

Preface

This thesis was submitted to the Technical University of Denmark (DTU) in partial fulfillment of the requirements for the degree of Doctor of Philosophy (Ph.D.) in Electronics and Communication. The work presented in this thesis was completed between July 1, 2019 and December 31, 2022 in part at d&b audiotechnik and in part at the Acoustic Technology Group of the Department of Electrical and Photonics Engineering, DTU, under the supervision of Associate Professor Finn T. Agerkvist, Associate Professor Jonas Brunskog, Associate Professor Efrén Fernández-Grande and researcher Elena Shabalina. The project was funded by d&b audiotechnik GmbH & Co. KG.

Abstract

Open air live events can be a powerful source of noise, in particular at low frequencies. Furthermore, the sound waves at these frequencies propagate over large distances with minimal attenuation from atmospheric absorption. Sound field control can reduce these low frequency noise emissions. This approach employs a secondary array behind the audience for this purpose. State of the art methods can provide up to 15 dB in noise reduction at approximately 130 m.

It is of interest to increase the working range and robustness of these systems. This thesis makes strides in this direction by focusing on two subproblems. The numerical method employed to synthesize the filters for the secondary array is the first subproblem and is directly connected to the spatial properties of the solution, ease of use and insertion loss. The limited range of these systems is mainly related to the degree of accuracy in the characterization of the propagation paths which constitutes the second subproblem investigated in this thesis.

A new iterative method is proposed to deal with the first subproblem. This method uses parameters that are directly related to physical quantities. This direct connection makes it easier to use and allows us to efficiently control amount of radiation outside of the quiet zone. This method has been experimentally validated using both measured and simulated transfer functions. The results show that this method using simulated transfer functions provides noise reduction performances on par with other methods with 10 dB broadband insertion loss and peaks of up to 20 dB. Solutions obtained from simulated transfer functions generalize better outside of the quiet zone and can be easily updated when propagation conditions change. Moreover, regularization not only balances the trade-off between noise reduction and amplitude of the solution but also controls the radiation pattern of the control array and the robustness of the solution against uncertainties and modelling errors.

The second subproblem can be dealt with by using measurements, but this strategy becomes increasingly impractical over large distances. Propagation models and simulations provide an alternative. However, there are many concurrent factors affecting sound propagation outdoors such as reflections from obstacles, trees, ground, and the influence of a moving and inhomogeneous medium. Characterizing and including all these effects is an enormous task. This thesis restricts itself to the effects produced by a moving inhomogeneous medium to extend the range. An accurate description of the medium is crucial to achieve reliable predictions of the two propagation paths. For this reason, this work reviews fundamental aspects of micrometeorology that allow to better understand and model the wind and temperature profiles. This project makes use of numerical simulations to analyze the importance of using the right model for the wind profile. The results show that the use of an unsuitable model introduces a phase error and misrepresents the interference pattern close to the ground leading to a deterioration of the performance of an active noise control system. This thesis studies how different parts of the profiles affect the error and how sensitive it is to parameters that characterize the lower atmosphere. Finally, these results are used to derive a range in which simpler profiles can still be used in simulations without affecting the accuracy of the results.

Resumé

Udendørs koncerter kan være til stor gene for nærliggende områder, specielt ved lave frekvenser som kun dæmpes moderat over større afstande. Lydfeltkontrol systemer med ekstra højttalere bag publikum kan reducere støjniveauet, og er opnået op til 15 dB ved en afstand på flere hundrede meter.

Denne afhandling adresserer de to delproblemer seperat: Design af kontrolfiltre til de sekundære højttalere og karakteriseringen af overføringsfunktionerne til kontrolområdet.

Det første delproblem er undersøgt både vha simuleringer og udendørs eksperimenter. En ny iterativ metode er introduceret, dens parametre er direkte forbundet til fysiske størrelser og derfor er metoden bedre egnet til at bla. at kontrollere udstrålingen udenfor kontrol zone. Metoden giver en dæmping svarende til andre metoder: fra 10 dB op til 20 dB. Eksperimenterne viser desuden at simulerede overføringsfunktioner leder til filtre og løsninger som generaliserer bedre til området udenfor kontrolzonen og nemmere kan justeres når vind- og temperatur-forholdene ændres. Den iterative metode tillader også nemt at regularisere løsningen og dermed udstålingsmønsteret og robustheden.

Det andet delproblem kan løses ved at måle overføringsfunktionerne, men kun for kortere afstand, bla. p.gr.a praktiske begrænsninger. Som alternativ kan de modelleres, men dette kræver nøjagtig information om udbredelsen af lyd i et inhomogent medium med flow. Afhandlingen behandler derfor også mikrometeorologi for at kunne beskrive vind og temperatur profilerne i atmosfæren. Numeriske simulering anvendes til at undersøge og illustrere betydningen af nøjagtigheden af vindprofilen for at minimere fase fejl og de begrænsninger i lyddæmpningen de vil medføre.

Med baggrund i de praktiske problemer forbundet med en direkte måling af vindprofilen undersøges muligheden for at anvende en machine-learning baseret model af overføringsfunktionerne. Modellen kan trænes på både målte og simulerede data til at til estimere vindprofilen udfra et relativt lille antal målte overføringsfunktioner. Denne metode vurderes dog til ikke at have den nødvendige modenhed til at kunne anvendes direkte på et problem af denne kompleksitet og mere forskning her er nødvendig.

Acknowledgements

I would like to thank all the people that helped me and supported me through this journey. I am really grateful to my supervisors and to Mark for their guidance. A special thanks to Finn, Elena and Toby that help me get through the harder times. Also a big thank to the colleagues at ACT for the interesting discussions, there are too many of you to thank individually but you know who you are. For the help with many of the practical aspects of this project I must thank the people at d&b audiotechnik and especially Kilian, Daniel and Jones. Last but not least, a huge thanks to my family and my friends.

List of publications

Paper A Libianchi, P., Agerkvist, F., and Shabalina, E. (**2022**). “A review of techniques and challenges in outdoor sound field control,” in *Proceedings of Inter·Noise 2022*, https://internoise2022.org/, International Congress and Exposition on Noise Control Engineering, Internoise 2022 ; Conference date: 21-08-2022 Through 24-08-2022. Published.

Paper B Libianchi P., Brunskog J., Agerkvist F., and Shabalina, E. (**2023**). “Active noise control at low frequencies for outdoor live music events using the conjugate gradient least square method,”. *Applied Acoustics*, 205, 2023. Published.

Paper C Libianchi, P. (**2022**). “Notes on the characterization of the wind profile in the atmospheric boundary layer,”. Unpublished manuscript.

Paper D Libianchi P., Shabalina, E., Kelly, M., Agerkvist F. and Brunskog J., (**2023**). “Sensitivity study of the pressure field to the wind profile in a conventionally neutral boundary layer,”. *The Journal of the Acoustical Society of America*, 154 (2), 2023. Accepted, to appear.

Paper E Libianchi, P., Kelly, M., Shabalina, E.,Agerkvist, F., and Brunskog, J. (**2023**). “Phase error sensitivity to the inversion strength and depth of the boundary layer in a conventionally neutral regime,” in Forum Acusticum 2023 ; Conference date: 11-09-2023 Through 15-09-2023. Accepted, to appear.

Technical Note F Libianchi, P. and Karakonstantis, X.. (**2022**). “Surrogate Modelling for Estimating Sound Speed Profiles,”. Internal Report, August 2023.

Additional papers written during the PhD. Not included due to overlapping content with other papers.

Libianchi, P., Agerkvist, F., Shabalina, E.. (**2021**). “A conjugate gradient least square based method for sound field control,” in Proceedings of InterNoise21, pages 1029–1040. Institute of Noise Control Engineering, 2021. International Congress and Expo on Noise Control Engineering, InterNoise21 ; Conference date: 01-08-2021 Through 05-08-2021. Published.

List of symbols

Abbreviations

MOST Monin-Obukhov Similarity Theory.

PINN Physically Informed Neural Network.

ABL Atmospheric Boundary Layer.

ACC Acoustic Contrast Control.

CGLS Conjugate Gradient Least Square.

CGLS Conjugate Gradient Least Square.

CNBL Conventionally Neutral Boundary Layer.

CNPE Crank-Nicholson Parabolic Equation.

FDTD Finite Difference Time Domain.

GTPE Generalized terrain parabolic equation.

LLJ Low-Level Jet.

MOST Monin-Obukhov Similarity Theory.

PA Public Address.

PCA Principal Component Analysis.

PINN Physically Informed Neural Network.

SIREN Sinusoidal Representation Network.

SVD Singular Value Decomposition.

TSVD Truncated Singular Value Decomposition.

ADMM Alternate Direction Method of Multipliers.

ANC Active Noise Control.

ASL Atmospheric Surface Layer.

DNS Direct Numerical Simulation.

FEM Finite Element Method.

FFP Fast Field Program.

FWI Full Waveform Inversion.

FxLMS Filtered x Least Mean Square.

LES Large Eddy Simulation.

MKE Mean kinetic energy.

MOST Monin Obukhov Similarity Theory.

PDE Partial Differential Equation.

PM Pressure Matching.

PML Perfectly Matched Layer.

RANS Reynolds Averaged Navier Stokes.

TKE Turbulent kinetic energy.

Greek symbols

ρ_0 Static background profile of the medium density.

$\tilde{\rho}$ Density of a perturbed medium.

$\boldsymbol{\kappa}$ Horizontal components of the wave-vector.

$\boldsymbol{\Sigma}$ Singular values - mode radiation efficiency.

$\boldsymbol{\sigma}$ Medium dependent stress tensor.

σ_i i-th singular value.

Γ Adiabatic lapse rate.

γ Vertical component of the wave-vector.

λ Regularization parameter/Acoustic wavelength.

ν Kinematic viscosity.

Ψ Velocity quasi-potential transformed with respect to t, x and y.

ω Angular frequency.

Ω_i i-th component of the vector of the angular velocity of the earth.

θ Potential temperature.

θ_0 Static background profile of the potential temperature.

Θ_v Mean virtual potential temperature.

$\tilde{\theta}$ Perturbed virtual potential temperature.

Latin symbols

w Fluctuating vertical component of the wind field.

b Buoyancy.

$\tilde{C}_i$ Scalar concentration of the i-th component in a perturbed medium.

c_{eff} Effective speed of sound.

c_p Specific heat capacity at constant pressure .

ϵ_{ijk} Alternating tensor.

f External forces.

f_i i-th component of the external forces.

g Gravitational acceleration.

$\mathbf{H}_s$ Matrix of secondary transfer functions at a single frequency.

L Obukhov length.

l Length scale of the perturbation.

N Brunt-Väisälä frequency.

$\hat{p}$ Pressure transformed with respect to t, x and y.

$\tilde{p}$ Perturbed pressure field..

$\tilde{p}$ Pressure in a perturbed medium.

P Mean pressure field.

p Fluctuating component of the velocity field.

$\mathbf{p}_p$ Vector of primary field complex pressures at a single frequency.

q Specific humidity.

Q_0 Surface heat flux.

Q_0 Surface heat flux.

$\mathbf{q}_s$ Vector of the source strength for the secondary array at as single frequency.

R_d Gas constant for dry air.

S Entropy in a perturbed medium.

σ_{ij} (i, j) component of the stress tensor.

T Temperature.

$\boldsymbol{u}$ Horizontal mean wind field vector.

$\boldsymbol{u}$ Horizontal mean wind velocity.

$\mathbf{U}$ Left singular vectors - pressure modes.

$\tilde{\mathbf{u}}$ Velocity vector in a perturbed medium.

$\widetilde{u}_i$ i-th component of the velocity vector in a perturbed medium.

U_i i-th component of the mean wind velocity.

u_i i-th component of the fluctuating velocity field.

$\mathbf{V}$ Right singular vectors - source modes.

$\mathbf{v}$ Particle velocity.

$\mathbf{W}$ Particle displacement.

z_s Reference height.

List of figures

1.1 Estimated noise emission for the festival *Made In America* 2017 (demo project from *NoizCalc* (d&b audiotechnik GmbH & Co. KG, 2019)). 2
1.2 A simulation of the active noise control system for open air events in action at 63 Hz. 3
1.3 A plot of the achievable insertion loss as a function of the magnitude and phase error between the primary and secondary fields. 5

2.1 An example of a setup for outdoor sound field control. The loudspeaker array at $x = 0$ m is the primary array and the one at $x = 20$ m is the secondary array meant to weaken the noise emission in the dark zone (DZA in the picture). The area between the two arrays is the audience area. Additional microphones arrays are used in this instance for monitoring purpose (Figure 1a in **Paper B** (Pierangelo Libianchi et al., 2023)). 11
2.2 The three experiments conducted to validate the proposed method based on the conjugate gradient least square. 15
2.3 An example of a fully connected neural network. 18
2.4 An overview of the setup used for the measurement session at DTU Risø campus. 20
2.5 Plot from **Paper B** showing the insertion loss (IL) from the measurements set using filters derived from simulated transfer functions. Top left: loss averaged over the dark zone. Top right: loss averaged over an array behind the dark zone. Bottom left: loss averaged over an array to the left of the mdark zone. Bottom right: loss averaged over an array to the right of the dark zone (Figure 2 in **Paper B** (Pierangelo Libianchi et al., 2023)). 23
2.6 Histograms with the insertion loss obtained from the 512 realizations averaged over space and frequency. Dashed lines show the overall mean and mean plus/minus one standard deviation. Left: $cgls_{k=1}$; center: $cgls_{k=2}$; right: $cgls_{k=3}$ (Figure 12 in **Paper B** (Pierangelo Libianchi et al., 2023).) . . 24
2.7 The five wind profiles and the temperature profile used for the sensitivity study (Figure 1 in **Paper D** (P. Libianchi et al., 2023b)). 27
2.8 A subset of the profiles used in **Paper E**. The plots show: the wind profiles in a CNBL (top), the corresponding logarithmic profiles (second) and their corresponding effective speed of sound (third and fourth, respectively). The plots show the profiles for four different ABL depths (including the shallowest and the deepest) and two inversion strengths: the smallest (N = 6 mHz, dashed) and the largest (N = 14 mHz, solid) (Figure 1 in **Paper E** (P. Libianchi et al., 2023a)). 28
2.9 Real part of the pressure field generated by a point source located at $x = -8.7$ m, $y = 0$ m as predicted by the network (Figure 3 (left) in **Technical Note F** (Libianchi and Karakonstantis, 2022)). 29

3.1 Singular value decomposition of the secondary transfer function matrix from the setup in Figure 2.1 at 125 Hz. 33
3.2 Summary of the approximations used to derive different outdoor propagation models starting from the full set of fluid dynamic equations (Figure 2.1 in (Ostashev and Wilson, 2015)). 38

3.3 Schematic of the atmospheric boundary layer (ABL) showing the ASL (between the straight dashed line and the ground), mixed layer, capping inversion (curvy dashed line), and free troposphere. Near-ground sound propagation for a high-wind condition, with the wind blowing from left to right, is depicted (Figure 1 in (Wilson et al., 2015)). 42
3.4 The time variation of the surface temperature flux observed in the Kansas experiment. The scatter in these one-hour averages is due to the day-to-day variations during the three weeks of midsummer observations (Figure 9.5 in (Wyngaard, 2010)). 44
3.5 Schematic of the ABL showing the ASL (between the straight dashed line and the ground), the mixed layer, capping inversion, and free atmosphere (Figure 1.7 in (Stull, 1988)). 45
3.6 Characteristic effective sound speed profiles for 4 limiting cases of the ASL. The profiles are arbitrarily offset along the horizontal axis so as to improve visibility (Figure 2 in (Wilson et al., 2015)). 46

Contents

Preface ii

Abstract iii

Resumé iv

Acknowledgements v

List of publications vi

List of symbols vii

List of figures xi

1 Introduction 1
- 1.1 Scope of the thesis . . . 7
- 1.2 Structure of the thesis . . . 8

2 State of the art and contributions 9
- 2.1 Active noise control for outdoor live events . . . 9
- 2.2 Characterization of the propagation paths . . . 15
- 2.3 Recovering the sound speed profile . . . 17
- 2.4 Summaries of the included papers . . . 19

3 Theory and background 31
- 3.1 Numerical solutions to the pressure matching problem . . . 31
- 3.2 Transfer functions in a moving inhomogeneous medium . . . 35

4 Conclusions 49

5 Future work 51

Bibliography 52

Papers 59
- **Paper A:** A review of techniques and challenges in outdoor sound field control . 59
- **Paper B:** Active noise control at low frequencies for outdoor live music events using the conjugate gradient least square method . . . 73
- **Paper C:** Notes on the characterization of the wind profile in the atmospheric boundary layer . . . 91
- **Paper D:** Sensitivity of the predicted acoustic pressure field to the wind and temperature profiles in a conventionally neutral boundary layer . . . 103
- **Paper E:** Phase error sensitivity to the inversion strength and depth of the boundary layer in a conventionally neutral regime . . . 115
- **Technical Note F:** A preliminary study for the use of a surrogate model in outdoor sound propagation and sound speed profile recovery . . . 125

1 Introduction

The exposure to noise has a deleterious effect on the health and well-being of individuals. The European Environment Agency report that an estimated 12000 deaths and 48000 new cases of ischemic heart disease per year are related to long-term noise exposure. Furthermore, 22 million people suffer chronic high annoyance, and 6.5 million people suffer chronic high sleep disturbance (European Environment Agency, 2020). Findings like these prompted international organization to develop guidelines (World Health Organization. Regional Office for Europe, 2018) and national and local governments to introduce stricter regulations on noise emissions (Hill and Shabalina, 2020). When talking about noise pollution, the focus is usually on traffic, railroads, or aircraft noise. However, any undesired sound can be perceived as noise and open-air live events are often perceived as such by individuals living close to the venues, see Figure 1.1. These type of events usually have a strong low frequency component (Elowsson and Friberg, 2017; Støfringsdal, 2018). This is of particular concern since low frequencies can travel very large distances with minimal attenuation (Bass et al., 1995). It is possible to control the radiation pattern of the main sound reinforcement system on stage, usually referred to as public address (PA). This can be done through careful selection of the loudspeakers based on their directivity pattern, their positioning and the use of electronic delays. This is often done to focus the radiation towards the audience and to limit spilling to the sides. However, the problem remains on the main axis of PA since it is where the audience is located. In (F. Heuchel et al., 2018) additional control sources are placed behind the audience. The purpose of this secondary array is to generate a secondary sound field that matches the main, or primary, sound field but with opposite phase to cancel noise emissions through destructive interference.

There are multiple techniques to approach this problem. A first distinction is between adaptive feedback methods and static feedforward methods. The first approach uses the signal from one or multiple error sensors to update the coefficients of the filters applied to the control sources. The main limitation of this approach is that the largest noise reductions occur where the sensors are located. Furthermore, multichannel systems using multiple sources and sensors, as in this case, are computationally expensive. Even though some of these limitations can be mitigated, static feedforward methods present a more suitable alternative since they have a lower computational cost.

These techniques are often used to create personal audio zones (Betlehem et al., 2015) to deliver different audio contents to small regions sharing the same space. A special application of these techniques aims to generate a bright zone, where the audio content is delivered, while keeping the surrounding space quiet. This is like the problem investigated in this thesis. The fundamental differences are that most of these techniques are used indoor, so the medium can be considered static and homogeneous, and they do not differentiate between primary and control source. These are important distinctions since in outdoor applications, the medium is moving and inhomogeneous. Moreover, a distinction between primary and secondary sources is necessary because it is not possible to intervene on the signal delivered to the PA since it would affect the sound field in the audience area.

The first study that deals with sound field control for outdoor live events is (F. Heuchel et al., 2018), which adapts the techniques used for personal audio zones to the problem studied in this thesis. This and following work on this topic used least square solutions with

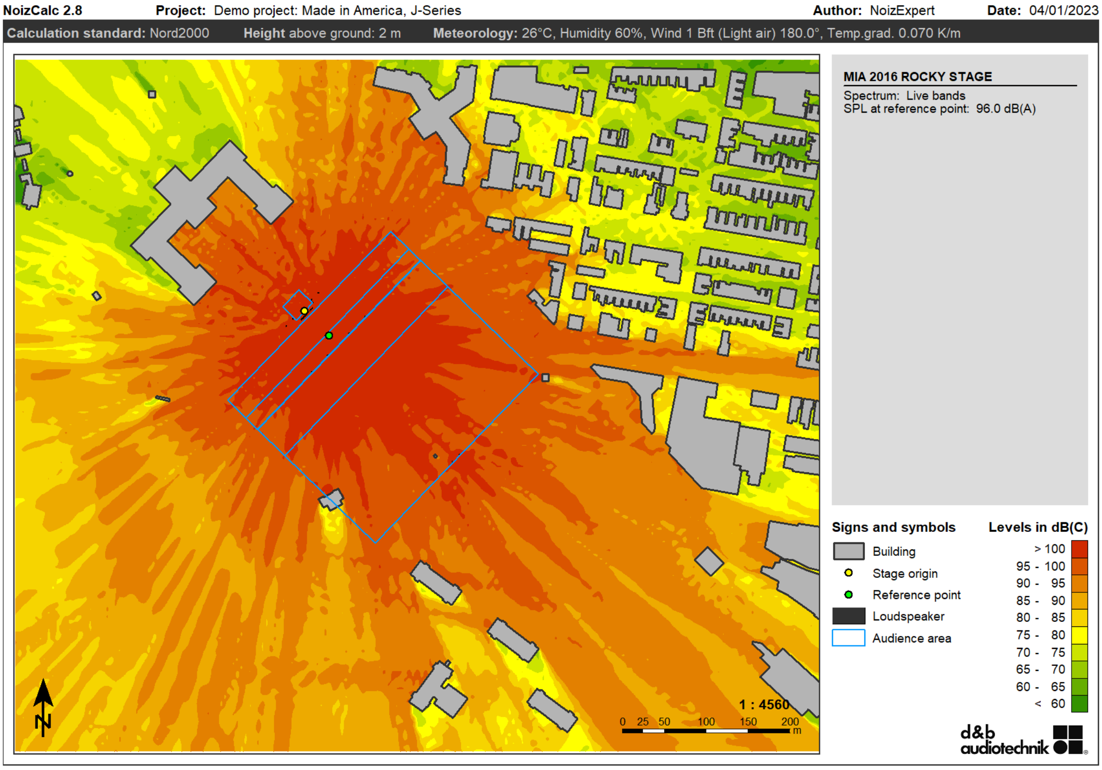

Figure 1.1: Estimated noise emission for the festival *Made In America* 2017 (demo project from *NoizCalc* (d&b audiotechnik GmbH & Co. KG, 2019)).

Tikhonov regularization to synthesize the filters for the secondary sources. Even though this approach is computationally efficient, it has the drawback that the regularization parameter has no direct physical meaning. Finding an optimal value for this parameter is not easy since it controls the level reduction, the radiation pattern of the control array and the amplitude of the filters. These aspects are very important since we want to avoid to reduce the level in one direction while increasing it somewhere else, thus shifting the issue from one area to another. Furthermore, the amplitude of the filters is also a concern since we want to avoid non-linear effects from the transducers. This thesis, as previous works, assumes that the control system is linear and any deviation from this assumption would degrade the achievable noise reduction.

One of the objectives of this thesis was to simplify the use of these systems. A more efficient, or intuitive, way to control the trade-offs between the issues described above would be a stride in such direction. This was the first task undertaken in this project. One of the methods considered at first was convex optimization with constrains on the amplitude of the solution. Even though this method allows to avoid possible non-linear behavior from the transducers and provides accurate and high-performance solutions, it is computationally demanding and harder to implement at a development stage. Furthermore, it is difficult to introduced constraints on the radiation pattern since it can easily lead to an empty feasible set.

Subspace methods, on the other hand, offer an intuitive way to control the directivity pattern of the control sources. These methods allow to decompose the transfer paths in source modes and the corresponding pressure modes. One can than select only source modes that excite pressure modes with desired spatial properties and the solution is com-

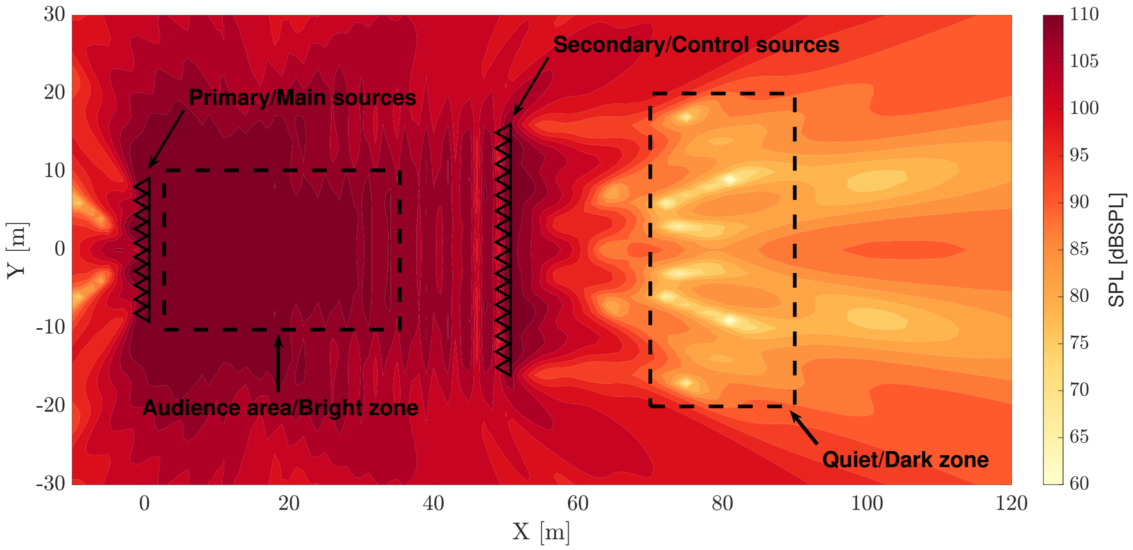

Figure 1.2: A simulation of the active noise control system for open air events in action at 63 Hz.

puted in the subspace resulting from this mode selection. However, this selection is hard to automate and needs to be repeated at each frequency. Furthermore, these methods do not provide a way to limit the amplitude of the solutions with the potential issue of introducing non-linearities.

The alternative investigated and proposed in this thesis consists of the conjugate gradient leas square algorithm (CGLS), an iterative subspace method where the number of iterations replace the regularization parameter and mode selection. The number of iterations can be easily controlled using stopping criteria. These criteria can be tuned to each specific application. In this application they are used to control the radiation pattern of the control source. In this way, a potential user can introduce regularization through intuitive and physically meaningful parameters instead of more abstract regularization terms. Furthermore, this method can be combined with an active set-type method to impose explicit amplitude constraints without incurring in an increase in the computational cost as occurs with convex optimization.

This method was first tested in anechoic conditions, then in a more realistic setting with reflections involved. However, the reflections made it harder to study the numerical properties of the solutions. Therefore, an additional test was designed to better study this method and the properties of its solutions also in comparison to solutions provided by the other methods described above. Section 2.1.1 briefly summarize this method and Section 2.1.2 recounts the three measurements sessions. The latest and more thorough measurement campaign and its results are also published in **Paper B**.

Measuring the performance of an active noise control system (ANC) outdoor and a low frequency is a challenging task. In general, it involves large transducers to control frequencies in the range of interest, from 30 to 120 Hz. Furthermore, the application of this project involves large spaces and long propagation distances. These two aspects together increase the logistical complexity if these experiments. The preparation of the required equipment, transportation and setting up the experiment was further complicated by a pandemic that affected the availability of support for these tasks and of suitable venues suitable. Some of these issues were mitigated by performing experiments at a 2:1 scale. Nonetheless, these complications introduced delays that hindered the outcomes of this project. Notwithstanding, the measurement campaigns highlighted the importance of properly modelling the medium. Even at short distances, a mismatch in the wind direction or the magnitude of the temperature or the wind speed can introduce a phase error that degrades the performance of the ANC system. This is in accordance with previous works ((Caviedes Nozal et al., 2019b; F. M. Heuchel et al., 2020). At larger distances, additional phenomena such as refraction from a moving inhomogeneous medium influence the phase and the magnitude of the pressure field on the ground. Some of these issues have been dealt with using either measurements or hybrid methods. The first approach presents a logistical challenge at large distances without considering that it is expensive and, as the weather condition changes, the accuracy of the measurements degrades. The work presented in (F. M. Heuchel et al., 2019) address this issue using a neural network to derive a delay compensation based on changing weather conditions to adapt the measured transfer functions. The hybrid approach used in (F. M. Heuchel et al., 2020) reduces both the number of measurements needed and the computation time that a pure model-based method would require. However, the model used in that case assumes a static and homogeneous medium. However, this is not an accurate description of the medium and more advance models are required to include its effects on sound propagation to extend the range of these ANC systems.

This thesis studies the possibility of using simulations to include more complex propagation scenarios and to avoid the use of physical sensors to improve the ease of use of these techniques in every-day applications. Some of the models analyzed are described in Section 3.2.1. For such an approach to work, it is required a sufficiently accurate description of the medium and a computationally efficient implementation of a propagation model computation time compatible with continuously changing propagation conditions.

Detailed modelling of the medium taking into account the dynamics and characteristics of the atmospheric boundary layer (ABL) were not considered in previous works on ANC for outdoor live event. The ABL is the lowest part of the atmosphere, the one that interfaces with the ground and where sound propagation takes place. A novelty in this thesis is the use of micrometeorology to make informed decision about what aspects and phenomena of the ABL are worth considering when applying ANC techniques to outdoor sound propagation. Based on this knowledge, it describes the most relevant propagation scenarios and present relevant models for the medium wind speed to facilitate accurate predictions using only few parameters to describe the medium. The basic theory describing the dynamics and main regimes of the ABL is described in Section 3.2.2 and more details are given in **Paper C**.

A better knowledge of the ABL, its regimes and its effects on the medium allows to make important considerations. For instance, at night the ABL is either stable or, closer to sunset and sunrise, neutral. In a stable boundary layer, the temperature increases with height, which results in a downward refracting atmosphere. This condition is the most favorable for sound propagation since results in an acoustic duct close to the ground and increases the propagation range of the noise emissions. Regulations are tighter at this time of the day to avoid sleep disturbances and stress related conditions. Hence, control of noise emissions from open air event is particularly important at nighttime. Moreover, in a stable boundary layer, the atmosphere close to the ground, where sound propagates, is stably stratified and the turbulence only occur above it. It means that, in this scenario, the turbulence are of less importance than the mean properties which can be modelled with larger accuracy. Furthermore, simulations using mean properties averaged at different positions provide more reliable results from simulations (Wilson et al., 2008). For these reasons, this thesis focuses on the mean properties of the medium instead of turbulence.

The effect of turbulence could be accounted for using simulations of multiple sound fields produced by different realizations of the turbulent wind and temperature fields and then use a robust optimization framework (El Ghaoui and Lebret, 1997).

A logarithmic function is often used to model the mean wind profile in acoustics (Van Den Berg, 2004; Taherzadeh et al., 1998; Hornikx et al., 2010). The use of this model is attractive since it is simple and easy to tune due to the low number of parameters. However, it is only suitable in a specific regime of the ABL which does not often occur. In one of the most common regime of the ABL (Wyngaard, 2010; Zilitinkevich and Esau, 2005), the wind speed and its gradient are larger than predicted by a logarithmic profile. It is then important to know when a logarithmic profile can still be used and within which range before the error it introduces can be neglected. This thesis presents studies that analyzed the error introduced by inaccurate descriptions of different sections of the wind profile and how sensitive this error is to different parameters that characterize the ABL. The results show that the main error introduced by using the logarithmic profile is in the phase which, while irrelevant for prediction of noise exposure levels, it is crucial in an active noise control application. As shown in Figure 1.3, noise reduction can only be achieved when the phase mismatch between primary and secondary field is smaller than 60°. The system produce amplification when the mismatch is larger than this threshold. An important outcome of the study undertaken in this thesis is that the phase error in the predictions made using a logarithmic profile are smaller than 60° until approximately 1 km. Beyond that point it largely depends on meteorological parameter that are hard to measure.

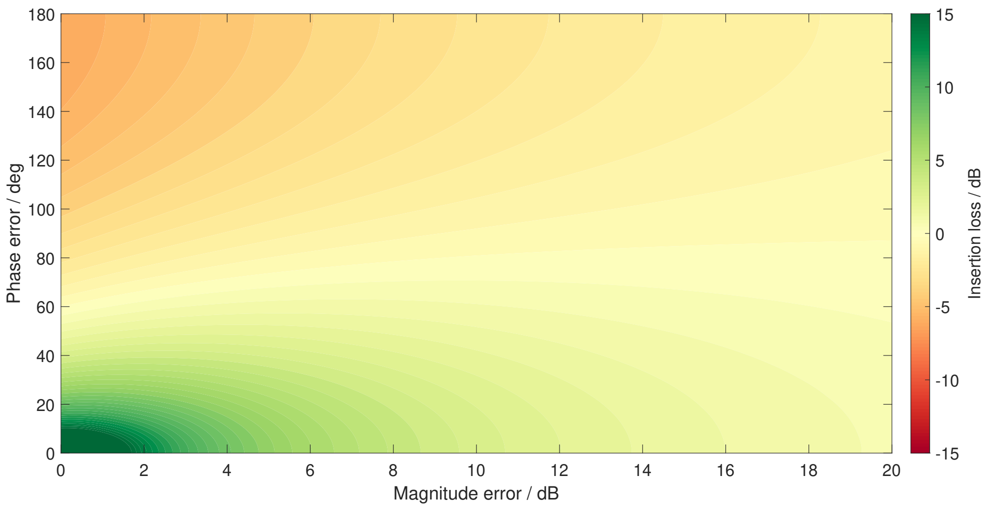

Figure 1.3: A plot of the achievable insertion loss as a function of the magnitude and phase error between the primary and secondary fields.

In parallel to these sensitivity studies, the thesis also investigated passive methods to measure the properties of the medium using techniques that can also be used to speed up simulations and make them a viable option for this application. Passive measurement methods consist of inferring the magnitude of a quantity by measuring a different quantity that is related by a known relationship to the first. This approach has been used previously in ocean acoustics (Gerstoft and Gingras, 1996; Park et al., 2010; Bianco and Gerstoft, 2016; Bianco and Gerstoft, 2017) and seismology (Virieux and Operto, 2009; Aghamiry et al., 2019; Aghamiry et al., 2021). In both cases, acoustic measurements were used to either derive the speed of sound in water or the composition of the ground below the surface. However, most of these approaches require a propagation model whose parameters are tuned using different optimization techniques. The time requirements of the propagation models are still too demanding for the application considered in this thesis. The use of a surrogate model instead of traditional numerical methods could potentially offer an alternative.

(Raissi et al., 2019) used a neural network to produce a surrogate model for different physical problems. With this aim, the networks were trained using the PDE describing the problem of interest by including it in the cost function. These types of networks are known as Physically Informed Neural Networks (PINN. (Sitzmann et al., 2020) used this type of network to model sound propagation through the earth and then combines it with measured data to recover the sound speed and composition of the ground below the surface. This approach was considered in this thesis since it can be used to solve the forward problem and speed up the simulations required to estimate the primary and secondary propagation paths. After the training phase these networks can quickly make a prediction at the desired position instead of computing it over the entire domain. Moreover, the combination of this technique with measured pressure data on the ground was also investigated to improve the accuracy of the estimation of the sound speed profile and further refine the predictions made by the surrogate model. **Technical Note F** presents the results of a preliminary study for the use of such technique for the current application. However, this approach will require additional investigation since it was found to be not mature enough to correctly simulate an inhomogeneous medium and the effect introduced by a reflective ground or to recover the sound speed profile correctly.

While developing the surrogate model, an additional measurement campaign was designed and undertaken to gather real-world data to investigate the capabilities of the surrogate model to recover the sound speed profile. These measurements took place at the DTU campus of Risø. The logistics of these measurements were quite complex since it was necessary to have large propagation distances to detect the effects of an inhomogeneous medium and then reconstruct the sound speed profile. Furthermore, it was necessary to have instruments at the measurement site that could provide a benchmark to test the reconstruction made by the surrogate model. For these reasons the campus at Risø was chosen since it is fitted with weather masts equipped with sonic anemometers placed at different heights that measure both temperature and wind speed, parameters that can be used to calculate the effective speed of sound. However, during the summer months it had been challenging to get access to the campus and to a suitable space within it where the propagation distance was large enough. Furthermore, the access to the site had to be coordinated with the renting and transportation of the measurement equipment which was complicated by a busy season due to the pandemic restriction being dropped and the resulting large amount of work experienced by the provider. Furthermore, an additional laser-based measurement system developed by the Photonik department was tested during this campaign which required further coordination. These logistical issues produced delays on the original timeline and additional technical problems affected the quality of the data gathered on this occasion.

An additional and larger measurement campaign was planned towards the end of this project to test adaptation strategies of the controller developed in this phase to changing propagation conditions. However, the complications described above, and additional setbacks prevented this experiment from happening. Furthermore, it was not possible to test the system during a real outdoor live event since almost none took place during this thesis. These challenges lead this thesis to focus more on the simulation work, by analyzing different propagation models and numerical techniques, and modelling effort through the study of the physics of the atmosphere and the description of the medium.

The surrogate model was supposed to provide the primary and secondary propagation paths required by the CGLS algorithm to generate the control filters. The original plan included an additional large-scale measurement campaign to assess the combined performance of such a system. This final experiment was designed for control over large distance, where the weather has a large impact on the performance and was going to take place on a grass landing strip of a small airport with no surrounding buildings to limit the number of parameters influencing the study. Unfortunately, this measurement campaign was cancelled due to the poor results obtained with the surrogate model, the technical difficulties encountered during the measurement campaign in Risø and the overall delays related to logistical complications, in part brought by the pandemic.

1.1 Scope of the thesis

The application of an ANC to outdoor live events still presents some challenges. At the start of this project, ANC systems for reduction of noise emissions from open air live event at low frequencies had already been tested and proved to work with different degrees of performance depending on the topological complexity of the venue and propagation conditions. Furthermore, their use required a noteworthy logistical and technical effort. So, the main research questions considered at the beginning of this project were two: 1) Is it possible to extend the working distance of these systems or make it more robust? 2) Are there other approaches that can simplify the use of these systems for every-day use? These general questions were found to have multiple ramifications during this project and were too large to be tackled entirely by this project. However, this thesis makes strides in such direction focusing mainly on the following aspects:

- *Provide a functional overview of the problem*: This is a problem that can be described in terms of two main building blocks. The overall limitations are defined by these fundamental components, so it is important to study each of them separately. In this way, these techniques can be better combined to improve performance. This approach also provides better insights on the limitations of the actual approach and what are the most important challenges to address to move forward. **Paper A** provides such an overview by looking at the techniques that have been employed so far and identifies their pros and cons.
- *Investigate the use of simulations in outdoor sound field control*: The use of measurements is a logistical challenge at large distance and it can hinder the use of these systems due to economical, technical or logistical reasons. **Paper B** looks into the use of simulations instead of measurements and compares the performance of the corresponding solutions. Furthermore, it analyses the robustness of such solutions against uncertainties in the modelling parameters.
- *Controlling the amplitude and directivity pattern of the solution*: Any outdoor ANC system should reduce the level in the dark zone but it should also ensure that it will not create new problems in other areas. Moreover, it should allow to control the amplitude of the solution to avoid non-linearities in the transducers. **Paper B** introduce an iterative method that easily allows to control the directivity pattern of the solution and its amplitude when paired with an active set-type method.
- *Characterization of the medium*: Simulating sound propagation over large distances

outdoor requires models that can account for a moving inhomogeneous medium. A good deal of methods has been developed over the years and this thesis describes some of the most used ones and their limitations. However, the prediction from each model is accurate only if the underlying assumptions are valid and the modelling parameters are accurate. **Paper C** gives an overview of the dynamics of ABL. This knowledge is used to derive numerical approximations for these parameters. However, these methods have limitations that are also described in **Paper C**. **Paper D** study the error introduced in the simulations when the wind and temperature dependency on height is modelled using profiles that are not appropriate for a particular regime of the ABL. From the results, it is evident that the wind and temperature profiles play a very large role in outdoor sound propagation. To really overcome these limitations, these profiles should be measured. Direct measurements techniques are prohibitive for this application. As a possible alternative, **Technical Note F** studies the use of physically informed neural networks (PINN) to reconstruct the wind profile indirectly from pressure measurements on the ground.

1.2 Structure of the thesis

This thesis is organized as a collection of manuscripts and is organized in two main parts. The first part starts with this Chapter which provides the background and motivations for the thesis, the challenges encountered in this type for application and the aim of this work. Chapter 2 provides a recount of the state of the art and the contributions made by this thesis. The first part of this section reviews the techniques used for personal sound zones which their adaptation to the current problem. The rest of the chapter focuses on the characterization of the propagation paths, from measuring or simulating them to the use of different propagation models and the importance of the modelling parameters. Chapter 3 provides the theoretical foundations behind the manuscripts. It is also divided into two main sections dealing with the theory of the two subproblems. The first section introduces inverse problems theory, the purpose of regularization and how it affects different aspects of the solutions. The second section, first introduces some of the most used outdoor sound propagation models together with the assumptions used to derive them and the limitations they introduce. Secondly, it provides a description of fundamental aspects of micrometeorology to better understand the medium and to model medium properties such as wind and temperature profiles. The reader that is already familiar with any of these topics can skip the corresponding section and move to the papers. Finally, Chapter 4 presents the main conclusions drawn from this thesis and the main gaps that still have to be filled for this type of application to further mature.

2 State of the art and contributions

This section describes the state of the art for outdoor sound field control and the contributions made in this thesis. For the theory behind the contributions and papers presented in this section, see Chapter 3. This part of the thesis is organized in four main sections:

1. The first describes the state of the art in active noise control and in particular its application to the reduction of noise emissions from outdoor live events. The section ends highlighting the knowledge gap found when analyzing the state of the art and the contributions made by **Paper A** and **Paper B** to address them.

2. The second part deals with the characterization of the propagation paths. The main knowledge gap addressed in this thesis revolves around the characterization of the medium. The contributions from **Paper C** , **Paper D** and **Paper E** are mainly aimed at addressing this gap. They are mainly focused on the analytical descriptions of such quantities and on the error introduced by the inaccurate model of the wind profile.

3. The third section focuses on the recovery of the medium properties. Even though direct measurements can be prohibitive for this application, indirect methods such as the ones used in ocean acoustics and seismology could provide a more practical alternative. **Technical Note F** , which was originally a report for specialization course, describes a preliminary study to adapt a state of the art technique used in seismology based on PINN to outdoor sound propagation. In contrast to the other manuscripts included in this thesis, this work was only at an exploratory stage and was not completed yet at the time of writing.

4. The fourth and last section provides a summary of each of the papers included in this thesis.

2.1 Active noise control for outdoor live events

There is rich literature describing different approaches and applications of ANC. Most ANC algorithms fall into two categories: feedback and feedforward methods (Nelson and Elliott, 1992). The former uses an error sensor to measure the mismatch between the primary/noise field and the control field. This signal is used to adapt a set of control filters to minimize the error signal, in this case the mismatch between the main sound field and the synthesized anti-field. One of the better known examples of this type of algorithm is the FxLMS (Nelson and Elliott, 1992). The feedforward methods might employ an error sensor but only to monitor the performance of the system and not for adaptation. These methods require a characterization of the primary and secondary paths which can be done in different ways as described in **Paper A**. Even if adaptation is lost, these methods offer the potential of avoiding the use of physical sensors and are computationally cheaper since there is no real-time adaptation. This makes them particularly suitable for large systems with multiple sources and sensors. During this thesis, only feedforward methods have been used thus this section focuses only on them.

Wave Field Synthesis (WFS) (Ahrens and Spors, 2012) could potentially be used to analytically generate the secondary sound field using a plane wave representation of the primary field. However, the finite and discrete nature of the secondary array, as shown in Fig. 1.2, limits the complexity of the sound field than can be generated (Ahrens and Spors, 2010). Furthermore, this method does not allow to easily include constraints to limit back-radiation and spilling outside of the dark zone which is crucial for the application studied in this thesis.

Recent developments in sound field control, and reduction of outdoor noise emissions, adapt methods and techniques that were first introduced for multi-zone applications. This concept, introduced in (Druyvesteyn and Garas, 1997), consists of delivering audio content within a confined region without increasing the level elsewhere. (Betlehem and Teal, 2011) used convex optimization for this purpose with an interior point algorithm (Boyd and Vandenberghe, 2004) to include constraints. The objective function was formulated as a pressure matching (PM, see Section 3) problem to generate the desired pressure field in the region where audio was delivered. They added a constraint on the source effort and one on the maximum pressure in other regions that were meant to be kept quiet. The method proposed was effective and the problem statement could be easily adapted to sound field control. They also showed, through the use of the Lagrangian (Boyd and Vandenberghe, 2004), how the convex optimization problem was connected to a weighted least square problem with regularization. The constraints had a physical meaning which made it easier to define them. On the other hand, it was found that it was harder to find an optimal value for the regularization parameter which was introduced for numerical reasons.

(Elliott et al., 2012) used a similar approach. The problem was first formulated as an acoustic contrast control (ACC), with the objective of maximizing the level difference between the bright and the quiet/dark zones. It was then written in terms of the Lagrangian of a convex problem with different formulations for the objective function and one of the constraints. An additional constraint was placed on the source effort. The different formulations showed different numerical properties and some were found to be more stable than others. The system developed in (Elliott et al., 2012) was designed for indoors, which meant that it did not have to deal with an inhomogeneous moving medium but it had to deal with reflections. Both the quiet and personal audio areas were generated by an array of two or three loudspeakers in an endfire configuration which did not differentiate between primary and control sources. This work also analyzed the influence from uncertainties coming from reflections, position, and response of the drivers. It used robust control theory (Morari and Zafiriou, 1989) to factor in these uncertainties. The deterministic pressure field in the cost functions was replaced by a spatial average of the pressure field including the contribution from the uncertain parameters.

The previous two approaches used ACC and PM. (Chang and Jacobsen, 2012) combined those formulations to create a bright zone surrounded by a quiet one using a double layer circular array and achieving contrast values of up to 40 dB. In (Pasco et al., 2017) the situation was reversed, a double layer circular array was used to generate a circular quiet zone within the array without affecting the surrounding primary field. They used the generalized singular value decomposition to separate the contributions from the loudspeakers to the dark and bright zone before applying ACC. Separating the contributions allowed an improved control over the leakage of the sources into the primary field. Many of the approaches described above, developed for multi-zone purposes, are summarized in (Betlehem et al., 2015). More recently, (Abhayapala et al., 2019) proposed a subspace method, where the secondary transfer function matrix is approximated by only a few components obtained through principal component analysis (PCA). A set of selected components provided a subspace where the solution lies. This approach allowed to control the spatial properties of the synthesized field according to the principles described in (Borgiotti, 1990). However, the decomposition and component selection had to the performed at each frequency reducing its practical applications.

The formulation of the problem in this thesis is a special case of the problem described above where we only consider one dark zone. However, the application to outdoor live events introduces a few critical differences and complications. The previous cases deal with indoor acoustics. This is an important distinction since the larger distances involved in this thesis and a moving inhomogeneous medium introduce a new set of challenges. Furthermore, in many instances the same sources generated both the bright and dark zones. In the case of live events, we must distinguish between primary and secondary sources since the primary sources are located at the stage and is not possible to interfere with the audio content delivered to them to not affect the experience of the audience. Furthermore, the size of the domain prevents placing the control sources around the control area.

(Wright and Vuksanovic, 1996) described the first application of ANC to outdoor problems and validated it experimentally using pure tones in (Wright and Vuksanovic, 1999). (F. Heuchel et al., 2018) further developed this application and applied it to real world systems. The problem was initially stated as a multi-objective minimization problem similar to (Chang and Jacobsen, 2012), allowing to control the trade-off between minimizing the level in the dark zone and limiting the spilling of the control sources in the audience area. It was then recast as a least square problem as in (Betlehem and Teal, 2011; Elliott et al., 2012). It used a two-layer array of control sources to limit the leakage of the secondary field into the bright zone. After experimental validation, it was found that a single array of cardioid subwoofers can replace the double-layer array leading to a setup similar to the one shown in Figures 1.2 and 2.1. This also simplifies the logistics and the objective function since a leakage reduction term is no longer needed.

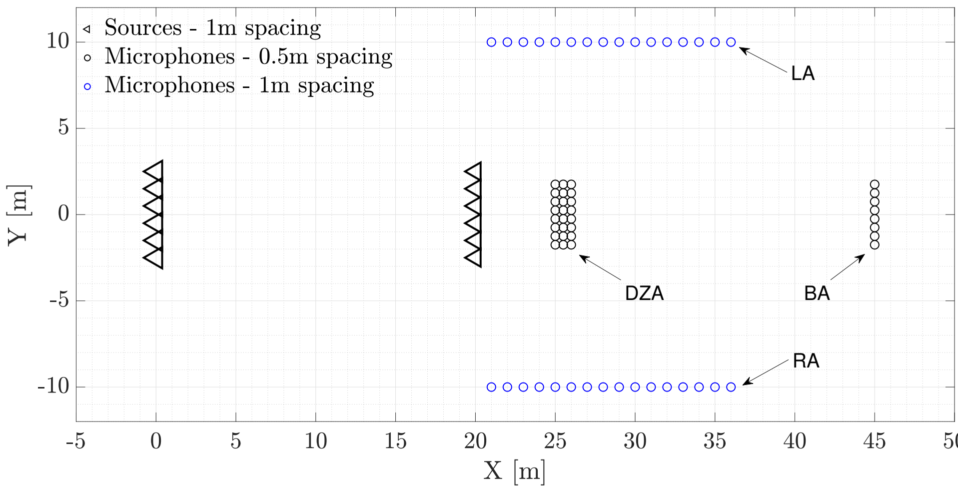

Figure 2.1: An example of a setup for outdoor sound field control. The loudspeaker array at $x = 0$ m is the primary array and the one at $x = 20$ m is the secondary array meant to weaken the noise emission in the dark zone (DZA in the picture). The area between the two arrays is the audience area. Additional microphones arrays are used in this instance for monitoring purpose (Figure 1a in **Paper B** (Pierangelo Libianchi et al., 2023)).

(Brunskog et al., 2019) presented a review of applications of sound field control to different environments with increasing topological complexity. The system performed well under conditions close to free-field and tended to deteriorate when reflections were present.

Larger propagation distances and the presence of obstacles reduced the effectiveness of the method. In (Caviedes Nozal et al., 2019a), a propagation model using a spherical harmonics expansion replaced the measured transfer functions. The coefficients of the expansion, the effective speed of sound and the noise were treated as stochastic variables. This approach used Bayes theorem to find the optimal values for these parameters. A likelihood distribution was built using the propagation model and normal and complex normal distributions were used as priors for the stochastic variables. These distributions were combined with a sparse dataset of measured transfer functions. The maximum a posteriori (MAP) of the resulting posterior distribution returned the optimal values for the parameters of the model. As shown in (F. M. Heuchel et al., 2020), this method vastly reduced the number of measurements needed for an ANC system and generalized well beyond the dark zone. This method also did not adapt to changing weather conditions. The match between the weather conditions at the time of the measurements and the one encountered at the time of using the system defined the overall performances. The limitations of this approach come mainly from the limitations of the propagation model: it did not allow to include reflections, either from the ground or obstacles, and the effects of an inhomogeneous moving medium, namely refraction. The filters were the least square solution with Tikhonov regularization as in previous cases and, as in those cases, it required the definition of an optimal regularization parameter to control the level reduction, the amplitude of the solution and the radiation pattern which complicated its use in practice. (Olsen and Møller, 2017) further described the dependence of the accuracy of the solution, thus the cancellation achieved, on temperature changes and how they could be mitigated to some extent by tuning the regularization parameter (Coleman et al., 2014).

We found that there is a gap in the study of the effects that all these approaches have outside of the region(s) under control. The noise reduction in the dark zone should not be achieved at the cost of increasing noise emissions in other directions, or at least not beyond a reasonable threshold. Indoor, and with sources surrounding the control region, this was done in (Betlehem and Teal, 2011; Elliott et al., 2012) using convex optimization and in (Abhayapala et al., 2019) by careful selection of the components of the subspace. However, the first is associated with a larger computational cost and the second is impractical due to the decomposition and mode selection that must be repeated at each frequency. The regularized least square can control the radiation pattern and the amplitude of the solution by tuning the regularization parameter. As pointed out in (Betlehem and Teal, 2011), finding the optimal value for this parameter is not a trivial task though.

Another gap consists of alternatives to convex optimization to enforce amplitude constraint on the solution at a cheaper computational cost. Limits on the amplitude are important in this application since the system is assumed to be linear and distortion from overdriving the control sources would degrade the performance. Furthermore, measuring the propagation paths can be expensive and, for this type of application, there has been no comparison with solutions obtained from simulations. The use of simulations instead of measurement could drastically simplify the deployment of this solution for practical applications.

2.1.1 Contributions

Paper B introduces a new approach for sound field control based on the conjugate gradient least square (CGLS). This is an iterative subspace method where the regularization parameter is replaced by the number of iterations. The regularization not only allows to control the trade-off between the amplitude of the solution and the residual but also the directivity pattern of the control array. The paper shows numerically why this is the case.

Replacing the regularization parameter with the number of iterations provides multiple advantages:

- Opposite to the regularization parameter, it is easy to set suitable stopping criteria. This approach swaps the nonphysical regularization parameter for meaningful stopping criteria in a similar way as in constrained convex optimization but without the increase in computational effort associated with it.
- The stopping criteria can be tailored to the requirements of a specific radiation pattern or any other problem-specific requirement.

The paper also addresses the second gap, describing how to include explicit constraints on the amplitude of the solution. This enforces a strict limit on the amplitude of the solution providing a precise control in contrast to the number of iterations or the regularization parameter. The only other method presented here that allows the definition of an amplitude constraint is convex optimization. However, the method proposed here is not as computationally demanding and presents lower requirements in terms of run-time and memory.

The method proposed is also compared with convex optimization and least square with regularization using both measured and simulated transfer functions. This allows the paper to address the third and last gap, highlighting the pros and cons of simulations against measurements.

Finally, **Paper A** contributes with a broad overview of the problem describing the milestones that have been achieved so far and the challenges to overcome to extend the range and generalization of these techniques. This work analyzes the original problem as two subproblems which allows to identify the weaknesses of each method used to solve each of the subproblems individually. The purpose of this paper is to provide a platform that serves as a starting point for future studies with the aim of further developing sound field control techniques for this type of application. The paper ends with a set of challenges that need to be addressed for these strategies to progress.

2.1.2 Experimental work

The method proposed in **Paper B** underwent a series of tests to validate its performance and analyse the advantages offered against other methods such as convex optimization and regularized least square. As mentioned in Chapter 1, the measurements required by this type of application are very demanding both in terms of equipment and logistics. Normally, the loudspeakers are large and heavy due to the frequency range that needs to be controlled. In addition, the venue where the tests take place needs to be large enough to accommodate the equipment, allow to test long range sound propagation and, in this case, the radiation properties of the secondary field outside the dark zone. Unfortunately, the pandemic affected this project and the planned measurement sessions in multiple ways. The personnel required for the preparation, transportation and setup of the equipment were largely unavailable due to reduced working hours. Furthermore, the candidate venues that could have been used were not available for the most part of this thesis. When available, it was possible to access them only with strong restrictions that hindered the extensiveness of the experimental validation. All the experiments performed to test the methods proposed in this thesis had to be performed in a 2:1 scale to counter some of these limitations.

The first test was a proof of concept undertaken in 2020, at the end of the first half of this project. This experiment had the sole purpose of showing that the selected algorithm could reduce the noise emission from a primary set of sources by synthesizing an anti-field with a second set of control sources. This experiment was conducted in the large semi-anechoic chamber at the d&b audiotechnik's facilities in Backnang, Germany. Figure 2.2a shows the setup used in this experiment which consisted of 5 primary source, spaced 0.5 m apart, and 4 secondary sources with a spacing of 1 m. The primary and secondary array were 7 m apart. An 8 by 4 rectangular microphone array was used to capture the performance of the system in the dark zone while two linear arrays of 10 microphones were placed along the side walls to capture the performance off-axis. An additional linear array of 12 microphones was placed 4 meters behind the dark zone to evaluate the level reduction beyond the dark zone. All the transfer functions used to generate the control filters were simulated. This experiment showed promising results that justified a second experiment in more realistic conditions.

The second experiment took place a short time after the first one and in open-air conditions. This experiment used the same configuration of source, both primary and secondary, and microphones to evaluate the performance as in the previous one. In this case, the control filters were generated using both simulated and measured transfer functions. Figure 2.2b shows the setup of this experiment which took place at a parking lot on the d&b audiotechnik's premises due to restrictions that forbade the use of any other space. The insertion loss achieved with the measured transfer functions reached a broadband level reduction of approximately 10 dB with little amplification outside the dark zone. The results with the simulated transfer functions provided an average reduction of 6 dB but with many fluctuations due to reflections from the buildings surrounding the parking lot that were not included in the simulations. Furthermore, the filters obtained with less regularization produced a level increase outside the dark zone. Even though the general results were positive, the experiment had a few limitations:

1. The presence of reflections made it harder to analyze different aspects of the results. One of these aspects is the level increases off axis which only occurred when using filters derived from simulations.
2. Only solutions obtained with 1 and 2 iterations of the algorithm proposed in **Paper B** could be tested. The number of control sources, since it was limited to four, did not allow to further increase the number of iterations.
3. The experiment was designed as proof of concept of the proposed algorithm in real conditions. However, it was not tested against other methods that have been used before in the literature.

For these reasons, a third and larger scale experiment took place on a football field the following year, when it was possible to access it. Figure 2.2c shows a picture of the setup. In this cases the number of primary and secondary sources was increased to 6 each and is the same as shown in Figure 2.1. This experiment was designed to avoid the limitations of the previous one and had the purpose of comparing the insertion loss and the spatial properties of the solution against other methods like convex optimization and regularized least square. The results of this experiment are presented in **Paper B**.

The original plan included an additional measurement campaign on a even larger scale that would have allowed us to observe effects produced by an inhomogeneous medium, such as refraction, on the performance of the system. However, this experiment had to be cancelled due to delays caused by complex logistics, further exacerbated by the pandemic, the negative outcomes from the development of a surrogate model for sound propagation, as detailed in **Technical Note F**, and the inconclusive results of an additional measurement campaign.

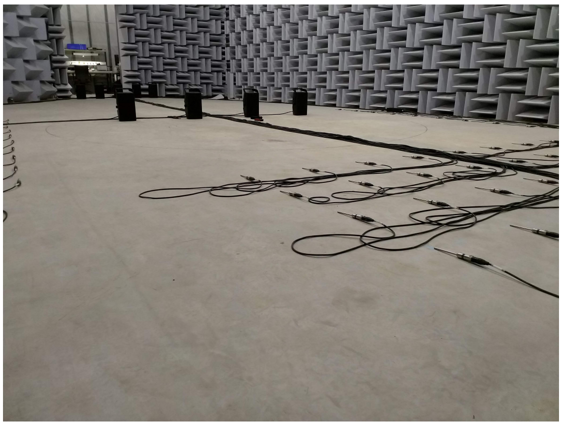

(a) Experiment in semi-anechoic conditions.

(b) Small scale outdoor experiment.

(c) Larger scale outdoor experiment (Figure 1c in **Paper B** (Pierangelo Libianchi et al., 2023)).

Figure 2.2: The three experiments conducted to validate the proposed method based on the conjugate gradient least square.

2.2 Characterization of the propagation paths

The characterization of the propagation paths can be done through measurements, simulations or using hybrid methods (F. M. Heuchel et al., 2020). Measurements become very expensive and logistically complicated over large distances. This thesis focused on simulations aiming to simplify the deployment of these techniques.

Simulations for outdoor sound propagation are used for multiple purposes. Different modelling techniques provide a tool-set to predict noise emissions from wind farms (McBride, 2017; Barlas et al., 2017; Kelly et al., 2018), traffic (Can et al., 2010; Mandjoupa et al., 2022; Abdur-Rouf and Shaaban, 2022; Tang et al., 2022; Zhang et al., 2022), etc.

There are many phenomena that affect sound propagation outdoor such as the ground effect (Taherzadeh and Attenborough, 1999; Attenborough, 2002), surface wave (Thomasson, 1976; Thomasson, 1977) and reflections from obstacles (Van Renterghem et al., 2005; Doc et al., 2015; Hornikx et al., 2010) among others. (Embleton, 1996; Attenborough, 2002) provide a summary of such effects. At large distances, it is important to properly characterize and model the medium, in particular the wind and temperature fields. (Wilson et al., 2014) provides a description of the main acoustic parameters outdoor and the effects introduced by the uncertainties in their estimation.

Many models have been developed over the years to model outdoor sound propagation. There are only a few analytical solutions to the problem of sound propagation in a moving inhomogeneous medium. These solutions are usually obtained using simple mathematical descriptions of the wind profile (Raspet et al., 1992; Attenborough et al., 1995). More complex and realistic conditions are modelled using numerical methods such as the Fast Field Program (FFP) (DiNapoli, 1970) , Crank-Nicholson Parabolic Equation (CNPE) (Ostashev et al., 1997), transmission line matrix (Hofmann and Heutschi, 2007), Finite Difference Time Domain (FDTD) (Ostashev and Wilson, 2015; Botteldooren, 1994) and the extended Fourier pseudo-spectral time-domain method (Hornikx et al., 2010) to name a few. A 3D parabolic equation method was developed in (Cheng et al., 2009). The 3D formulation allows to include a wind with a turning profile and the paper highlights the importance of properly including the wind instead of using the effective speed of sound approximation. The error is small when there is no crosswind and the height of the source and observer are similar. Otherwise, the approximation should not be used and whenever possible the 3D version should replace the 2D one. However, numerical methods tend to be time consuming and recent studies investigated the use of neural networks to provide surrogate models to speed up the simulations.

(Pettit and Wilson, 2020) uses a PINN, introduced in (Raissi et al., 2019), to provide a surrogate model for the FFP. However, the approaches tested failed to provide accurate predictions of the sound field and the latent variables included in the loss function of the network. This is consistent with the results presented in **Technical Note F**, which uses a surrogate model for the Helmholtz equation in an inhomogeneous medium.

Some of these methods are derived using approximations such as the effective speed of sound, horizontally homogeneous medium, use of the outgoing wave only, etc. Section 3.2.1 presents some of these approximation and the corresponding limitations. The accuracy of the models, and what they are capable of, depends on such limitations and the accuracy of the modelling parameters.

The influence of the temperature and wind fields on outdoor sound propagation is well documented (Caviedes Nozal et al., 2019b; Wilson et al., 2008; Cheinet et al., 2018). Nevertheless, there is a gap in the way the wind profile is modelled and the dynamics of the ABL are not considered in sound field control. The most used descriptor for the wind is the logarithmic profile (Bian et al., 2020; Gilbert and White, 1989; Van Den Berg, 2004; Elizabeth González et al., 2016; Taherzadeh et al., 1998; Hornikx et al., 2010) even though it can only be observed when the ABL is in a truly neutral regime and as an average property of the medium. In other regimes, the logarithmic profile needs a stability correction and Monin-Obukhov Similarity Theory (MOST should be used instead (Wilson et al., 2008). In other instances, the medium is only described as down or upward refracting without any specific profile (Salomons, 1998; Junker et al., 2007).

2.2.1 Contributions

Paper C describes the different regimes of the ABL, their characteristics and the corresponding stability corrections that should be applied to the wind and temperature profiles. Furthermore, it describes the limits and different factors that can compromise the accuracy of such profiles: stability conditions at the top of the ABL, the dependency of the wind direction on height, horizontal temperature gradient and other transitory phenomena. Even though it is impossible to predict the pressure in a deterministic sense, wind profiles averaged over space and time provide the most robust predictions (Wilson et al., 2008). Even though this is common knowledge in micrometeorology, some of these aspects are often overlooked when dealing with sound propagation and have not been considered for sound field control before.

While **Paper C** gives an overview of the effects that determine the wind profile, **Paper D** look more into the details of the profile in a neutral regime with stable stratification aloft, the so called conventionally neutral boundary layer (CNBL). This is one of the most common regimes for the ABL (Kelly et al., 2018; Zilitinkevich and Esau, 2005) and the logarithmic profile underestimates the wind speed over most of the height of the ABL (Wyngaard, 2010; P. Libianchi et al., 2023b). When the logarithmic profile is used in these conditions, it introduces a phase error and underestimates the energy refracted downward leading to a wrong prediction of the sound field on the ground. This paper quantifies this error, connects it to different section of the profile and provides a simple approximation to model the wind in such a regime. However, the results from this paper are limited to a fixed ABL depth and inversion strength. **Paper E** overcome this limitation and extend the study to a more comprehensive range of ABL depths and the inversion strengths. It shows the limits of the logarithmic profile and the range where it can be used without affecting the accuracy of the simulation. An important take away is that this range depends on the size of the low-level jet typical of a CNBL (see section 3.2.2 and **Paper C**) which depends on the inversion strength that can be modelled through the Brunt-Väisälä frequency.

2.2.2 Open issues

Paper D and **Paper E** provide important insights on how to model the wind and temperature profiles in one of the most common regime of the ABL. However, the influence of turbulence should also be included as it is expected to affect the interference pattern produced by the refracted waves. Furthermore, the ABL can be found in other two regimes: unstable and stable. The latter should be investigated more thoroughly since it produces conditions that are often favourable to sound propagation (see section 3.2.2). In this regime, turbulence are not important since they are confined to the residual layer above the surface. On the other hand, the change in wind direction with height can be as large as 45° over an ABL depth of 100-200 m and its effect on sound propagation should be assessed.

2.2.3 Experimental work

No experimental work was carried out for this part of the thesis. All the contributions made in this section came from either theory well established in micrometeorology or simulations.

2.3 Recovering the sound speed profile

The previous section highlights the importance of knowing the wind and temperature, and hence the profile of the speed of sound. It is possible to directly measure these quantities using SODAR, LIDAR or anemometers placed at different heights. The problem with this approach is its scalability. LIDAR and SODAR usually consist of expensive, heavy, and delicate equipment whose use is hard to justify for an outdoor live event, even more so if considering the limited time window in which they take place. Anemometers are cheaper and easier to handle but one would have to place several of them at different heights which would turn out to be difficult for events of transitory nature. Indirect or passive measurements provide a more promising approach. These methods do not measure the quantity of interest directly. Instead, they measure another variable that is easier to appraise and that is related to the quantity of interest. Examples of such approaches are commonly found in ocean acoustics to recover the sound speed profiles from measurement of the pressure, usually at a vertical array of sensors. (Park et al., 2010) back-propagated the pressure waves from a vertical array of sensors back to the sources. At each step it reconstructs the vertical sound speed profile, the experimental geometry and the geoacoustic

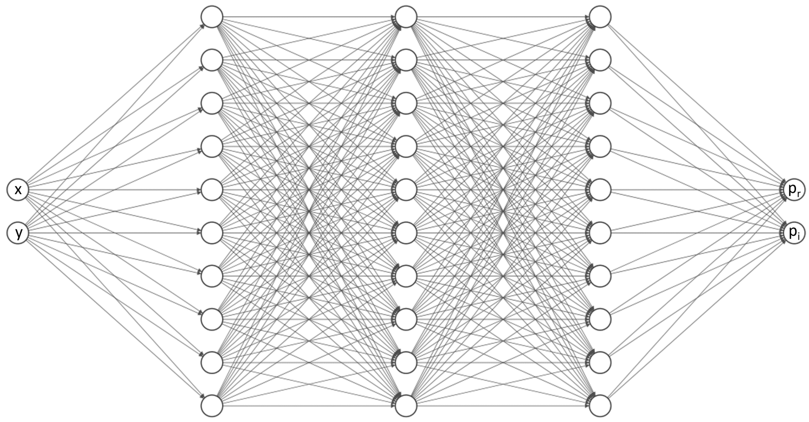

Figure 2.3: An example of a fully connected neural network.

parameters. The results showed good agreement with *in situ* measurements. (Gerstoft and Gingras, 1996) used a global optimization approach using Monte Carlo search based on genetic algorithms to solve the same problem. The predicted geoacoustic parameters and pressure field provided a good match with measurements and the stability of the parameters was improved performing the inversion at multiple frequencies. Another alternative is compressive sensing as proposed in (Bianco and Gerstoft, 2016). (Bianco and Gerstoft, 2017) replaced traditional empirical orthogonal functions with dictionary learning to generate a set of shape functions to be used for sparse processing. This approach led to increased accuracy with a negligible increase in computational effort.

In open air, (F. M. Heuchel et al., 2019) proposed a fully connected neural network, similar to the one shown in Fig. 2.3, to derive a correction in the form of a delay to apply to the transfer functions to compensate for changes in the weather conditions relative to a reference set of measured transfer function. This method allowed to reduce the phase error introduced by a variable weather, but it does so only for the direct wave. However, the results were promising, and the method can be an effective tool for distances smaller than 300 m. At larger distances, effects produced by an inhomogeneous moving medium such as refraction become relevant and affect the transfer functions in a more complex way that cannot be compensated for by a simple delay.

An alternative can be found in the full waveform inversion, (FWI)) (Aghamiry et al., 2019), a method first developed and used in seismology. This method was first introduced in (Virieux and Operto, 2009). It was formulated as a convex optimization problem: the main objective is to match predictions to measured data with the constraint given by the discretized governing partial differential equation (PDE). Optimization can be formulated in different ways, with different degrees of complexity. Lately, the alternate direction method of multipliers (ADMM) provided an effective way to deal with this problem (Aghamiry et al., 2019). Recently, classic numerical methods have been replaced by neural networks. An example is the neural-FWI from (Sitzmann et al., 2020), which uses PINN (Raissi et al., 2019) to learn a surrogate model for outdoor sound propagation replacing the discretized PDE. In a second step, this method tunes the acoustic parameter of the medium using measurements of the sound field. The potential advantage of this method is that, once the network is trained, it can quickly provide a prediction at a query point that does not have to lie on a predefined grid.

2.3.1 Preliminary work

Some preliminary work has been done in this thesis to use a the neural-FWI for outdoor sound propagation problem. **Technical Note F** describes this preliminary work and uses the method described in (Sitzmann et al., 2020) to develop a surrogate model for outdoor sound propagation and to recover the sound speed profile from pressure measurements.

The use of a surrogate model has shown potential to solve both these tasks. The results are promising when using a PML. However, more work is required to include boundary conditions to model the influence of the ground and to regularize the solution when recovering the sound speed profile. The findings in this work are consistent with the findings in (Pettit and Wilson, 2020) and this type of network still has difficulties in modelling the pressure field due to its spatial complexity. Furthermore, the surrogate model was not yet able to recover the underling sound speed profile from pressure data and more work is required to introduce additional constraints for the surrogate model and for the optimization routine.

This type of network uses a cost function that is a combination of the PDE governing the problem, boundary conditions and possibly additional regularization terms. The gradient associated to terms that are not the PDE has shown the tendency to vanish. As a consequence, the model tends to overfit the PDE term. The poor predictions obtained when using boundary conditions might be a result of this and could be improved using adaptive weights applied to the different terms of the cost function (Wang et al., 2021). The same problem might be affecting the reconstruction of the speed of sound. Furthermore, additional regularization on the wavenumber of the speed of sound field could be used to achieve a better reconstruction.

The data used to recover the sound speed profile was initially synthesized artificially using the finite element method (FEM). The original plan was to then use data gathered during a measurement session conducted at DTU's Risø campus in August 2022 so that the prediction of the surrogate model could be compared with data from the sonic anemometer on site. Figure 2.4 shows the setup. The purpose of this experiment was to gather a set of transfer functions in outdoor settings with a propagation range large enough to include effects of a moving inhomogeneous medium, such as refraction. To this end the setup counted with a subwoofer as an acoustic source and a linear array of 4 microphones at 295 m from the source and with a spacing of 10 m. This distance places the microphones within the caustic field produced by the interaction of direct, refracted and reflected waves.

Unfortunately, the surrogate model was not mature enough for this step and the measurement session provided inconclusive data due to logistical and technical complications. Due to time constraints, it was not possible to repeat this experiment. However, similar measurements are important for further development of a surrogate model for outdoor sound propagation and should be repeated. The data gathered must include the effects produced by phenomena such as refraction. This can be done only when propagation occur over large distances.

2.4 Summaries of the included papers

Paper A: A review of techniques and challenges in outdoor sound field control (published in Proceedings of Inter·Noise 2022, International Congress and Exposition on Noise Control Engineering)

The paper provides an overview of the different techniques recently applied to re-

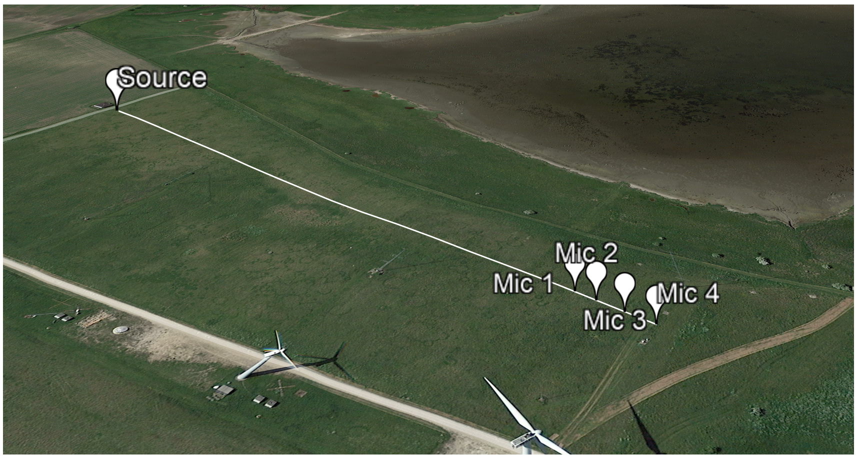

(a) Satellite view of the measurement setup. The distance between the source and mic 4 is approximately 326 m.

(b) Microphones 1 to 4.

(c) Close-up of a microphone in the field.

Figure 2.4: An overview of the setup used for the measurement session at DTU Risø campus.

duce noise emissions from outdoor live events and the challenges to further improve their range and generalization.

The paper first introduces the use of control sources to reduce the noise emission in a target zone usually referred to as quiet or dark zone and the use of pressure matching to find a solution (see Section 3). It then frames the problem as two subproblems: the design of the filters to apply to the control sources and how to characterize the propagation paths from the noise and control sources to the dark zone.

For the first sub-problem, it distinguishes between feedforward and feedback algorithms (Nelson and Elliott, 1992). The methods considered for the former are the least square with Tikhonov regularization (F. M. Heuchel et al., 2020), iterative subspace methods (see **Paper B**) and constrained convex optimization (Betlehem and Teal, 2011). The paper then describes the advantages and disadvantages of each of these methods. They are mainly related to the definition of the regularization parameter or the constraints, the computational requirements, and the control of the radiation pattern produced by the control sources.

The FxLMS (Nelson and Elliott, 1992) provides an example of a feedback method. Opposite to the previous approaches, this one provides filters that adapts over time to changes in the propagation conditions. This method also comes with some drawbacks related to the computational burden of multi-channel systems and the location of the quiet areas that can be mitigated using the methods from(Spors and Buchner, 2008) and (Plewe et al., 2020), respectively.

All the methods in this section require a characterization of the secondary transfer functions and, for the feedforward methods, also of the primary propagation paths, which leads to the second section of the paper.

The paper outlines three possible strategies to deal with the second sub-problem:

- Data-based: The two propagation paths can be accurately described with a dense enough measurement grid. However, this approach is hard to scale presenting logistical limitations. Furthermore, the solutions obtained with this approach degrade as the propagation conditions deviate from the conditions encountered during the measurements. A way to counter this problem at short distances (less than 300 m) is illustrated in (F. M. Heuchel et al., 2019).
- Model-based: Outdoor sound propagation models can replace the measurements and simulate the propagation paths. Each model has its limitations that are a result of the approximations used to derive their governing equations. The paper provides a brief description of the main advantages and disadvantages of some of the most established numerical methods such as FFP, CNPE and FDTD. The main advantage of these methods is that the solutions could potentially be updated as the propagation conditions change. The main drawback of this strategy is the computational effort and run-time involved.
- Hybrid: This strategy was proposed in (Caviedes Nozal et al., 2019a) and applied in (F. M. Heuchel et al., 2020). It uses a sparse measured dataset to fit a propagation model based on spherical harmonics using Bayesian inference. The coefficients of the spherical harmonics expansion, a generic delay accounting for the properties of the medium and the background noise are cast as stochastic variables with normal or complex normal prior distributions. This allows to vastly reduce the number of measurements while keeping most of the accuracy of the data-based approach. It also shows good generalization outside of the dark zone. The limitations are given mainly by the propagation model which does not include reflections and refraction from a stratified medium. As the data based approach, also the performance of this method is tied to the match between the weather conditions during the measurement/fitting and the conditions during the use of the system.

The paper ends giving an overview of the phenomena that affect outdoor sound propagation and whose characterization is necessary for any propagation model. There are multiple factors that must be considered. However, the paper focuses on ground reflections and sound speed profiles. Many models have been developed to deal with the former whose accuracy depends on the type of ground. An overview can be found in (Attenborough et al., 2011). The sound speed profiles are hard to measure, change over time and depends on the regime of the ABL. The paper describes the probability distribution of the different regimes according to (Kelly and Gryning, 2010) and different models (Kelly et al., 2019; Zilitinkevich and Esau, 2005; Gryning et al., 2007) for the commonly occurring conventionally neutral (or quasi-neutral) boundary layer.

After this broad overview of the different techniques, the paper concludes that the results at shorter distances are promising even though work is still needed to improve range and generalization. It highlights areas where improvement is most needed and how it is crucial to chose the right combination of methods to solve both sub-problems depending on the specific requirement of any specific application to maximize the outcomes.

Paper B: Active noise control at low frequencies for outdoor live music events using the conjugate gradient least square method (published in Applied Acoustics, 205, 2023)

The premise of this paper is that other methods used in sound field control such as regularized least square and convex optimization present drawbacks that can make their day to day use impractical. Such drawbacks usually revolve around the difficulty of finding the optimal parameters, control over the directivity of the secondary array, amplitude constraints and computational effort, or the combination of the above. This paper proposes the use of the CGLS algorithm for sound field control. This is an iterative subspace method that replaces the regularization parameter with the number of iterations. This simplify the choice of the regularization through the introduction of suitable stopping criteria.

The paper starts by introducing the theory behind the proposed method and its numerical properties. It describes how the number of iterations replaces the regularization parameter and how it can be used to control the directivity of the control array. It also describes a method that can be paired with the CGLS to enforce explicit amplitude constraint on the solution. Alternatively, this would be possible only with convex optimization but at a larger computational cost.

The paper then compares the proposed method to convex optimization and least mean square with Tikhonov regularization in an experiment performed in outdoor conditions. The setup is the same shown in Figure 2.1 and in the picture in Figure 2.2c. The paper uses the insertion loss as the metric to compare the performance provided by each method. Figure 2.5 shows the results at the four microphone array displayed at the setup. The top left plot shows the performance measured in the dark zone. The reduction achieved with the different approaches are similar with the exception of the method proposed in the paper with a single iteration, since it applies a larger regularization. The plot on the top right show the insertion loss at the array at the far back and illustrates the drop in performance beyond the dark zone for this particular setup. The two plots at the bottom show the performance at the array to the left and right of the dark zone, respectively. These results show how the methods that provides the largest level reduction in the dark zone are also more prone to increase the sound pressure level in other directions. After this consideration, the paper analyze the spatial properties of each solution. Furthermore, it is possible to use either measured or simulated transfer functions to derive the control filters and this experiment also study the difference in the solutions provided by each of these two approaches. The results show that, using simulated transfer functions, the uncertainties encountered in practical applications reduce the predicted gap between the performance obtained using different algorithms and amount of regularization, leading to similar noise reduction.

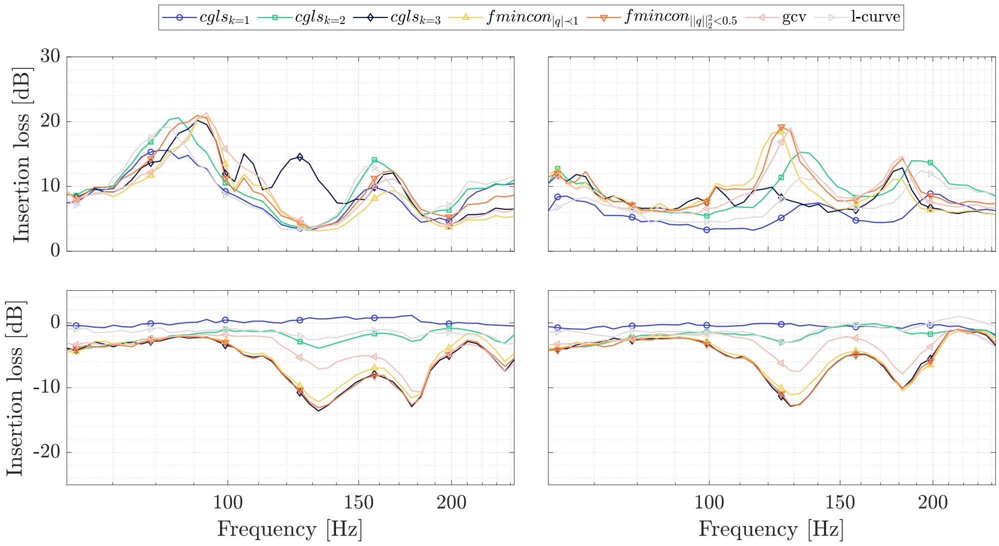

Figure 2.5: Plot from **Paper B** showing the insertion loss (IL) from the measurements set using filters derived from simulated transfer functions. Top left: loss averaged over the dark zone. Top right: loss averaged over an array behind the dark zone. Bottom left: loss averaged over an array to the left of the mdark zone. Bottom right: loss averaged over an array to the right of the dark zone (Figure 2 in **Paper B** (Pierangelo Libianchi et al., 2023)).

The use of measured transfer functions results in larger insertion loss within the dark zone but these solutions tend to not generalize as well beyond it, in particular when there are reflections.

The paper then studies the numerical properties of each method and their connection to the directivity pattern of the control array. The regularization affects the weights applied to a given source mode which will then define the strength of the corresponding pressure mode in the solution. Solutions with weaker regularization tend to place larger weights on high order modes. These modes present complex spatial properties and are responsible for radiation outside of the dark zone.

The paper also presents a sensitivity study of the proposed method to uncertainties in the speed of sound that can be caused by temperature or wind fluctuations. The filters are computed simulating the primary and secondary paths using a specific speed of sound. Afterwards, the filters are applied to transfer functions simulated using 512 different speed of sounds following a gaussian distribution centered at the value used to derive the filters. Figure 2.6 shows the histograms with the distribution of insertion losses provided by the proposed method with the uncertain transfer functions for an increasing number of iterations, i.e., decreasing regularization. The solution with the strongest regularization is the most robust one; even though it can achieve a smaller maximum insertion loss. The solution with the weakest regularization is less robust but the maximum achievable insertion loss is 10 dB higher. The smaller regularization has the effect of increasing the amplitude of the solution, which in this case hits the constraints. This has the effect of limiting the maximum achievable insertion loss and its dispersion. When the regularization is somewhere in between, the solution does not hit the constraints and reaches the largest achievable insertion loss under the conditions of the simulation. It also shows a larger dispersion than the other cases cases which means larger potential gains at the cost of reduced robustness.

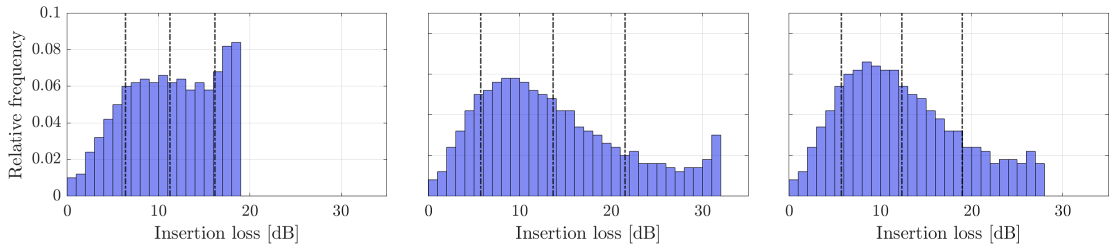

Figure 2.6: Histograms with the insertion loss obtained from the 512 realizations averaged over space and frequency. Dashed lines show the overall mean and mean plus/minus one standard deviation. Left: $cgls_{k=1}$; center: $cgls_{k=2}$; right: $cgls_{k=3}$ (Figure 12 in **Paper B** (Pierangelo Libianchi et al., 2023).)

.

Finally, the paper present a convergence study. In this section the filters are obtained using different number of iterations and simulated transfer functions using grids of different resolutions. In general, the simulations show that increasing the resolution also increase the insertion loss. However, when these filters are applied to measured transfer function, the gain offered by the finer resolution is largely lost. The increase in details makes these solutions more sensitive to modelling errors. It is different for the filters obtained using the weakest regularization when applied to measured transfer functions. In this case, at low frequencies, the rough resolutions return solutions with amplitudes that hit the constraints. This drastically reduces the performance. Finer grids lead to better conditioned problems whose solutions have smaller amplitudes that do not violate the constraints and provide much better results.

Paper C: Notes on the characterization of the wind profile in the atmospheric boundary layer (unpublished manuscript)

This paper elaborates on the theory introduced in Section 3.2.2. The main purpose is to describe how the wind profile can be modelled in the different regimes of the ABL and in which scenarios these profiles might fail. It starts by providing a description of the three main regimes of the ABL and introduces the surface heat flux Q_0 and the Obukhov length L, two common stability measures used for the surface layer. The following section describes the stability corrections that need to be applied to the widely used logarithmic profile depending on the regime of the ABL. It shows how these expressions can be derived using Monin-Obukhov Similarity Theory (MOST) and the Buckingham Pi theorem. However, this method, and the profiles that can be derived using it, has limits. The reason is that its derivation only considers the dynamics of the surface layer, the lowest 10% of the ABL. This is a problem when the profile needs to be extended beyond the surface layer or when particular stratification conditions at the top of the ABL affect the wind profile also close to the ground. The manuscript references different models that can be used in such circumstances and the strategies behind some of them.

An additional limitation with traditional profiles is that they do not consider the change of direction with height. The manuscript shows how to derive the range of such change by considering a steady, horizontally homogeneous mean flow in Eq. (3.19) from Section 3.2.2 in the case of a non-turbulent limit and within the ABL. The direction is usually given relative to the isobars and is referred to as cross-isobaric angle. The paper references expressions found in the literature to calculate this angle in a stable, truly and conventionally neutral boundary layer. It also describes additional factors that affect the direction of the wind and its rate of change depending on the regime of the ABL.

Finally, the manuscript focuses on the stable ABL, which tends to occur at nighttime and is favourable to sound propagation. It highlights some transitory phenomena that can disrupt the models for the wind profiles and even though they are hard to predict and account for, they are worth knowing to explain possible deviation and inaccuracies between simulations and measurements.

Paper D: **Sensitivity study of the predicted acoustic pressure field to the wind profile in a conventionally neutral boundary layer** (to appear in The Journal of the Acoustical Society of America, 154 (2), 2023)

The logarithmic profile is one of the most widely used descriptors for the wind speed across the ABL in outdoor sound propagation (Bian et al., 2020; Gilbert and White, 1989; Van Den Berg, 2004; Elizabeth González et al., 2016; Taherzadeh et al., 1998; Hornikx et al., 2010). However, this profile is not accurate when the ABL is not neutral and MOST should be used instead (Wilson et al., 2008). Neutral and quasi-neutral regimes occur often (Kelly and Gryning, 2010) with the caveat that they usually also present a stable stratification close to the top of the ABL (Zilitinkevich and Esau, 2005) leading to a CNBL. This scenario produces a speed increase known as Low-Level Jet (LLJ) characterized by a larger speed than predicted by the logarithmic profile that peaks at super-geostrophic speeds close to the top of the ABL before decreasing and converging to the geostrophic wind speed. The aim of this paper is to analyze the error introduced by the use of the logarithmic profile in a CNBL to find a range limit where this profile can be used and to quantify the effect of the LLJ on the pressure field on the ground.

The first step is to introduce a correction to the logarithmic profile to achieve a better approximation of the wind dependence on height in a CNBL. The same is done for the temperature profile, where the effect of the stable stratification appears as an increase in potential temperature with a slope proportional to the Brunt-Väisälä frequency N squared. The theory section ends with the introduction of the vertical wavenumber for a stratified moving medium. The vertical wavenumber allows to calculate the highest turning point and maximum elevation angle for a given set of wind and temperature profiles.

The paper considers five profiles as illustrated in Figure 2.7: absence of wind, a logarithmic profile, a realistic CNBL profile, a CNBL profile without an LLJ and one with a stronger LLJ. The figure also shows the profile of the potential temperature, even though its influence is negligible compared to the wind, and the corresponding effective speed of sound profiles. The profiles are determined using a fixed ABL depth h'. In addition, the model for the wind in a CNBL also uses the parameter h to define the height where the wind speed peaks and Δh for the thickness of the layer where the stable stratification is located.

These profiles were chosen so that the corresponding sound fields could be compared in pairs to study the contributions made by different sections:

- The sound fields produced in absence of wind and by the logarithmic profile (p1 and p2, in the figure) were compared to show the effect produced by the downward refraction generated by the latter against its absence in the former.

- The sound fields produced by the logarithmic profile and by the CNBL profile without LLJ (p2 and p4) were compared to study the effect of the mismatch in wind speed and its gradient close to the ground.

- The sound fields produced by the CNBL profile with and without the LLJ (p3 and p4) were compared to study the effect of the LLJ.

- The sound fields produced by the CNBL profile with the stronger LLJ and without (p5 and p4) were compared to asses the effect of a stronger inversion, hence a stronger LLJ.

Each profile was used to simulate the corresponding sound field using the wide-angle CNPE implemented in (Wilson, 2015). Using different metrics, the study shows that the logarithmic profile in this regime introduces different errors. First it underestimates the wind speed, introducing a phase error in the direct wave that increases with the distance. In addition, it underestimates the highest turning point and the amount of energy refracted downward which leads miscalculations of the contributions at large distances and not properly modelling the interference pattern.

However, it is enough to account for the speed increase for distances shorter than 2 km. The modelling of the wind can be simplified in this way. The LLJ should be included for distances larger than 2 km where the contributions from the refraction are not negligible anymore.

Paper E: **Phase error sensitivity to the inversion strength and depth of the boundary layer in a conventionally neutral regime** (to appear in proceedings of Forum Acusticum 2023)

This paper extends the study performed in **Paper D** that analyzed the prediction error introduced by using a logarithmic wind profile in a CNBL. In that case, the focus was on different portion of the profiles and how they shape the error. However, the study was conducted for a fixed ABL depth and inversion strength. In this work, the focus is on the sensitivity of the error to these two parameters. This paper uses the profile proposed by (Luoqin Liu and Stevens, 2022) which consists of a logarithmic profile plus a correction that depends on both the ABL depth and the inversion strength. For the study to be representative, the analysis included 14 ABL depths ranging from 200 m to 1000 m, and 20 inversion strength represented by a Brunt-Väisälä frequency ranging from 6 mHz to 14 mHz. The choice was based on values commonly found in the literature (Kelly et al., 2019). A pair of profiles, with and without the correction term, was computed for each combination of these two parameters. Figure 2.8 shows a subset of the wind profiles, with and without the correction term, and the corresponding effective speed of sound profiles. The CNPE was used to simulate the sound field produced by each pair and then compared them to study the dependency of the error on the ABL depth and inversion strength.

The results show how the phase error presents two overlapping patterns: one with a low and one with a high wavenumber. The low wavenumber pattern is due to

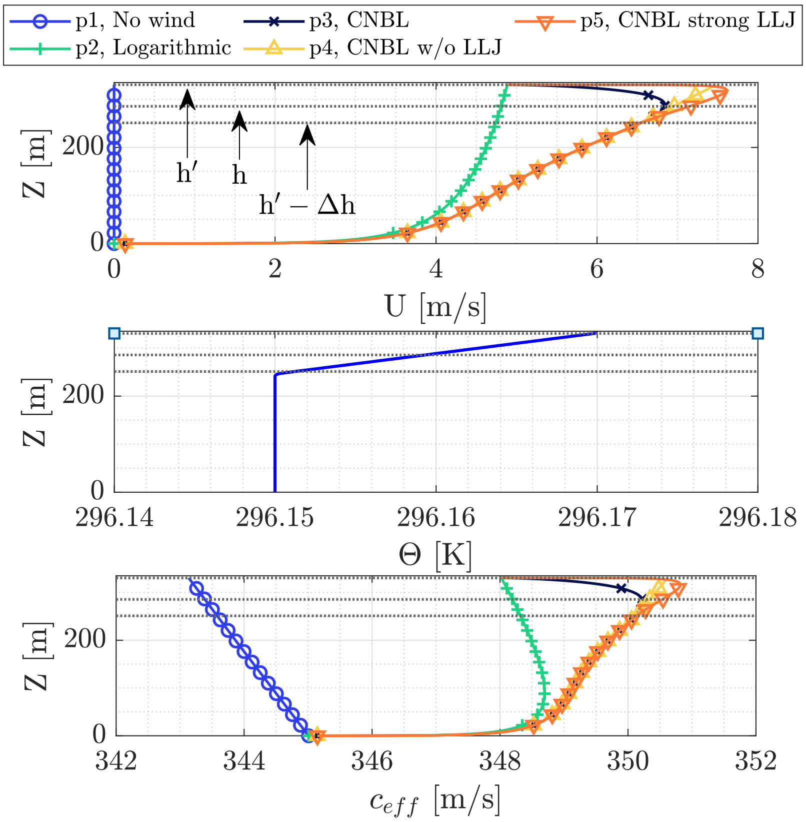

Figure 2.7: The five wind profiles and the temperature profile used for the sensitivity study (Figure 1 in **Paper D** (P. Libianchi et al., 2023b)).

the different wind speed and gradient close to the ground between the profile with the correction term and the corresponding one without. This error increases with distance and is strongly dependent on the inversions strength. As the inversion strength increases, the difference in wind speed increases with distance at a higher rate. The high wavenumber pattern is produced by interference at the ground produced by different amount of energy that is refracted downward. The interference pattern becomes more complex and occurs closer to the source as the downward refracting regions gets taller. This region gets taller when either the ABL depth or the inversion strength increase. The magnitude error only presents the high wavenumber pattern since it is produced by a shift in the interference pattern which is in turn a result of the different refraction introduced by the profiles thus depends on both the ABL depth and inversion strength. Finally, the study found that the error introduced by using a logarithmic profile in a CNBL is negligible at distances smaller than 1 km. At larger distances the phase error cannot be neglected anymore, even though it depends on the inversion strength which cannot be measured close to the ground. This conclusions generalize the results from **Paper D**.

Technical Note F: A preliminary study for the use of a surrogate model in outdoor sound propagation and sound speed profile recovery (unpublished manuscript)

This manuscript presents a preliminary study of the use of a surrogate model for outdoor sound propagation and its aim is twofold. First, analyze the possibility of

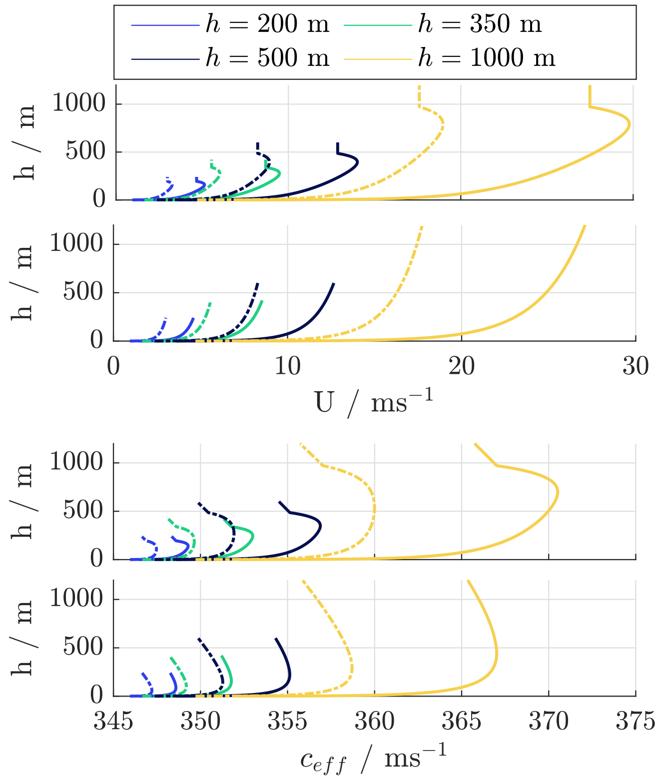

Figure 2.8: A subset of the profiles used in **Paper E**. The plots show: the wind profiles in a CNBL (top), the corresponding logarithmic profiles (second) and their corresponding effective speed of sound (third and fourth, respectively). The plots show the profiles for four different ABL depths (including the shallowest and the deepest) and two inversion strengths: the smallest (N = 6 mHz, dashed) and the largest (N = 14 mHz, solid) (Figure 1 in **Paper E** (P. Libianchi et al., 2023a)).

using a surrogate model for the Helmholtz equation to speed up the acoustic simulations in a large domain with a moving inhomogeneous medium using a PINN (Raissi et al., 2019). In this particular instance, we use a periodic activation function that showed encouraging results in similar problems (Sitzmann et al., 2020). This type of network is known as SIREN (Sinusoidal Representation Network). Second, study the use of modified network so the model can be used to recover the sound speed of the medium using sparse pressure measurements on the ground by employing a neural-FWI approach (Sitzmann et al., 2020).

The network used in this study returns the real and imaginary components of the complex pressure at one query point whose normalized coordinates are provided as an input. Knowledge of the problem, i.e. the Helmholtz equation, is provided to the network through its loss function using automatic differentiation (Güneş Baydin et al., 2018). The manuscript starts by modelling the Helmholtz equation in a homogeneous field under free-field conditions. This is done by defining a homogeneous sound speed and modelling the free-field conditions using a perfectly matched layer (PML) included in a modified Helmholtz equation. Figure 2.9 shows the real component of the pressure field predicted by the surrogate model. The prediction closely match the analytical solution in this case. The following experiments consist of replacing the PML with problem specific boundary conditions. The study tests an impedance boundary condition to simulate the ground and a ρc condition enforced by appending the corresponding terms to the loss function. Even though the network predicts the reflections from the boundary, the interference pattern only slightly resembles the ground truth simulated using the FEM in COMSOL.

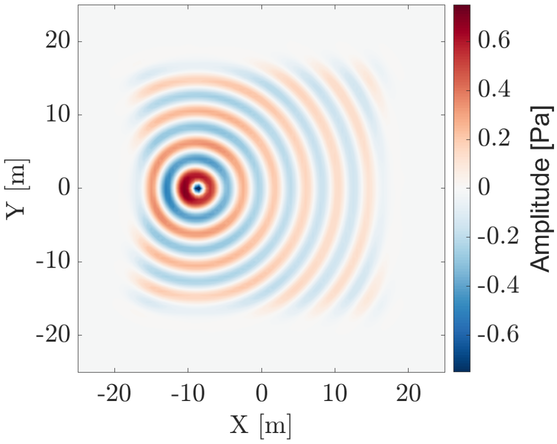

Figure 2.9: Real part of the pressure field generated by a point source located at $x = -8.7$ m, $y = 0$ m as predicted by the network (Figure 3 (left) in **Technical Note F** (Libianchi and Karakonstantis, 2022)).

The second part of the paper deals with an inhomogeneous medium and with the inverse problem of reconstructing the sound speed profile. The network is trained using a sound speed that is only a rough approximation of the ground truth. This work employed different sound speed fields: homogeneous with a circular discontinuity at the center, homogeneous with a sound speed increasing in the shape of a gaussian pulse and linearly increasing with height. In all the cases the network failed to properly model the sound and sound speed fields in both the forward and inverse problems. It shows a tendency to over-fit the PDE term in the loss function. As it was the case with the boundary conditions, this might be due to a vanishing gradient for all the terms in the loss functions except for the PDE and could be possibly mitigated using adaptive weights applied to each of the terms in the loss function separately (Wang et al., 2021).

3 Theory and background

In this section we present some of the fundamental theory that is used in the different papers that compose this thesis. The reader who is familiar with the theory presented in any of these sections can just skip it and directly read the paper.

In this application, we want to generate a secondary field that matches a desired field, in this case the field produced from the sources on stage. This is a pressure matching problem and the starting point of this section.

The pressure matching problem can be formulated as follows:

$$\min_{\mathbf{q}_s} ||\mathbf{H}_s\mathbf{q}_s - \mathbf{p}_p||_2^2, \tag{3.1}$$

where $\mathbf{p}_p \in \mathbb{C}^M$ is the primary pressure field at the M receiver points, $\mathbf{q}_s \in \mathbb{C}^N$ is the strength of each of the N sources and $\mathbf{H}_s \in \mathbb{C}^{M\times N}$ is the transfer functions matrix that maps source strength to pressure, that is $\mathbf{H}_s : \mathbf{q}_s \mapsto \mathbf{p}_s$, where $\mathbf{p}_s \in \mathbb{C}^M$ is the secondary pressure field. The solution to this problem allow us to generate a secondary sound field that matches the desired primary field. For the fields to cancel each other, the solution will need to have its phase inverted so as to be in opposition of phase with the primary field.

This problem can be solved in different ways. Independently of the method chosen, it is necessary to characterize the primary and secondary propagation paths. It is useful to look at this problem as a combination of two sub-problems: finding the optimal source strengths and characterize the primary and secondary paths. This is the approach taken in **Paper A** and that is also used throughout this thesis, this section included.

The rest of this section is then divided in two main subsections. The first looks mainly at the basics of solving inverse problems, since the pressure matching problem is often solved using this framework. The second part of this thesis focuses on sound propagation outdoor. This section is further organized in two parts: outdoor sound propagation models, describing their approximations and limitations, and fundamentals of micrometeorology.

3.1 Numerical solutions to the pressure matching problem

The pressure matching problem from Eq. 3.1 can be solved in different ways. This section describes how to find a solution using the method reviewed in **Paper A** and applied in **Paper B**. In these paper the approach to obtain the solution sought after is by framing the pressure matching problem as an inverse problem.

3.1.1 Inverse problems

The pressure matching problem is an inverse problem since it looks for the weights $\mathbf{q}_s$ that can be seen as the causal factors producing the sound field $\mathbf{p}_p$ using the propagation model given by $\mathbf{H}_s$. A trivial solution to this problem is $\mathbf{q}_s = \mathbf{H}_s^{-1}\mathbf{p}_p$. Although, this is not possible in most cases. Since the number of sensors is often larger than the number of sources ($M > N$), the matrix $\mathbf{H}_s$ is not square, the problem is over-determined and has no exact solution. An approximate solution can be found by minimizing the residual. This can be done by taking the differential of Eq. (3.1) to obtain the corresponding normal equation. Setting the normal equation to 0 and solving for $\mathbf{q}_s$ we obtain the approximate solution:

$$\tilde{\mathbf{q}}_s = (\mathbf{H}_s^{\mathsf{H}}\mathbf{H}_s)^{-1}\mathbf{H}_s^{\mathsf{H}}\mathbf{p}_p, \tag{3.2}$$

where the $^{\mathsf{H}}$ stands for the Hermitian transpose. The term on the right hand side multiplying the pressure is often referred to as the Moore-Penrose pseudo-inverse. The solution in Eq. 3.2 is the ordinary least square solution. However, in most cases this solution cannot be used as it is. This problem is ill-conditioned and this solution is prone to overfitting the noise and can lead to unstable solutions. This means that small changes in the data in $\mathbf{p}_p$, due to either background noise from measurements or numerical errors owned to finite precision from simulations, produce large changes in the solution Hansen, 2010.

To see why that is the case we need to introduce the Singular Value Decomposition (SVD). Using this decomposition, we can write $\mathbf{H}$ as follows:

$$\mathbf{H}_s = \mathbf{U}\mathbf{\Sigma}\mathbf{V}^{\mathsf{H}} \tag{3.3}$$

With:

- $\mathbf{U} \in \mathbb{C}^{M\times M}$ are the left singular vector and form an orthonormal basis for the pressure field, i.e. each column can be seen as a mode of the pressure field. These vectors are also the eigenvectors of the matrix $\mathbf{H}_s\mathbf{H}_s^{\mathsf{H}}$.

- $\mathbf{\Sigma} = diag(\sigma_1, \sigma_2, ..., \sigma_N) \in \mathbb{R}^{M\times N}$ is a diagonal matrix with the singular values, which express the radiation efficiency of each mode and where $\sigma_1 \geq \sigma_2 \geq \ldots \geq \sigma_N$. The singular values are equivalent to the eigenvalues of the matrices $\mathbf{H}_s\mathbf{H}_s^{\mathsf{H}}$ and $\mathbf{H}_s^{\mathsf{H}}\mathbf{H}_s$.

- $\mathbf{V} \in \mathbb{C}^{N\times N}$ are the right singular vectors and form a complex orthonormal basis for the source strength field, i.e. each column can be seen as a source mode. These vectors are also the eigenvectors of the matrix $\mathbf{H}_s^{\mathsf{H}}\mathbf{H}_s$.

It is usually the case to have more receiver points than sources so $M > N$, thus when we multiply $\mathbf{U}$ by $\mathbf{\Sigma}$, only the first N modes are retained. This means that the number of sources employed defines the complexity, i.e. the maximum spatial frequency, of the pressure field. The pressure modes from $N+1$ to M are not active, they can be seen as if weighted by 0 singular values.

The pressure modes show an increase in complexity and spatial frequency (wavenumber) as the mode order increases (see Figure 3.1a). The source mode i generates the pressure mode i and this mode is radiated with an efficiency given by the i-th singular value. For instance, if $\mathbf{q}_s$ is equal to the first source mode in Figure 3.1c, it will generate a sound field in the shape of the first pressure mode from Figure 3.1a with an amplitude given by the first singular value in Figure 3.1b. Similarly, more complex source strength vectors can be described as a superposition of the source modes which in turn define which pressure modes are active and the weight applied to them.

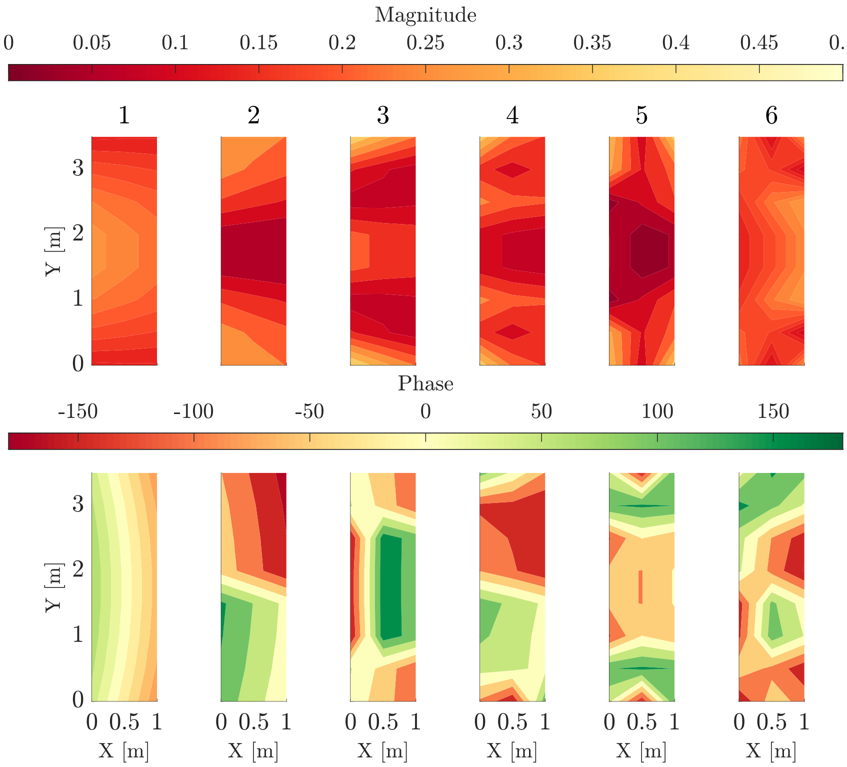

(a) Left singular vectors/Pressure modes (Figure 8 in **Paper B** (Pierangelo Libianchi et al., 2023)).

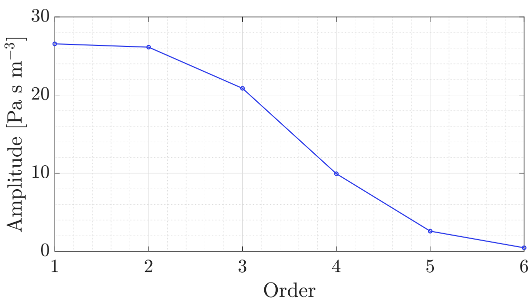

(b) Singular values/Radiation efficiency.

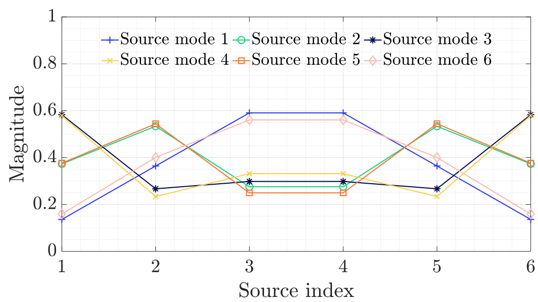

(c) Right singular vectors/Source modes.

Figure 3.1: Singular value decomposition of the secondary transfer function matrix from the setup in Figure 2.1 at 125 Hz.

Using the SVD we can rewrite Eq. (3.2) as follows:

$$\tilde{\mathbf{q}}_s = \mathbf{V}\mathbf{\Sigma}^{-1}\mathbf{U}^{\mathsf{H}}\mathbf{p}_p. \tag{3.4}$$

We can see here that the singular values need to be inverted to compute the solution. We also see that the amplitude of the singular values decreases for increasing order. This means that small singular values, associated to modes that do not radiate efficiently, become large amplification factors when inverted. After inversion, high order modes, which are often activated by noise due to their higher spatial frequency, are amplified making the solution unstable. Furthermore, the amplitude of the amplification factors, especially for high order modes, play a large role not only on the amplitude of the solution but also on the directivity pattern of the control array due to the different spatial characteristics of each mode.

The condition number is a measure of how unstable or ill-conditioned a problem is. It is defined as the ratio between the largest and smallest singular values. This value depends on multiple factors such as the spacing between the control sources, the spacing between receivers and the distance between the secondary sources and the dark zone. In general, the problem has a better conditioning when the sensors are closely spaced and the dark zone is close to the secondary sources. The latter is mainly due to the fact that, when close to the secondary array, the sensors are in the near field of the array where the spatial frequency is relatively high which excites high order modes resulting in an increase in amplitude of the smallest singular values. However, these modes are not radiated efficiently and do not propagate to the far-field, where we usually want to achieve noise reduction. The result is that the solutions achieved with the dark zone close to the control sources tend to not generalize well beyond the dark zone.

To improve generalization we might want to move the dark zone further away from the control sources. This would make the problem more ill-posed. These problems require regularization to avoid the stability problems described previously.

3.1.2 Regularization and directivity

The introduction of regularization has the purpose of limiting the amplitude growth of the high order singular values after inversion. Regularization works similarly to a filter that leaves singular values, and corresponding vectors, that are smaller than a threshold out of the solutions.

A simple way to introduce regularization is to perform the SVD and only retain singular values and vectors below a user-defined order. All the singular values and vectors whose order is larger than the truncation order k are discarded. This method is commonly referred to as truncated SVD.

What has been just described is a regularization strategy called TSVD (Truncated Singular Value Decomposition). Alternatively, it is possible to select the singular vectors based on their spatial characteristics. This allow to control the directivity of the secondary array as described in (Borgiotti, 1990). The disadvantage of the TSVD, or the selection of specific modes, is that it requires the computation of the SVD at each frequency and it can be a computationally expensive task when it comes to large matrices.

Instead of truncation, it is also possible to penalize, instead of discarding, modes above a certain order or whose amplitude falls below a certain threshold. The latter is how the Tikhonov regularization works. The Tikhonov regularization introduces filter coefficients ϕ_i that multiply the corresponding singular values σ_i after inversion. The filter factors are given by (Hansen, 2010):

$$\phi_i = \frac{\sigma_i^2}{\lambda^2 + \sigma_i^2}, \tag{3.5}$$

where λ is the chosen threshold. The filter coefficients ϕ_i are equal to 1 when $\sigma_i \gg \lambda$ and are equal to σ_i^2/λ^2 when $\sigma_i \ll \lambda$.

In contrast to the TSVD, Tikhonov regularization can be applied in a least square problem without the need of computing the SVD explicitly (Hansen, 2010). The least square regression with Tikhonov regularization applied to the pressure matching problem can written as:

$$\min_{\mathbf{q}_s} ||\mathbf{H}_s\mathbf{q}_s - \mathbf{p}_p||_2^2 + \lambda||\mathbf{q}_s||_2^2 \quad (3.6)$$

This problem has the following closed-form solution:

$$\tilde{\mathbf{q}}_s = (\mathbf{H}_s^{\mathsf{H}}\mathbf{H}_s + \lambda\mathbf{I})^{-1}\mathbf{H}_s\mathbf{p}_p = \mathbf{V}(\mathbf{\Sigma}^2 + \lambda\mathbf{I})^{-1}\mathbf{\Sigma}\mathbf{U}^{\mathsf{H}}\mathbf{p}_{\mathbf{p}}. \quad (3.7)$$

When we express the solution in terms of singular values and vectors, we can see that the regularization parameter offsets the amplitude of the singular values and effectively introduces a lower limit on their amplitude. The solution is more stable because the amplitude of the singular values is now larger and they will introduce less amplification after inversion.

However, the parameters used in both TSVD and Tikhonov regularization do not bear a physical meaning which makes it hard to find an optimal value.

Alternatively, the regularization is provided by the number of iterations in iterative algorithms. This allows to trade the nonphysical regularization parameter for stopping criteria that bear a physical meaning and can be tailored to the problem at hand. This is the principle behind the use of the conjugate gradient least square algorithm in **Paper B** where the stopping criteria are used to avoid pressure level increases outside of the dark zone and effectively control the radiation pattern of the control array.

Regularization can be applied in different ways as described in this section. In general, with a stronger regularization (smaller k in TSVD, large λ in Tikhonov, or small number of iterations in iterative algorithms) the solutions tends to have smaller amplitude (as more modes are suppressed), more uniform spatial properties (as low order modes with small spatial variation dominate the solution) and an increase in the error/residual (since removing high order modes impede to model features of the sound field with high spatial frequency). The opposite occurs when using weak regularization. In this case and for this application, one has to be careful because the increased spatial variation of the solution often present side lobes that increase the energy radiated outside of the dark zone.

3.2 Transfer functions in a moving inhomogeneous medium

This section introduces the effects of the atmosphere on the transfer functions. Different models have been developed to deal with such effects. The starting point for the derivation of the governing equations for any model is the full set of fluid-dynamic equations. The differences and limits of each model depend on which approximations have been done to reach the corresponding governing equations. The approximations and corresponding limitations will be briefly described in Sec. 3.2.1. Every model described here requires the knowledge of environmental variable such as ground impedance, wind and temperature profile. There are many models that can be used to obtain the ground impedance, with some more suited to hard grounds and others to more porous grounds (Attenborough et al., 2011). The profiles of the wind and temperature can be obtained through simulations using Direct Numerical Simulation (DNS), large eddy simulations (LES) and Reynolds Averaged Navier Stokes (RANS). These tools provide different degrees of accuracy and computational cost. Because of the large running time, these methods cannot be used for sound field control, at least not online. A cheaper alternative in terms of computational cost is to use simpler models for the profiles. These models are derived usually from observation and similarity theory, assuming that only a finite set parameters are necessary to capture the dynamics of the atmospheric surface layer (ASL). Things get more complicated when one wants to extend the profile beyond the ASL to the entire ABL as additional parameters are needed (see **Paper C**). Section 3.2.2 provides an introduction to the ABL useful to understand how to model it and to distinguish between the main features of each regime of the ABL. The knowledge of these characteristics helps to determine when the use of a sound field control system is more or less critical and which parameters have to be modelled and their relative importance. The starting point for both sections in this chapter is the Navier-Stokes equation:

$$\tilde{\rho}\frac{D\tilde{\mathbf{u}}}{Dt} = \tilde{\rho}\left(\frac{\partial}{\partial t} + \tilde{\mathbf{u}}\cdot\nabla\right)\tilde{\mathbf{u}} = -\nabla\tilde{p} + \nabla\cdot\boldsymbol{\sigma} + \mathbf{f}, \tag{3.8}$$

where ρ is the medium density, **u** the medium velocity, p the medium pressure, $\boldsymbol{\sigma}$ the medium dependent stress tensor and **f** the external forces. The tilde indicate that the medium is subject to a perturbation and can be written as $\tilde{x} = X + x$, to distinguish the mean and the fluctuating components. In Sec. 3.2.1, when applying this equation in acoustics, the perturbation is an acoustic wave propagating through the medium. In Sec. 3.2.2, when dealing with the dynamics of the ABL, the perturbation due to turbulence.

Eq. (3.8) cannot be applied as is. It requires to specify an expression that depends on the fluid for $\boldsymbol{\sigma}$ and, in case the fluid is not assumed to be incompressible, also an equation of state and an energy conservation equation. We will see that depending on the application, acoustics or micrometeorology, the assumptions, the expressions and the force terms differ.

Eq. (3.8) is in vector form and this is how is often expressed in acoustics. In micrometeorology, and studies of the ABL, is common to used the tensor form instead:

$$\tilde{\rho}\frac{D\tilde{u}_i}{Dt} = \tilde{\rho}\left(\frac{\partial\tilde{u}_i}{\partial t} + \tilde{u}_j\frac{\partial\tilde{u}_i}{\partial x_j}\right) = -\frac{\partial\tilde{p}}{\partial x_i} + \frac{\partial\sigma_{ij}}{\partial x_j} + f_i, \tag{3.9}$$

where $i, j = 1, 2, 3$ are the indices of the spatial coordinates/directions. When indices are repeated, the terms are to be summed over 1, 2 and 3, e.g. the divergence operator applied to the velocity in tensor form is: $\partial u_i/\partial x_i = \partial u_1/\partial x_1 + \partial u_2/\partial x_2 + \partial u_3/\partial x_3$.

3.2.1 Outdoor propagation models

For short distances (less than 300 m) it is possible to neglect the effects of the atmosphere and simple model such as the complex directivity point source (CDPS (Feistel, 2014)) can be used effectively. When the distance between control sources and dark zone increases, the inhomogeneities of the medium causes can have very large effects on the sound field and cannot be neglected. Many different models have been developed over the year. (Attenborough et al., 1995) presents a comparison of some of the most used algorithms for outdoor sound propagation. Derivations from many of these models can be found in (Ostashev et al., 2005; Salomons, 2001). In this section we give a brief review of the approximations needed to derive the equations solved by different model. We refer in this chapter to the derivations for FFP, CNPE and FDTD that can be found in (Ostashev et al., 2005). To maintain a consistent notation across the thesis, the wind speed **v** is replaced by **u** and the turbulent component of the density field η by ρ.

The starting point for deriving the governing equation for the different models considered is always the full set of fluid dynamic equations. In (Ostashev et al., 2005), the fluid is not assumed to be incompressible from the start and the momentum equation is paired with the equation of state, conservation of mass, scalar and entropy:

$$
\begin{aligned}
&\left(\frac{\partial}{\partial t}+\widetilde{\mathbf{u}}\cdot\nabla\right)\widetilde{\mathbf{u}}+\frac{1}{\widetilde{\varrho}}\nabla\widetilde{P}-\mathbf{g}=\mathbf{f}\\
&\widetilde{P}=\widetilde{P}\left(\widetilde{\varrho},\widetilde{S},\widetilde{C}_1,\widetilde{C}_2,\ldots,\widetilde{C}_n\right)\\
&\left(\frac{\partial}{\partial t}+\widetilde{\mathbf{u}}\cdot\nabla\right)\widetilde{\varrho}+\widetilde{\varrho}\nabla\cdot\widetilde{\mathbf{u}}=\widetilde{\varrho}Q\\
&\left(\frac{\partial}{\partial t}+\widetilde{\mathbf{u}}\cdot\nabla\right)\widetilde{C}_i=0,\quad i=1,2,\ldots,n,\\
&\left(\frac{\partial}{\partial t}+\widetilde{\mathbf{u}}\cdot\nabla\right)\widetilde{S}=0.
\end{aligned}
\tag{3.10}
$$

The tildes denote that these are variables of perturbed field and can be written as the sum of a mean and a fluctuating component, i.e. $\tilde{x}=X+x$. The fluctuations in the medium are caused by an acoustic wave propagating through it and their amplitude is considered to be much smaller than the mean. The first step is to linearize the system of equations around their base state (see Figure 3.2).

Other models not analyzed here is the transmission line matrix (Hofmann and Heutschi, 2007) and the extended Fourier pseudo-spectral time-domain method (Hornikx et al., 2010). The latter can model complex media and reflections from ground and obstacles with limited computational and storage requirements. It has though some accuracy problem with arbitrarily shaped boundaries and at high frequencies in upwind conditions if compared to an FFP solution.

The approximations presented in the next sections and the equations derived from them are summarized in Figure 3.2.

Fast Field Program

After linearizing Eq. (3.10), the medium is assumed to be vertically stratified and horizontally homogeneous. With this assumptions, the equations can be combined in a single equation describing the perturbation of the background pressure due to a propagating wave. This expressions is valid for both gravity and acoustic wave. For acoustics this equation can be further simplified since frequencies used in acoustics are much higher than the Brunt-Väisälä frequency N. Additional simplifications can be made on the base of scaling arguments and are valid as long as the angular frequency ω is much larger than the rate of change with height of the speed of sound and wind speed perturbations normalized by the mean speed of sound. This equation only depend on z and it is convenient to Fourier transform it with respect of the horizontal components of the wave-vector $\boldsymbol{\kappa}=(k_x,k_y)$. These equations are equivalent to the equations from the velocity quasi-potential from (Pierce, 1990) when $\lambda \ll l$. These equations, within one layer and after transformation with respect to time and horizontal coordinates, are:

$$
\begin{aligned}
&\hat{p}=-i\rho(\omega-\boldsymbol{\kappa}\cdot\boldsymbol{u})\Psi\\
&\frac{d^2\Psi}{dz^2}+\gamma^2\Psi=-Q(w)\delta\left(z-z_s\right)\\
&\mathbf{w}=\frac{1}{\omega-\boldsymbol{\kappa}\cdot\boldsymbol{u}}\left(-\kappa_x,-\kappa_y,i\frac{d}{dz}\right)\Psi
\end{aligned}
\tag{3.11}
$$

Where $\hat{p}$ is the pressure in the transformed domain, $\boldsymbol{u}$ is the horizontal wind velocity, Ψ is the velocity quasi-potential in the transformed domain, γ is the vertical component of the wave-vector and the term into parenthesis is the gradient operator in the transformed domain with k_x and k_y being the horizontal components of the wave-vector. The

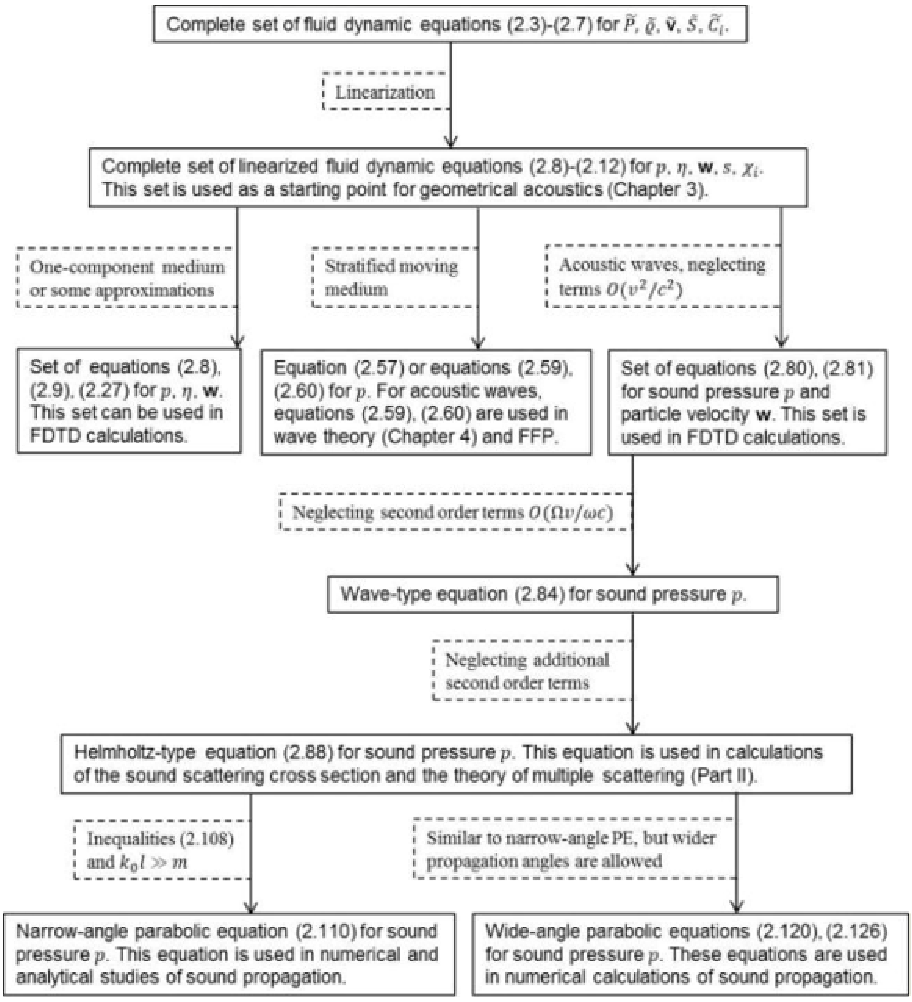

Figure 3.2: Summary of the approximations used to derive different outdoor propagation models starting from the full set of fluid dynamic equations (Figure 2.1 in (Ostashev and Wilson, 2015)).

ground can be modelled in different ways: assuming a locally reacting ground and using an impedance boundary condition or as a homogeneous half-space with its density and speed of sound. The former could be less accurate than the latter due to the locally reacting assumption (Ostashev et al., 2005). A radiation conditions is used at the edges and a continuity condition at the interfaces between layers. Once the equation is solved numerically, the solution is transformed back to the spatial domain.

This method in general is accurate and computationally efficient. There are few assumptions made in the derivation of these equations that can affect simulating sound propagation. The first is the assumption of an horizontally homogeneous medium, which does not allow to make the wind field range dependent and the ground can only be flat. Furthermore, these equations are valid when $\lambda \ll l$ which in general is not a problem unless turbulence should be included. Furthermore, the vertical component of the wind is not taken into account. This is not a problem unless the source is not close to the ground or if the domain extends beyond the ASL. In these cases, the vertical component of the wind is not negligible and not including it in the model can cause wrong estimations for the turning points and the interference pattern on the ground.

Crank-Nicholson Parabolic Equation

The derivation of the equations for this method is more lengthy and involve more approximations than the two other methods described here, as it can be seen in Figure 3.2. Again, the starting point is the linearized fluid dynamics equations obtained from Eq. (3.10). These equations are then rearranged, and after neglecting terms of the order u^2/c^2, reduced to a system of two equations. These are the same two Equations, Eq. 3.14, used for FDTD in Section 3.2.1. These equations are further simplified by neglecting terms that are small if time scale of the changes of the mean horizontal wind speed is much larger than the time scale of the acoustic quantities. This allows to combine the previous two equations in a single one (Eq. 2.84 in (Ostashev et al., 2005)). Additional terms are neglected, based of the assumption that the acoustic variables change much faster than any medium variables. The resulting equation is then Fourier transformed leading to an Helmholtz type equation (Eq. 2.88 in (Ostashev et al., 2005)). The x-axis is assumed to be close to the propagation path. The narrow-angle and the wide-angle versions of the parabolic equation can be derived depending on the approximations made form this point on.

Additional terms are dropped for the narrow-angle approximation. Some of these terms have an effect on the accuracy of the predictions. The equation that results from dropping these terms (Eq. 2.106 in (Ostashev et al., 2005)) is only valid if $k_0 l \gg 1$, $x \ll k_0^3 l^4$ and there is little back-scattering.

This expressions is further simplified using the high frequency approximation $k_0 l \gg m$ where m is a large number depending on small number parameters such as the Mach number, the variation in density and the angle between the wave propagation and the x-axis (leading to Eq. 2.110 in (Ostashev et al., 2005)). Finally, the effect of the wind is approximated using the effective speed of sound $c_{eff} = c + \boldsymbol{\kappa} \cdot \boldsymbol{u}$ and the vertical components of the wind is neglected. In a 2D implementation, as the one considered in (Ostashev et al., 2005), the horizontal derivatives perpendicular to the propagation path are discarded leading to the narrow-angle parabolic equation:

$$\frac{\partial A}{\partial x} = ik_0 \frac{1}{2k_0^2}\left[\frac{\partial^2}{\partial z^2} + k^2(x,z) - k_0^2\right] A(x,z), \tag{3.12}$$

where A is the complex amplitude related to the pressure as follows $\hat{p}(x,z) = A(x,z)e^{ik_0 x}$ and $k(x,z) = \omega / c_{eff}$.

The Crank-Nicholson method consists of a finite difference method using a centered approximations:

$$\left.\frac{\partial A}{\partial x}\right|_{x_{m+1/2}} \simeq \frac{A\left(x_{m+1}\right) - A\left(x_m\right)}{\Delta x}, \quad A\left(x_{m+1/2}\right) \simeq \frac{A\left(x_{m+1}\right) + A\left(x_m\right)}{2} \tag{3.13}$$

The wide-angle approximation replaces a term in the Fourier transformed equation (Eq. 2.88 in (Ostashev et al., 2005)) and assumes that the x-axis is close to the propagation path. The equation is rewritten using a pseudo-differential operator that allows to divide the equation in two parts, one for the outgoing and one for the incoming wave. The latter is neglected. The pseudo-differential operator is replaced with the Padé (1,1) approximation.

The narrow angle approximation is only valid for elevation angles up to 20°. Wide angle approximation for extended range. The wide-angle approximation allows elevation angle of up to 40°.

Many of the models based on these equations use the effective speed of sound approximation. This approximation includes the influence of the wind by modelling it as a correction to the speed of sound thus modifying the propagation speed of the medium. This misses the effects introduced by a moving medium which produces a Doppler shift and a more complex dispersion relationship $\omega = k(z)/c(T(z)) + \kappa \cdot \boldsymbol{v(z)}$. The use of the approximation introduces a phase error, which can develop into a magnitude error when there are more than one source interacting.

One should also be careful on which starting field is used to model the source to limit numerical errors. In (Ostashev et al., 2005) two different starting fields are described, one for the narrow-angle and one for the wide-angle approximation. These starting field consider a monopole as a source. (Vecherin et al., 2011) describes a method to include more complex sources with their specific directivities.

Furthermore, the vertical component of the wind is neglected so the method is only accurate close to the ground. Back-scattering and reflections cannot be included in neither the narrow-angle or wide-angle approximations due to the assumption made during their derivation.

An advantage offered by this method over the previous one is the possibility of making the medium properties range dependent and the terrain topology does not need to be flat. This can be done using the conformal mapping method or the Generalized Terrain PE (GTPE as described in (Salomons, 2001).

CNPE is compared to FFP and analytical solutions, when available, in (Attenborough et al., 1995) and the differences in the solutions are attributed to the assumptions in the models. A 2D implementation does not model the effect of the cross-wind. (Cheng et al., 2009) describes a 3D version of the parabolic equation. They use a wind with a turning profile and highlight the importance of properly including the wind instead of using the effective speed of sound approximation. The error is small when there is no cross-wind and the height of the source and observer are similar. Otherwise the approximation should not be used and possibly the 3D version should be used instead of the 2D one. Another 3D parabolic equation for underwater sound propagation can be found in (Lin et al., 2012).

Finite Difference Time Domain

The derivation of these equations requires only few steps and approximations. The starting point are again the linearized versions of the fluid dynamics equations from Eq. (3.10). These equations are then rearranged and reduced to a system of three equations for p, ρ and u_z, the turbulent parts of the pressure, density and vertical component of the wind fields. The equations for the pressure and the momentum are simplified by neglecting terms of order u^2/c^2 or smaller. Additional terms that do not affect acoustic applications are eliminated for the same scaling reasoning. After these simplification, the system of three equations is reduced to the following system of two equations:

$$\begin{aligned} \frac{\partial p}{\partial t} &= -(\mathbf{u} \cdot \nabla)p - K\nabla \cdot \mathbf{v} + KQ \\ \frac{\partial \mathbf{v}}{\partial t} &= -(\mathbf{u} \cdot \nabla)\mathbf{v} - (\mathbf{v} \cdot \nabla)\mathbf{u} - b\nabla p + b\mathbf{F} \end{aligned} \tag{3.14}$$

The main drawback of this method is its computational requirements. To improve on this aspect, (Van Renterghem et al., 2005) uses this method close to the source and the obstacles nearby. The solution provide the starting field for the parabolic equation that provides a solution for larger distances. It is the most heavy of the methods presented here but it is also the most accurate. It does not have any of the limitations of the previous methods and can be used to model complex environments with an inhomoegenous moving medium and reflections from obstacles. The only limitation is given by neglecting the terms of order u^2/c^2 or smaller. Close to the ground $u/c \approx 5e-2$ but it can be important in the upper atmosphere since it can be larger than 0.1. This means that this method is not accurate when the upper atmosphere must be taken into account. This is the case for sources high above the ground or for large distance and strong wind in a downward refracting atmosphere, since the highest turning points will be well within the upper atmosphere.

The CNPE is the quickest of the three methods described here. It has been used in **Paper D** to study the error introduced by using an unsuitable wind profile in the prediction of the sound field close to the ground. This study considered a large simulation domain which would have been computationally expensive to model using any of the other methods. For this particular study, the approximations typical of the CNPE method were not an issue. The use of FFP was considered in case of simulations with multiple sources and the FDTD if obstacles had to be included. In the end, the study only considered the sound field produced by a point source and in free-field conditions thus making the use of FFP and FDTD, and the associated increase in computational requirement, unnecessary. More complex environments will be considered in future work.

3.2.2 Foundations of micrometeorology

When dealing with outdoor sound propagation, it is useful to have a basic knowledge of micrometeorology, the study of small scale atmospheric phenomena. Knowing the differences and the characteristics between different regimes of the ABL, the lowest part of the atmosphere, give an idea of what is important and what can be neglected when modelling acoustics propagation outdoor. In this section we take a look at the basics of the ABL starting with a description of its structure. We then introduce the Navier-Stokes equation in tensor notation including all the terms needed to model the dynamics of such environments. From this equation we derive the mean and turbulent flow equations and finally the mean and turbulent kinetic energy equations. These equations describe the dynamics of the lower atmosphere in different regimes and allow a characterization that can be used to improve modelling of acoustic phenomena.

Structure of the ABL

The troposphere is the bottom part of the atmosphere and it extends up to 11 km above the surface. However, only a small portion of it, the ABL, is affected by the underlying surface (Stull, 1988), while the rest is referred to as free atmosphere. This layer provides the interface with the ground and its height changes during the day from a few hundred meters at nighttime to approximately 1 km at daytime. This layer has complex dynamics and can be divided in two sub-layers where different approximations can be applied: the surface layer, which covers approximately the lower 10% of the ABL, and the mixed layer, as shown in figure 3.3. Sometimes the ABL is further divided in convective mixed layer, residual layer and stable boundary layer depending on the regime (more on this in Section 3.2.2). The surface layer is the most important one when it comes to sound propagation from sources close to the ground. The most well known approximations, such as the logarithmic wind profile and the Monin-Obukhov similarity theory (MOST), make use of strong assumptions that can only be made in this layer. Sound propagation in the surface layer is affected mostly by the velocity and temperature fields. These two fields can also be decomposed in a mean and a turbulent field:

$$\tilde{x}(\mathbf{x}, t) = X(\mathbf{x}, t) + x(\mathbf{x}, t) = X + x, \tag{3.15}$$

with **x** $= (x_1, x_2, x_3) = (x, y, z)$. This is a common notation in micrometerology. The tilde denotes the full field, the capital letter the mean filed and the lower-case letter the fluctuation/turbulent field. The mean field can be considered constant for 10 minutes or longer, up to approximately 1 hour (Kelly et al., 2018). The turbulent component vary on time scales ranging between seconds and minutes and is mostly responsible for scattering and random phase fluctuations. The two approximation named above deal with the mean profile only.

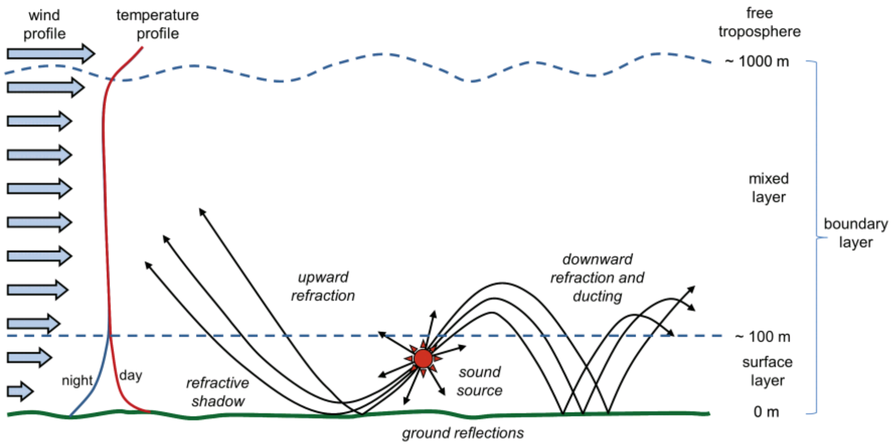

Figure 3.3: Schematic of the atmospheric boundary layer (ABL) showing the ASL (between the straight dashed line and the ground), mixed layer, capping inversion (curvy dashed line), and free troposphere. Near-ground sound propagation for a high-wind condition, with the wind blowing from left to right, is depicted (Figure 1 in (Wilson et al., 2015)).

The equations of the ABL

In this section we briefly derive some of the most important equations needed to describe the complex dynamics of the ABL. We only reproduce the main steps here, a more detailed derivation can be found in (Wyngaard, 2010). We only look here at the momentum equation. Additional equations are needed for the temperature and scalar concentration but it is beyond the scope of this work to reproduce their derivation. Even though the starting equations are different, the same steps described here can be used to derive the mean, turbulent and energy/variance equations.

The starting point here is the Navier-Stokes equation (3.16). After linearizing the pressure gradient in the deviations about the base state we get:

$$\frac{\partial \tilde{u}_i}{\partial t} + \tilde{u}_j \frac{\partial \tilde{u}_i}{\partial x_j} = - \underbrace{\frac{1}{\rho_0}\frac{\partial \tilde{p}}{\partial x_i}}_{\text{pressure gradient}} - \underbrace{2\epsilon_{ijk}\Omega_j\tilde{u}_k}_{\text{Coriolis term}} + \underbrace{\frac{g}{\theta_0}\tilde{\theta}_\mathrm{v}\delta_{3i}}_{\text{Buoyancy term}} + \underbrace{\nu\frac{\partial \tilde{u}_i}{\partial x_j \partial x_j}}_{\text{viscous dissipation}} , \tag{3.16}$$

where $\tilde{u}_i$ is the i-th component of the velocity, Ω_j is the j-th components of the vector of angular velocity of the earth, g is the gravitational acceleration, δ_{3i} is the Dirac delta which is different than 0 only for $i = 3$, hence in the vertical direction, θ_0 is the static background potential temperature that only depends on height, θ_v is the virtual potential temperature, ν is the kinematic viscosity and ϵ_{ijk} is the alternating tensor: $\epsilon_{123} = \epsilon_{231} = \epsilon_{312} = 1$, $\epsilon_{321} = \epsilon_{213} = \epsilon_{132} = -1$ and the rest of combinations are 0. $\theta_\mathrm{v} = \theta(1 + 0.61q)$ with q being the specific humidity. The potential temperature θ is defined as:

$$\theta(z) = T(z)\left[\frac{p(0)}{p(z)}\right]^{\frac{R_\text{d}}{c_p}}. \tag{3.17}$$

An approximation to this expression is given in (Stull, 1988):

$$\theta(z) = T(z) + \Gamma \cdot (z - z_s), \tag{3.18}$$

where $\Gamma = g/c_p = 9.8$ K/km and z_s is a reference height.

After assuming incompressiblity of the fluid, i.e. $\partial \tilde{u}_i / \partial x_i = 0$, rearranging terms and ensemble averaging Eq. (3.16) one obtains the mean flow equation:

$$\frac{\partial U_i}{\partial t} + U_j \frac{\partial U_i}{\partial x_j} + \underbrace{\frac{\partial}{\partial x_j}\overline{u_i u_j}}_{\text{Reynolds stress}} = -\frac{1}{\rho_0}\frac{\partial P}{\partial x_i} - 2\epsilon_{ijk}\Omega_j U_k + \frac{g}{\theta_0}\Theta_\text{v}'\delta_{3i}. \tag{3.19}$$

where U_i is the i-th component of the mean velocity field. The averaging follows the Reynolds averaging rules (Wyngaard, 2010; Reynolds, 1895). It is often not possible to perform an ensemble average of the observational data given the dependency of the mean properties on both space and time and ergodicity is used instead: the time average of a stationary random variable and the spatial average of a homogeneous random variable converges to the ensemble average (Wyngaard, 2010). The Reynolds stress term, or virtual mean stress, only exists as a results of the averaging process and does not correspond to a physic phenomenon. The viscous dissipation term has been removed since it is only relevant very close to the surface in case of the mean flow. This equation can be used to study the mean flow, as in (Wyngaard, 2010) where is used to derive a range of values for the angle between the wind and the pressure gradient (see **Technical Note A**).

Subtracting the mean equation Eq. (3.19) from the full equation Eq. (3.16) lead to the equation for the fluctuating velocity field:

$$\begin{aligned}\frac{\partial u_i}{\partial t} + U_j \frac{\partial u_i}{\partial x_j} + u_j \frac{\partial U_i}{\partial x_j} + \frac{\partial}{\partial x_j}\left(u_i u_j - \overline{u_i u_j}\right) = \\ -\frac{1}{\rho}\frac{\partial p}{\partial x_i} - 2\epsilon_{ijk}\Omega_j u_k + \frac{g}{\theta_0}\theta_\text{v}\delta_{3i} + \nu\frac{\partial^2 u_i}{\partial x_j \partial x_j}.\end{aligned} \tag{3.20}$$

Eq. (3.19) can also be used to obtain the mean kinetic energy equation (MKE). This can be done multiplying Eq. (3.19) by U_i and dividing by 2:

$$\begin{aligned}\frac{\partial}{\partial t}\frac{U_i U_i}{2} = -\frac{\partial}{\partial x_j}\left(\frac{U_i U_i U_j}{2} + \overline{U_i u_i u_j} - \nu\frac{\partial}{\partial x_j}\frac{U_i U_i}{2}\right) - \underbrace{\frac{U_i}{\rho}\frac{\partial P}{\partial x_i}}_{\substack{\text{mean pressure}\\ \text{gradient production}}} \\ - 2\epsilon_{ijk}\Omega_j U_k U_i + \frac{g}{\theta_0}\Theta\text{v} U_i \delta_{3i} - \nu\frac{\partial U_i}{\partial x_j}\frac{\partial U_i}{\partial x_j} + \overline{u_i u_j}\frac{\partial U_i}{\partial x_j}.\end{aligned} \tag{3.21}$$

The terms in parenthesis are the divergences of different types of flux. These terms sum to zero when integrated over the whole ABL, which means that they are neither sources nor sinks but they move kinetic energy through the ABL. The second to last term, viscous dissipation, can be neglected except close to solid boundaries (Wyngaard, 2010).

In a similar way we can obtain the turbulent kinetic energy equation (TKE). After multiplying Eq. (3.20) by u_i, divide by 2 and ensemble averaging, we obtain:

$$\begin{aligned}\frac{1}{2}\frac{\partial}{\partial t}\overline{u_i u_i} = &- \underbrace{\frac{U_j}{2}\frac{\partial}{\partial x_j}\overline{u_i u_i}}_{\text{mean advection}} - \underbrace{\overline{u_i u_j}\frac{\partial U_i}{\partial x_j}}_{\substack{\text{mean gradient}\\ \text{production}}} - \underbrace{\frac{1}{2}\frac{\partial}{\partial x_j}\overline{u_i u_i u_j}}_{\text{turbulent transport}} \\ &- \underbrace{\frac{1}{\rho}\frac{\partial}{\partial x_i}\overline{p u_i}}_{\text{pressure transport}} - 2\epsilon_{ijk}\Omega_j\overline{u_k u_i} - \frac{g}{\theta_0}\overline{\theta_{\mathsf{v}} u_i}\delta_{3i} - \underbrace{\nu\overline{\frac{\partial u_i}{\partial x_j}\frac{\partial u_i}{\partial x_j}}}_{\text{viscous dissipation}}\,.\end{aligned} \tag{3.22}$$

The advection, turbulent transport and pressure transport only move energy through the boundary layer but they are neither a source nor a sink. The second term on the right hand side appears with opposite sign in Eq. (3.21). This term is a source for the TKE and a sink for MKE. It models the energy transfer from the mean flow to the turbulent field. While the viscous term can be ignored most of the time in Eq. 3.21 it is not the same in this case since it is the only sink and the terms on the right hand side sums to zero in the case of a steady flow (Wyngaard, 2010).

ABL regimes

This section is elaborated on in **Paper C**. Even thought the dynamics of the ABL are very complex, one can have a basic understanding of its main feature by looking at the three main regimes of the ABL: unstable, neutral and stable. In the TKE equation Eq. (3.22) we saw that many terms only move energy through the medium and we identified a source in the mean gradient production and a sink in the viscous dissipation. The role of the Coriolis parameter in turbulence production is beyond the scope of this work. It can be used to understand atmospheric processes such as geostrophic adjustment (Persson, 1998). The only term left is buoyancy. Depending on the sign, this term can act both as a source or as a sink which determines which regime the ABL is in. The sign of the buoyancy term is given by the surface heat flux $Q_0 = \overline{\theta_{\mathsf{v}} w}$ where w is the fluctuating vertical component of the velocity field. The surface heat flux is proportional to the temperature gradient and is then the main indicator of the state of the ABL. Figure 3.4 shows the daily cycle of the surface heat flux and how its magnitude and sign change depending on the surface energy budget.

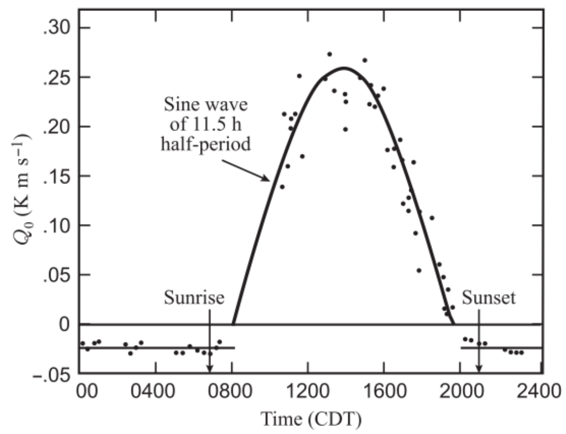

Figure 3.4: The time variation of the surface temperature flux observed in the Kansas experiment. The scatter in these one-hour averages is due to the day-to-day variations during the three weeks of midsummer observations (Figure 9.5 in (Wyngaard, 2010)).

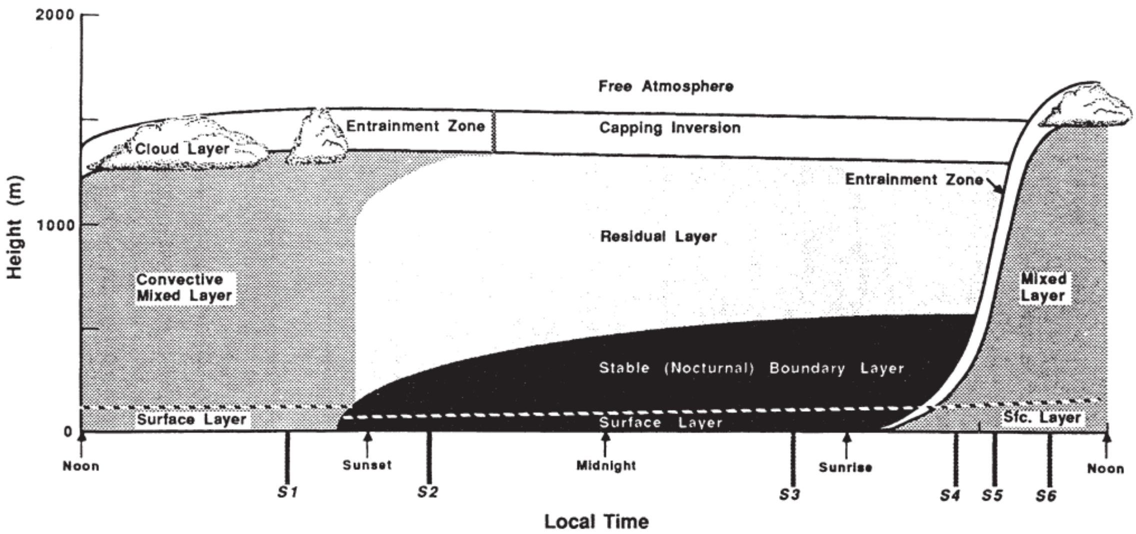

Figure 3.5: Schematic of the ABL showing the ASL (between the straight dashed line and the ground), the mixed layer, capping inversion, and free atmosphere (Figure 1.7 in (Stull, 1988)).

During a clear day, the sun radiation heats up the ground producing a negative temperature gradient, i.e. the temperature decreases with height. In this circumstances, the air parcels closer to the ground are warmer than the one above. They experience a buoyant force that accelerates them upward creating columns of raising warm air and descending cold air. In this case the surface heat flux is positive and the buoyancy term act as a source term. In this conditions the turbulence are strong and their size increases with time as the energy builds up until an equilibrium is reached. The ABL height also increases pushed upward by the turbulence ($\approx$ 100-200 meters in winter and $\approx$ 1km or more during summer). This the unstable ABL and scalars such as the temperature are well mixed because the turbulence help in the diffusion process. In this conditions, wind is of the utmost importance for sound propagation. Temperature can be neglected and might play only a small role upwind, i.e. when sound propagated against the direction of the wind.

At nighttime, the situation is reversed. The temperature gradient is positive and the air parcels close to the ground are colder than the one above. In this case they experience a force that tends to make them oscillate around an equilibrium position and the buoyancy becomes a destruction term, effectively suppressing turbulence. The height of the ABL also reduces accordingly to 100-200 meters. This is the stable ABL. The atmosphere close to the ground is stably stratified and only above it we find the turbulent field left after sunset by unstable regime at daytime. These two layers are sometime referred to as the stable boundary layer and the residual layer (S. Liu and Liang, 2010). The eddies that survive in this scenario are much smaller than in an unstable ABL and the temperature is strongly stratified leading to strong downward refraction. This constitutes the worst case scenario for noise pollution since it is the most favourable for sound propagation. This is confirmed in (Kelly et al., 2018), where weakly stable stratification resulted in the largest noise emissions.

The third and last regime is neutral. This can occur during transition between stable and unstable during sunrise and sunset, as per figure 3.4, or when the temperature gradient is not very strong like during a cloudy day. A typical value of the temperature gradient for neutral conditions in air that is unsaturated by water vapor is given by the adiabatic lapse rate Γ. The value of Γ changes with latitude (L. Liu et al., 2021) but a representative value for mid-latitudes is -9.8 K/km. In Figure 3.5 there is sketch of the daily development of the different regimes from (Stull, 1988). It is important to notice that these considerations assume a horizontally homogeneous surface. A few more complex cases are discussed in (Wyngaard, 2010) and **Paper C**.

Sound propagation scenarios

To conclude this section, we connect the three regimes described in the previous sections to four different sound propagation scenarios described in (Wilson et al., 2015). Such scenarios are shown in Figure 3.6. In this figure, the weather scenarios are plotted according to the effective speed of sound as a function of height. It is convenient to use the speed of sound as it combines the two main quantities affecting sound propagation, namely temperature and wind speed. It is important to point out that the effective speed of sound approximation, even though useful here, introduces a phase error that translates to a magnitude error when the contributions from multiple sources are combined (Ostashev and Wilson, 2015). It is also important to notice that these scenarios assume an almost flat terrain which in turns allows to assume an horizontally homogeneous wind and temperature field.

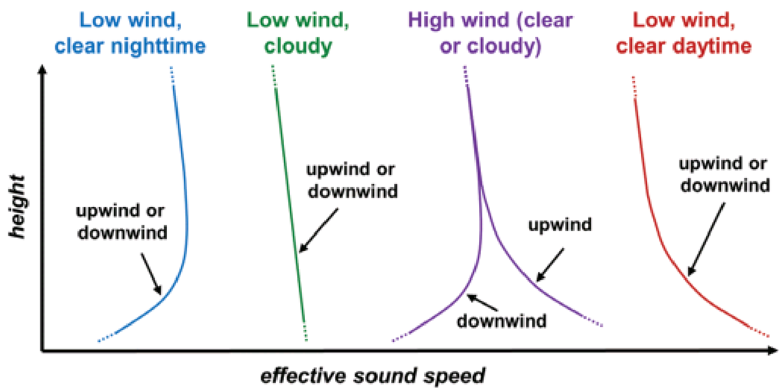

Figure 3.6: Characteristic effective sound speed profiles for 4 limiting cases of the ASL. The profiles are arbitrarily offset along the horizontal axis so as to improve visibility (Figure 2 in (Wilson et al., 2015)).

The four scenarios are the following:

- *Low wind, clear nighttime*: In the case we find the ABL in a stable regime. The turbulence can be neglected close to the ground and since the wind is low, the temperature gradient define how sound will propagate: strong downward refraction in every direction.
- *Low wind, cloudy*: The ABL tends to be in a neutral regime under this conditions. The turbulence are weak and since the gradient of the temperature follows the adiabatic lapse rate, it is negative which leads to upward refraction in any directions. This is a quite volatile state that can quickly transition to stable or unstable.
- *High wind, clear or cloudy*: This lead to an unstable ABL. The wind shear dominates over the temperature thus refraction depends only on the wind speed and its direction relative to the sound propagation. The temperature can play a small role upwind but the pressure level in such direction is already quite diminished. Turbulence are created mainly by the wind shear.

- *Low wind, clear daytime*: A negative temperature gradient lead to an unstable stratification and upward refraction. Turbulence are mainly generated by buoyancy.

Downward refracting conditions result in the worst-case scenario in terms of noise pollution. These conditions generate an acoustic duct close to the ground (Blom and Waxler, 2012) that enhance the range of noise emissions. This scenario occurs when downwind and/or with a positive temperature gradient. Considering the four propagation scenarios above, clear nighttime and high wind are the most problematic conditions. However, high wind only results in downward refraction when the angle between sound propagation and wind direction is small. On the other hand, the positive temperature gradient typical of clear nighttime produce downward refraction in every direction. Due to low wind and the buoyancy term in Eq. (3.22) acting as a sink, turbulence play a small role in these conditions.

For these reasons, this thesis focuses on models for the mean wind and temperature profiles instead of turbulence with special emphasis on the stable and neutral regimes. The first because of its high relevance when dealing with noise emissions and the latter because it is the regime that occur most often (Kelly and Gryning, 2010). Furthermore, transitory phenomena occurring in the stable regime, such as the one described in **Paper C**, can cause the ABL to temporarily transition to a neutral regime. One of these phenomena is the Low-Level Jet (LLJ) whose effect on the sound field on the ground has been studied in **Paper D** and **Paper E**.

4 Conclusions

This thesis addresses the problem of reducing noise emissions from open air live events at low frequencies. From this thesis, and the manuscripts developed during this project, the following conclusions can be drawn:

- The different techniques developed so far to deal with this problem can be analyzed in terms of two subproblems: the synthesis of the filters for the control sources and the characterization of the primary and secondary propagation paths. **Paper A** shows how each problem can be solved independently in different ways. The method employed to solve the first subproblem determines the amplitude of the solution, its spatial characteristics, and its robustness against model inaccuracies. The strategy employed for the second subproblem determines the range where the solutions are accurate. Finally, their combinations determine the overall performance in terms of insertion loss.

- Traditional approaches using regularized least square can be replaced by iterative methods. **Paper B** introduces an iterative method to replace the non-physical regularization parameter with the number of iterations controlled by problem-specific stopping criteria. This approach provides a large improvement since it not only controls the balance between the level of reduction in the dark zone and the energy of the solution, but also the spatial characteristics of the solution, which are crucial to avoid side lobe, and the robustness of the solution against modelling errors and changes in the propagation conditions.

- Using simulations instead of measurements to characterize the primary and secondary propagation paths simplifies these techniques. **Paper B** shows that, even though using simulations often provides smaller insertion loss in the dark zone, it is much easier to employ and it tends to generalize better outside of the dark zone in complex topologies. Furthermore, it is easier to update as propagation conditions change. The choice of the propagation model sets the range where solutions are accurate: distances beyond approximately 100 m require more advanced models that account for the effects produced by a moving inhomogeneous medium.

- Regardless of the propagation model used, the medium must be characterized accurately. **Paper D** shows that using the wrong model for the wind profile can introduce large phase errors that compromise the performance of the active noise control system at distances beyond 100 m. The error grows with distance. Stability conditions at the top of the ABL, that are hard to identify and measure, affect the sound field close to the ground which further increases the prediction error. **Paper E** described how sensitive this error is to the stability conditions and depth of the ABL. The error is mainly in the phase. A simple logarithmic profile can still be used, even when is not the most accurate model, with little error at distance smaller than 1 km independently of the stability conditions. Beyond that distance, the accuracy of the prediction varies wildly depending on parameters of the ABL that are hard to quantify.

  Technical Note F investigated the use of a surrogate model to speed up the simulations and to recover properties of the medium from a sparse dataset of pressure measurements on the ground. While such a method has the potential to simplify measuring medium properties outdoor. However, the results suggest that this technique is not yet mature enough to deal with the complexity of a sound field produced by a moving inhomogeneous medium.

- When performing simulations, it is crucial to identify in which regime of the ABL the sound propagation is taking place. The regimes are vastly different. The stable boundary layer is the most critical one when it comes to noise control and sound propagation as highlighted in **Paper C**. This regime tends to occur at nighttime when individuals are most sensitive to noise exposure. It is characterized by a positive temperature gradient that produces downward refraction in every direction, which effectively creates an acoustic duct close to the ground that enhances the range of the noise emissions. The positive temperature gradient also turns the buoyancy term in the TKE budget into a destruction term. This means that turbulence can be ignored close to the ground. Turbulence are expensive to model and this is an important simplification. **Paper C** also shows that in this regime, the direction of the wind can change up to 45° across the entire ABL which would require a 3D model to account for it.

5 Future work

There are still many challenges to tackle to improve systems for active noise control for open air events. A robust optimization framework (El Ghaoui and Lebret, 1997) could be used to improve the robustness of the system against the fluctuations caused by turbulence. However, focusing on the characterization of the propagation paths will provide larger improvements. As described in this thesis and in (Wilson et al., 2015), the mean profiles are crucial for accurate predictions of the sound fields. Hence, future work should focus on the second subproblem.

There are two main branches that require further work to improve the range of these systems and their adaptability to changes in propagation conditions:

1. **Deriving more efficient sound propagation modelling techniques**: The mean properties of the medium can be considered as static for time windows of 10 minutes and up to approximately 1 hour (Kelly et al., 2018). Current modelling tools for outdoor sound propagation in 3D present excessive run-times that prevent practical use in changing weather conditions. A line of investigation should focus on deriving more efficient modelling techniques for this type of application. Even though neural networks are not yet mature enough to deal with this problem, the fast pace of the developments in this field is encouraging. Different architectures such as PINN (Raissi et al., 2019), SIREN (Sitzmann et al., 2020), DeepONet (Lu et al., 2021) and WaveNet (Moseley et al., 2018) could provide a faster alternative to traditional numerical tools.
2. **Medium characterization or atmospheric profile characterization**: The other branch should focus on the characterization of the medium instead, considering the large error that a wrong estimation of the wind and temperature profiles introduces in the predictions. Direct measurements are prohibitive for this application due to practical reasons. Indirect methods that combine measurements of pressure data and physical knowledge of the problem are the most promising for this task. They have been successfully used in underwater acoustics (Gerstoft and Gingras, 1996; Park et al., 2010; Bianco and Gerstoft, 2016; Bianco and Gerstoft, 2017) and seismology (Aghamiry et al., 2019; Aghamiry et al., 2021; Gholami et al., 2022). Physical knowledge can be introduced using a discretized version of the governing equations or through a surrogate model provided by a neural network (Sitzmann et al., 2020). In this case, pressure measurements at frequencies above 150 Hz, which are not affected by the active noise control system, could be used to recover the wind and temperature profiles. The updated profiles could then be used to update the propagation model and the primary and secondary propagation paths.
3. **Large scale outdoor propagation measurements**: Perform a large scale experiment for the characterization of the sound speed profile and its effect on sound propagation. Ideally these measurements should be taken at different times of the day to account for the more relevant effects in the different regimes of the ABL. This data could then be used to train a surrogate model across many different working conditions and validate numerical simulations.

Bibliography

Abdur-Rouf, K. and K. Shaaban (Feb. 2022). “Development of prediction models of transportation noise for roundabouts and signalized intersections,” in: *Transportation Research Part D-Transport and Environment* 103. ISSN: 1361-9209. DOI: 10.1016/j.trd.2022.103174.

Abhayapala, T. D. et al. (2019). “Limits of noise control over space,” in: *Proceedings of the 23rd International Congress on Acoustics*. 1. Aachen, pp. 47–54.

Aghamiry, H. S., A. Gholami, and S. Operto (2019). “Improving full-waveform inversion by wavefield reconstruction with the alternating direction method of multipliers,” in: *Geophysics* 84.1, R139–R162. ISSN: 19422156. DOI: 10.1190/geo2018-0093.1. arXiv: 1809.00891.

– (2021). “Full waveform inversion by proximal Newton method using adaptive regularization,” in: *Geophysical Journal International* 224.1, pp. 169–180. ISSN: 1365246X. DOI: 10.1093/gji/ggaa434.

Ahrens, J. and S. Spors (2010). “Sound field reproduction using planar and linear arrays of loudspeakers,” in: *IEEE Transactions on Audio, Speech and Language Processing* 18.8, pp. 2038–2050. ISSN: 15587916. DOI: 10.1109/TASL.2010.2041106.

– (2012). “Wave field synthesis of a sound field described by spherical harmonics expansion coefficients,” in: *The Journal of the Acoustical Society of America* 131.3, pp. 2190–2199. DOI: 10.1121/1.3682036.

Attenborough, K. (2002). “Sound propagation close to the ground,” in: *Annual Review of Fluid Mechanics*, pp. 51–82.

Attenborough, K., I. Bashir, and S. Taherzadeh (May 2011). “Outdoor ground impedance models,” in: *The Journal of the Acoustical Society of America* 129.5, pp. 2806–2819. ISSN: 0001-4966. DOI: 10.1121/1.3569740.

Attenborough, K. et al. (1995). “Benchmark cases for outdoor sound propagation models,” in: *Journal of the Acoustical Society of America* 97.1, pp. 173–191. ISSN: NA. DOI: 10.1121/1.412302.

Barlas, E. et al. (2017). “Consistent modelling of wind turbine noise propagation from source to receiver,” in: *The Journal of the Acoustical Society of America* 142.5, pp. 3297–3310. ISSN: 0001-4966. DOI: 10.1121/1.5012747.

Bass, H. E. et al. (Jan. 1995). “Atmospheric absorption of sound - further developments,” in: *Journal of the Acoustical Society of America* 97.1, pp. 680–683. ISSN: 0001-4966. DOI: 10.1121/1.412989.

Betlehem, T. and P. D. Teal (2011). “A constrained optimization approach for multi-zone surround sound,” in: *ICASSP, IEEE International Conference on Acoustics, Speech and Signal Processing - Proceedings* September, pp. 437–440. ISSN: 15206149. DOI: 10.1109/ICASSP.2011.5946434.

Betlehem, T. et al. (2015). “Personal sound zones: Delivering interface-free audio to multiple listeners,” in: *IEEE Signal Processing Magazine* 32.2, pp. 81–91. ISSN: 10535888. DOI: 10.1109/MSP.2014.2360707.

Bian, H. et al. (2020). “An efficient rectilinear Gaussian beam tracing method for sound propagation modelling in a non-turbulent medium,” in: *The Journal of the Acoustical Society of America* 148.6, pp. 4037–4048. ISSN: 0001-4966. DOI: 10.1121/10.0002966.

Bianco, M. and P. Gerstoft (2016). “Compressive acoustic sound speed profile estimation,” in: *The Journal of the Acoustical Society of America* 139.3, EL90–EL94. ISSN: 0001-4966. DOI: 10.1121/1.4943784.

– (2017). “Dictionary learning of sound speed profiles,” in: *The Journal of the Acoustical Society of America* 141.3, pp. 1749–1758. ISSN: 0001-4966. DOI: 10.1121/1.4977926. arXiv: 1609.04840.

Blom, P. and R. Waxler (2012). “Impulse propagation in the nocturnal boundary layer: Analysis of the geometric component,” in: *The Journal of the Acoustical Society of America* 131.5, pp. 3680–3690. ISSN: 0001-4966. DOI: 10.1121/1.3699174.

Borgiotti, G. V. (1990). “The power radiated by a vibrating body in an acoustic fluid and its determination from boundary measurements,” in: *Journal of the Acoustical Society of America* 88.4, pp. 1884–1893. ISSN: NA. DOI: 10.1121/1.400211.

Botteldooren, D. (1994). “Acoustical finite-difference time-domain simulation in a quasi-Cartesian grid,” in: *Journal of the Acoustical Society of America* 95.5, pp. 2313–2319. ISSN: NA. DOI: 10.1121/1.409866.

Boyd, S. and L. Vandenberghe (Mar. 2004). *Convex Optimization*. Cambridge University Press. ISBN: 0521833787.

Brunskog, J. et al. (2019). “Full-scale outdoor concert adaptive sound field control,” in: *Proceedings of the International Congress on Acoustics* 2019-Septe.September, pp. 1170–1177. ISSN: 24151599. DOI: 10.18154/RWTH-CONV-239890.

Can, A. et al. (2010). “Traffic noise spectrum analysis: Dynamic modeling vs. experimental observations,” in: *Applied Acoustics* 71.8, pp. 764–770. ISSN: 0003-682X. DOI: https://doi.org/10.1016/j.apacoust.2010.04.002. URL: https://www.sciencedirect.com/science/article/pii/S0003682X10000836.

Caviedes Nozal, D. et al. (2019a). “A Bayesian spherical harmonics source radiation model for sound field control,” in: *The Journal of the Acoustical Society of America* 146.5, pp. 3425–3435. ISSN: 0001-4966. DOI: 10.1121/1.5133384.

Caviedes Nozal, D. et al. (2019b). “The effect of atmospheric conditions on sound propagation and its impact on the outdoor sound field control,” in: *INTER-NOISE 2019 MADRID - 48th International Congress and Exhibition on Noise Control Engineering*.

Chang, J. and F. Jacobsen (2012). “Sound field control with a circular double-layer array of loudspeakers,” in: *The Journal of the Acoustical Society of America* 131.6, pp. 4518–4525. ISSN: 0001-4966. DOI: 10.1121/1.4714349.

Cheinet, S. et al. (2018). “An experimental study of the atmospheric-driven variability of impulse sounds,” in: *The Journal of the Acoustical Society of America* 144.2, pp. 822–840. ISSN: 0001-4966. DOI: 10.1121/1.5047750.

Cheng, R., P. J. Morris, and K. S. Brentner (2009). “A 3D parabolic equation method for sound propagation in moving inhomogeneous media,” in: *The Journal of the Acoustical Society of America* 126.4, p. 1700. ISSN: 00014966. DOI: 10.1121/1.3203934.

Coleman, P. et al. (Apr. 2014). “Acoustic contrast, planarity and robustness of sound zone methods using a circular loudspeaker array,” in: *Journal of the Acoustical Society of America* 135.4, pp. 1929–1940. ISSN: 0001-4966. DOI: 10.1121/1.4866442.

d&b audiotechnik GmbH & Co. KG (2019). *NoizCalc*. Visited on 29-12-2022. URL: https://www.dbaudio.com/global/en/products/software/noizcalc (visited on 04/27/2019).

DiNapoli, F. R. (1970). “Fast Field Program,” in: *The Journal of the Acoustical Society of America* 47.1A, pp. 100–100. DOI: 10.1121/1.1973765.

Doc, J. et al. (2015). “Three-dimensional parabolic equation model for low frequency sound propagation in irregular urban canyons,” in: *The Journal of the Acoustical Society of America* 137.1, pp. 310–320. ISSN: 0001-4966. DOI: 10.1121/1.4904700.

Druyvesteyn, W. F. and J. Garas (Sept. 1997). “Personal sound,” in: *Journal of the Audio Engineering Society* 45.9. 101st Convention of the Audio-Engineering-Society, Los Angeles, CA, NOV 08-11, 1996, pp. 685–701. ISSN: 0004-7554.

El Ghaoui, L. and H. Lebret (1997). “Robust solutions to least-squares problems with uncertain data,” in: *SIAM Journal on Matrix Analysis and Applications* 18.4, pp. 1035–1064. ISSN: 08954798. DOI: 10.1137/S0895479896298130.

Elizabeth González, A., P. Gianoli Kovar, and M. Deambrosi Papini (2016). “Environmental noise due to large wind turbines : what we have learnt,” in: *Proceedings of the 22nd International Congress on Acoustics Environmental*. February. Buenos Aires.

Elliott, S. J. et al. (2012). “Robustness and regularization of personal audio systems,” in: *IEEE Transactions on Audio, Speech and Language Processing* 20.7, pp. 2123–2133. ISSN: 15587916. DOI: 10.1109/TASL.2012.2197613.

Elowsson, A. and A. Friberg (May 2017). “Long-term Average Spectrum in Popular Music and its Relation to the Level of the Percussion,” in: *Audio Engineering Society Convention 142*. URL: http://www.aes.org/e-lib/browse.cfm?elib=18638.

Embleton, T. F. W. (1996). “Tutorial on sound propagation outdoors,” in: *The Journal of the Acoustical Society of America* 100.1, pp. 31–48. ISSN: 0001-4966. DOI: 10.1121/1.415879.

European Environment Agency (2020). *Noise pollution is a major problem, both for human health and the environment*. URL: https://www.eea.europa.eu/articles/noise-pollution-is-a-major (visited on 12/16/2022).

Feistel, S. (2014). “Modeling the radiation of modern sound reinforcement systems in high resolution,” PhD thesis. RWTH Aachen. ISBN: 9783832537104.

Gerstoft, P. and D. F. Gingras (1996). *Parameter estimation using multifrequency range□dependent acoustic data in shallow water*. DOI: 10.1121/1.414818.

Gholami, A., H. S. Aghamiry, and S. Operto (2022). “Extended-space full-waveform inversion in the time domain with the augmented Lagrangian method,” in: *Geophysics* 87.1, R63–R77. ISSN: 0016-8033. DOI: 10.1190/geo2021-0186.1.

Gilbert, K. E. and M. J. White (1989). “Application Of The Parabolic Equation To Sound Propagation In A Refracting Atmosphere,” in: *Journal of the Acoustical Society of America* 85.2, pp. 630–637. ISSN: NA. DOI: 10.1121/1.397587.

Gryning, S. E. et al. (2007). “On the extension of the wind profile over homogeneous terrain beyond the surface boundary layer,” in: *Boundary-Layer Meteorology* 124.2, pp. 251–268. ISSN: 00068314. DOI: 10.1007/s10546-007-9166-9.

Güneş Baydin, A. et al. (2018). “Automatic differentiation in machine learning: A survey,” in: *Journal of Machine Learning Research* 18, pp. 1–43. ISSN: 15337928. arXiv: 1502.05767.

Hansen, P. C. (2010). *Discrete Inverse Problems: Insight and Algorithms*. English. Fundamentals of Algorithms FA07. Society for Industrial and Applied Mathematics. ISBN: 978-0-89871-696-2. DOI: 10.1137/1.9780898718836.

Heuchel, F., D. Caviedes Nozal, and F. T. Agerkvist (2018). “Sound Field Control for Reduction of Noise from Outdoor Concerts,” in: *Proceedings of the Audio Engineering Society*, p. 8.

Heuchel, F. M. et al. (2019). “Adapting transfer functions to changes in atmospheric conditions for outdoor sound field control,” in: *Proceedings of the International Congress on Acoustics* 2019-Septe.1, pp. 1178–1183. ISSN: 24151599. DOI: 10.18154/RWTH-CONV-239982.

Heuchel, F. M. et al. (2020). “Large-scale outdoor sound field control,” in: *The Journal of the Acoustical Society of America* 148.4, pp. 2392–2402. ISSN: 0001-4966. DOI: 10.1121/10.0002252.

Hill, A. J. and E. Shabalina (2020). “Sound exposure and noise pollution at outdoor events,” in: *Journal of the Audio Engineering Society* 68.6, p. 145.

Hofmann, J. and K. Heutschi (2007). "Simulation of outdoor sound propagation with a transmission line matrix method," in: *Applied Acoustics* 68.2, pp. 158–172. ISSN: 0003682X. DOI: 10.1016/j.apacoust.2005.10.006.

Hornikx, M., R. Waxler, and J. Forssén (2010). "The extended Fourier pseudospectral time-domain method for atmospheric sound propagation," in: *The Journal of the Acoustical Society of America* 128.4, pp. 1632–1646. ISSN: 0001-4966. DOI: 10.1121/1.3474234.

Junker, F. et al. (2007). "Meteorological classification for environmental acoustics - practical implications due to experimental accuracy and uncertainty," in: *19th International congeess on acoustics*. September. Madrid.

Kelly, M., E. Barlas, and A. Sogachev (2018). "Statistical prediction of far-field wind-turbine noise, with probabilistic characterization of atmospheric stability," in: *Journal of Renewable and Sustainable Energy* 10.1. ISSN: 19417012. DOI: 10.1063/1.5012899.

Kelly, M., R. A. Cersosimo, and J. Berg (2019). "A universal wind profile for the inversion-capped neutral atmospheric boundary layer," in: *Quarterly Journal of the Royal Meteorological Society* 145.720, pp. 982–992. ISSN: 1477870X. DOI: 10.1002/qj.3472.

Kelly, M. and S. E. Gryning (2010). "Long-Term Mean Wind Profiles Based on Similarity Theory," in: *Boundary-Layer Meteorology* 136.3, pp. 377–390. ISSN: 00068314. DOI: 10.1007/s10546-010-9509-9.

Libianchi, P and X Karakonstantis (May 2022). "Surrogate Modelling for Estimating Sound Speed Profiles," Internal report.

Libianchi, P. et al. (2023a). "Phase error sensitivity to the inversion strength and depth of the boundary layer in a conventionally neutral regime," English. In: *Proceedings of Forum Acusticum 2023*. Forum Acusticum 2023; Conference date: 11-09-2023 Through 15-09-2023.

Libianchi, P. et al. (Aug. 2023b). "Sensitivity of the predicted acoustic pressure field to the wind and temperature profiles in a conventionally neutral boundary layer," in: *The Journal of the Acoustical Society of America* 154 (2). Reproduced with the permission of AIP Publishing.

Libianchi, Pierangelo et al. (2023). "Active noise control at low frequencies for outdoor live music events using the conjugate gradient least square method," English. In: *Applied Acoustics* 205. ISSN: 0003-682X. DOI: 10.1016/j.apacoust.2023.109235.

Lin, Y., J. M. Collis, and T. F. Duda (2012). "A three-dimensional parabolic equation model of sound propagation using higher-order operator splitting and Padé approximants," in: *The Journal of the Acoustical Society of America* 132.5, EL364–EL370. ISSN: 0001-4966. DOI: 10.1121/1.4754421.

Liu, L., S. N. Gadde, and R. J. A. M. Stevens (2021). "Geostrophic drag law for conventionally neutral atmospheric boundary layers revisited," in: *Quarterly Journal of the Royal Meteorological Society* 147.735, pp. 847–857. ISSN: 1477870X. DOI: 10.1002/qj.3949.

Liu, Luoqin and Richard J. A. M. Stevens (May 2022). "Vertical structure of conventionally neutral atmospheric boundary layers," en. In: *Proceedings of the National Academy of Sciences* 119.22, e2119369119. ISSN: 0027-8424, 1091-6490. DOI: 10.1073/pnas.2119369119. URL: https://pnas.org/doi/full/10.1073/pnas.2119369119 (visited on 04/15/2023).

Liu, S. and X. Z. Liang (2010). "Observed diurnal cycle climatology of planetary boundary layer height," in: *Journal of Climate* 23.21, pp. 5790–5809. ISSN: 08948755. DOI: 10.1175/2010JCLI3552.1.

Lu, L. et al. (Mar. 2021). "Learning nonlinear operators via DeepONet based on the universal approximation theorem of operators," in: *Nature Machine Intelligence* 3.3, pp. 218–229. ISSN: 2522-5839. DOI: 10.1038/s42256-021-00302-5.

Mandjoupa, L. et al. (2022). “3D noise modeling of an urban environment: Simulated and measured noise characteristics of the University of the District of Columbia campus,” in: *The Journal of the Acoustical Society of America* 151.4, A37–A37. DOI: 10.1121/10.0010581. eprint: https://doi.org/10.1121/10.0010581.

McBride, S. M. (2017). “A Comprehensive Hamiltonian Atmospheric Sound Propagation Model for Prediction of Wind Turbine Noise,” in.

Morari, M. and E. Zafiriou (1989). *Robust Process Control*. Prentice Hall, Englewood Cliffs.

Moseley, B., A. Markham, and T. Nissen-Meyer (2018). “Fast approximate simulation of seismic waves with deep learning,” in: *arXiv preprint arXiv:1807.06873*.

Nelson, P. A. and S. J. Elliott (1992). *Active Control of Sound*. 1st ed. London: Academic Press Ltd. ISBN: 0-12-515425-9.

Olsen, M. and M. B. Møller (2017). “Sound zones: On the effect of ambient temperature variations in feed-forward systems,” English. In: *142nd Audio Engineering Society International Convention 2017, AES 2017*. Cited By :14.

Ostashev, V. E., D. Juvé, and P. Blanc-Benon (1997). “Derivation of a wide-angle parabolic equation for sound waves in inhomogeneous moving media,” in: *Acta Acustica* 83.3, pp. 455–460. ISSN: 00017884.

Ostashev, V. E. and D. K. Wilson (Sept. 2015). *Acoustics in Moving Inhomogeneous Media*. CRC Press. ISBN: 9780429176494. DOI: 10.1201/b18922.

Ostashev, V. E. et al. (Feb. 2005). “Equations for finite-difference, time-domain simulation of sound propagation in moving inhomogeneous media and numerical implementation,” in: *Journal of the Acoustical Society of America* 117.2, pp. 503–517. ISSN: 0001-4966. DOI: 10.1121/1.1841531.

Park, C. et al. (2010). “Geoacoustic inversion using backpropagation,” in: *IEEE Journal of Oceanic Engineering* 35.4, pp. 722–731. ISSN: 03649059. DOI: 10.1109/JOE.2010.2040659.

Pasco, Y. et al. (2017). “Interior sound field control using generalized singular value decomposition in the frequency domain,” in: *The Journal of the Acoustical Society of America* 141.1, pp. 334–345. ISSN: 0001-4966. DOI: 10.1121/1.4973952.

Persson, A. (1998). “How Do We Understand the Coriolis Force?,” in: *Bulletin of the American Meteorological Society* 79.7, pp. 1373–1385. ISSN: 00030007. DOI: 10.1175/1520-0477(1998)079<1373:HDWUTC>2.0.CO;2.

Pettit, C. L. and D. K. Wilson (2020). “A physics-informed neural network for sound propagation in the atmospheric boundary layer,” in: *Proceedings of Meetings on Acoustics* 42.1. ISSN: 1939800X. DOI: 10.1121/2.0001383.

Pierce, A. D. (June 1990). “Wave-Equation for sound in fluids with unsteady inhomogeneous flow,” in: *Journal of the Acoustical Society of America* 87.6, pp. 2292–2299. ISSN: 0001-4966. DOI: 10.1121/1.399073.

Plewe, D. et al. (2020). “Analysis of model based virtual sensing techniques for active noise control,” in: *Proceedings of 2020 International Congress on Noise Control Engineering, INTER-NOISE 2020*.

Raissi, M., P. Perdikaris, and G. E. Karniadakis (2019). “Physics-informed neural networks: A deep learning framework for solving forward and inverse problems involving nonlinear partial differential equations,” in: *Journal of Computational Physics* 378, pp. 686–707. ISSN: 10902716. DOI: 10.1016/j.jcp.2018.10.045.

Raspet, R., G. Baird, and W. Wu (1992). “Normal Mode Solution For Low-Frequency Sound Propagation In A Downward Refracting Atmosphere Above A Complex Impedance Plane,” in: *Journal of the Acoustical Society of America* 91.3, pp. 1341–1352. ISSN: NA. DOI: 10.1121/1.402463.

Reynolds, O. (1895). “IV. On the dynamical theory of incompressible viscous fluids and the determination of the criterion,” in: *Philosophical Transactions of the Royal Society of London. (A.)* 186, pp. 123–164. DOI: 10.1098/rsta.1895.0004.

Salomons, E. M. (1998). “Caustic diffraction fields in a downward refracting atmosphere,” in: *The Journal of the Acoustical Society of America* 104.6, pp. 3259–3272. ISSN: 0001-4966. DOI: 10.1121/1.423966.

– (2001). *Computational Atmospheric Acoustics*. Dordrecht: Springer Netherlands. ISBN: 978-1-4020-0390-5. DOI: 10.1007/978-94-010-0660-6.

Sitzmann, V. et al. (2020). “Implicit Neural Representations with Periodic Activation Functions,” in: ISSN: 10495258. arXiv: 2006.09661.

Spors, S. and H. Buchner (2008). “Efficient massive multichannel active noise control using Wave-Domain adaptive filtering,” in: *2008 3rd International Symposium on Communications, Control, and Signal Processing, ISCCSP 2008*, pp. 1480–1485. DOI: 10.1109/ISCCSP.2008.4537461.

Støfringsdal, B. (2018). “Expected sound levels at concert venues for amplified music,” in: *Proceedings of the Institute of Acoustics* 40.October, pp. 654–660. ISSN: 14786095.

Stull, R. B. (1988). *An Introduction to Boundary Layer Meteorology*. Ed. by Roland B. Stull. Dordrecht: Springer Netherlands. ISBN: 978-90-277-2769-5. DOI: 10.1007/978-94-009-3027-8.

Taherzadeh, S. and K. Attenborough (1999). “Deduction of ground impedance from measurements of excess attenuation spectra,” in: *The Journal of the Acoustical Society of America* 105.3, pp. 2039–2042. ISSN: 0001-4966. DOI: 10.1121/1.426744.

Taherzadeh, S., K. M. Li, and K. Attenborough (1998). “Some practical considerations for predicting outdoor sound propagation in the presence of wind and temperature gradients,” in: *Applied Acoustics* 54.1, pp. 27–44. ISSN: 0003682X. DOI: 10.1016/S0003-682X(97)00069-8.

Tang, J. et al. (Nov. 2022). “Dynamic modeling for noise mapping in urban areas,” in: *Environmental Impact Assessment Review* 97. ISSN: 0195-9255. DOI: 10.1016/j.eiar.2022.106864.

Thomasson, S. I. (1976). “Reflection of waves from a point source by an impedance boundary,” in: *Journal of the Acoustical Society of America* 59.4, pp. 780–785. ISSN: NA. DOI: 10.1121/1.380943.

– (1977). “Sound propagation above a layer with a large refraction index,” in: *Journal of the Acoustical Society of America* 61.3, pp. 659–674. ISSN: NA. DOI: 10.1121/1.381352.

Van Den Berg, G. P. (2004). “Effects of the wind profile at night on wind turbine sound,” in: *Journal of Sound and Vibration* 277.4-5, pp. 955–970. ISSN: 0022460X. DOI: 10.1016/j.jsv.2003.09.050.

Van Renterghem, T., E. M. Salomons, and D. Botteldooren (2005). “Efficient FDTD-PE Model for sound propagation in situations with complex obstacles and wind profiles,” in: *Acta Acustica united with Acustica* 91.4, pp. 671–679. ISSN: 16101928.

Vecherin, S. N., D. K. Wilson, and V. E. Ostashev (2011). “Incorporating source directionality into outdoor sound propagation calculations,” in: *The Journal of the Acoustical Society of America* 130.6, pp. 3608–3622. ISSN: 0001-4966. DOI: 10.1121/1.3655881.

Virieux, J. and S. Operto (Nov.–Dec. 2009). “An overview of full-waveform inversion in exploration geophysics,” in: *Geophysics* 74.6, S, WCC1–WCC26. ISSN: 0016-8033. DOI: 10.1190/1.3238367.

Wang, S., Y. Teng, and P. Perdikaris (2021). “Understanding and mitigating gradient flow pathologies in physics-informed neural networks,” in: *SIAM Journal on Scientific Computing* 43.5, pp. 3055–3081. ISSN: 10957197. DOI: 10.1137/20M1318043. arXiv: 2001.04536.

Wilson, D. K. (2015). *Outdoor Sound Propagation Calculator*. In: V. E. Ostashev and D. K. Wilson, Acoustics in Moving Inhomogeneous Media (second edition), Taylor & Francis.
Wilson, D. K., V. E. Ostashev, and C. L. Pettit (2015). "Sound Propagation in the Atmospheric Boundary Layer," in: *Acoustics today* 11.2, pp. 44–53.
Wilson, D. K. et al. (2008). "Dependence of predictive skill for outdoor narrowband and broadband sound levels on the atmospheric representation," in: *Noise Control Engineering Journal* 56.6, pp. 465–477. ISSN: 07362501. DOI: 10.3397/1.3010733.
Wilson, D. K. et al. (2014). "Description and quantification of uncertainty in outdoor sound propagation calculations," in: *The Journal of the Acoustical Society of America* 136.3, pp. 1013–1028. ISSN: 0001-4966. DOI: 10.1121/1.4890644.
World Health Organization. Regional Office for Europe (2018). *Environmental noise guidelines for the European Region*. World Health Organization, xviii + 160 p. ISBN: 9789289053563.
Wright, S. E. and B. Vuksanovic (Feb. 1996). "Active control of environmental noise," in: *Journal of Sound and Vibration* 190.3, pp. 565–585. ISSN: 0022-460X. DOI: 10.1006/jsvi.1996.0079.
– (May 1999). "Active control of environmental noise, IV: Practical extensions to ECAS theory," in: *Journal of Sound and Vibration* 222.4, pp. 635–668. ISSN: 0022-460X. DOI: 10.1006/jsvi.1998.2094.
Wyngaard, J. C. (2010). *Turbulence in the Atmosphere*. Cambridge: Cambridge University Press. ISBN: 9780511840524. DOI: 10.1017/CBO9780511840524.
Zhang, X. et al. (2022). "The effect of rail shields on railway rolling noise," in: *International Journal of Rail Transportation*. ISSN: 2324-8378. DOI: 10.1080/23248378.2022.2106599.
Zilitinkevich, S. S. and I. N. Esau (2005). "Resistance and heat-transfer laws for stable and neutral planetary boundary layers: Old theory advanced and re-evaluated," in: *Quarterly Journal of the Royal Meteorological Society* 131.609, pp. 1863–1892. ISSN: 00359009. DOI: 10.1256/qj.04.143.

Paper A

A review of techniques and challenges in outdoor sound field control

Pierangelo Libianchi[1]
d&b audiotechnik GmbH & Co. KG
Eugen-Adolff-Str. 134, 71522 Backnang, Germany

Finn T. Agerkvist[2]
DTU
Ørsteds Plads, Building 352, 2800 Kgs. Lyngby

Elena Shabalina[3]
d&b audiotechnik GmbH & Co. KG
Eugen-Adolff-Str. 134, 71522 Backnang, Germany

ABSTRACT

The application of sound field control to outdoor live events at low frequencies is a recent one due to increased concerns regarding noise pollution and stronger regulations. Here is presented an overview of the techniques being recently investigated based on model, data or hybrid approaches. The approaches presented here provide encouraging results but they all deal with the problem at relatively short distances (approximately 100 m). Translating these results to larger distances is going to be a challenge as a new set of problems needs to be addressed. An overview of the most relevant issues encountered in long range applications such as uneven terrain, properties of the medium, ground and obstacles interactions is also presented.

1. INTRODUCTION

The effects that noise has on the health of individuals are well know by now [1]. This has led to increasingly strict law regarding noise emissions. Previous legislation focused on A-weighted measurements to assess such emission effectively leaving out low frequency emissions. Nowadays, updated laws are starting to use C-weighting and more encompassing measures that will make it harder to organize outdoor live events since they can be a nuisance for non participants and can be powerful noise emitters and contain a strong low frequency component which can propagate over large distances with minimal atmospheric attenuation [2]. In the coming years, the proliferation of such regulations might lead to the break up of the large events we have today to smaller ones to reduce their noise footprint. Alternatively, such events could be moved further away from residential areas

[1]pierangelo.libianchi@dbaudio.com

[2]ftag@dtu.dk

[3]elena.shabalina@dbaudio.com

but this will require additional infrastructures and be damaging for wildlife with both consequences going against the UN sustainability goals [3]. Sound reinforcement system have been optimized to limit radiation off axis to limit noise pollution. This still leaves strong emission on axis where an audience is present. Noise barriers are not the best solution in this case due to limited performances at low frequencies. The use of active noise barriers can improve such performances but, as pointed out in [4], they can introduce reflections in the audience area. Furthermore, many of the events considered here take place on borrowed spaces instead of permanent venues so installing physical barriers is just not an option in many cases. Recently, [5] proposed to use active noise control to weaken such emissions. The system employed is shown in fig. 1 and consists of an additional set of control sources placed behind the audience. These sources are used to generate a secondary field that matches, in specific area, the sound field coming from the stage but with opposite phase to weaken its emissions. In this way it is possible to generate a quiet area usually referred to as dark zone. It is important for this system to not be noticeable by the audience. This can be achieved by either using cardiod control sources or an additional array of sources to limit the spill into the audience area [6]. Another important aspect to consider in this type of application is the non-linear nature of the transducers. It is very important that the filters designed for the control source do not introduce any amplification of the driving signal to avoid distortion from the loudspeakers as it could drastically reduce the performance of the system.

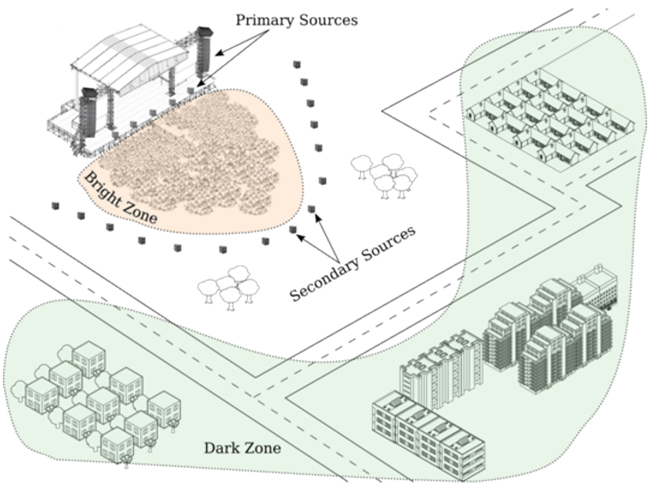

Figure 1: A sketch of a possible sound field control setup.

This field is still in its infancy but different strategies have been proposed. In this work we will look at these strategies by first looking at the general problem and its formulation. We will see that the general problem can be further divided in two sub-problems. How these two sub-problems are dealt with is the root of the differences between the different strategies. This will be the focus of the first part of this paper. The second part will present a brief overview of some of the main challenges when distances larger than 100 m are involved. We will look at different models that deal with outdoor sound propagation, their advantages or disadvantages and finally, describe two of the most important model parameters.

2. THE PRESSURE MATCHING PROBLEM

All the methods presented here have the ultimate purpose of generating a set of filters to apply to a set of control sources. These filters should be designed in way such that the sound field synthesized by the control sources matches the primary field in the dark zone to weaken the noise emissions. The general problem is a pressure matching problem and can be formulated as follows:

$$\min_{\mathbf{q}} \|\mathbf{p} - \mathbf{H}\mathbf{q}\|_2^2, \tag{1}$$

$\mathbf{H} \in \mathbb{C}^{MxL}$ is the secondary path transfer function matrix from L control sources to M microphones, $\mathbf{p} \in \mathbb{C}^{M}$ is the primary sound field in the dark zone and $\mathbf{q} \in \mathbb{C}^{L}$ are the volume velocities of the secondary sources.

This problem can be further divided in two sub-problems: how to design the filters and how to obtain $\mathbf{p}$ and $\mathbf{H}$. The ways we can deal with these two sub-problems constitute the main differences between the approaches used until now in this type of application. The first sub-problem will be the main focus of the first part of this section while the second part will focus on the second sub-problem.

2.1. Sub-problem 1: designing the filters

All the algorithms presented here can be described by the general block diagram in fig. 2 In general, the reference signal $x(\omega)$ is provided directly from the mixing desk and the frequency response of the controller $Q(j\omega)$ is obtained in different ways which will be the focus of this section. According to the definition of feedback and feedforward from [7] we can make a first distinction between the families of algorithms analyzed here. In a feed-forward method, an error sensor can be used to monitor the performances of the system but it is not used to directly design or modify the filters. The filters are then static and are obtained offline from $\mathbf{p}$ and $\mathbf{H}$ no matter how they have been obtained. The feedback approach instead uses the signal from the error sensor(s) to dynamically adapt the frequency response of the filters. Also in this case estimations of $\mathbf{p}$ and $\mathbf{H}$ might be needed, depending on the implementation, and potentially any method can be used to obtain them.

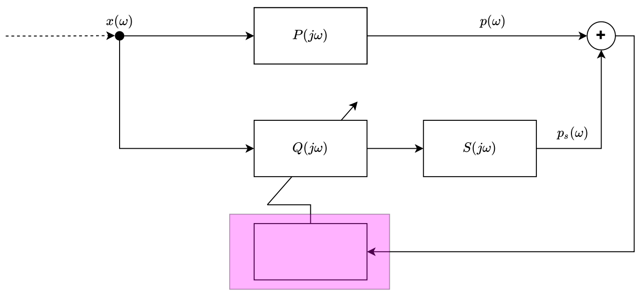

Figure 2: General scheme used in active noise control. The box encloses the only module used in feedback system that is not present in feedforward approaches.

Feed-forward methods

The problem in eq. 1 is usually an ill-posed problem being under-determined ($M \gg L$). Most of the methods described here employ a regularization parameter to ensure stability of the solution by reducing the effect of noise and/or rounding errors due to finite accuracy. It also controls the balance between the amplitude of the solution and the amplitude of the error/residual. It can also be used to control the spatial properties of the synthesized sound field. In general, the amount of regularization affects the accuracy but also the robustness. Large regularization can help to keep the amplitude of the solution below a given threshold, control the spatial properties of the secondary field and increase the robustness to uncertainties in $\mathbf{p}$ and $\mathbf{H}$ due to mismatches or changes in weather conditions, but at the expense of performance.

All the feed-forward methods can lead to similar performances in terms of insertion losses. What should drive one to chose a method instead of the other are the practical aspects of each of them and the limits and properties of a given application, as will be discussed in the following. Further details about these methods together with a comparison between them can be found in [8].

– Ridge regression

$$\min_{\mathbf{q}} ||\mathbf{p} - \mathbf{H}\mathbf{q}||_2^2 + \lambda||\mathbf{q}||_2^2 \tag{2}$$

In this case a penalty term is added to the original pressure matching problem from eq.1. The regularization parameter λ controls the trade-off between accuracy and amplitude of the solution. Larger regularization parameters lead to solution with a smaller amplitude at the cost of increasing the magnitude of the error. Also know as least square problem with Tikhonov regularization, this is one of the most used method to solve a least square problem [9]. The main advantages of this method are that it is easy to implement and computationally efficient. The main drawback is the need to find the optimal regularization parameter. This might require some trial and error. Automatic selection methods like the *l-curve* [10], *generalized cross validation* [11], *normalized cumulative periodogram* [12] or *discrepancy principle* [9] can help finding the optimal compromise between amplitude of the residual and of the solution. The solutions found this way might not be viable though. There is no guarantee that the solution resulting from this compromise does not amplify the driving signal which is something to be avoided to not incur in non-linear behavior in the transducer spoiling the results. A strict and explicit amplitude constraint cannot be applied. Furthermore, the radiation pattern resulting from such solution might not be not acceptable and one would have to manually tweak the regularization parameter.

– Convex optimization:

$$\min_{\mathbf{q}} ||\mathbf{p} - \mathbf{H}\mathbf{q}||_2^2 \quad \text{s.t.} \quad f_i(\mathbf{q}) < b_i \tag{3}$$

The original problem may be treated as a convex optimization problem and explicit constraints can be used. The constraints can be used to enforce a limit on the amplitude of the solution. Such constraints can be applied to each coefficient of the solution ($|\mathbf{q}| \leq 1$, the limit here is unity gain) or on the array effort ($||\mathbf{q}||_2^2 \leq 0.5$, a limit of -6 dB was used in [8]). The first option is more desirable as it guarantees that not a single coefficient will produce amplification. On the other hand, sometimes it is too strict and lead to an empty feasible set. In such cases one case use the more relaxed second option. The constraint can be formulated in different way and additional constraints can be used. This has to be done with care though to avoid empty feasible sets. This method can provide the most accurate solutions since it searches for them only in the feasible set so that any potential solution will comply with the constraints. The drawback is that it is computationally expensive and implementations to solve these problems are available either as external modules or in commercial software. Furthermore, constraints on the radiation pattern can easily lead to empty feasible sets. This can limit the application of this method when it is important to avoid side lobes.

– Subspace/Iterative methods:

$$\min_{\mathbf{q}} ||\mathbf{p} - \hat{\mathbf{H}}\mathbf{q}||_2^2 \tag{4}$$

There a few methods of this kind and the common thread is to replace $\mathbf{H}$ with a lower rank approximation $\hat{\mathbf{H}}$ to provide regularization. This can be done by applying a decomposition to $\mathbf{H}$ such as singular value decomposition, eigenvalue decomposition or principal component analysis. A subset of the vectors in the basis obtained in the previous step will provide the low rank approximation. The vector of pressure $\mathbf{p}$ can be projected onto this subspace and be used to compute the solution [13]. This selection process is what provides regularization and allows to select components with desired spatial properties. The drawbacks are the lack of an amplitude constraint and the decomposition and selection process can be time consuming. The first problem can be addressed by using a fixed basis such as discrete cosine transform, discrete Fourier transform, etc. This solution does not fix the lack of an amplitude constraint and the basis chosen is not adapted to the current problem though. Iterative algorithm such as the conjugate gradient least square can alleviate both of these problems. In this case the regularization, and so the amplitude of the solution and its spatial properties, is provided in discrete steps and controlled by the number of iterations. This allows to include stopping criteria designed specifically for a given application. In this way is possible to control the radiation patter and, to some extent, the amplitude of the solution. An explicit constraint on the amplitude of the solution can be enforced by pairing this method with the active set-type method described in [14].

Feedback methods

In this family of methods the difference between primary and secondary sound fields is captured by the error sensors and used to update the frequency response of the filters.

These methods also set to minimize eq. 1 using gradient descent. Taking the derivatives of eq. 1 with respect to the coefficients and setting it to 0, one can obtain the following update rule:

$$\mathbf{w}(n+1) = \mathbf{w}(n) - \mu e(n)\hat{\mathbf{r}}(n), \tag{5}$$

where $\mathbf{w} \in \mathbb{R}^N$ are the coefficients of the filter of length N, μ is convergence factor or slope rate, e is the error measured at the microphone and $\hat{\mathbf{r}} \in \mathbb{R}^N$ is either the reference signal $\mathbf{x}(n)$, as in traditional least mean square (LMS), or the reference signal filtered by the secondary path to improve stability as in FxLMS [7]. This implementation is in the time domain and n represent the time step. Furthermore, it is for one control source and one microphone. A multichannel approach is in [15] together with some implementation details to improve performances and reduce computational effort. The downside of this method is that it requires the measurement or simulation of the secondary path transfer functions. It is important to have an accurate estimation of them since the FxLMS algorithm will not converge if the phase difference is larger than 90° [16]. This can be a limitation when large distances are involved and the system has to work for long periods of time. The atmospheric conditions change over time introducing an estimation error that gets larger with distance as the influence of the medium gets larger as well.

These methods can achieve large noise reduction at the position of the microphone. Notably the best performances are achieved in places not accessible by people. The extension of the quiet are can be increase is the system consist of enough error microphone placed close to enough to sample the incoming wavefront. In this way the entire wavefront is weakened and the quiet are can be extended beyond the microphones. The size of this extension depends on the density of the sampling and the complexity of the topology.

Another way to introduce losses in areas that are not occupied by the microphones is proposed in [17]. This work uses virtual sensor placing to create quiet areas away from the sensors. The traditional FxLMS is coupled to a model used to predict the transfer function in positions where there are no physical sensors. In this way it is possible to achieve large reductions in position that are now accessible.

Finally, [18], introduces a new method that allows reduction in a large area by surrounding in it with control sources and error microphones. This makes this quite area accessible but it requires many microphones and sources. This is usually a limit with traditional FxLMS approaches. In this work, the authors propose an eigenspace and wave-domain adaptive filtering to overcome this issue. The filters are derived from a circular harmonics representation of the reference and the error signals. The filter coefficients, after being computed in this transformed domain, are then transformed back before being applied to the control sources. In this way they minimize the cross-correlation between channels and, once they are decoupled, treat them as separate single adaptive filtering problems.

2.2. Sub-problem 2: Obtaining the two sound fields

A second sub-problem consists in obtaining the vector of pressures **p** and the matrix of transfer functions **H** necessary to compute the filters. This can be done in different ways. Each way has its own benefits and drawbacks as we will see in this section.

However, some general consideration can be made regarding the spacing and positioning of control sources and sensors. The spacing between control sources and sensors and the spacing between sensors affect the condition number of the transfer function matrix which in turn affects the regularization that has to be applied and the set of solutions that can be obtained. In [19] is shown that the condition number of **H** is at its smallest when the spacing between sensors and between sensors and control sources is equal to the spacing between the control sources. This configuration might not be ideal for this application though. First, a spacing between sources of approximately 2 m would be fine enough to provide control and limited spatial aliasing up to around 120 Hz while the resolution of the measurement grid should be finer than that to properly sample the sound field. Second, the solutions tend to not generalize well when the sensors are placed so close to the sources. There are multiple reasons for it: the secondary wavefront is more curved than the primary one, the rate of decay of the amplitude of the two fields are also very different and near-field effect are recorded that do not propagate to the far field.

Model based approach

The primary field and secondary path transfer functions can be obtained from simulation using a suitable propagation model. This method is the least demanding in terms of practical effort since it does not require any measurement. In terms of computation time it is less clear since it vastly depends on the complexity of the model used. The accuracy of potential solutions depends on how well the model matches reality. This approach has been proposed in [8] using the complex directivity point source model (CDPS, [20]) to generate **H** and **p**. At the moment there is no experimental data available for this approach. This is a simple model that only considers far-field and free-field conditions and a static and homogeneous medium. From simulations, we can expect large insertion losses when these conditions are met. The actual sensitivity of the solution to these uncertainties depends on the algorithm chosen to derive the filters and the amount of regularization. More advanced models should be used in case of reflections or propagation over distances larger than 100 m, where the influence of the atmosphere cannot be neglected. This simple model can help extend the quiet area beyond the dark zone when there are reflection. In general, solutions obtained from transfer function measured in the dark zone do not generalize well beyond it when reflections are involved. The interference pattern sampled is specific to that microphone location and as we move away from it, the interference patter will change. When CDPS is used, one only corrects for the direct field which will keep propagating beyond the dark zone and its properties will not change as quickly as they would if reflections were to be included.

Data based approach

This method has been used in multiple works like [6, 21] is quite straightforward since it consists of measuring both **p** and **H**. This is the most time consuming of approaches presented here and at the same time potentially the most accurate for a limited amount of time. Both **p** and **H** change with time as the weather does [16]. The performance of the solution will then depend on how close the weather conditions match the ones encountered when **p** and **H** were measured. The sensitivity to the mismatch will depend instead on the algorithm chosen to derive the filters and the amount of regularization. Some work has been done in [22] to adapt the measurements to changes in temperature and wind and the model used can be effective when the distances involved are not larger than approximately 100 m. From this distance, the effects produced by changes in the properties of the atmosphere requires more complex modelling than what proposed.

[21] presents results from different measurement sessions using this approach and Ridge regression to obtain the filters. The insertion losses reach a peak of 12-14 dB and at least 8 dB between 30 Hz and 120 Hz in the case where reflections were limited (Refshaleøen, Copenhagen [6, 21]). In more complex environments (Tivoli, Copenhagen and Kappa FuturFestival, Turin [21]) the insertion losses dropped to an average of 5 dB with peaks of 8 dB. In these last two cases, the sound fields where much more complex due to reflections. In this case, also the effect of changes in the weather is magnified. In free-field, only the direct field is affected by these changes. When there are reflections, also the reflections will be affected and in different ways depending on their direction and the direction of the wind dramatically changing the interference pattern that was measured under different weather conditions.

Hybrid approach

In [23], a dataset of sparsely measured transfer functions is used to fit a propagation model based on a spherical harmonics expansion. Such model is then used to infer the transfer functions at positions that were not measured; drastically reducing the burden in the previous approach. This method first assumes sources with an identical axi-symmetric radiation pattern. In this model, the transfer function between a loudspeaker and a receiver at $\mathbf{r} = (r, \theta, \phi)$ in spherical coordinates can be expressed in terms of a spherical harmonics expansion:

$$\hat{h}(\mathbf{r}, \mathbf{a}) = \sum_{m=0}^{M} a_m h_m^{(2)}(kr) \mathrm{P}_m(\cos(\theta)), \tag{6}$$

where $\mathbf{a} = [a_0, a_1, \ldots, a_m]^T \in \mathbb{C}^{M+1}$ are the complex coefficients, $h_m^{(2)}$ are the spherical Hankel functions of the second kind, P_m are the Legendre polynomials of order m, $M + 1$ is the number of modes included and $k = 2\pi f/c$. In dry air, the speed of sound $c = \sqrt{\gamma RT}$ where $\gamma = 1.401$, $R = 287$ J/kg K is the universal gas constant and T is the temperature in K. Since it is assumed that the sources have the same radiation patter, also the coefficients a_m will be the same for all sources so that they can be modelled with parameters $(\mathbf{a}, T)$. T is modelled here as a frequency dependent parameter that includes the effect of both temperature and wind. This model is then fitted to a set of measured transfer functions $\mathbf{h} \in \mathbb{C}^{LN_S}$ between the L loudspeakers and a subset N_S of the M sensors. The model to solve, after including the measurement noise $\mathbf{n} \in C^{KN_S}$, is:

$$\mathbf{h} = \hat{\mathbf{h}}(\mathbf{a}, T) + \mathbf{n}, \tag{7}$$

where the dependency of the wavenumber on the temperature has been included. The variables $\mathbf{a}$, T and $\mathbf{n}$ are treated as stochastic variables following either a proper complex normal distribution or a normal distribution. In this way is possible to write the likelyhood distribution, i.e. the distribution of the measured data conditioned on the unknowns and using Bayes theorem, the posterior distribution is then written in terms of the likelyhood and the priors:

$$\pi(\mathbf{a}, T, \sigma_{\mathbf{n}} | \mathbf{h}) \propto \pi(\mathbf{h} | \mathbf{a}, T, \sigma_{\mathbf{n}}) \pi(\mathbf{a}) \pi(T) \pi(\sigma_{\mathbf{n}}), \tag{8}$$

where $\sigma_{\mathbf{n}}$ is the standard deviation of the noise and is an hyperparameter following a normal distribution. One can obtain the parameters $\mathbf{a}$ and T by finding the maximum a posteriori (MAP) of the previous expression which is the set of unknowns that maximizes the posterior distribution. The model can then used to compute the transfer function to positions where there is no physical sensor. In this work, a least square solution is found using Tikhonov regularization but other methods could have been used.

This method provides the best compromise between the previous two. Much of the accuracy that one has by measuring the transfer function is retained but the cost of the measurement itself is diminished by having to measure only at limited locations K instead of the entire quiet zone with enough microphones M to properly sample the sound field.

[23] shown how this method achieves spatially averaged insertion losses with peaks beyond 20 dB and at least 10 dB broadband. It noted though, how this method works well in free field conditions but it might struggle with more complex topologies with many reflections. In addition, like the other methods, the performance of the system is strongly related to the atmospheric conditions and are affected even by moderate changes. The larger the distance between the control zone and the control sources, the more sensitive is the system to these changes.

3. LONG RANGE CHALLENGES

For propagation over more than 100 m one has to take into account the effects of the ground, the atmosphere and obstacles.

These challenges can be reduced to the calculation of $\mathbf{p}$ and $\mathbf{H}$. The model approach could be used for this purpose. There are few models developed for outdoor sound propagation able to handle a moving inhomogeneous medium, ground reflections and, in some cases, reflections from obstacles. These models together with some of their main parameters will be the focus of this section.

The measurement approach might be too demanding for any real practical application in this case. The amount of microphone depends on the extension of the dark zone and considering the distances involved there are high chances to have signal distribution problems. Even without this problem this approach is not expected to perform well for long amounts of time. As it was said before, the transfer functions will change over time and the error introduced by these changes gets larger with distance. Correcting the transfer functions might not be easy here since effects such as obstacles, ground reflections and refraction must be considered.

A hybrid approach might provide a way to use measured data to reduce uncertainty in the model parameters but has not been developed as of yet for this application.

3.1. Outdoor propagation models

There are few models suited for outdoor sound propagation. A first distinction can be made into frequency and time domain models. In general, time domain models such as Finite-Difference Time-Domain (FDTD) [24] tend to be more precise allowing to faithfully represent a specific environment. The main drawback is that they are computationally expensive and usually require a long time to provide a solution. The computation time is a factor that narrowly restrict the models that can be used. Average atmospheric properties can be considered constant only in small time windows. Any model that requires any time close to this window would make the solution useless since the atmospheric conditions would have already changed.

Frequency domain approaches tends to be less accurate than their time domain counterparts for the simple fact that obstacles cannot be included and admit limited irregularities of the terrain. On the other hand, they usually provide more efficient implementations. Many of the frequency domain models such as Fast Field Programming (FFP) [25], Crank-Nicholson Parabolic Equation (CNPE) [26], Green's Function Parabolic Equation (GFPE) [27] use the effective wavenumber approximation. The effect of moving medium is include by using the effective speed of sound $c_{eff} = c(T) + \mathbf{v} \cdot \mathbf{n}$, where the $c(T)$ is the temperature dependant speed of sound, v is the wind velocity vector and n is the normal to the wavefront. This is approximation produces phase distortion and if more than one source is involved even amplitude distortion due to their interaction [24]. Ray tracing with caustic diffraction field [27] is inherently less accurate at low frequencies even without using the effective wavenumber approximation.

Even though the time domain models tend to be more accurate, one has to take into account also the uncertainty in the parameters. Regardless of the model, the ground impedance and the sound speed profile (and indirectly the temperature and wind profiles) are needed and their accuracy will

Table 1: Pros and cons of different outdoor propagation models.

Method	Pros	Cons
FFP	Fast	Obstacles cannot be included Properties of the medium and of the ground cannot change with distance Only flat terrain Effective wavenumber assumption No vertical wind component
CNPE	Possible to have an irregular terrain	Obstacles cannot be included Limited shapes possible for the terrain Effective wavenumber assumption No vertical wind component
GFPE	Possible to have an irregular terrain Efficient 3D implementation	
Ray model including caustic diffraction field	Possible to have irregular terrain	Reduced low frequency accuracy
FDTD	Possible to include obstacle Possible to include irregular terrain	Computationally expensive

affect the final solution. Some more details on these two parameters will be provided in the following sections. In the case of time domain model, all the impedances, from the ground to the obstacles, have to be formulated in the time domain.

It seems clear that even though the model approach is viable for this application, further effort should be placed in developing a propagation model suited for the task.

The main advantages of the individual methods are resumed in Table 1 and a comparison of the performances of some of them can be found in [28].

3.2. Ground impedance

In a downward refracting atmosphere, the sound waves will hit the ground and be reflected multiple times before reaching a sensor or the dark zone. The interactions between, direct, reflected and refracted waves is crucial to accurately model the sound field. It is necessary though, to have a good estimate of the ground impedance. There is a vast literature about modelling the ground impedance and many models have been proposed with different degrees of complexity and accuracy. Some models tend to work better with certain types of terrain. Due to such extensive literature and the fact that a thorough descriptions of such models is beyond the scope of this work, we refer the reader to [29] for an overview, description and comparison of different methods.

3.3. Sound speed profile

Direct measurement of the sound speed profile can be demanding in terms of equipment and cost. There are many models in the literature for the potential temperature and the wind speed [30–32]. A first selection of such model can be done depending on which state the atmospheric boundary layer (ABL) is in: stable, unstable or neutral. Depending on the state the expressions used in these models can differ. The state also affect the height of the ABL which in turn can potentially affect the size of the domain to be modelled. In [33] is shown how in most cases the atmosphere is in a neutral or quasi-neutral state. Furthermore, in [34] they distinguish between a truly neutral and conventionally neutral boundary layer. The first has no heat flux both at the bottom and at the top of the ABL while the second has zero heat flux only at the bottom. The second one is most common of the two. In this type of conditions, different models have been proposed and some of them are compared in [35]. It can be seen how the models agree close to the surface, where the Monin-Obukov similarity theory holds. As we move further from the surface the models tend to diverge introducing large uncertainties. The sensitivity of the propagation models to this uncertainty is under investigation at the moment. The models that seems more accurate use quantities related to the top of the ABL which are hard to measure thus can introduce additional uncertainty.

4. CONCLUSIONS

Even though outdoor active noise control is a new field, the results so far for relatively short distances (less than 100 m) have been promising. A variety of approaches are available with different degrees of complexity, requirements and characteristics. All the methods and their combinations presented here have the potential to deliver satisfactory performances in terms of insertion losses. No combination is generally better than others. One should pick the right combination depending on the characteristics and limitations of the application. Different methods are able to achieve broadband insertion loss of at least 10 dB in relatively simple topologies. When the environments get more complex and reflections are involved, the results are not as good. More work is required for this type of scenarios by either using more advanced models, adapt the measured transfer functions or used a hybrid method with a model able to include reflections. Larger distances represent a challenge mostly because there is no one outdoor sound model perfectly suited to model the various physical phenomena affecting the sound propagation over a large range and when they do, the computational time required is not acceptable for this kind of application. The bottlenecks are the accuracy and computation time, since no model excel in both aspects. Further research should focus on this topic. The development of an hybrid approach for long distances is also of interest since it could allow to reduce the uncertainty in model parameters through measured data.

ACKNOWLEDGEMENTS

REFERENCES

[1] World Health Organization. Regional Office for Europe. *Environmental noise guidelines for the European Region*. World Health Organization. Regional Office for Europe, 2018.

[2] Adam J. Hill and Elena Shabalina. Sound exposure and noise pollution at outdoor events. *Journal of the Audio Engineering Society*, 68(6):145, 2020.

[3] UN. Sustainable development goals. https://sdgs.un.org/goals. Accessed: 01/06/2022.

[4] Daniel Plewe. *A Quiet Zone System for Open Air Concerts*. PhD thesis, 2021.

[5] Franz M Heuchel, Diego Caviedes Nozal, Jonas Brunskog, Efren Fernandez Grande, and Finn T Agerkvist. An adaptive, data driven sound field control strategy for outdoor concerts. In *Proceedings of 2017 AES International Conference on Sound Reinforcement*, Struer, 2017. Audio Engineering Society.

[6] Franz Heuchel, Diego Caviedes Nozal, and Finn T. Agerkvist. Sound Field Control for Reduction of Noise from Outdoor Concerts. In *Proceedings of 145th Audio Engineering Society Convention*, page 8, New York, 2018. Audio Engineering Society.

[7] P.A. Nelson and S.J. Elliott. *Active Control of Sound*. Academic Press Ltd., London, 1 edition, 1992.

[8] Pierangelo Libianchi, Finn T. Agerkvist, and Elena Shabalina. A conjugate gradient least square based method for sound field control. In *Proceedings of InterNoise21*, Proceedings of Inter-

noise 2021 - 2021 International Congress and Exposition of Noise Control Engineering, pages 1029–1040. Institute of Noise Control Engineering, 2021.

[9] Per Christian Hansen. *Discrete Inverse Problems: Insight and Algorithms*. Society for Industrial and Applied Mathematics, USA, 2010.

[10] D Calvetti, S Morigi, L Reichel, and F Sgallari. Tikhonov regularization and the l-curve for large discrete ill-posed problems. *JOURNAL OF COMPUTATIONAL AND APPLIED MATHEMATICS*, 123(1-2, SI):423–446, NOV 1 2000.

[11] Gene H. Golub, Michael Heath, and Grace Wahba. Generalized cross-validation as a method for choosing a good ridge parameter. *Technometrics*, 21(2):215–223, 1979.

[12] Jesper Gomes and Per Christian Hansen. A study on regularization parameter choice in near-field acoustical holography. volume 123, pages 3385–3385. A I P Publishing LLC, 2008. Acoustics'08 ; Conference date: 29-06-2008 Through 04-07-2008.

[13] Thushara D Abhayapala, Jihui Zhang, Prasanga Samarasinghe, and Wen Zhang. Limits of noise control over space. In *Proceedings of the 23rd International Congress on Acoustics*, number 1, pages 47–54, Aachen, 2019.

[14] S. Morigi, L. Reichel, F. Sgallari, and F. Zama. An iterative method for linear discrete ill-posed problems with box constraints. *Journal of Computational and Applied Mathematics*, 198(2):505–520, 2007.

[15] Daniel Plewe, Finn T. Agerkvist, and Jonas Brunskog. A quiet zone system, optimized for large outdoor events, based on multichannel FxLMS ANC. In *Audio Engineering Society*, pages 1–13, New York, 2018.

[16] Diego Caviedes Nozal, Franz Maria Heuchel, Finn T. Agerkvist, and Jonas Brunskog. The effect of atmospheric conditions on sound propagation and its impact on the outdoor sound field control. In *Proceedings of internoise 2019*. International Institute of Noise Control Engineering, 2019. 48th International Congress and Exhibition on Noise Control Engineering, inter.noise 2019 ; Conference date: 16-06-2019 Through 19-06-2019.

[17] Daniel Plewe, Finn T. Agerkvist, Efren Fernandez Grande, and Jonas Brunskog. Analysis of model based virtual sensing techniques for active noise control. *Proceedings of 2020 International Congress on Noise Control Engineering, INTER-NOISE 2020*, 2020.

[18] Sascha Spors and Herbert Buchner. Efficient massive multichannel active noise control using Wave-Domain adaptive filtering. *2008 3rd International Symposium on Communications, Control, and Signal Processing, ISCCSP 2008*, pages 1480–1485, 2008.

[19] P.A. Nelson and S.H. Yoon. Estimation of Acoustic Source Strength By Inverse Methods: Part I, Conditioning of the Inverse Problem. *Journal of Sound and Vibration*, 233(4):643–668, 2000.

[20] Stefan Feistel. *Modeling the radiation of modern sound reinforcement systems in high resolution*. PhD thesis, RWTH Aachen, 2014.

[21] Jonas Brunskog, Franz Maria Heuchel, Diego Caviedes Nozal, Minho Song, Finn T. Agerkvist, Efren Fernandez Grande, and Enrico Gallo. Full-scale outdoor concert adaptive sound field control. In *Proceedings of 23rd International Congress on Acoustics*, pages 1170–77. German Acoustical Society (DEGA), 2019. 23rd International Congress on Acoustics , ICA 2019 ; Conference date: 09-09-2019 Through 13-09-2019.

[22] Franz Maria Heuchel, Diego Caviedes Nozal, Efren Fernandez Grande, Jonas Brunskog, and Finn T. Agerkvist. Adapting transfer functions to changes in atmospheric conditions for outdoor sound field control. In *Proceedings of 23rd International Congress on Acoustics*, pages 1178–83. Deutsche Gesellschaft für Akustik e.V., 2019. 23rd International Congress on Acoustics , ICA 2019 ; Conference date: 09-09-2019 Through 13-09-2019.

[23] Franz M. Heuchel, Diego Caviedes-Nozal, Jonas Brunskog, Finn T. Agerkvist, and Efren Fernandez-Grande. Large-scale outdoor sound field control. *The Journal of the Acoustical Society of America*, 148(4):2392–2402, 2020.

[24] Vladimir E. Ostashev and D. Keith Wilson. *Acoustics in Moving Inhomogeneous Media*. CRC Press, sep 2015.

[25] F. R. DiNapoli. Fast Field Program. *The Journal of the Acoustical Society of America*, 47(1A):100–100, jan 1970.

[26] V. E. Ostashev, D. Juvé, and P. Blanc-Benon. Derivation of a wide-angle parabolic equation for sound waves in inhomogeneous moving media. *Acta Acustica*, 83(3):455–460, 1997.

[27] Erik M. Salomons. *Computational Atmospheric Acoustics*. Springer Netherlands, Dordrecht, 2001.

[28] K. Attenborough, S. Taherzadeh, H. E. Bass, X. Di, R. Raspet, G. R. Becker, A. Güdesen, A. Chrestman, G. A. Daigle, A. L'Espérance, Y. Gabillet, Y. Gilbert, Y. L. Li, M. J. White, P. Naz, J. M. Noble, and H. A.J.M. van Hoof. Benchmark cases for outdoor sound propagation models. *Journal of the Acoustical Society of America*, 97(1):173–191, 1995.

[29] Keith Attenborough, Imran Bashir, and Shahram Taherzadeh. Outdoor ground impedance models. *The Journal of the Acoustical Society of America*, 129(5):2806–2819, may 2011.

[30] Mark Kelly, Roberto Alessio Cersosimo, and Jacob Berg. A universal wind profile for the inversion-capped neutral atmospheric boundary layer. *Quarterly Journal of the Royal Meteorological Society*, 145(720):982–992, 2019.

[31] Sergej S. Zilitinkevich and Igor N. Esau. Resistance and heat-transfer laws for stable and neutral planetary boundary layers: Old theory advanced and re-evaluated. *Quarterly Journal of the Royal Meteorological Society*, 131(609):1863–1892, 2005.

[32] Sven Erik Gryning, Ekaterina Batchvarova, Burghard Brümmer, Hans Jørgensen, and Søren Larsen. On the extension of the wind profile over homogeneous terrain beyond the surface boundary layer. *Boundary-Layer Meteorology*, 124(2):251–268, 2007.

[33] Mark Kelly and Sven Erik Gryning. Long-Term Mean Wind Profiles Based on Similarity Theory. *Boundary-Layer Meteorology*, 136(3):377–390, 2010.

[34] S. S. Zilitinkevich and I. N. Esau. On integral measures of the neutral barotropic planetary boundary layer. *Boundary-Layer Meteorology*, 104(3):371–379, 2002.

[35] Luoqin Liu, Srinidhi N. Gadde, and Richard J.A.M. Stevens. Universal Wind Profile for Conventionally Neutral Atmospheric Boundary Layers. *Physical Review Letters*, 126(10):104502, 2021.

Paper B

Applied Acoustics 205 (2023) 109235

Contents lists available at ScienceDirect

Applied Acoustics

journal homepage: www.elsevier.com/locate/apacoust

Active noise control at low frequencies for outdoor live music events using the conjugate gradient least square method

Pierangelo Libianchi [a,b,*], Jonas Brunskog [a], Finn Agerkvist [a], Elena Shabalina [b]

[a] Acoustic Technology Group, Department of Electrical and Photonics Engineering, Technical University of Denmark, Building 352, Ørsteds Plads, Kongens Lyngby DK-2800, Denmark
[b] d&b audiotechnik GmbH & Co. KG, Eugen-Adolff-Str. 134, Backnang 71522, Baden Wüttember, Germany

ARTICLE INFO

Article history:
Received 27 October 2022
Received in revised form 1 January 2023
Accepted 20 January 2023
Available online 17 February 2023

Keywords:
Active noise control
Sound field control
Outdoor live music events
Conjugate gradient least square
Active set-type method

ABSTRACT

Sound field control can be applied to the problem of reducing noise emissions from outdoor live music events. One method employed in this type of applications is pressure matching. Different approaches can be used to find a solution to this problem. Many of these methods can provide reduction of more than 10 dB in the frequency range of a subwoofer, between 30 and 120 Hz, thus reducing the loudness to half the original. Such a performance is adequate, but it comes with drawbacks and/or practical limitations such as side lobes that can create new problems in new areas, computational cost, difficult parameter selection, etc. The method proposed here uses the conjugate gradient least square to compute a solution while providing an easier way to find a suitable regularization and at the same time controlling the radiation pattern of the solution to reduce the possibility of side lobes. In addition, the use of an active set-type methods allows to include explicit constraints on the amplitude of the solution to avoid amplification and non-linear behavior of the transducers. After introducing the theory, the performances are compared to other more established methods through simulations and outdoor measurements performed at a 2:1 scale to show properties and practical aspects of the method proposed. These experiments show that 10 dB insertion loss are achieved over a broad frequency range with peaks larger than 20 dB. We investigate the difference in performance between the different methods and use simulated versus measured transfer functions to derive the filters. We also analyze the numerical properties of the solutions provided by the different methods and relate them to the spatial properties of the corresponding sound fields. Furthermore, we present a convergence study to evaluate the effect that grids of different resolutions used in the simulations have on the insertion loss for different degrees of regularization. Finally, we present also a sensitivity analysis of the proposed method to uncertainties in the speed of sound and show how the regularization directly affects the robustness of the method against such inaccuracies.

1. Introduction

The effects that noise has on the health and well-being of individuals is more clear now than ever [1]. The legislation is also following suit and becoming more and more restrictive [2]. Outdoor live events present a special case of noise source that comes with particular challenges and characteristics. Sound at these events usually contains a strong low frequency component (30 to 120 Hz [3,4]) that can travel over large distances with minimal attenuation from the atmosphere [5]. At the same time, these components are integral to the experience of the audience and cannot simply be tuned down [6]. In the last years, the use of active noise control systems has been studied to weaken the noise emissions from live events using additional control sources placed behind the audience [7,8]. These methods apply ad hoc filters to the control sources to create an anti-field that, through destructive interference, reduces the noise emissions generated by the sources at the stage in a given area, usually referred to as dark zone. A common way to derive these filters is by solving a pressure matching problem which consists of minimizing $\|\mathbf{Hq}+\mathbf{p}\|_2^2$, where $\mathbf{H} \in \mathbb{C}^{M\times N}$ is the transfer function matrix between M receivers in the dark zone and N control sources, $\mathbf{q} \in \mathbb{C}^N$ is the vector with the complex amplitude coefficients of the transfer functions for N control sources and finally $\mathbf{p} \in \mathbb{C}^M$ is the vector of the primary pressure field at the M receivers in the dark zone. This approach was first introduced in [9] which also provides a study of the influence of the secondary (control) array on the sound field in the audience

* Corresponding author.
E-mail address: pielbia@dtu.dk (P. Libianchi).

https://doi.org/10.1016/j.apacoust.2023.109235
0003-682X/

area using a double layer of control sources or a single layer of cardioid subwoofers. The performance of such a system was further investigated in [8] which present results from different practical applications with different degrees of complexity: presence of buildings and large time frames with changing weather conditions which affects the transfer functions and thus the final result [10]. In both these works, the primary sound field $\mathbf{p}$ and the secondary transfer functions $\mathbf{H}$ necessary to compute the filters are measured. An alternative is provided in [7], where the transfer functions are modelled using a spherical harmonic expansion. The coefficient of each mode and the effective speed of sound, related to wind speed and temperature on the ground, have been cast as stochastic variables. The propagation model is then combined with measured data to find the best estimates for such variables. With this approach the results generalize better than if using only measurements. Furthermore, it drastically reduces the number of measurements needed to compute the filters.

One of the challenges in this type of applications is to avoid that the sound field generated by the control sources spills into the audience area; the control system should go undetected by the audience to not affect their experience. To do so, it is possible to use a double array: one array to reduce the level in the dark zone and one array to limit the effects in the audience area [11]. This approach was first applied to this problem in [12]. The problem has been reformulated as a double objective minimization problem allowing to control the balance between the reduction of the pressure levels in the dark zone and the spill of the control source in the audience area. However, [9] showed that it is sufficient to use a single layer if the subwoofers have a cardiod directivity pattern.

The method should be computationally efficient and produce a solution for all frequencies in a short time: the weather conditions change with time and affect sound propagation, thus modifying the transfer functions [10]. A solution is most effective when the actual weather conditions match the ones encountered when the transfer functions were measured or simulated [7]. An additional challenge is to avoid high gain filters that produce non-linearities in the loudspeakers, thus leading to distortion. The system here is assumed to be linear and any deviation from this assumption will negatively impact the performance. In general, this is less of a problem if the secondary sources are the same as the primary sources and/or if the distance between them is large. A thorough discussion about this aspect is beyond the scope of this paper.

The pressure matching problem can be formulated and solved in different ways, each one with its pros and cons:

- Least square problem with Tikhonov regularization: This method is computationally efficient [13] and has been used effectively in this type of applications [7]. The main drawback is that the only way to avoid filters with high gain or to control the radiation pattern of the secondary array is through the regularization parameter. Automatic search methods like l-curve [14], generalized cross validation (GCV) [15] or normalized cumulative periodogram (NCP) [16] can find the best compromise between accuracy and amplitude of the solution. The filters generated by this compromise might still have a gain too large for this type of application and/or an undesirable radiation patter. This makes it necessary, at least for this type of application, to manually adjust the gain of the solutions obtained from these methods or to manually search for the best regularization parameter. Furthermore, the regularization parameter is also the only way to control the radiation pattern of the secondary array which, if not taken into account, can lead to side-lobes that can potentially increase noise emissions outside of the dark zone.
- Convex optimization: This method allows to include explicit constraints on the amplitude of the solutions [17]. This restrict the search for a solution in a feasible set that do not violates the constraints. The constraints are therefore applied from the beginning and not after finding a solution which makes it potentially the most accurate option. The main drawbacks are its computational cost, the difficulty in controlling the radiation pattern and, when there are many control sources, it might not find a feasible solution. In this case, the constraints on the amplitude of the solution have to be relaxed. A new constraint is defined over the array effort but it does not strictly avoid high gains in some of the sources in the asrray.
- Subspace/projection methods: This family of methods uses a lower dimensional representation of $\mathbf{H}$ and then project $\mathbf{p}$ on it to find the solution [18]. The lower dimensional representation is obtained through a decomposition of $\mathbf{H}$ using either the singular value decomposition, eigenvalues decomposition or principal components analysis. A subset of the basis vectors is then used to compute the solution. The main advantage of this method is the potential of controlling the radiation patter by selecting basis vectors with the desired spatial properties. The drawbacks come from the need of performing the decomposition at each frequency, which can be computationally expensive for large-scale problems and is likely to introduce audible spectral artifacts. The lack of amplitude constraints on the solution and the basis vector selection that can be hard to automate and time consuming to perform manually.

In this paper we propose a method based on the conjugate gradient least square (CGLS) as an alternative that can provide similar performance to the aforementioned approaches but avoiding some of the drawbacks, making it better suited to a practical application.

The paper is organised as follows: In Section 2 we show how the drawbacks of the subspace/projection methods can be avoided using the *Krylov subspace* that can be efficiently accessed using the conjugate gradient least square. A similar approach was used in [19] where the conjugate gradient (CG) was used to find a basis for an acoustic contrast application as a less expensive alternative to other methods. It offered a large reduction in complexity at the cost of a reduction in performance. In this case, we use the conjugate gradient least square algorithm to directly compute the solution at each frequency without necessarily worsening the performance. We also show that a way to include explicit amplitude constraints without incurring in the computational cost associated with a convex optimization problem using an active set-type method. We also provide an alternative to the selection of a regularization parameter using problem specific stopping criteria that can be easily implemented given the iterative nature of the algorithm. The use of stopping criteria additionally helps to control the radiation pattern as it is explained in details in Section 4.1. The theory presented here is then be validated through measurements in Section 3 where we employed filters obtained using both measured and simulated transfer functions $\mathbf{H}$ and primary field $\mathbf{p}$. Here, the results obtained from the method proposed are also be compared to the ones obtained with least square with Tikhonov regularization and automatic search methods and constrained convex optimization. The methods are compared in term of the insertion loss they provide, the spatial properties of the corresponding secondary sound fields, including the connection between spatial and numerical properties of the method, and their computation time. In addition, we provide an analysis of the robustness of the method to uncertainties in the speed of sound in Section 4.2 and a convergence analysis using grid of receivers with different resolutions in Section 4.3.

2. Theory and methods

2.1. Krylov subspace and CGLS

The use of subspace/projection methods is interesting for this application since they allow the selection of basis vectors with desirable spatial properties to control the radiation pattern of the secondary array. Thus, with these methods it is possible to limit radiation outside the dark zone. The drawback of having to perform a decomposition at each frequency can be mitigated by providing a set of basis vectors such as the ones in a discrete cosine transform (DCT), discrete Fourier transform (DFT), a plane wave decomposition (PWD) or a random matrix instead of computing the Singular Value Decomposition (SVD) [13]. The main disadvantage of this approach is that such basis vectors are not adapted to the problem, in other words, it might be necessary to use many components of the basis to be able to properly model the problem. For example, if we consider a sound field created by an array with large spatial variation, either because in its near field or due to spatial aliasing, it can require the superposition of many basis vectors from a DFT, with different frequencies, to model it accurately. We would like, instead, to find a basis where the first few vectors allow us to model the main features of such sound field. A basis like this is provided by the Krylov subspace, which is defined as:

$$\mathcal{K}_k \equiv \mathrm{span}\{\mathbf{H}^{\mathrm{H}}\mathbf{p}, (\mathbf{H}^{\mathrm{H}}\mathbf{H})\mathbf{H}^{\mathrm{H}}\mathbf{p}, \ldots, \left(\mathbf{H}^{\mathrm{H}}\mathbf{H}\right)^{k-1}\mathbf{H}^{\mathrm{H}}\mathbf{p}\}. \tag{1}$$

This subspace is built iteratively, with k being the number of iterations, and its components are based on increasing powers of the covariance matrix $\mathbf{H}^{\mathrm{H}}\mathbf{H}$ and projections of the primary pressure field $\mathbf{H}^{\mathrm{H}}\mathbf{p}$. The value of k also defines the dimension of the subspace and it cannot exceed rank($\mathbf{H}$) since any additional iteration would add vectors that are not linearly independent.

The problem of the Krylov subspace is that increasing powers of the covariance matrix $\mathbf{H}^{\mathrm{H}}\mathbf{H}$ result in vectors that are richer in the direction of the first right singular vector of $\mathbf{H}$ [13]; this is the vector corresponding to the largest singular value. The basis obtained in this way would have components that are not orthogonal. A modified Gram-Schmidt algorithm can be used to obtain a new basis whose vectors follow the directions of the right singular vectors of $\mathbf{H}$ thus providing a better representation. This might seem more cumbersome than computing the SVD and selecting the basis vectors. However, the conjugate gradient (CG) algorithm [20] applied to the normal equations $\mathbf{H}^{\mathrm{H}}\mathbf{H}\mathbf{q} = \mathbf{H}^{\mathrm{H}}\mathbf{p}$, associated to the unregularized least square problem $||\mathbf{H}\mathbf{q} - \mathbf{p}||_2^2$, actually computes a solution that lies in the Krylov subspace without the need to orthonormalize and store all the basis vectors [13]. It turns out that this is exactly what the conjugate gradient least square (CGLS) algorithm does. This algorithm is more expensive than CG but is still very efficient since it requires two matrix–vector products per iteration and its memory allocations is essentially independent of the number of iterations [21]. Furthermore, it allows to solve problems where $\mathbf{H}$ is not necessarily square or positive definite without the need to explicitly compute $\mathbf{H}^{\mathrm{H}}\mathbf{H}$.

The k-iterate solution is the minimizer of the following problem:

$$\mathbf{q}^{(k)} = \min_{\mathbf{q}} ||\mathbf{H}\mathbf{q} - \mathbf{p}||_2^2 \quad \text{s.t.} \quad \mathbf{q} \in \mathcal{K}_k(\mathbf{H}^{\mathrm{H}}\mathbf{H}, \mathbf{H}^{\mathrm{H}}\mathbf{p}). \tag{2}$$

Since the solution $\mathbf{q}^{(k)}$ provided by the CGLS algorithm consists of a linear combination of the basis vectors in the Krylov subspace [13], it can be written as

$$\mathbf{q}^{(k)} = c_1\mathbf{H}^{\mathrm{H}}\mathbf{p} + c_2(\mathbf{H}^{\mathrm{H}}\mathbf{H})\mathbf{H}^{\mathrm{H}}\mathbf{p} + \ldots + c_k(\mathbf{H}^{\mathrm{H}}\mathbf{H})^{(k-1)}\mathbf{H}^{\mathrm{H}}\mathbf{p}, \tag{3}$$

where c_i are weights scaling the corresponding i-th Krylov basis vector. The SVD decomposition of the transfer function matrix is $\mathbf{H} = U\Sigma V^{\mathrm{H}}$, which means that $\mathbf{H}^H\mathbf{H} = V\mathbf{\Sigma}^2\mathbf{V}^{\mathrm{H}}$. A relation between the CGLS algorithm and the SVD decomposition can be found by rewriting $\mathbf{H}$ in Eq. (3) in terms of its singular values and singular vectors,

$$\begin{aligned}\mathbf{q}^{(k)} &= (c_1 + c_2V\mathbf{\Sigma}^2\mathbf{V}^{\mathrm{H}} + c_3V\mathbf{\Sigma}^4\mathbf{V}^{\mathrm{H}} + \ldots + c_kV\mathbf{\Sigma}^{2(k-1)}\mathbf{V}^{\mathrm{H}})V\mathbf{\Sigma}U^{\mathrm{H}}\mathbf{p}\\ &= \mathbf{V}(c_1\mathbf{\Sigma}^2 + c_2\mathbf{\Sigma}^4 + c_3\mathbf{\Sigma}^6 + \ldots + c_k\mathbf{\Sigma}^{2k})\mathbf{\Sigma}^{-1}\mathbf{U}^{\mathrm{H}}\mathbf{p}\\ &= \mathbf{V}\Phi^{(k)}\mathbf{\Sigma}^{-1}\mathbf{U}^{\mathrm{H}}\mathbf{p}\end{aligned} \tag{4}$$

which means that the CGLS solution is a solution to an inverse problem where the singular values are filtered by the coefficients in $\Phi^{(k)}$. In this way it is possible to see how the CGLS algorithm applies a regularization to the problem that depends on the number of iterations. This is similar to a truncated singular value decomposition (TSVD, where the coefficients are 1 before truncation and 0 after) or a Tikhonov regularized least square (where the i-th coefficient is given by $\sigma_i^2/(\lambda^2 + \sigma_i^2)$). The main difference is that the role of the regularization parameter here is played by the number of iterations. The more iteration the smaller the residual but also at the same time the larger the energy in the solution,

$$||\mathbf{q}^{(k)}||_2 \leqslant ||\mathbf{q}^{(k+1)}||_2, \quad ||\mathbf{H}\mathbf{q}^{(k)} - \mathbf{p}|| \geqslant ||\mathbf{H}\mathbf{q}^{(k+1)} - \mathbf{p}||. \tag{5}$$

The main consequence is that it is not necessary to find a truncation order or the value of a regularization parameter but it is possible to include stopping criteria suited to the problem; the algorithm will stop when these criteria are met. This allows to avoid the practical limitation encountered with a least mean square solution with Tikhonov regularization since its execution can be automated while fulfilling the amplitude or other requirement that a problem might present. Furthermore, this criteria can be more refined and not limited to looking for the best balance between amplitude of the solution and amplitude of the residual as done by GCV, NCP and l-curve. For instance, they can be used to easily control the radiation pattern of the secondary array as other subspace/projection methods and opposite to the least square solutions as it will be explained in Section 2.2.

Even though it is beyond the scope of this paper, it is worth knowing that CGLS also allows the use of a Bayesian preconditioner to provide a priori knowledge of the solution [22]. This can be useful, for example, to control how the energy in the solution is distributed between the different sources to avoid over-driving a subset of them. On the other hand, one has to consider the side-effects of doing so as it will also change the radiation pattern of the secondary array and possibly increase radiation towards the sides.

2.2. Number of iterations and spatial properties of the solution

The use of the stopping criteria in the CGLS algorithm allows to include problem specific requirements that can go beyond the magnitude of the solution or the amplitude of the residual. It was shown in [23] that the number of iterations of the CGLS algorithm can also be used to control the radiation pattern of the control array. In this application, the left and right singular vectors constitute pressure modes and source strength modes [24], respectively. The singular values encode the radiation efficiency of each of the modes or amplification factors once inverted [25]. The number of iterations can control the weight that each source strength mode has on the solution and in turns how large is the excitation of each of the pressure modes. The larger the number of iterations the larger are the weights applied to higher order modes. High order pressure modes tends to have a higher spatial frequency and more energy is directed towards the sides. Knowing this, it is possible to control radiation outside of the dark zone by controlling the number of iterations through a specific stopping criterion. For examples, one can monitor the total pressure field at control points outside of the dark zone and stop the algorithm when an increase above a certain threshold is detected. This feature is very important for this application since it allows to avoid side lobes that could create problems outside of the dark zone. When using least squares with Tikhonov regularization, it would be necessary to compute the solution for multiple regularization parameters to obtain the same result. The range over which one performs this search and the size of the steps would depend on the condition number of the transfer functions matrix, which is both setup and frequency dependent. On the other hand, the CGLS algorithm searches for the solution in the Krylov subspace that is molded by the transfer function matrix from the get go.

2.3. Active set-type method

The solution provided by Eq.(2) contains the complex filters coefficients to be applied to each secondary source at a given frequency. These filters should not amplify the driving signal to the point where non-linear effects from the transducers become significant. This means that the gain applied to each source should be smaller or equal to a user defined threshold (in this case set to 1, so $|q_i| \leqslant 1$ or $20\log_{10}(|q_i|) < 0$ dB). The stopping criteria allow, to some extent, to control the amplitude of the solution. In this way one can stop the algorithm when any component of the solution becomes larger than the user defined threshold. Even if this is an improvement over other methods, it does not provide explicit amplitude constraints and could prevent the use of a meaningful solution because it violates the amplitude requirements even by a small amount. The active set-type method introduced in [26] allows to include explicit amplitude constraints on the solution of the CGLS algorithm. So, once one obtains a CGLS solution complying with user requirements but that violates the amplitude constraints, the active set-method can be employed to find a correction that allows the solution to fulfill the amplitude limits. The main idea is to fix the coefficients that are equal to the constraints and redistribute the energy from the coefficients that are larger than the threshold to the ones that are smaller. This is done by computing a correction $\tilde{\mathbf{y}}$ to be applied to the solution allowing it to fulfill the constraints. This correction must not affect the coefficients equal to the constraints, i.e. $\tilde{y}_i = 0$ for $|q_i| = 1$ in this case. The index i of these coefficients are stored in the active set $\mathbb{A}_u(\mathbf{q})$. The original method applies box constraints to the solution and hence uses two sets, one for the lower bound and one for the upper bound. Since we are applying the constraints to the magnitude of the solution we are interested only in the upper bound.

The coefficients violating the constraints are clipped to the threshold providing an approximate solution $\hat{\mathbf{q}}$ which is used to compute the new residual:

$$\hat{\mathbf{r}} = \mathbf{H}\hat{\mathbf{q}} - \mathbf{p} \tag{6}$$

The method then introduces a matrix $\mathbf{D} = \mathrm{diag}(d_1, d_2, \ldots, d_n)$ with entries:

$$d_k = \begin{cases} 0, & k \in \mathbb{A}_u(\mathbf{q}) \\ 1, & \text{otherwise} \end{cases}. \tag{7}$$

This matrix allows to not affect the coefficients in the active sets. The CGLS algorithm is then used again to find an approximate solution to the problem:

$$\mathbf{HDz} = -\hat{\mathbf{r}}. \tag{8}$$

The correction sought after is given by $\tilde{\mathbf{y}} = \mathbf{D}\mathbf{z}^{(k)}$ that can be used to obtain the new alternative solution $\hat{\mathbf{q}} = \mathbf{q} + \tilde{\mathbf{y}}$. This new solution could also violate the constraints in which case the steps described here should be repeated. Since the residual vector $\hat{\mathbf{r}}$ does not decrease monotonically, the algorithm is not guaranteed to terminate. This could lead to cycling, however in the current application such behavior has not been encountered so far. Furthermore, since this algorithm redistributes the energy between the coefficients of the solutions, it tends to work better when the solution has many coefficients since it offers more degrees of freedom. Solutions with few coefficients might not exploit the advantages offered by this method and it might not offer any improvement over just reducing the amplitude of the solution by an offset.

2.4. Experimental methods

The strategy proposed in Section 2.1–2.3 has been tested with the experimental setup shown in Fig. 1. Due to space limitations, the experiment was performed with a 2:1 scale so the frequency range has been shifted to the interval starting from 60 Hz and ending at 240 Hz and the distances have been halved to be consistent with the new scaling. The experiment was performed outdoor in semi free-field conditions on a football field with a small hill on the left, a set of trees at the back and a hedge with a river behind it on the right as it can seen in Fig. 1b.

The primary and secondary sources consisted of two arrays of 6 d&b audiotechnik Y10 loudspeakers that can be considered as omnidirectional in the frequency range of interest. The loudspeakers were driven by D80 amplifiers from d&b audiotechnik. The spacing between the sources was 1 m, corresponding to 2 m on a real scale, which is a realistic spacing for a real setup. The dark zone started 5 m from the control sources which in turn were placed at 20 m from the primary sources. To evaluate the performances in the dark zone (DZA from now), 24 microphones were arranged in 8 rows of 3 with 0.5 m spacing between them. Furthermore, an array of 8 microphones (BA), also spaced 0.5 m, was placed 45 m from the primary sources to evaluate the level reduction beyond the dark zone and two arrays of 16 microphones spaced 1 m were placed to the left (LA) and right (RA) of the main axis and at 10 m from it to measure possible side lobes. All the microphones were Beyer Dynamics MM1 provided with wind shields. The microphones were then connected to four Yamaha Tio 1608-D interfaces that performed the analog to digital conversion and returned the signal through a Dante network. The reference signal fed to the loudspeakers and the signal measured at the microphones were processed in MATLAB and distributed using a Dante virtual sound-card at a sampling frequency of 48 kHz. MATLAB was also used to compute the ideal filters from the different algorithms. These filters were then implemented as arbitrary-phase finite impulse response (FIR) filters and uploaded directly to the DSP integrated in the amplifiers. Both the sources and the microphones were placed close to the ground to minimize the interferences from ground reflections in the frequency range of the experiment. The weather data was measured using a Davis Vantage Vue weather station set at a height of 2 meters plus an additional sensor on the ground.

2.5. Performance evaluation and comparison

The performance of the algorithm was evaluated using filters derived by a primary field $\mathbf{p}$ and secondary transfer functions $\mathbf{H}$ that were both measured and simulated. Both measurements and simulations used only the sensors in the DZA. The microphones were moved randomly within a circle of 15 cm diameter before evaluating the performance to avoid committing an inverse crime.

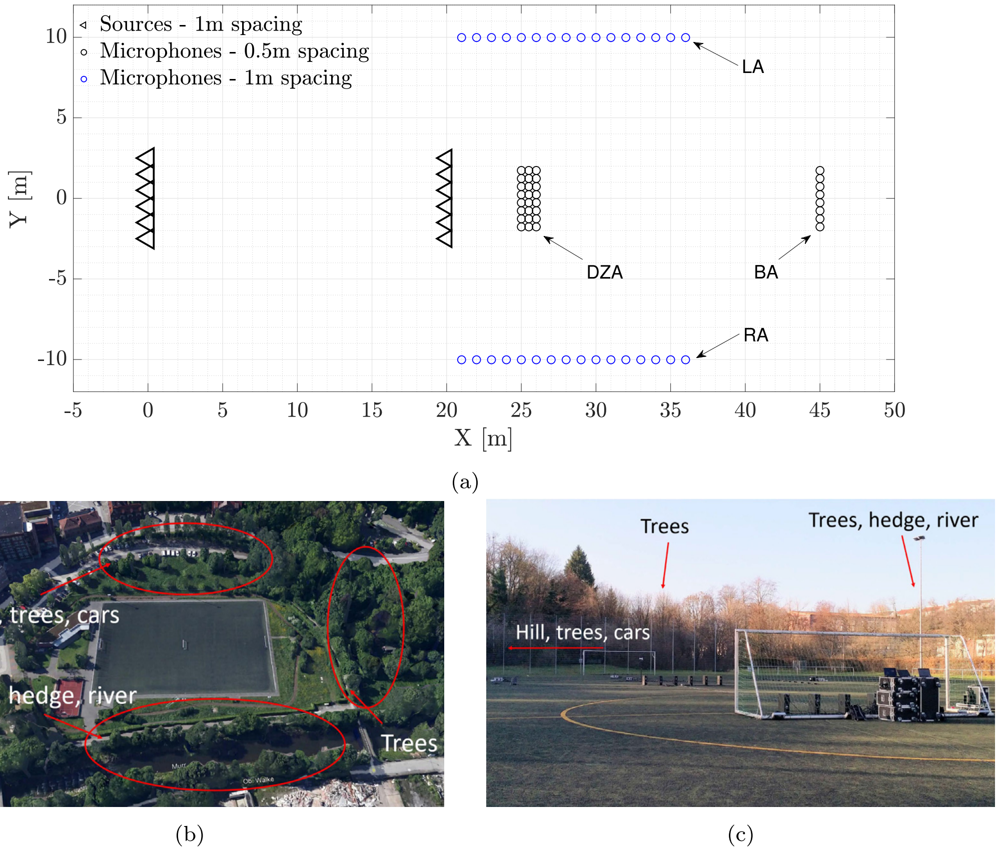

Fig. 1. Overview of the measurement setup (a) with the 8x3 microphones array in the dark zone (DZA), the array of 8 microphones at the back (BA) and the arrays of 12 microphones on the left and right of the main axis (LA and RA). At the bottom the satellite view of the venue (b) and a picture of the setup (c).

Table 1
Weather conditions during the measurement of the primary field and the transfer functions of the secondary sources. The secondary/control source are numbered from the rightmost with respect to the main axis (bottom in Fig. 1a) to the leftmost (top in Fig. 1a). The wind direction is relative to the main axis of the setup: 0° corresponds to wind blowing in the direction of propagation; 90° blowing towards the right of the main axis and −90° to the left.

Index	Source	$T_{z=2m}$ [°C]	$T_{z=0m}$ [°C]	Wind speed [m/s]	Wind direction [°]
1	Primary (all)	4.9	4	0.4	−135
2	Control 1	4.9	3.9	0	-
3	Control 2	4.9	3.9	0	-
4	Control 3	4.9	3.9	0	-
5	Control 4	4.9	3.9	0	-
6	Control 5	4.9	3.9	0	-
7	Control 6	4.9	3.9	0.4	22.5

A summary of the weather conditions found during such measurements is included in Table 1. Having both measurements and simulations allowed to quantify the improvements that the measurements can bring when there are reflections and effects not taken into account by the model. Details of the simulations can be found in Section 2.6.

The performance of the system have been evaluated computing the insertion loss (IL) at each microphone. They are then averaged over the different evaluation areas: dark zone (DZA), back array (BA), left array (LA) and right array (RA),

$$\langle \mathrm{IL} \rangle = \frac{1}{N}\sum_{n=1}^{N} 20\log\left(\frac{|p_n^p|}{|p_n^t|}\right), \tag{9}$$

where p is the complex pressure at the microphone n within a given area and by the main array alone p_n^p or by the main and control arrays together p_n^t.

The algorithm proposed here has been evaluated using different number of iterations, ranging from 1 to 3. The active set-type method from [26] was used to limit the magnitude of the filters to 1 (0 dB) even though it was triggered only after three iterations of the CGLS algorithm. In addition, the method proposed has been compared to least square with Tikhonov regularization where the l-curve and GCV have been used to select the regularization parameter and the gain of the solutions has been adjusted when violating the amplitude constraint. The problem has also been formulated within a convex optimization framework and solved in MATLAB using the *fmincon* function. In this case we used two types of constraints, one on the amplitude of each individual source ($|\mathbf{q}| \preceq 1$) and one on the array effort ($||\mathbf{q}||_2^2 \leqslant 0.5$). In each case the solution has been computed at 49 different frequencies in 1/24th octave bands. A summary of the methods can be found in Table 2. The table, also shows the running time of each method. These values comprises all the 49 runs to compute the solution

Table 2
Summary of the methods tested, their defining equations, parameters, parameter selection method and running time.

Tag	Equation	Param search method	Param	Running time [ms]	
				Mean	Standard deviation
$cgls_{k=1}$	Eq. (2) + [26]	k = 1	User def	5.2	1.1
$cgls_{k=2}$	Eq. (2) + [26]	k = 2	User def	6.1	1.2
$cgls_{k=3}$	Eq. (2) + [26]	k = 3	User def	25.7	5.3
$fmincon_{\lvert q\rvert \prec 1}$	$\min_{\mathbf{q}} \lvert\lvert \mathbf{p} - \mathbf{Hq} \rvert\rvert_2^2$ s.t. $\lvert \mathbf{q} \rvert \prec b$	b = 1	User def	2571.2	235.2
$fmincon_{\lvert\lvert q\rvert\rvert_2^2 < 0.5}$	$\min_{\mathbf{q}} \lvert\lvert \mathbf{p} - \mathbf{Hq} \rvert\rvert_2^2$ s.t. $\lvert\lvert \mathbf{q} \rvert\rvert_2^2 < b$	b = 0.5	User def	2204.5	244.6
gcv	$\min_{\mathbf{q}} \lvert\lvert \mathbf{p} - \mathbf{Hq} \rvert\rvert_2^2 + \lambda \lvert\lvert \mathbf{q} \rvert\rvert_2^2$	λ	[15]	3.2	0.7
$l-curve$	$\min_{\mathbf{q}} \lvert\lvert \mathbf{p} - \mathbf{Hq} \rvert\rvert_2^2 + \lambda \lvert\lvert \mathbf{q} \rvert\rvert_2^2$	λ	[14]	3.0	0.5

at each frequency. The statistics are estimated running the algorithm in MATLAB 128 times on a Windows 10 laptop PC with Intel Core i7-8750H CPU at 2.20 GHz and using 16 GB of RAM.

2.6. Simulations

The simulations were performed using the complex directivity point source method (CDPS) [27]. This model relies on free-field conditions, so it does not really match the conditions of the experiment due to the obstacles highlighted in Fig. 1b. The simulations were performed reproducing the setup shown in Fig. 1a, using the same loudspeakers, same sensitivity and directivity pattern, a temperature of 5°C and no wind to match the weather conditions encountered when the same transfer functions were measured (see Table 1). In a first step, the simulations were used to obtain the primary field **p** and secondary transfer functions **H** only within the dark zone (DZA). The point grid in the DZA in the simulation matched the position of the microphones during the measurements. These data was used to generated the filters for the control sources using the methods in Table 2. In a second step, the points in the simulated DZA had been moved modifying their coordinates by drawing a correction from a normal distribution, mimicking the shift applied in the real experimental setup. Then, the primary field **p** and secondary transfer function **H** have been computed again in the DZA and also at LA, RA, and BA. Then, the different methods have been evaluated applying the filters obtained in the first step to the newly simulated transfer functions and computing the insertion loss as defined in Eq. (9).

3. Results

The results presented in this section are all obtained from physical measurements. Simulations are used to generate the filters in Section 3.1 and only in the case of Fig. 3 to calculate also the insertion loss.

3.1. Simulated transfer functions

3.1.1. Insertion loss

The insertion loss produced by the different algorithms using simulated transfer functions are shown in Fig. 2. The insertion loss are calculated from measured pressure fields obtained applying the filters computed from simulated transfer functions. The insertion loss in the dark zone provided by the different algorithms are quite close to each other. According to simulations, the differences were supposed to be much larger, as shown in Fig. 3. The insertion loss presented in this figure are the only one in this paper where simulations are used to derive the filters and to calculate the insertion loss. Inaccuracies in the model, that fails to take into account reflections, inhomogeneities in the medium and wind, reduced the gap and the overall performance. Solutions obtained using larger regularization such as the CGLS with one iteration, $cgls_{k=1}$, and *l-curve*, that were supposed to give the worst performances, have degraded much less than the others and are more robust to such inaccuracies (more in Section 4.2). On the other hand, *fmincon* was supposed to provide insertion loss of more than 30 dB over a large frequency range according to the simulations described in

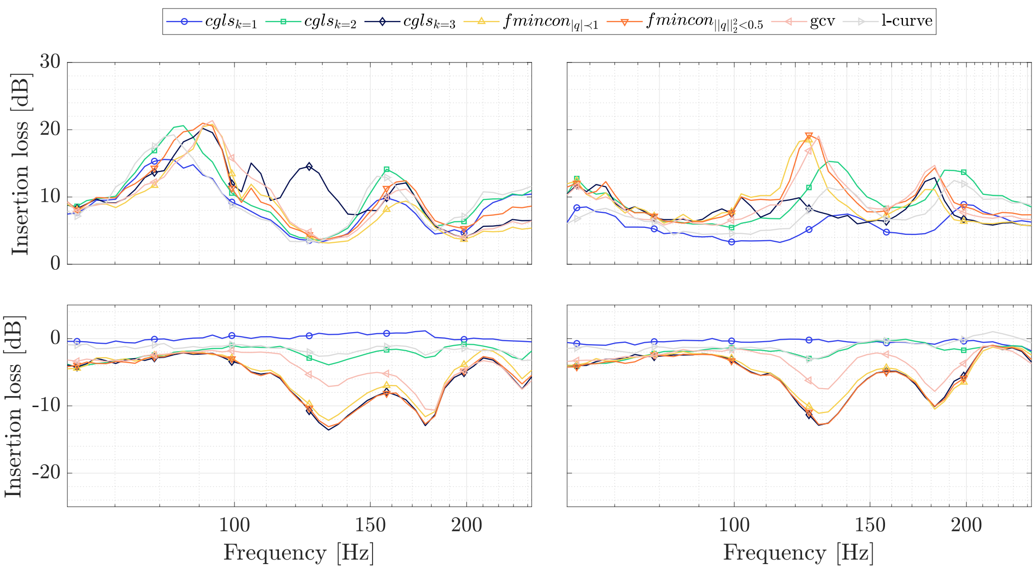

Fig. 2. Insertion loss IL from the measurements set with filters derived from simulated transfer functions, see Table 3. Top left: loss averaged over the dark zone. Top right: loss averaged over the array at the back. Bottom left: loss averaged over the left array LA from Fig. 1a. Bottom right: loss averaged over the right array RA in Fig. 1a.

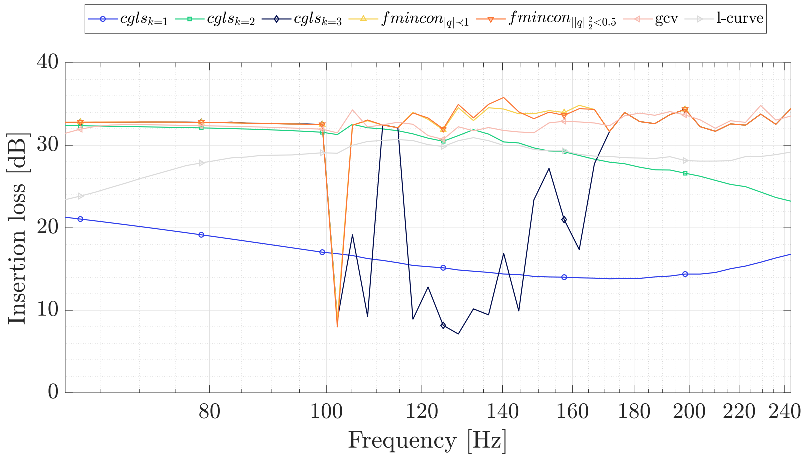

Fig. 3. Spatially averaged insertion loss IL in the dark zone. In this case only, simulations are used to compute both the filters and the insertion loss are calculated from the simulated filters and simulated transfer functions in the two-step process described in Section 2.4.

Section 2.6 and whose results are shown in Fig. 3. To achieve such large reductions, the magnitude and phase of the primary field need to be matched to such an accuracy that is not achievable with all the uncertainties that can be encountered in a real setting. The insertion loss provided by the 3 iterations CGLS method, $cgls_{k=3}$, between 100 and 150 Hz are much larger than for any other method. The real sound field in this frequency range present a dip, probably due to interactions with the surrounding obstacles, and the model used for the simulations tends to overestimate the sound pressure level in the DZA. The amplitude match between the primary and the secondary field is poor for most methods leading to a decrease in insertion loss. $cgls_{k=3}$ is the only solution where the active set-type method is active. This method redistributes the energy between the coefficients to comply with the constraints without any knowledge of the primary field. In doing so, it introduces a phase relationship between the sources in the middle of the array and the one at the extremes that also produce a dip in amplitude in the dark zone. This proves to be a much closer match to the amplitude of the primary field thus producing larger insertion loss.

The algorithms with smaller regularization show an improvement beyond the dark zone, at the back array. A possible explanation is that, with lower regularization, the secondary field better matches the first one in the dark zone while higher regularization matches only some of the largest spatial features of the primary field but not accurately enough to translate to larger distances and progressively degrade as the mismatch grows.

It is very important to also see what is happening off-axis. The algorithms that on the paper were supposed to provide the larger insertion loss are also the ones that increase the most the sound pressure level outside of the dark zone in Fig. 1. It can be seen how, as the regularization decreases, the insertion loss become more and more negative thus indicating an increased SPL in these positions. Solutions with weaker regularization excite more higher order pressure modes that present strong radiation off-axis (more in Section 4). The resulting secondary field is more prone to present side lobes. In this instance though, the total sound field, produced by the superposition of the primary and secondary fields, does not present side lobes itself but a level increase where the primary field alone had low sound pressure levels. This is the main reason for the negative side lobes and it is a result of the choice of the regularization combined with a mismatch between the simulated and the real sound fields as explained in the next section.

3.1.2. Primary and secondary sound fields

The negative insertion loss could be interpreted as side lobes. In this particular case though, the negative insertion loss are caused by dips in the primary field. In Fig. 4 we can see the measurements corresponding to $cgls_{k=3}$ as function of microphone position and frequency for the microphone array on the left of the dark zone (LA in Fig. 1a). The sound field that results from the interaction of primary and control sources does not present side lobes. It is increasing the overall level if compared with the primary field alone and is doing so at frequencies and points where the level of the primary field alone was quite low. This suggest that the problem it creates is not as bad as the insertion loss alone might suggest. It can still be a problem because the level increase is quite large and if there is a building in such a direction the difference will be very much noticeable. The control point stopping criterium discusses in Section 2.2 and implemented in the CGLS algorithm takes into account such situation. The larger the regularization (see $cgls_{k=1}$, $cgls_{k=2}$ and $l-curve$) the closer to 0 the insertion loss. This is because with a stronger regularization, the secondary sound field is more focused on the dark zone with limited radiation outside of it; resulting in a minimal level increase with respect to the primary field alone. The insertion loss at the left and right arrays (LA and RA) are similar but the amplitude and positions of the dips do not totally agree due to the asymmetry of the sound field produced by the different obstacles at the left and right sides of the domain, as it can be seen in Fig. 1b.

3.2. Measured transfer functions

To study the effect that simulated or measured transfer functions have on the performance of the system, a new set of filters has been computed using the measured transfer functions from Table 1. The resulting insertion loss have been compared to the ones obtained by using simulated transfer functions. We omitted the graphics corresponding to the LA and RA for $cgls_{k=1}$ and $cgls_{k=2}$ for clarity since the results using measured and simulated transfer functions match very closely. The results for $cgls_{k=1}$ are shown in Fig. 5a. The difference is quite noticeable in the dark zone. The measured transfer functions provide a better performance on average even though not much larger than with the simulated ones. Measuring the transfer functions provides an accurate description of the sound field in the dark zone. The main difference is located between 100 and 150 Hz due to a model mismatch. The

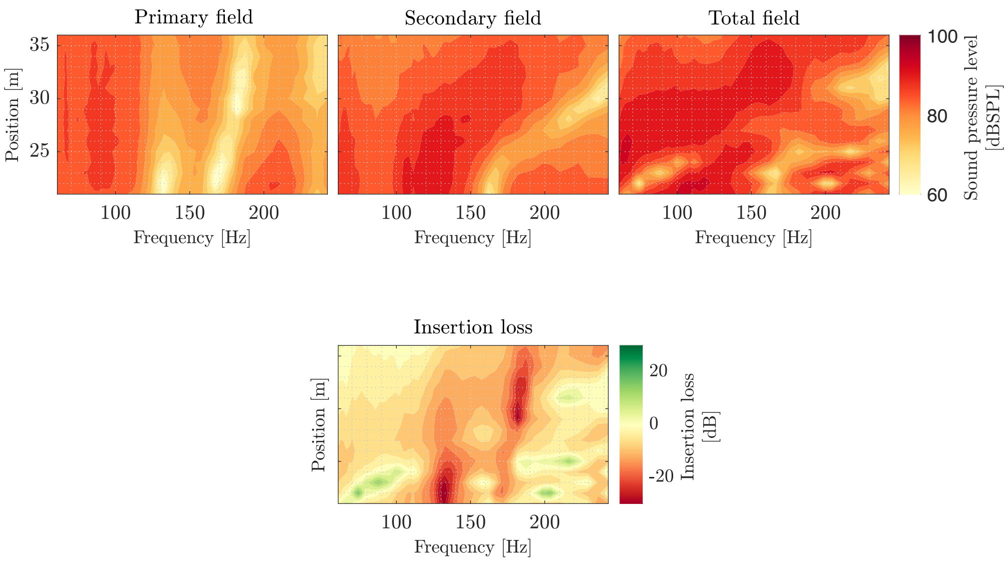

Fig. 4. Overview of the sound fields and insertion loss IL at the left array (LA in Fig. 1a) for the set of filters obtained with $cgls_{k=3}$ and simulated transfer functions. First: primary field; Second: secondary field; Third: total field; Fourth: insertion loss.

model tends to overestimates the amplitude of the sound field between 100 and 150 Hz where the primary field present a dip. The amplitude mismatch results in the drop in performance when using simulated transfer functions. In cases such as this one, where reflections are involved, the interference pattern outside of the measured area will be quite different. Because of this difference, the performance in the dark zone do not generalize well to other areas. This is confirmed by the measurements at the array at the back (BA, in Fig. 1a). Here the performances from the measured transfer functions degrade more than with simulations.

Increasing the number of iterations to 2 improves the performance of both sets of filters in the dark zone as it can be seen in Fig. 5b. The set derived from the measured transfer functions provide very irregular performance over frequency but it still presents an improvement over simulations. This solution can provide better results than the one iteration version but it is more sensitive to inaccuracies. The weather conditions changed from the time when the transfer functions were measured to the time when the insertion loss were obtained. While the temperature did not change, the direction of the wind changed approximately 110 degrees while keeping its speed (see Table 3, entry number 23 compared to Table 1). Considering this shift, the accuracy of the match between primary and secondary field can change rather quickly with frequency and/or space since it does not only affect the direct field but also the reflections and thus the interference pattern. This can cause abrupt changes in the performance considering the high level of reduction reached here (up to 24 dB). However, even if there are large drops, the insertion loss are over 10 dB for most frequencies. The simulated transfer functions provide a smaller reduction but are not as irregular. This smoothness is due to the lack of reflections in the simulations. When there is a difference between the weather conditions used to compute the filters and the real one, their impact on the results are not as big. This is because these filters are matching only the direct field that does not changes as much as the interference pattern. In addition, also here the largest difference is between 100 and 150 Hz. The reason is the same as with $cgls_{k=1}$. This time the difference is even larger and this is due to the increased number of iterations. We can see here that when the propagation paths are accurately characterized, the increased accuracy of the algorithm lead to larger insertion loss. On the other hand, the algorithm is also more sensitive to errors which cause the drop in performance due to the model mismatch described in Section 3.1.

Finally, the losses in the dark zone using 3 iterations are shown in Fig. 5c and they have an overall trend similar to the previous ones. This solution further reduce the residual providing larger insertion loss than $cgls_{k=1}$ and $cgls_{k=2}$. The performance from simulated transfer functions is now closer to the measured ones between 100 and 150 Hz. As explained in Section 3.1, the active set-type method introduce a phase relationship between the secondary sources that produce a dip in level in such frequency range. This counterbalance the model overestimating the amplitude of the sound field in this region and range, providing a better match between the primary and secondary fields. The performance in this case is limited by the fact that the solution hits the amplitude constraints and it is even more sensitive to uncertainties. We can see here that the insertion loss reach peaks of more than 25 dB and is above 10 dB over the entire frequency range. At the back, the performance of the measured transfer functions is similar to the ones obtained with two iterations. When simulated transfer function are used instead, the insertion loss are worse than with 2 iterations. $cgls_{k=3}$ is even more sensitive to uncertainties due to the weaker regularization. The changes in the interference pattern outside of the dark zone introduce a larger drop in performance than in the previous case.

For all the algorithm tested, not only for $cgls_{k=1}$ and $cgls_{k=2}$ but also the other, the insertion loss at LA and RA from measured transfer functions closely match the results from simulated transfer functions in Fig. 2. The only exception is $cgls_{k=3}$. This is the reason why we show these results only for this case. The performance of the filters derived from measured transfer functions do not produce a large increases of the sound pressure level off axis. On the other hand, there is a large increase when the simulated transfer functions are used instead. The background noise in the measured transfer functions actually improve the conditioning of the corresponding transfer function matrix. The higher spatial frequency associated with the noise field increases the amplitude of the high order singular values. This result in a more stable solution, with a smaller amplitude and that does not hit the amplitude constraints. It behaves as a solution with a stronger regularization with weak radiation off-axis. The worse conditioning of the simulated secondary transfer function matrix lead to a solution with a larger

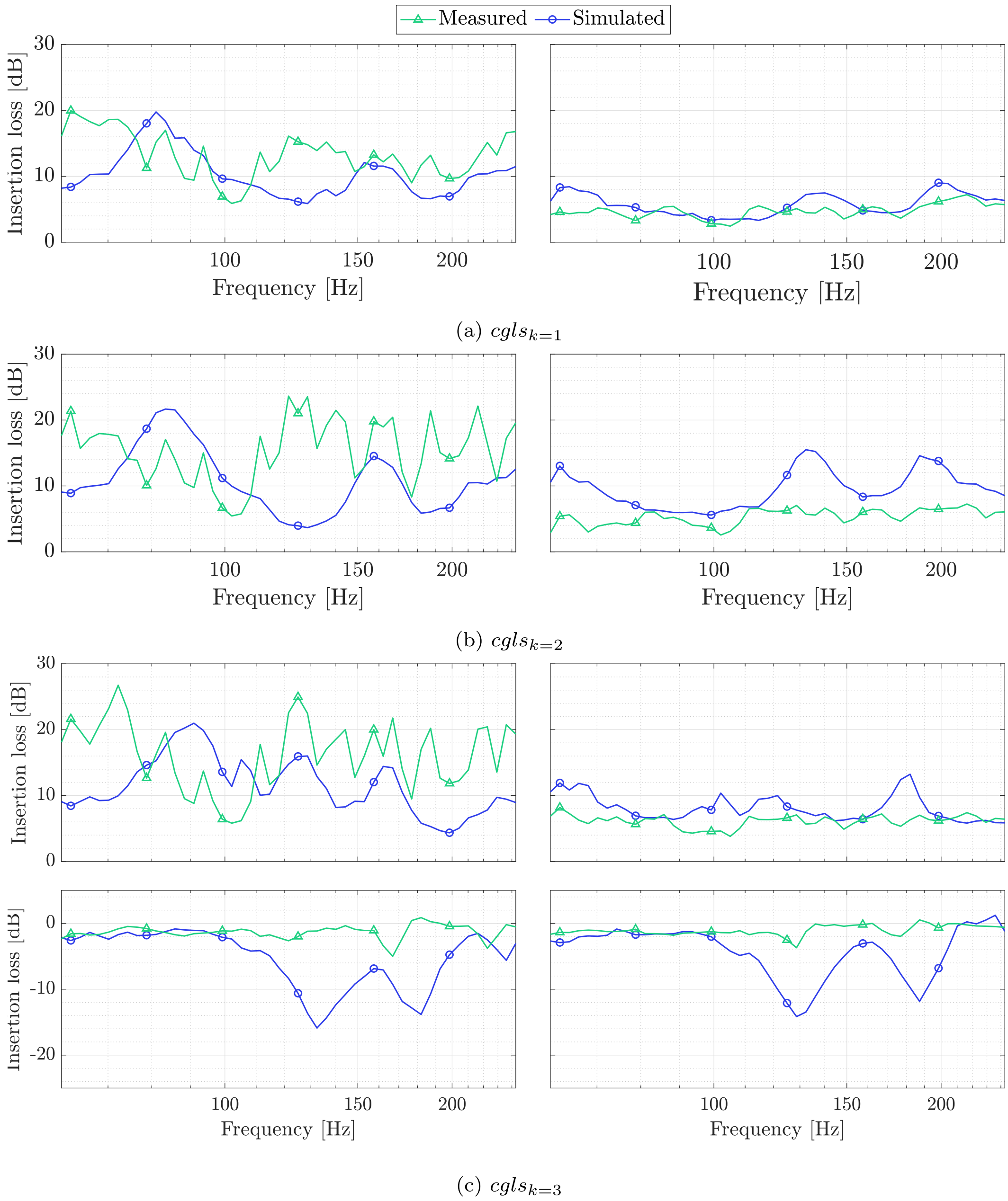

Fig. 5. Insertion loss from the measurements using filters from $cgls_{k=1}$ $cgls_{k=2}$ and $cgls_{k=3}$ for simulated and measured transfer functions. The insertion loss are averaged over the DZA (left) and at the BA (right) as defined in Fig. 1a. The last row contains the insertion loss at the LA (left) and RA (right) for $cgls_{k=3}$. They are not shown in for the other case since the results form simulations and measurements closely match.

amplitude that hits the constraints and produce a stronger radiation outside the dark zone. This discrepancy between measured and simulated transfer functions only occurs in this case because it is the one with the weakest regularization. All the other solutions based on inverse problems have a stronger regularization and the better conditioning of the measured transfer function matrix does not produce such a striking difference. It does however produce a smaller level increase at LA and RA than the solutions from simulations do. The method based on convex optimization are affected differently by the noise and the amplitude of the solution keeps being large thus produce an increase in sound pressure level off-axis.

The effect of the regularization and the level increase seen when using the simulated transfer function is also related to a mismatch between the predicted and real primary pressure fields. Because of this, the secondary pressure field fails to match the primary field on the sides and it increases the level where the primary field had a small amplitude. This does not occur in the dark zone because it is closer to the main axis and well within the main lobe of both arrays.

To facilitate the comparison, the primary field from simulation and from measurements at the left microphones array are plotted in Fig. 6. Away from the main axes, the simulated primary field present a dip that moves closer to the main axis as the frequency increases. In the measurements, this dip has a different extension in space and it behaves differently in both space and frequency. The possible reasons for this difference are reflections and a mismatch in the speed of sound due to temperature and wind. The sec-

Table 3
Summary of the weather conditions encountered during the measurements displayed in this paper. The wind direction is relative to the main axis of the setup: 0° corresponds to wind blowing in the direction of propagation; 90° blowing towards the right of the main axis and −90° to the left. The complete table can be found in the supplementary material.

Index	Transfer functions	Array	Method	$T_{z=2m}$ [°C]	$T_{z=0m}$ [°C]	Wind speed [m/s]	Wind direction [°]
1	Simulated	Both	$cgls_{k=1}$	4.4	12.6	0	-
2	Simulated	Both	$cgls_{k=2}$	4.4	11.6	0.9	−22.5
3	Simulated	Both	$cgls_{k=3}$	4.4	11.2	0.4	135
4	Simulated	Both	$fmincon_{\|q\|<1}$	4.6	11.1	0.9	−180
5	Simulated	Both	$fmincon_{\|\|q\|\|_2^2<0.5}$	4.6	11.1	1.3	157.5
6	Simulated	Both	gcv	4.6	11.1	1.3	157.5
7	Simulated	Both	$l-curve$	4.6	11	1.8	157.5
10	Simulated	Primary	$cgls_{k=3}$	4.4	11.2	0.4	135
17	Simulated	Control	$cgls_{k=3}$	4.4	11.2	0.4	135
22	Measured	Both	$cgls_{k=1}$	5	3.7	0	-
23	Measured	Both	$cgls_{k=2}$	5	3.7	0.4	112.5
24	Measured	Both	$cgls_{k=3}$	5	3.7	0.4	112.5
31	Measured	Primary	$cgls_{k=3}$	5	3.7	0.4	112.5
38	Measured	Control	$cgls_{k=3}$	5	3.7	0.4	112.5

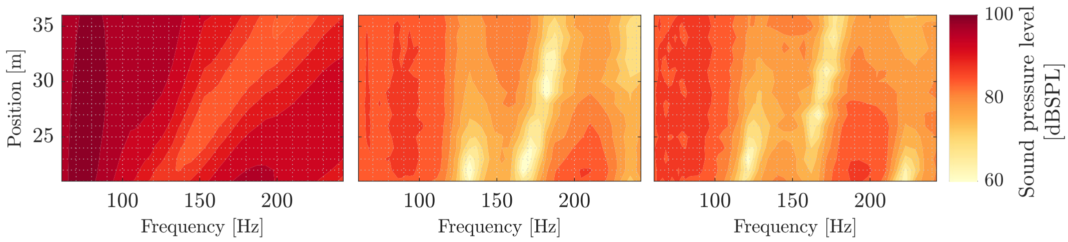

Fig. 6. Overview of the primary field at the left array: simulated (left) and measured at two different times (center corresponding to entry 10 and right to entry 31 in Table 3).

ond and third plots in the figure both represent the measured primary field but at two different times that had a temperature difference of approximately 8°C (entries 10 and 31 in Table 3). They show how a difference in temperature can change the shape of the radiation pattern.

Now looking at the secondary fields in Fig. 7 we see how using filters generated by $cgls_{k=3}$ from simulations we obtain a good match with the simulated primary field but not with the measured one. The main difference is the large sound pressure level introduced by the secondary field in positions and frequencies where the level of the primary field was much lower. This results in the large dips observed in Fig. 5c. When we look at the secondary field generated with $cgls_{k=3}$ using measured transfer functions we see how it provides a closer match to the measured primary field with overall lower sound pressure levels.

4. Analysis

4.1. Numerical properties of the solutions

In this section the focus is brought to the numerical properties of the secondary transfer functions and to the solutions provided by the different algorithms.

It is possible to analyze the solutions obtained using the CGLS or any other method in terms of which pressure modes they excite and in which measure. Using the SVD, one can express the secondary field $\mathbf{p_s}$ as

$$\mathbf{p_s} = \mathbf{Hq} = U\Sigma V^{\mathrm{H}}\mathbf{q} = \mathbf{Uw}, \tag{10}$$

where $\mathbf{w} = \Sigma V^{\mathrm{H}}\mathbf{q}$ is a vector of weights or amplification coefficients applied to the pressure modes. We can study why some solution might be problematic outside of the dark zone by looking at the amplitude of the weights and the shape of the corresponding pressure modes.

Fig. 8 shows the magnitude and phase of the left singular vectors, equivalent to pressure modes, of the simulated transfer functions $\mathbf{H}$ at 125 Hz. The domain used for the simulations was symmetric and as a consequence it can be seen how the odd order modes are also symmetric while the even ones are anti-symmetric. Another important observation regards the energy distribution within each mode. First of all, low order modes have a lower spatial frequency and second, the energy is more focused at the center while it moves towards the sides as the order increases. The different algorithms and regularization combine these modes in different ways and with different weights which determine the spatial characteristics of the solutions.

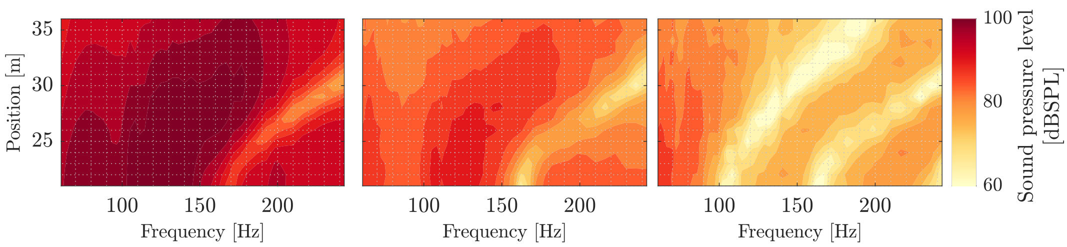

Fig. 7. Overview of the secondary field at the left array: simulated (left), measured applying the filters from simulations (center, entry 17 in Table 3) and measured applying the filters obtained from measurements (right, entry 38 in Table 3).

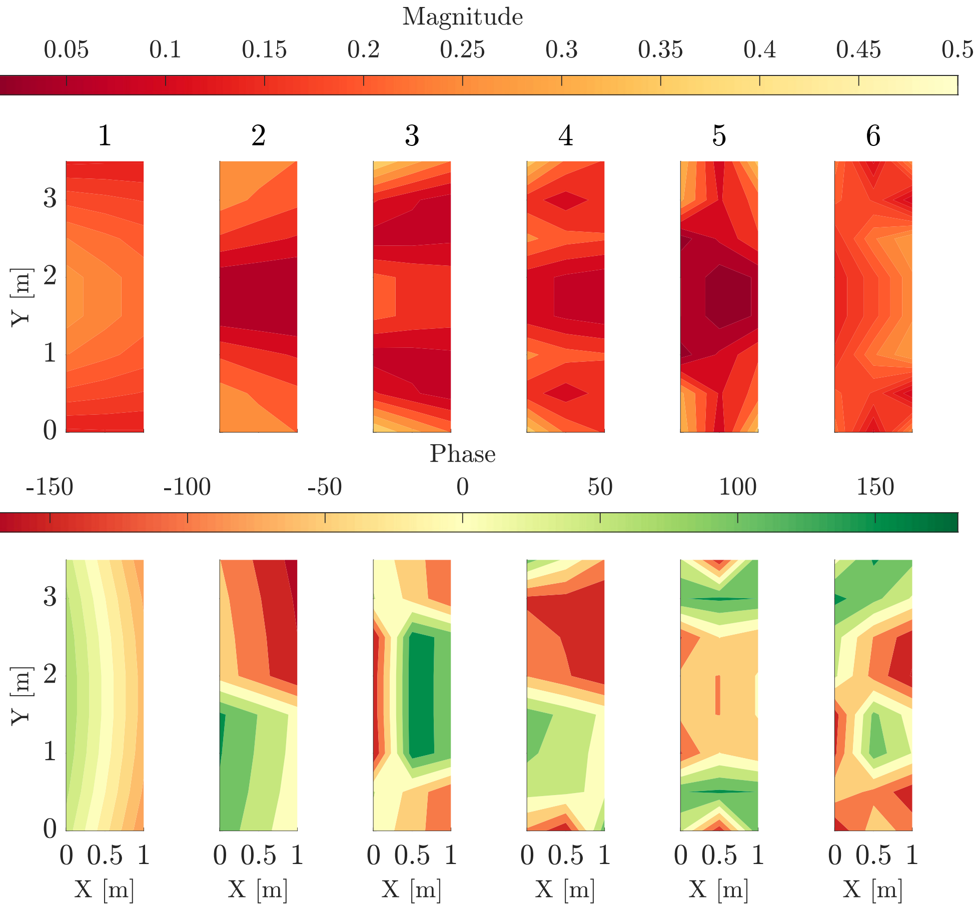

Fig. 8. Magnitude (top) and corresponding phase (bottom) of the all the pressure modes, both symmetric and anti-symmetric, of the simulated transfer functions at 125 Hz.

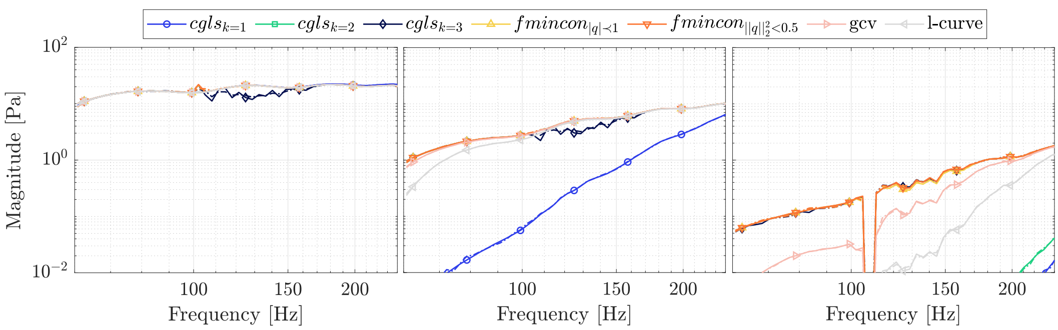

Fig. 9. Magnitude of the coefficients from the solutions obtained with simulated transfer functions that are applied to the pressure modes: 1 (left), 3 (center) and 5 (right).

The solutions from the different algorithms excite these modes with different weights that can be obtained applying Eq. (10). These weights are shown in Fig. 9 as a function of frequency. Considering that in the simulations, both the primary field and the secondary transfer functions are symmetric, the even order modes are not excited at all and have been omitted for clarity. Odd order modes have weights that in general decrease with the order. The first mode has approximately the same amplitude in each solutions. The amplitude of the third mode increases with frequency starting at one order of magnitude lower than the first mode and reaching approximately half its amplitude at the top of the frequency range. This is approximately the same for every solutions except for *l-curve* and $cgls_{k=1}$. The *l-curve* present a slightly smaller amplitude than the other methods. However, $cgls_{k=1}$ has an amplitude of various orders of magnitude smaller than the first mode except at high frequencies. This mean that for this solution, only the first mode is relevant up to a frequency of approximately 200 Hz, so the third mode can be ignored for all practical purposes. The fifth mode is much smaller than the previous ones. It can be seen here that the solutions where the amplitude of this mode is larger are also the ones that in Fig. 2 had more energy radiated towards the sides. $cgls_{k=1}$ is the one radiating the least amount of energy towards the sides because only the first mode has a large amplitude and it focuses the energy towards the main axis. The dip in the coefficients of the fifth mode is a numerical artifact due to how the modes are sorted in MATLAB.

4.2. Sensitivity analysis

The weather conditions, specifically temperature and wind and as a consequence the speed of sound, affect the transfer functions between a source and a set of receivers as describe in [10]. The performance of an outdoor active noise control system depends on how close the weather conditions are to when the transfer function were measured/simulated as explained in [7]. In this section, we present an analysis of the robustness of the *cgls* algorithm to inaccuracies in the speed of sound. The filters were computed using simulated transfer functions obtained using a speed of sound of 334.4 m/s corresponding to a temperature of 5°C as recorded when the transfer functions were measured during the experimental validation. Three different sets of filters were obtained by running the algorithm for 1, 2 and 3 iterations. An additional 512 realizations of the primary field and secondary transfer functions were computed using speed of sounds following a Gaussian distribution with mean 334.4 m/s and a standard deviation of approximately 2.5 m/s. The speed of sound was calculated using the dry air approximation $c = 20.05\sqrt{273.15 + T}$ [28] with T the temperature in °C. The distribution of speed of sound are shown in Fig. 10. Each set of filters was then applied to each of the 512 realizations of the secondary transfer functions and the resulting insertion loss in the dark zone have been averaged over space and frequency. The relative frequency of the insertion loss for $k = 1, k = 2$ and $k = 3$ are shown in Fig. 11.

In general, the symmetric distribution of the speed of sound is now asymmetric. The reason is that as the estimation error of the speed of sound increases, regardless if due to underestimation or overestimation, the performance gets worse and the insertion loss decreases. Furthermore, the histograms for $cgls_{k=1}$ and $cgls_{k=2}$ present a sharp rise at high insertion loss. This is a consequence of using the mean speed of sound to also calculate the filters. It follows that error in estimating the speed of sound follows a Gaussian distribution with mean 0 and the same standard deviation as the distribution of the speed of sound. This means that small errors occur more often leading to larger relative frequencies for high insertion loss. Moreover, a sharper increase means that large insertion loss are achieved in more realizations hinting to a larger robustness of the method due to a larger tolerance to errors. $cgls_{k=3}$ is an exception since it does not show the same sharp rise at high insertion loss. Even when the error is small, in this case the performance is limited by the amplitude constraints and the active-set type method that is triggered only in this case. The performance from $cgls_{k=1}$ are worse both in absolute and average terms than the others. $cgls_{k=2}$ can provide the largest insertion loss when the speed of sound used to compute the filters is accurate. $cgls_{k=3}$ provides slightly worse performance in the best case scenario. This is again a result of the constraints. Since this limitation is intrinsic to the solution and independent from the accuracy of the sound speed, on average the losses tends to be worse than the for $cgls_{k=2}$. The shape of the frequency distributions for $cgls_{k=2}$ and $cgls_{k=3}$ are rather similar and the center of gravity occurs at insertion loss comprised between the mean and the mean minus one standard deviation. The main difference is that $cgls_{k=3}$ has a smaller tail at higher insertion loss and larger relative frequencies at the center of gravity. This is reflected in the lower average value and a smaller standard deviation. $cgls_{k=1}$ is very different since the center of gravity is well distributed between plus/minus one standard deviation from the mean. Furthermore, the largest insertion loss have the largest relative frequencies. In this case, the mean is smaller than in the other two cases but also the standard deviation is considerably smaller meaning that $cgls_{k=1}$ is the most consistent in terms of performance.

The main take-away from this analysis is that $cgls_{k=1}$ is more robust and deliver consistent performance across a larger range of speed of sound even though the mean and absolute insertion loss are smaller than in the other cases. $cgls_{k=3}$ fails to deliver the improvement that one might expect by increasing the number of iterations due to the amplitude constraints. $cgls_{k=2}$ should be chosen if one desires larger insertion loss than the ones $cgls_{k=1}$ can provide.

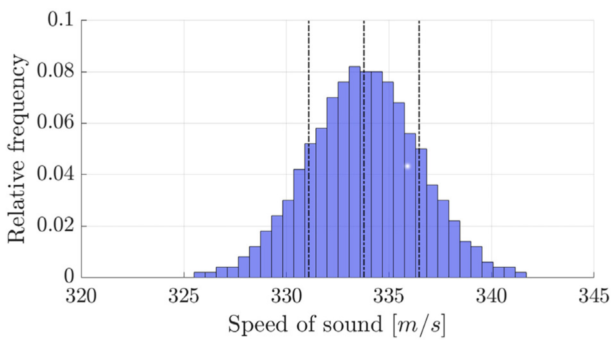

Fig. 10. Probability distributions of the temperatures (left) and corresponding speed of sound (right) used in the simulations. The dashed line represent the mean and the mean plus/minus one standard deviation.

4.3. Convergence analysis

In this section the focus is on the effect that different grid resolutions have on the final performance of the algorithm for different number of iterations. The transfer functions used to compute the filters were computed over grids of receivers with resolutions of: 1 m, 0.75 m, 0.5 m, 0.25 m, 0.1 m, 0.05 m and 0.01 m. The filters were then applied to transfer functions simulated over a grid with a resolution of 0.5 m but with receivers at different locations than

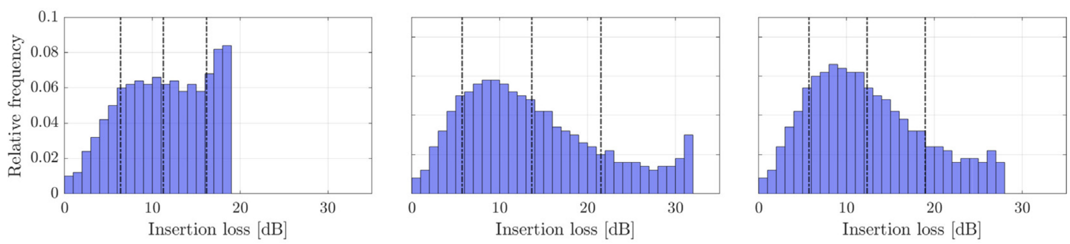

Fig. 11. Histograms with the insertion loss from each of the 512 realizations averaged over space and frequency. Dashed lines show the overall mean and mean plus/minus one standard deviation. Left: $cgls_{k=1}$; center: $cgls_{k=2}$; right: $cgls_{k=3}$.

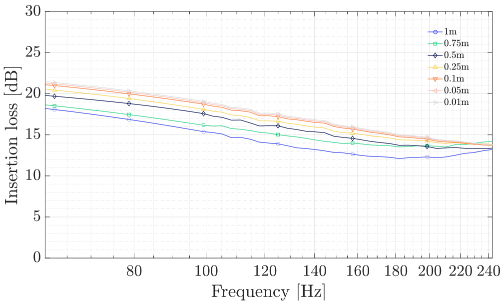

(a) Filters from $cgls_{k=1}$ applied to simulated transfer functions

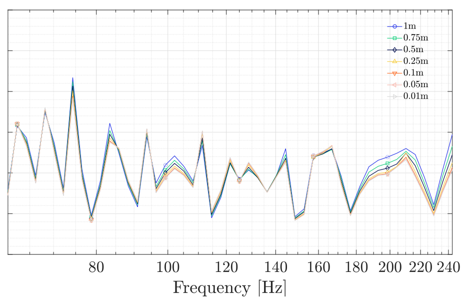

(b) Filters from $cgls_{k=1}$ applied to measured transfer functions

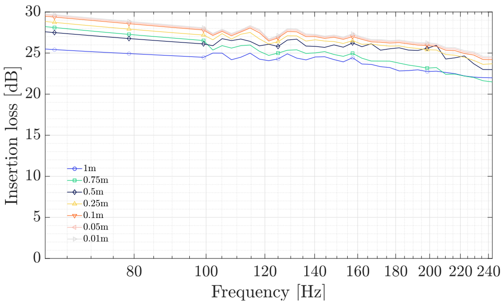

(c) Filters from $cgls_{k=2}$ applied to simulated transfer functions

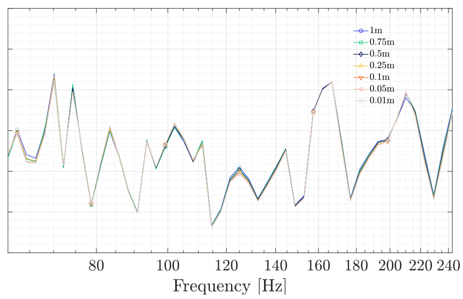

(d) Filters from $cgls_{k=2}$ applied to measured transfer functions

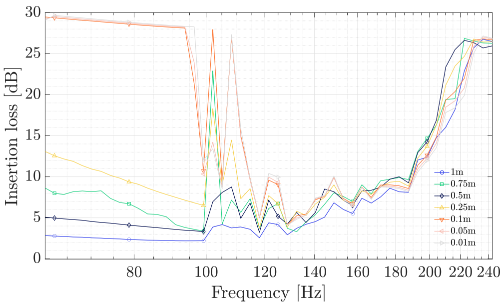

(e) Filters from $cgls_{k=3}$ applied to simulated transfer functions

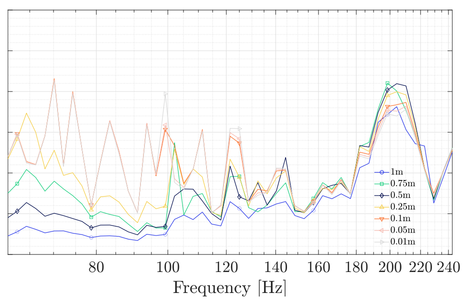

(f) Filters from $cgls_{k=3}$ applied to measured transfer functions

Fig. 12. Insertion loss from filters computed using different number of iterations of the CGLS algorithm and secondary transfer functions with different grid resolutions. The filters are then applied to either simulated (left) or measured transfer functions (right).

the ones used to compute the filters. In addition, the filters were also applied to the transfer functions that were actually measured on the field.

In Fig. 12 the insertion loss averaged over the dark zone are shown for the different grid resolutions and number of iterations of the CGLS algorithm. When the filters obtained after 1 iteration are applied to the simulated transfer functions (Fig. 12a), the insertion loss increase as the resolution gets finer. The sound field is better captured with finer grids and the resulting anti-field matches the primary field more closely up to approximately 200 Hz where the relation between resolution and performance is not as clear. The results seems to converge for grid resolutions smaller than 0.1 m. When the filters are applied to the measured transfer functions (Fig. 12b), the finer resolutions do not affect the insertion loss. This is due to the fact that for better performance, the tolerance to errors gets smaller and the real world uncertainties spoil the gain in performance provided by increasing the sampling resolution. As a matter of fact, at some frequencies the coarser grids perform better than the finer ones because they are not modelling finer details and then do not suffer when such details do not exactly match the reality.

Similar conclusions can be drawn when the algorithm ran for 2 iterations. In this case the simulated insertion loss (Fig. 12b are larger than with $cgls_{k=1}$ as one might expect. On the other hand, when the filters are applied to real transfer function (Fig. 12b), both the gain from a finer grid and the additional iteration fade and the performance are quite similar to the ones shown in Fig. 12b. This is due to the fact that this solution is less robust and the real world uncertainties affect all the solutions regardless of the grid size used.

The situation is different when the algorithm ran for 3 iterations. When the filters are applied to simulated transfer functions (Fig. 12b) we see a big difference at low frequencies when grids with a resolution finer than 0.1 m are employed. At mid frequencies there is a trend similar to the previous cases where the performance improves by making the grid finer, reaching convergence for a resolution of 0.1 m. At higher frequencies the effect of the grid resolution on the performance is not clear. When the filters are applied to measured transfer functions (Fig. 12b) we see a trend similar to the one saw when using simulations and, as it happened in the previous two cases, the improvements are not as big as one might expect, except at low frequencies. The reason why in this

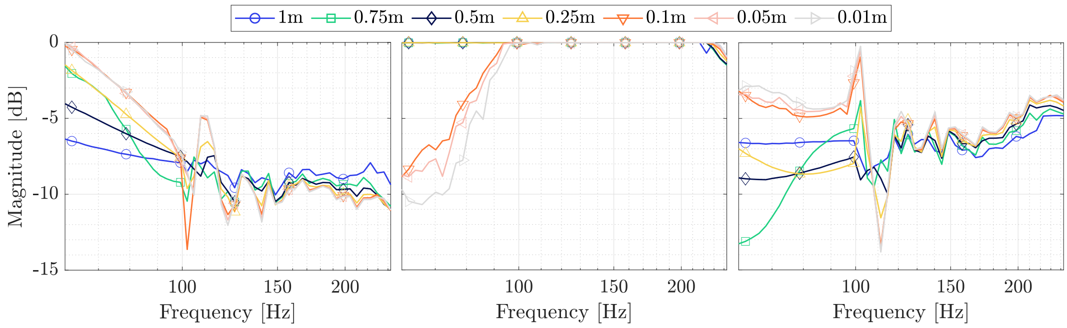

Fig. 13. Filters obtained from the different grid resolutions used to obtain the transfer functions fed to the CGLS algorithm with 3 iterations. Left: outermost sources; Middle: second and fifth sources; Right: innermost sources.

case there is such a big difference using different grid resolutions, and why this difference is also present in the measured transfer functions, can be found inspecting the actual filters in Fig. 13.

In this particular case the solutions hit the amplitude constraints forcing the active set-type method to kick in and find an alternative solution with a magnitude smaller than one. The solutions with grids finer than 0.1 m do not hit the constraints below 100 Hz. This is the reason why, up to this frequency, these solutions provide much larger insertion loss. Above 100 Hz, all solutions hit the constraints and the different grid resolutions do not matter as much anymore and the performance in terms of insertion loss drop dramatically. The high frequency inconsistencies might be due to how the active set-type method works. Instead of just clipping the solution, this method fix the coefficients of the solution hitting the constraints, and redistribute the energy between the coefficient above and below the constraints. In this way, it finds an alternative solution with no coefficient larger than the user-defined threshold. For this reason, it is not straightforward to find a relation between grid resolutions and insertion loss. Finer resolutions do not hit the constraints at low frequencies because the corresponding transfer function matrices have larger singular values. Even the high order singular values are close to unity. This means that when they are inverted to compute the solution, they do not boost the amplitude of the filters as much as the singular values corresponding to the coarser grids do, so the corresponding solutions are more stable. This can only be seen with $cgls_{k=3}$ because in this case the smaller regularization lead to higher order modes having a larger weight on the solution making the amplitude of the high order singular values more significant.

5. Discussion

In Section 2 it was explained how the number of sources determines $rank(\mathbf{H})$ which in turns limits the number of iterations of the *cgls* algorithm. In the experiment presented in Section 2.4, we ran the algorithm a maximum of 3 iterations because of the symmetric nature of the primary field and secondary transfer functions used in the simulations. This symmetry halved the degrees of freedom and subsequent iterations would not have added any new information or improvement to the solutions. We can also see this in Section 4.1 where only three of the six pressure modes were active in all the solutions from the different algorithms.

The iterative nature of this algorithm can be both a strength and a limitation. It is a strength since it makes it easier to select the appropriate regularization by controlling the number of iterations and monitoring relevant performance criteria in between iterations. On the other hand, the amount of regularization changes in discrete steps going from very large at the first iteration to almost no regularization. However, this limitation is lessened when the number of secondary sources increases. When more sources are used, the maximum number of iterations increases too. This would result in more discrete steps and smoother changes in the regularization. More sources are also beneficial for the active set-type method. More sources means more degrees of freedom, allowing this algorithm to find a better alternative solution. Few degrees of freedom and large violations of the constraints, as it was the case with $cgls_{k=3}$, can lead to solutions with discontinuities because the algorithm has to intervene more aggressively with fewer options for redistributing the energy between coefficients. Such discontinuities can make the implementation of the filters problematic, they can add signal artifacts and a drop in performance in a limited frequency range that could spoil the overall performance of the system. It was also noticed that the number of iterations should be kept constant across frequency. The reason for this is that different number of iterations means different energy in the solution. When different number of iterations are used for adjacent frequencies, the solution can present jumps that would make it harder to implement the resulting filters. Furthermore, even if the number of iterations is kept constant, this method still provide the advantage of a frequency dependent regularization. As it was seen in Section 2, the regularization provided depends on the filter coefficients that in turn depends on $\mathbf{H}$ and $\mathbf{p}$ that are both frequency dependent.

It can be beneficial to use measured transfer function instead of simulations when increasing the number of iterations. Inaccuracies in the model can be amplified and the noise reduction in the dark zone is accompanied by an increase in the sound pressure level outside of it. The disadvantage is that during the day, weather conditions can drastically change reducing the improvements. In addition, when there are reflections, solutions obtained using measured transfer functions do not generalize well beyond the dark zone while with simulations, since they only compensate for the direct field, the performance do not degrade as much. This agrees with [7] since the interference pattern generated by reflections in the dark zone does not just propagate beyond it without substantial changes. On the other hand, the direct sound field can be extrapolated out of the dark zone and it still constitutes the most prominent component of the sound field.

In case it is not possible to measure the transfer functions and the primary field, it can be a better option to use simulations and *cgls* with a low number of iterations. The results obtained in this case are comparable to results obtained in [7] and in [8], for cases with a similar topological complexity. This means that it is possible to avoid measuring the transfer functions, thus reducing the practical limitations for the use of such a system in day-to-day applications. One can also use more advanced modelling tools reducing the gap between simulations and measurements. Furthermore, large insertion loss obtained in simulations are often not achieved in practice due to uncertainties in the modelling parameters. Solutions obtained with a small number of iterations are in general preferable since they tend to be more robust to limitations of the model or inaccurate medium parameters as described in Section 4.2 and therefore present a lower risk of increasing the sound pressure level outside the dark zone.

The experimental setup described in Section 2.4 was not designed to maximize the loss outside of the dark zone. The main purpose was to compare the different algorithms in terms of insertion loss and radiation patterns. Placing the dark zone further away from the secondary sources would have produced better results at the BA and at larger distances in general. A dark zone close to the secondary array present a lower condition number than one further away [29]. This is due to the fact that there is larger spatial variation in the pressure field due to near field effects and this results in larger singular values for the higher order modes. At the same time, because near field effects are included in the solution, this tends to not generalize well when moving away from the dark zone. Furthermore, the rate of decay of the level of the two sound fields can be quite different leading to an increasing mismatch between primary and secondary field thus performance that degrade with distance.

When the dark zone is placed far from the secondary sources, the far-field is being modelled instead, allowing for a better generalization. The improved performance in this case is also related to the wavefronts of the two fields becoming more plane and similar. The drawback is an increase of the condition number. The main consequence is that instability in the solution can occur with a smaller number of iterations.

The proposed method is slightly more heavy than regularized least square but still in the same order of magnitude. The increase in the number of iterations has a small effect on the total running time. The active set-type method produce a more noticeable increase but allows to include explicit amplitude constraints. The alternative is constrained convex optimization, although, in this case the running time increases by two orders of magnitude compared to $cgls_{k=3}$. However, the running times presented in Table 2 are all considered as acceptable for this type of application since changes in the mean properties of the medium occur on a much larger time scale: from 10 min to approximately 1 h [30].

In this work, we did not include compensations for changing propagation conditions and thus the corresponding variations in the transfer functions. Instead, we run the measurements in small time windows of approximately 10 min, in which we can consider the mean properties of the medium to be quasi-static, to minimize the influence of such changes. The influence of the medium and the robustness of the proposed method has been analyzed in Section 4.2. However, at short distances, it is possible to correct variations in the transfer functions caused by changes in the propagation conditions as described in [31]. At larger distances the effects of the moving inhomogeneous medium are more complex and harder to compensate for.

Finally, all filters have been implemented as arbitrary-phase Finite Impulse Response (FIR) filters. The implemented filters do not show pre-ringing or other time-domain artifacts. The filters obtained from simulations look very similar with small differences in time and amplitude, which increases as the regularization decreases, as expected. It is different when using measurements. First, the filters are longer since also the reflections are taken into account. *fmincon* produces solutions that are different from the other algorithms and present larger oscillations and longer response. The difference between the two *fmincon* solutions using different constraints is minimal. The rest of the algorithms resemble each other closely except for small differences in amplitude and time.

6. Conclusions

In Section 3 it was shown that the CGLS based method proposed here provides performance comparable to regularized least square and constrained optimization in terms of insertion loss and to other studies with similar topological complexity. It was also shown how it is possible to include amplitude constraints on the solution using an active set-type method [26] without drastically increasing the computational effort in contrast with constrained convex optimization (Table 2). The advantages of these two methods and their combination increases with the scale of the problem. In Section 2.2 was shown how it is possible to control the directivity pattern of the secondary array by controlling the number of iterations using application-specific stopping criteria. This is an efficient way to incorporate a feature that would normally require careful and manual selection of a regularization parameter in a regularized least square approach, mode selection in a subspace/projection method or additional constraints in a convex optimization setting.

In Section 4.1 was found that the magnitude of the regularization is not only important to control the amplitude of the solution but also the directivity pattern of the control array. A sensitivity study in Section 4.2 also shown how regularization directly affects the robustness of the solution against model inaccuracies, noise in the measurement or uncertainty in the simulation parameter such as the speed of sound. In general, it was noticed that stronger regularization focus the energy of the solution into the dark zone limiting the risk of a level increase outside of it thus avoiding creating new problem and complaints in new areas. Even though, on paper, stronger regularization is associated with larger residuals, which translates to lower insertion loss, it was found that this is not necessarily the case in practice. Large insertion loss tolerate very small magnitude and phase errors between the primary and secondary fields that are hard to achieve in a dynamic environment with changing weather conditions and possibly reflections from obstacles and from the ground. In general, solutions obtained with stronger regularization are recommended. Moreover, it was found that measured transfer functions can provide better insertion loss than simulations. However, the simulated transfer function do better in complex topologies since they only model the direct field. The measurements include both direct field and reflections which is harder to model correctly thus the tendency of presenting larger errors outside of the dark zone or with changing weather conditions.

Finally, a convergence study in Section 4.3 showed that grids with higher resolution can provide larger insertion loss due to the increased accuracy in the sampling of the sound field during simulations. In practical applications tough, these gains might be cancelled by a mismatch between the model and the dynamic properties of the propagation paths. Furthermore, it showed that increased grid resolutions results in a better conditioning of the problem allowing to achieve more stable solutions even with a relatively large number of iterations.

Future work should focus on the application of this method in the time domain and/or in combination with an adaptive method to compensate for changes in the propagation conditions in real time.

CRediT authorship contribution statement

Pierangelo Libianchi: Conceptualization, Methodology, Software, Validation, Formal analysis, Investigation, Resources, Data curation, Writing - original draft, Writing - review & editing, Visualization. **Jonas Brunskog:** Formal analysis, Writing - review & editing, Supervision. **Finn Agerkvist:** Formal analysis, Writing - review & editing, Supervision, Project administration, Funding acquisition. **Elena Shabalina:** Formal analysis, Writing - review & editing, Supervision, Project administration, Funding acquisition.

Data availability

The authors do not have permission to share data.

Declaration of Competing Interest

The authors declare the following financial interests/personal relationships which may be considered as potential competing interests: Pierangelo Libianchi reports financial support, equipment, drugs, or supplies, and travel were provided by d&b audiotechnik GmbH & Co. KG. Pierangelo Libianchi reports a relationship with d&b audiotechnik GmbH & Co. KG that includes: employment.

Acknowledgements

Funding: d&b audiotechnik GmbH & Co. KG. A particular thanks goes to Kilian Köhler for his help with the measurements and to Jonas Wagner and his team for providing the equipment.

References

[1] World Health Organization. Regional Office for Europe, Environmental noise guidelines for the European Region, World Health Organization, 2018.
[2] Hill AJ, Shabalina E. Sound exposure and noise pollution at outdoor events. J Audio Eng Soc 2020;68(6):145.
[3] Elowsson A, Friberg A. Long-term average spectrum in popular music and its relation to the level of the percussion, in. Audio Eng Soc Convention 2017;142:49–53. http://www.aes.org/e-lib/browse.cfm?elib=18638.
[4] Støfringsdal B. Expected sound levels at concert venues for amplified music. Proc Inst Acoust 2018;40(October):654–60.
[5] Bass H, Sutherland L, Zuckerwar A, Blackstock D, Hester D. Atmospheric absorption of sound: Further developments (vol 97, pg 680, 1995). J Acoust Soc Am 1996;99(2):1259. https://doi.org/10.1121/1.415223.
[6] Toole F, Sound Reproduction, in: Sound Reproduction: The Acoustics and Psychoacoustics of Loudspeakers and Rooms, 1st Edition, Focal Press, Burlington, 2008, pp. 1–490. doi:10.4324/9780080888019-8.
[7] Heuchel FM, Caviedes-Nozal D, Brunskog J, Agerkvist FT, Fernandez-Grande E. Large-scale outdoor sound field control. J Acoust Soc Am 2020;148 (4):2392–402. https://doi.org/10.1121/10.0002252.
[8] Brunskog J, Heuchel F, Caviedes Nozal D, Song MH, Agerkvist FT, Fernandez Grande E, Gallo E, Full-scale outdoor concert adaptive sound field control, Proceedings of the International Congress on Acoustics 2019-Septe (September) (2019) 1170–1177. doi:10.18154/RWTH-CONV-239890.
[9] Heuchel F, Caviedes Nozal D, Agerkvist FT, Sound Field Control for Reduction of Noise from Outdoor Concerts, Proceedings of the Audio Engineering Society (2018) 8. URL: http://www.aes.org/e-lib/inst/browse.cfm?elib=19833.
[10] Caviedes-Nozal D, Heuchel FM, Agerkvist F, Brunskog J, The effect of atmospheric conditions on sound propagation and its impact on the outdoor sound field control, Inter-noise 2019 Madrid - 48th International Congress and Exhibition on Noise Control Engineering (2019).
[11] Nelson P, Elliott S. Active Control of Sound. 1st Edition. London: Academic Press Ltd.; 1992.
[12] F. Heuchel, D. Caviedes Nozal, J. Brunskog, E. Fernandez Grande, F. Agerkvist, An adaptive, data driven sound field control strategy for outdoor concerts, in: Proceedings of 2017 AES International Conference on Sound Reinforcement, Audio Engineering Society, 2017, p. 10.
[13] Hansen PC. Discrete Inverse Problems: Insight and Algorithms. USA: Society for Industrial and Applied Mathematics; 2010.
[14] Calvetti D, Morigi S, Reichel L, Sgallari F. Tikhonov regularization and the l-curve for large discrete ill-posed problems. J Comput Appl Math 2000;123(1–2):423–46. https://doi.org/10.1016/S0377-0427(00)00414-3.
[15] Golub GH, Heath M, Wahba G. Generalized cross-validation as a method for choosing a good ridge parameter. Technometrics 1979;21(2):215–23. https://doi.org/10.1080/00401706.1979.10489751.
[16] Gomes J, Hansen P. A study on regularization parameter choice in near-field acoustical holography. Acoust Soc Am J 2008;123(5). https://doi.org/10.1121/1.2934037. acoustics'08; Conference date: 29–06-2008 Through 04–07-2008 3385–3385.
[17] Boyd S, Vandenberghe L. Convex Optimization. Cambridge: Cambridge University Press; 2004.
[18] T.D. Abhayapala, J. Zhang, P. Samarasinghe, W. Zhang, Limits of noise control over space, in: Proceedings of the 23rd International Congress on Acoustics, no. 1, Aachen, 2019, pp. 47–54.
[19] L. Shi, T. Lee, L. Zhang, J.K. Nielsen, M.G. Christensen, A fast reduced-rank sound zone control algorithm using the conjugate gradient method, in: ICASSP, IEEE International Conference on Acoustics, Speech and Signal Processing - Proceedings, Vol. 2020-May, 2020, pp. 436–440. doi:10.1109/ICASSP40776.2020.9054461.
[20] Hestenes M, Stiefel E. Methods of conjugate gradients for solving linear systems. J Res National Bureau f Standards 1952;49(6):409. https://doi.org/10.6028/jres.049.044.
[21] Calvetti D, Somersalo E. Introduction to Bayesian Scientific Computing, Vol. 2. Tokyo: Springer Japan; 2007.
[22] Calvetti D, Pitolli F, Somersalo E, Vantaggi B. Bayes meets krylov: Statistically inspired preconditioners for CGLS. SIAM Review 2018;60(2):429–61. https://doi.org/10.1137/15M1055061.
[23] P. Libianchi, F. Agerkvist, E. Shabalina, A conjugate gradient least square based method for sound field control, in: Proceedings of InterNoise21, Proceedings of Inter-noise 2021–2021 International Congress and Exposition of Noise Control Engineering, Institute of Noise Control Engineering, 2021, pp. 1029–1040. doi:10.3397/IN-2021-1736.
[24] Hamdan EC, Fazi FM. Three-channel crosstalk cancellation mode efficiency for sources in the far-field. In: Tew T, Williams D, editors. 2019 AES International Conference on Immersive and Interactive Audio, York, ENGLAND. p. 27–9.
[25] Borgiotti GV. The power radiated by a vibrating body in an acoustic fluid and its determination from boundary measurements. J Acoust Soc Am. 1990;88 (4):1884–93. https://doi.org/10.1121/1.400211.
[26] Morigi S, Reichel L, Sgallari F, Zama F. An iterative method for linear discrete ill-posed problems with box constraints. J Comput Appl Math 2007;198 (2):505–20. https://doi.org/10.1016/j.cam.2005.06.053.
[27] Feistel S. Modeling the radiation of modern sound reinforcement systems in high resolution. RWTH Aachen; 2014. Ph.D. thesis.
[28] V.E. Ostashev, D.K. Wilson, Acoustics in moving inhomogeneous media, second edition, Acoustics in Moving Inhomogeneous Media, Second Edition, CRC Press, 2015, cited By:16. URL: www.scopus.com.
[29] Nelson P, Yoon S. Estimation of Acoustic Source Strength By Inverse Methods: Part I, Conditioning of the Inverse Problem. J Sound Vib 2000;233(4):643–68. https://doi.org/10.1006/jsvi.1999.2837.
[30] Kelly M, Barlas E, Sogachev A. Statistical prediction of far-field wind-turbine noise, with probabilistic characterization of atmospheric stability. J Renewable Sustainable Energy 2018;10(1). https://doi.org/10.1063/1.5012899.
[31] F.M. Heuchel, D. Caviedes-Nozal, E. Fernandez-Grande, J. Brunskog, F.T. Agerkvist, Adapting transfer functions to changes in atmospheric conditions for outdoor sound field control, Proceedings of the International Congress on Acoustics 2019-Septe (1) (2019) 1178–1183. doi:10.18154/RWTH-CONV-239982.

Paper C

Notes on the characterization of the wind profile in the atmospheric boundary layer

Pierangelo Libianchi[1,2]

[1]**Department of Electrical and Photonics Engineering, Technical University of Denmark, Ørsted Plads, DK-2400 Kgs. Lyngby, Denmark**
[2]**d&b audiotechnik GmbH & Co. KG, Eugen-Adolff-Straße 134, 71522 Backnang, Germany**

ABSTRACT

Simulation of outdoor sound propagation provide prediction of noise emissions from multiple types of sources and potentially for applications of active noise control in open air. Regardless of the model used, accurate estimates of the medium parameters are fundamental to achieve reliable predictions. The expressions that describe parameters such as wind and temperature are different depending on the regime of the atmospheric boundary layer (ABL). This paper is a review of the literature describing these regimes and the Monin-Obukhov Similarity Theory (MOST), which can be used to derive the wind and temperature profile in the atmospheric surface layer (ASL). However, this method is an approximation and, as such, has limits that are important to know since they affect the accuracy of the simulations. This manuscript also presents limitations such as the dependency of the wind direction on height and stability conditions above the ASL that are not included in MOST as described in fundamental micrometeorology works. Furthermore, it provides a short description of transitory phenomena that can further disrupt the prediction of the wind and temperature profiles and recommendations on how best to apply such models for sound field control applications.

Keywords: ABL, wind profile

1 INTRODUCTION

Simulations of outdoor sound propagation are used for multiple applications from prediction of noise emissions from sources such as explosions [1, 2, 3, 4, 5], traffic [6, 7, 8, 9], wind farms [10, 11, 12] or for the estimation of propagation paths for sound field control [13, 14]. Our main interest is the latter application but the concepts described in this work can be applied to any of the other as well.

The development of suitable propagation models and accurate description of the medium parameters are still challenges that need to be overcome to improve the range and generalization of the sound field strategies actually in use. This application, and in general any application where multiple waves interact, requires a precise prediction of the phase of the sound field. The model parameters need to accurately describe the medium to have a reliable prediction of the sound field and its phase. The logarithmic profile is often used to describe the wind profile in acoustics [15, 16, 17, 18, 19, 20]. We see in [21] why this is not accurate when the atmospheric boundary layer (ABL) is not neutral and Monin-Obukhov similarity theory (MOST) is preferred. The aim of this paper is to provide an understanding of why this is the case by looking into the dynamics of the atmospheric boundary layer (ABL) and its regimes. We further describe additional factors that affect the accuracy of the wind and temperature profile and that are not modelled by the logarithmic profile or traditional MOST.

This paper is a compact review of the relevant micrometeorology literature describing the different regimes of the ABL and their characteristics. Knowledge of these dynamics provides the reasoning behind MOST and allows to formulate stability corrections applied to the logarithmic profile to extend its range of applicability to different stability conditions. The paper shows the importance of including such corrections and the variety of profiles that one can obtain depending on the stability conditions.

In micrometeorology literature is well known that MOST is an approximation and is only valid in the atmospheric surface layer (ASL). The stability conditions at the top of the ABL can also affect the profiles close to the ground. This can cause the profiles to deviate from the predictions provided by MOST. The paper describes this effect and provides resources describing some more advanced models that can extend the profiles beyond the ASL including the stability conditions at the top of the ABL.

The following sections introduce additional considerations that can limit the accuracy of the wind profiles but that are harder to account for: the height dependency of the wind direction on height, effects of an uneven terrain and other transitory phenomena.

The modelling techniques reviewed in this paper improve the accuracy of the simulations for outdoor sound propagation. However, it is important to keep in mind their limitations since they can help to identify possible source of errors and mismatch with actual measurements.

2 ABL REGIMES

Even thought the dynamics of the ABL are very complex, one can have basic understanding by looking at the three main state of the ABL: unstable, neutral and stable. These three states are closely related to the presence of turbulence. This is also a complex topic that is described fully by the Navier-Stokes equations [22]. Here many terms are involved in the generation, destruction and energy transfer of turbulence. For the scope of this paper we are mostly concerned with only one of them: buoyancy.

During a clear day, the sun radiation heats up the ground producing a negative potential temperature gradient, i.e. the potential temperature decreases with height. In this circumstances, the air parcels closer to the ground are warmer than the one above. They experience a buoyant force that accelerates them upward creating columns of raising warm air and descending cold air. In this case, buoyancy act as a source term. In this conditions, the turbulence are strong and their size increases with time as the energy builds up until an equilibrium is reached. As the size of the turbulence increases, so does the height of the ABL ($\approx$ 100-200 meters in winter and $\approx$ 1km or more during summer). In this conditions, the ABL is said to be unstable. The turbulence enhance the diffusion process and make the distribution of scalars such as temperature fairly homogeneous over the entire ABL. The wind is of the utmost importance for sound propagation. Temperature can be neglected and might play only a small role upwind, i.e. when sound propagated against the direction of the wind.

At nighttime, the situation is reversed. The temperature gradient is positive and the air parcels close to the ground are colder than the one above. In this case they experience a force that tends to make them oscillate around an equilibrium position and the buoyancy become a destruction term, effectively suppressing turbulence. The height of the ABL also reduces accordingly to 100-200 meters. This is the stable ABL. In this regime, the height of the ABL present little seasonal variation [23, 24]. It is characterized by a stable stratification and laminar flow close to the ground. The turbulence that survive are smaller than in the previous case and confined in a region above the stable stratification which is at time called residual layer [25]. Due to the stable stratification and the positive potential temperature gradient, this regime produce downward refraction. These conditions create an acoustic duct in the lower atmosphere [26] that is favourable to sound propagation making this the worst scenario in terms of noise emissions.

Between these two conditions is the neutral scenario. This can occur during transition between stable and unstable, for instance at sunrise and sunset, or when the temperature gradient is not very strong, like during a cloudy day. A typical value of the temperature gradient for neutral conditions in air that is unsaturated by water vapor is –0.0098°C/m, commonly know as adiabatic lapse rate.

Although, at times it is not straightforward to identify in which regime the ABL is. It can happen that warmer air blows on top of a cooler surface, for instance moving from land to water, creating a stable stratification. Entrainment at the top of the ABL of warmer air aloft can also make the ABL stable. These cases are described in [22] and show in Figure 1. A precise indicator of the state of the ABL is the surface temperature flux $Q_0 = \overline{w\theta}$, where w is the vertical component of the turbulent wind field, θ is the fluctuating component of the temperature field and the overbar indicates ensemble averaging (that can be replaced by a spatial average under homogeneity conditions or a time average under stationarity conditions [22]). This quantity is positive when air warmer than its surrounding is moved upward or when cooler air is moved downward. This occurs when the ABL is unstable. This quantity is negative when the ABL is stable and close to 0 when neutral. A derived measure of stability often used in micrometeorology is the Obukhov length $L = -u_*^3\theta_0/kgQ_0$, where u_* is the friction velocity, θ_0 is the potential temperature at the surface, $k = 0.4$ is the Von-Kármán constant and g is the gravitational acceleration. A physical interpretation of $|L|$ during the day, when $Q_0 > 0$, is that it corresponds to the height where the contribution from buoyancy and wind shear to the production of turbulent kinetic energy are equal.

3 STABILITY CORRECTIONS

Since the dynamics of each regime are different, going from a laminar flow to a turbulent one, it is apparent that the logarithmic profile cannot be representative in each of these regimes. It is necessary to consider such differences when formulating a model for the profiles of wind, temperature or any other scalar. [21] confirms that

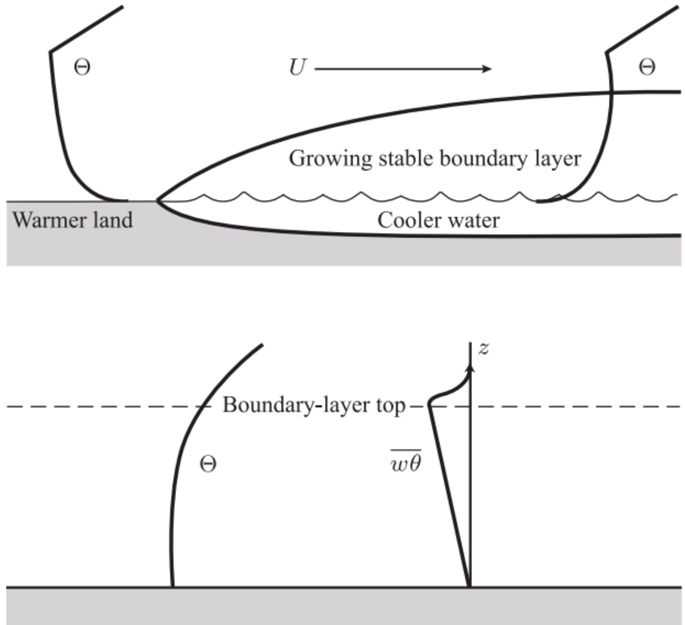

Figure 1. Two additional stability scenarios described n [22]. Production of a stable stratification by warmer air moving over a cooler surface (upper) and entrainment of warmer air aloft (Figure 9.7 in [22]).

the widely used logarithmic profile does not adequately model the wind outside of the neutral regime. A better alternative is MOST, a common way to model this quantities close to the surface, in the ASL. The foundation of this approach is based on dimensional analysis and the Buckingham Pi theorem [22]. The MOST assumes that the turbulence structure above a flat, horizontally homogeneous surface depends on five parameters: the length scale of the turbulence which on the surface is taken as the Obukhov length L, a velocity scale taken as the friction velocity u_*, mean temperature flux Q_0, the mean surface flux of conserved scalar constituent C_0 and the buoyancy parameter g/θ_0. The Buckingham Pi theorem says that there are two independent dimensionless quantities that are functionally related. MOST takes one as the dependent variable normalized by z, u_*, $T_* = -Q_0/u_*$, $c_* = -C_0/u_*$ and the other as z/L. MOST implies that the gradient of mean wind speed, mean temperature and mean water vapor mixing ratio behave as [22]:

$$\frac{kz}{u_*}\frac{\partial U}{\partial z} = \phi_m\left(\frac{z}{L}\right), \tag{1}$$

$$-\frac{kzu_*}{Q_0}\frac{\partial \Theta}{\partial z} = \frac{kz}{T_*}\frac{\partial \Theta}{\partial z} = \phi_h\left(\frac{z}{L}\right), \tag{2}$$

where the functions ϕ_i are universal, the same in all locally homogeneous, quasi-steady surface layer.

In [22] are cited versions of this functions for a stable stratification from [27], which after gives the following profiles:

$$\begin{aligned} U(z) &= \frac{u_*}{k}\left[\ln\frac{z}{z_0} + 4.8\frac{z}{L}\right], \\ \Theta(z) &= \Theta(z_r) + \frac{T_*}{k}\left[\ln\frac{z}{z_0} + 7.8\frac{z}{L}\right] \end{aligned} \tag{3}$$

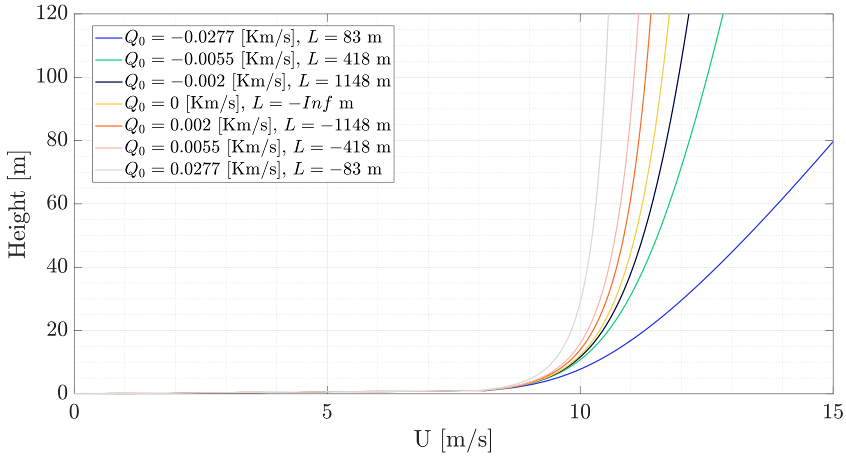

Figure 2. Different wind profiles obtained with different surface heat flux/Obukhov length ranging from very stable to very unstable (according to the definitions in [29]). Parameters used to compute the profiles from Eq. (3) and (4): $u_* = 0.32$ m/s, $z_0 = 2.8e-5$ m,

For an unstable stratification, it cites the profiles from [28] which are reported here:

$$\begin{aligned} U(z) &= \frac{u_*}{k}\left[\ln\frac{z}{z_0} - f_m(z)\right] \\ \Theta(z) &= \Theta(z_r) + \frac{P_t T_*}{k}\left[\ln\frac{z}{z_0} - f_h(z)\right], \end{aligned} \tag{4}$$

where

$$f_i(z) = 3\ln\left(\frac{1+\sqrt{1+\gamma_i|z/L|^{2/3}}}{1+\sqrt{1+\gamma_i\,|z_0/L|^{2/3}}}\right), \tag{5}$$

and $P_t = 0.95$, $\gamma_i = 3.6$ for $i = m$ and $\gamma_i = 7.9$ for $i = h$.

From these models we can see that when we are in a neutral regime, i.e. $L^{-1} = 0$, all the model collapse to a logarithmic profile.

3.1 Beyond the ASL

Since MOST is based on surface parameters, it is not very accurate beyond the ASL or when the stability conditions at the top of the ABL affect the profile close to the ground. For instance, depending on the stability conditions at the top of the ABL ,[30] distinguish between a truly neutral and a conventionally neutral boundary layer (CNBL). They both have $Q_0 = 0$ but they differ at the top where the Brunt–Väisälä frequency N , which is another measure of stability, is 0 in the first case and positive in the second. The truly neutral regime is short-lived and tends to be local. In this case traditional MOST gives realistic results. In a long-lived conventionally neutral boundary layer, there is an inversion of potential temperature at the top of the ABL which causes downward entrainment of higher potential temperature leading to stable stratification within the ABL. Traditional MOST tends to underestimate the speed of the wind in this conditions. Different model have been proposed to deal with this scenario [31, 29, 32, 33]. A common way to extend the profile beyond the surface layer is by defining additional length scales that includes stability measure characteristic of different regions of the ABL. While the Obukhov length L is still used for the profile close to the surface, [33, 29] also define two additional length scales for the middle and upper boundary layer. A generalized length scale is than obtained using interpolation between the different length scales and then to calculate the profiles.

A similar distinction is made in [33] also for the stable layer where they distinguish between a short-lived nocturnal stable ($N = 0$) and a long-lived thoroughly stable ($N > 0$). Also in this case tradition MOST works to the short-lived case and they propose a new model for the thoroughly stable case.

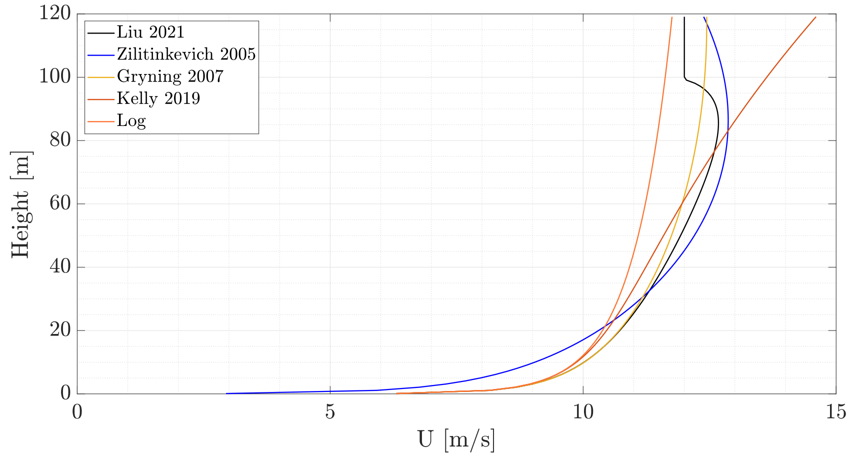

Figure 3. Wind profiles in a CNBL from [31, 33, 29, 32] and the logarithmic profile. The parameters used for the models were: $u_* = 0.32$ m/s, $Zi = N/|f| = 88.7$, $Ro = u_*/(|f|z_0) = 45000$, $G = 12$ m/s, $z_0 = 2.8e-5$ m, $h' = 100$ m and $\theta_0 = 293$ K.

It should be noted that these profiles only describe the average properties of the medium and not the instantaneous properties. Furthermore, these profiles tends to change over space due to changes in the topological features, horizontal temperature gradients, the direction of the wind changes with height (see Section 4) and can be disrupted by transitory phenomena (see 5).

4 CROSS-ISOBARIC ANGLE

The wind speed is not the only wind parameter that changes with height. The direction of the wind also tends to change with height and it does so differently depending on different factors and regimes of the ABL. This direction is usually referred to in form of the cross-isobaric angle which is the angle between the direction of the wind and of the isobars. [22] gives an estimation of the range of variation of wind direction. The starting point is the mean momentum equation in steady and horizontally homogeneous conditions. Near the non-turbulent flow limit, in tensor notations, it reduces to:

$$\frac{1}{\rho_0}\frac{\partial P}{\partial x_i} + 2\varepsilon_{ijk}\Omega_j U_k = 0, \tag{6}$$

where ρ_0 is the static and vertical dependent medium density, P is the mean pressure, ε_{ijk} is the alternating tensor, Ω is the rotation rate of earth and U_k is the k-th component of the mean wind field. It is a balance between pressure gradient and Coriolis force. The Coriolis term is perpendicular to $\mathbf{U}$. By multiplying the previous expression by $\mathbf{U}$ we obtain:

$$\frac{U_i}{\rho_0}\frac{\partial P}{\partial x_i} = 0 \tag{7}$$

which means that the wind is parallel to the isobars. Entering the ABL, the stress divergence term cannot be neglected and the mean momentum equation in steady horizontally homogeneous conditions is:

$$\frac{\partial \overline{u_i u_j}}{\partial x_j} + \frac{1}{\rho_0}\frac{\partial P}{\partial x_i} + 2\varepsilon_{ijk}\Omega_j U_k = 0, \quad i = 1, 2 \tag{8}$$

This expression multiplied by U_i leads to:

$$\frac{\partial}{\partial x_j} U_i \overline{u_i u_j} - \overline{u_i u_j}\frac{\partial U_i}{\partial x_j} + \frac{U_i}{\rho_0}\frac{\partial P}{\partial x_i} = 0 \tag{9}$$

This can be interpreted as a mean kinetic energy equation. The first term is a transport term that only moves kinetic energy but neither a source nor a sink. The Coriolis term is 0 since is perpendicular to $\mathbf{U}$. The second term is a loss since it models the transfer of energy from the mean to the turbulent flow. The last term must then be a source which means that the mean wind flow cannot be parallel to the isobars. It follows that the direction of the wind has to change along the height of the ABL to match these limit values. In the stable ABL, since the buoyancy term is a loss, the turbulence must extract energy from the mean flow and the cross-isobaric angle is typically 45°; the adjustment to the geostrophic flow occurs over the depth of the ABL. In an unstable ABL, the buoyancy term is a source so the cross-isobaric angle is smaller. Due to diffusivity from the turbulence, the adjustment occurs in the interfacial layer, where the ABL transition into the free atmosphere. This means that in stable conditions the wind direction changes more over height than it does in an unstable ABL.

In a truly neutral boundary layer, an expression for the geostrophic wind G and the cross-isobaric angle can be determined using classic geostrophic law [30]:

$$
\begin{aligned}
A &= \ln\left(C_g \,\mathrm{Ro}\right) - \frac{k}{C_g}\cos\alpha_0, \\
B &= \pm\frac{k}{C_g}\sin\alpha_0,
\end{aligned}
\tag{10}
$$

where $C_g = u_*/G$, G being the geostrophic wind, α is the cross-isobaric angle, $Ro = G/|f|z_0$ is the Rossby number and A and B are universal constants. The minus sign is used for the Northern hemisphere and the plus for the Southern hemisphere. In a conventionally neutral ABL, where $N > 0$, A and B are not constants anymore and depend on the stability parameter $\mu_N = N/|f|$ [31]:

$$
\begin{aligned}
A &= -am + \ln\left(a_0 + m\right) - \ln\left(\frac{|f|h}{u_*}\right) \\
B &= \frac{|f|h}{u_*}\left(b_0 + bm^2\right)
\end{aligned}
\tag{11}
$$

$a = 1.4$ and $b = 10$ are constant from similarity theory, $a_0 = 1.65$ and $b_0 = -2$ are empirical corrections and m is the composite stratification parameter:

$$
m = \left[1 + \left(C_m \mu_N\right)^2\right]^{1/2} \frac{|f|h}{u_*} \tag{12}
$$

where $C_m = 0.1$ is an empirical constant. The height of the ABL h in a CNBL can be obtained from:

$$
h = \left(1 + \mu_N C_R^2/C_N^2\right)^{-1/2} C_R \frac{u_\psi}{|f|} \tag{13}
$$

Where $C_N = 1.6$. Figure

The results obtained in [35] agree with the theory. In addition, the study found dependencies to additional variables:

- Latitude: the turning increases with latitude with the exception of the polar regions. The reason could be related to stability conditions since the measurements in such regions were performed in coastal areas where the ABL tends to be less stable.
- Seasonal and diurnal cycles: the largest angles are found during winter and the smallest during the summer, which is related to the stratification of the ABL. Also, in general the angle tends to be larger at night than during the day also for stratification reasons.
- ABL height: also here it follows from stability. Lower ABL height are associated with stable regimes where the turning angle is larger.

5 OTHER PHENOMENA

The stable boundary layer tends to occur at nighttime and presents a positive temperature gradient leading to downward refraction in every direction without including the wind. This regime is of particular concern since it is favourable to sound propagation at large distances and for the sensitive time of the day at which it tends to occur.

The stable boundary layer is often characterized by anomalous turbulent events. Intermittent heat, moisture and momentum fluxes are often associated with these anomalies [36].

Some of the anomalies described in [36] and their effect on the wind profile are the following:

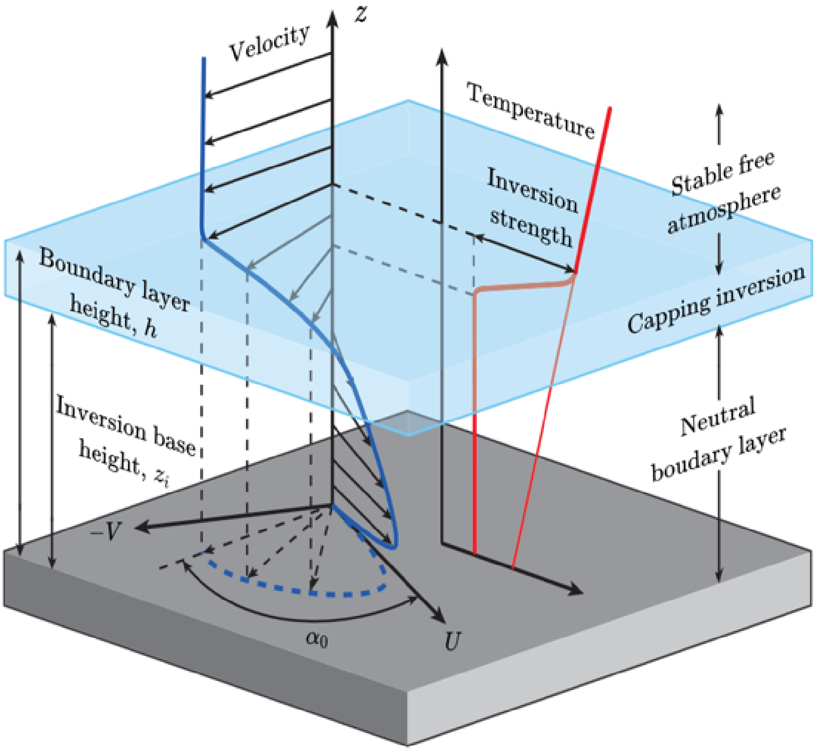

Figure 4. An illustration of the wind profile and its change in direction in a neutral boundary layer (from [34]).

- **Kelvin-Helmholtz shear instability**: A stratified shear flow excites certain gravity wave modes which grow until they become unstable and finally break. By this breaking process, the energy dissipated by the waves generates new turbulence. This is a transitory event and MOST predictions are accurate before and after the event. During the event, MOST overestimates the wind speed due to the sudden instability brought by the newly generated turbulence.

- **Density current**: It consists of an air flow generated by a difference in density that increases the wind speed and alter the temperature profile. It can occur in different ways in coastal regions, inland sites and hilly terrains and at different scales. The smaller scale density currents, which occur close to the ground ($\approx$ 10m), can be generated by density differences of only a few percent. The are characterized by a head and a tail. The head produces a speed increase and a drop in temperature that cause the surface heat flux to depart from MOST. The tail produces intermittent shear instability which lead to non-stationary turbulence. Thus, MOST cannot be applied during the event and becomes accurate again once the disturbance is over.

- **Low level jet (LLJ)**: It is produced by multiple mechanisms. One of them is the stable stratification close to the top of the ABL in a CNBL. Larger wind speeds increase shear production overwhelming buoyant destruction and leading to continuous and stationary turbulence. The increase of turbulence, reduces the overall speed of the wind across the ABL thus MOST in this case overestimates the wind speed.

6 DISCUSSION

An accurate description of the wind and temperature profiles across the ABL is necessary to obtain reliable acoustic predictions outdoor. When simulating sound propagation outdoor, the first step is to define in which regime of the ABL the simulation is performed. The regimes are vastly different between them both in terms of their dynamics, potential approximations and shape of the wind and temperature profiles.

In the unstable regime, which typically occur on clear days, the wind speed tends to be lower and is characterized by strong turbulence that needs to be included in the simulation. On the other hand, the wind direction does not change across the ABL so 2D simulations can be used effectively. Opposite to this scenario is the stable regime. In this case, the mean wind speeds are higher and turbulence play a little role in sound propagation close to the ground. Modelling turbulence is expensive and in this case they can be ignored with little effect on the accuracy of the simulation. However, in this regime the wind direction changes across the entire ABL with variations of up to 45°. In this case, 3D simulations should be used to account for this effect and further studies should focus on an accurate description of the dependency of the wind direction on height.

The stable regime is the most critical when it comes to sound propagation and the prediction of noise emissions. This regime is characterized by a positive temperature gradient which generates downward refraction resulting in an acoustic duct close to the ground that enhances the range of sound propagation. A stable boundary layer tend to occur on clear nights or when warmer air moves over a cooler surface. This is the case when there is a body of water downwind within the simulation domain. In this case it is critical to have range-dependent wind and temperature profiles. This scenario places a limit on which propagation models can be used. For instance, Fast Field Program is not suitable in this scenario since it does not allow to include profiles that change with the distance.

In these two regimes, MOST should be used to model the wind and temperature profiles. The logarithmic profile without any stability corrections can be used in the neutral regime. This regime tend to occur at transitions, sunset and sunrise, and in cloudy conditions.

These considerations improve the reliability of the simulations since the medium is modelled more realistically. However, the ABL often present stability conditions at its top that affect the profiles even close to the ground. These stability conditions limit the validity of MOST and are harder to model. This is the case in the CNBL, where an LLJ caused by a stable stratification aloft produces a speed increase that is not modelled under MOST. These effect introduce a modelling error that reduce the accuracy of the simulations close to the ground.

Finally, the accuracy of the profiles under a stable regime can also be limited by transitory events that can be hardly predicted and modelled. However, it is important to know of their existence since they can explain possible discrepancies between simulations and actual measurements.

7 CONCLUSIONS

The use of MOST in simulations for outdoor sound propagation increases the accuracy of the predictions. It is crucial to define in which regime of the ABL the simulation is taking place and use accurate surface parameters. The correct parameters can be easily obtained from wind and temperature measurements close to the ground when the correct expression for the profile is used.

Modelling the wind profile in a stable boundary layer is further complicated by the large change of direction of the wind across the ABL.

It is important to notice that, even though MOST provides accurate descriptions of the mean profiles in the ASL, it does not extend to the entire ABL and it does not model entrainment processes at the top of the ABL that can affect the wind profile even close to the ground. Furthermore, transitory phenomena can temporarily disrupt the shape of the profile across the entire ABL. These limitations are hard to detect and model but they can provide a partial explanation for deviations of the simulations from real world measurements.

REFERENCES

[1] D. G. Albert and L. R. Hole, "Blast noise propagation above a snow cover," *Journal of the Acoustical Society of America*, vol. 109, no. 6, p. 2675 – 2681, 2001. Cited by: 10.

[2] S. Cheinet, M. Cosnefroy, F. Königstein, W. Rickert, M. Christoph, S. L. Collier, A. Dagallier, L. Ehrhardt, V. E. Ostashev, A. Stefanovic, T. Wessling, and D. K. Wilson, "An experimental study of the atmospheric-driven variability of impulse sounds," *The Journal of the Acoustical Society of America*, vol. 144, no. 2, pp. 822–840, 2018.

[3] D. Luquet, R. Marchiano, and F. Coulouvrat, "Long range numerical simulation of acoustical shock waves in a 3d moving heterogeneous and absorbing medium," *Journal of Computational Physics*, vol. 379, pp. 237–261, FEB 15 2019.

[4] W. Cheng, P. Teng, J. Lu, P. Ji, and Y. Dai, "Energy estimation of explosion sound source based on atmospheric sound propagation theory," *Acta Physica Sinica*, vol. 70, DEC 20 2021.

[5] C. Mahapatra and A. R. Mohanty, "Optimization of number of microphones and microphone spacing using time delay based multilateration approach for explosive sound source localization," *Applied Acoustics*, vol. 198, SEP 2022.

[6] K. Abdur-Rouf and K. Shaaban, "Development of prediction models of transportation noise for roundabouts and signalized intersections," *Transportation Research Part D-Transport and Environment*, vol. 103, FEB 2022.

[7] L. Mandjoupa, D. Davis, S. Gaye, S. Mohamed, E. Etochukwu, W. Mahmoud, L. Wan, and M. Denis, "3d noise modeling of an urban environment: Simulated and measured noise characteristics of the university of the district of columbia campus," *The Journal of the Acoustical Society of America*, vol. 151, no. 4, pp. A37–A37, 2022.

[8] J. Tang, B. Lin, J. Hwang, L. Chen, B. Wu, H. Jian, Y. Lee, and T. Chan, "Dynamic modeling for noise mapping in urban areas," *Environmental Impact Assessment Review*, vol. 97, NOV 2022.

[9] X. Zhang, D. Thompson, J. Ryue, H. Jeong, and G. Squicciarini, "The effect of rail shields on railway rolling noise," *International Journal of Rail Transportation*.

[10] E. Barlas, W. J. Zhu, W. Z. Shen, K. O. Dag, and P. Moriarty, "Consistent modelling of wind turbine noise propagation from source to receiver," *The Journal of the Acoustical Society of America*, vol. 142, no. 5, pp. 3297–3310, 2017.

[11] S. M. McBride, "A Comprehensive Hamiltonian Atmospheric Sound Propagation Model for Prediction of Wind Turbine Noise," 2017.

[12] M. Kelly, E. Barlas, and A. Sogachev, "Statistical prediction of far-field wind-turbine noise, with probabilistic characterization of atmospheric stability," *Journal of Renewable and Sustainable Energy*, vol. 10, no. 1, 2018.

[13] F. M. Heuchel, D. Caviedes Nozal, J. Brunskog, F. T. Agerkvist, and E. Fernandez Grande, "Large-scale outdoor sound field control," *The Journal of the Acoustical Society of America*, vol. 148, no. 4, pp. 2392–2402, 2020.

[14] P. Libianchi, F. T. Agerkvist, and E. Shabalina, "A review of techniques and challenges in outdoor sound field control," in *Proceedings of Inter·Noise 2022*, 2022. 51¡sup¿st¡/sup¿ International Congress and Exposition on Noise Control Engineering, Internoise 2022 ; Conference date: 21-08-2022 Through 24-08-2022.

[15] K. E. Gilbert and M. J. White, "Application Of The Parabolic Equation To Sound Propagation In A Refracting Atmosphere," *Journal of the Acoustical Society of America*, vol. 85, no. 2, pp. 630–637, 1989.

[16] S. Taherzadeh, K. M. Li, and K. Attenborough, "Some practical considerations for predicting outdoor sound propagation in the presence of wind and temperature gradients," *Applied Acoustics*, vol. 54, no. 1, pp. 27–44, 1998.

[17] G. P. Van Den Berg, "Effects of the wind profile at night on wind turbine sound," *Journal of Sound and Vibration*, vol. 277, no. 4-5, pp. 955–970, 2004.

[18] M. Hornikx, R. Waxler, and J. Forssén, "The extended Fourier pseudospectral time-domain method for atmospheric sound propagation," *The Journal of the Acoustical Society of America*, vol. 128, no. 4, pp. 1632–1646, 2010.

[19] A. González, P. Kovar, M. Deambrosi, M. Hernández, and M. Urban, "Environmental noise due to large wind turbines: what we have learnt," 02 2021.

[20] H. Bian, R. Fattah, S. Zhong, and X. Zhang, "An efficient rectilinear Gaussian beam tracing method for sound propagation modelling in a non-turbulent medium," *The Journal of the Acoustical Society of America*, vol. 148, no. 6, pp. 4037–4048, 2020.

[21] D. K. Wilson, M. S. Lewis, J. W. Weatherly, and E. L. Andreas, "Dependence of predictive skill for outdoor narrowband and broadband sound levels on the atmospheric representation," *Noise Control Engineering Journal*, vol. 56, no. 6, pp. 465–477, 2008.

[22] J. C. Wyngaard, *Turbulence in the Atmosphere*. Cambridge: Cambridge University Press, 2010.

[23] A. K. Georgoulias, D. K. Papanastasiou, D. Melas, V. Amiridis, and G. Alexandri, "Statistical analysis of boundary layer heights in a suburban environment," *Meteorology and Atmospheric Physics*, vol. 104, no. 1, pp. 103–111, 2009.

[24] C. Rey-Sanchez, S. Wharton, J. Vilà-Guerau de Arellano, K. T. Paw U, K. S. Hemes, J. D. Fuentes, J. Osuna, D. Szutu, J. V. Ribeiro, J. Verfaillie, and D. Baldocchi, "Evaluation of atmospheric boundary layer height from wind profiling radar and slab models and its responses to seasonality of land cover, subsidence, and advection," *Journal of Geophysical Research: Atmospheres*, vol. 126, no. 7, 2021.

[25] S. Liu and X. Z. Liang, "Observed diurnal cycle climatology of planetary boundary layer height," *Journal of Climate*, vol. 23, no. 21, pp. 5790–5809, 2010.

[26] P. Blom and R. Waxler, "Impulse propagation in the nocturnal boundary layer: Analysis of the geometric component," *The Journal of the Acoustical Society of America*, vol. 131, no. 5, pp. 3680–3690, 2012.

[27] U. L. F. Högström, *Non-Dimensional Wind and Temperature Profiles in the Atmospheric Surface Layer: A Re-Evaluation*, pp. 55–78. Dordrecht: Springer Netherlands, 1988.

[28] D. K. Wilson, "An alternative function for the wind and temperature gradients in unstable surface layers," *Boundary-Layer Meteorology*, vol. 99, no. 1, p. 151 – 158, 2001.

[29] S. E. Gryning, E. Batchvarova, B. Brümmer, H. Jørgensen, and S. Larsen, "On the extension of the wind profile over homogeneous terrain beyond the surface boundary layer," *Boundary-Layer Meteorology*, vol. 124, no. 2, pp. 251–268, 2007.

[30] S. S. Zilitinkevich and I. N. Esau, "On integral measures of the neutral barotropic planetary boundary layer," *Boundary-Layer Meteorology*, vol. 104, no. 3, pp. 371–379, 2002.

[31] L. Liu, S. N. Gadde, and R. J. A. M. Stevens, "Geostrophic drag law for conventionally neutral atmospheric boundary layers revisited," *Quarterly Journal of the Royal Meteorological Society*, vol. 147, no. 735, pp. 847–857, 2021.

[32] M. Kelly, R. A. Cersosimo, and J. Berg, "A universal wind profile for the inversion-capped neutral atmospheric boundary layer," *Quarterly Journal of the Royal Meteorological Society*, vol. 145, no. 720, pp. 982–992, 2019.

[33] S. S. Zilitinkevich and I. N. Esau, "Resistance and heat-transfer laws for stable and neutral planetary boundary layers: Old theory advanced and re-evaluated," *Quarterly Journal of the Royal Meteorological Society*, vol. 131, no. 609, pp. 1863–1892, 2005.

[34] L. Liu and R. J. A. M. Stevens, "Vertical structure of conventionally neutral atmospheric boundary layers," *Proceedings of the National Academy of Sciences*, vol. 119, p. e2119369119, May 2022.

[35] J. Lindvall and G. Svensson, "Wind turning in the atmospheric boundary layer over land," *Quarterly Journal of the Royal Meteorological Society*, vol. 145, no. 724, pp. 3074–3088, 2019.

[36] Y. Cheng, M. B. Parlange, and W. Brutsaert, "Pathology of Monin-Obukhov similarity in the stable boundary layer," *Journal of Geophysical Research*, vol. 110, no. 6, pp. 1–10, 2005.

Paper D

Sensitivity of the predicted acoustic pressure field to the wind and temperature profiles in a conventionally neutral boundary layer

Pierangelo Libianchi,[1] Elena Shabalina,[2] Mark Kelly,[3] Jonas Brunskog,[1] and Finn Agerkvist[1]

[1)] *Acoustic Technology Group, Department of Electrical and Photonics Engineering, Technical University of Denmark, Building 352, Ørsted Plads, DK-2800 Kongens Lyngby, Denmark*[a]

[2] *German Institute of Textile and Fiber Research Denkendorf, Koerschtalstrasse 26, 73770 Denkendorf, Germany*

[3] *Department of Wind Energy, Risø Lab/Campus, Technical University of Denmark, Frederiksborgvej 399, DK-4000 Roskilde, Denmark*

Simulations are widely used to predict noise emissions from traffic, railroad, aircraft, and wind farms and for sound field control. The latter employs multiple sources interacting and it requires accurate phase information. Acoustic models require precise characterization of the medium properties. The logarithmic profile is one of the most commonly used forms to model the wind speed. However, this profile is accurate only in neutral conditions, i.e. when there is not heat flux at the surface. The conventionally neutral boundary layer (CNBL) is the most frequently occurring neutral regime. In this case, the logarithmic profile underestimates the wind speed. This paper analyses the effect that this modelling error has on the sound field close to the ground, for near-ground sources. The first section introduces an approximation of the wind and temperature profiles in such a regime. Afterwards, the sound fields corresponding to the logarithmic profile, a representative CNBL profile, and three more test cases are simulated using the Crank-Nicholson parabolic equation; these are compared employing different metrics. The difference in wind speed introduces a phase error that increases with distance. Moreover, wind speed underestimations also lead to underpredictions of the energy refracted downward.

 [http://dx.doi.org(DOI number)]

[XYZ] Pages: 1–10

I. INTRODUCTION

Reliable simulations are important to many practical outdoor sound propagation calculations and applications, since analytical solutions for propagation in a moving inhomogeneous medium are only available for very simple topologies and formulations of the sound speed profile (Raspet *et al.*, 1992). More realistic environments require simulations to predict or localize noise emissions from explosions (Albert and Hole, 2001; Luquet *et al.*, 2019), traffic (Abdur-Rouf and Shaaban, 2022; Tang *et al.*, 2022), wind-farms (Barlas *et al.*, 2017; Kelly *et al.*, 2018) or for other applications such as sound field control (Caviedes Nozal *et al.*, 2019; Heuchel *et al.*, 2020; Libianchi *et al.*, 2022). We are mainly interested in the latter applied to open air live events at low frequencies where the noise sources are typically subwoofers placed on/near the ground. In this scenario, it is necessary to accurately model the sound field with particular focus on the phase accuracy, since the sound fields generated by multiple coherent sources will be interacting. Many different phenomena can affect the accuracy of simulations, such as the ground effect (Attenborough, 2002; Embleton *et al.*, 1976), surface waves (Thomasson, 1977), and obstacles (Hornikx *et al.*, 2010; Van Renterghem *et al.*, 2005). While all these effects need to be accurately modelled, here we focus on the effects produced by the wind profile and the error induced by employing the inappropriate model for a given regime of the atmospheric boundary layer (ABL).

In many outdoor sound propagation studies, the effect of an inhomogeneous and/or moving medium is incorporated via simplified models for the vertical profiles of wind and temperature (and thus the speed of sound). In many instances the profiles are assumed to be logarithmic, based on simple similarity theory and surface-layer assumptions (Hornikx *et al.*, 2010; Taherzadeh *et al.*, 1998; Van Den Berg, 2004). In some cases the profiles are just classified by the effect they have on sound propagation, namely upward- or downward-refracting profiles (e.g., Junker *et al.*, 2007; Salomons, 1998). It is important to first notice that these profiles exist only as an average, and not an instantaneous, property of the medium. The logarithmic wind profile can only be observed in the atmospheric surface layer (bottom tenth of the ABL) when the flow is in a neutral regime, i.e.

[a)] pielbia@dtu.dk

unaffected by buoyancy. In other flow regimes, the logarithmic profile needs a correction.

Micrometeorologial quantities can be expressed as the sum of a mean and a fluctuating components. In this work, we use the a common convention(Wyngaard, 2010) where the tilde denotes the total field, and upper- and lower- case symbols are used for mean and fluctuating components, respectively, i.e. $\tilde{\theta} = \Theta + \theta$. The ABL has three stability regimes, which can be diagnosed through the heat flux $\overline{w\theta}$ in the surface layer, where like other scalar fluxes, can be considered as constant (Wyngaard, 2010). Here w indicates the fluctuating (turbulent) vertical component of the wind velocity and θ the fluctuating component of the potential temperature. The overbar indicates the ensemble average operation, which can be replaced by a time or spatial average under stationary or homogeneous conditions, respectively (Wyngaard, 2010). The mean potential temperature Θ is related to the mean temperature T through (Wyngaard, 2010):

$$\Theta(z) = T(z) \left[\frac{P(0)}{P(z)}\right]^{\frac{R_d}{c_p}}. \tag{1}$$

However, here we use a first order approximation (Stull, 1988) where:

$$\Theta(z) = T(z) + \gamma(z - z_s), \tag{2}$$

where $\gamma = g/c_P = 9.8$ K/km is the adiabatic lapse rate in dry air. A lapse rate that includes humidity can also be used ($\sim$ 6K/km for a saturated atmosphere).

The heat flux $\overline{w\theta}$ is positive when air parcels warmer than their surroundings ($\theta > 0$) are transported upward ($w > 0$) or when air cooler than its surroundings ($\theta < 0$) is transported downwards ($w < 0$). Depending on the value of $\overline{w\theta}$, we can find the ABL in one of the following regimes:

1. Unstable ($\overline{w\theta} > 0$): warmer air parcels at the ground move upward due to buoyancy and act as a source of turbulent kinetic energy. This is typical of sunny daytime conditions, due to a heated surface as a result of solar radiation. It is characterized by large and strong eddies and the largest ABL depths observed (O{1 km}).

2. Stable ($\overline{w\theta} < 0$): air parcels displaced vertically suffer an opposite buoyant acceleration, resulting in a sink of turbulent kinetic energy. This regime is typical of clear nights when the surface is cooling down; it is characterized by weak turbulence and small eddies, or laminar flow.

3. Neutral ($\overline{w\theta} = 0$): this regime occurs with overcast conditions or during transitions, i.e., sunset and sunrise.

Another stability measure, derived from the heat flux, is the reciprocal Obukhov length $L^{-1} \equiv -\kappa(g/\theta_0)\overline{w\theta}/u_*^3$, with θ_0 the potential temperature in the surface-layer (typically $z \lesssim 10\,\mathrm{m}$), $\kappa = 0.4$ the von-Kármán constant, $g = 9.8\ \mathrm{m/s^2}$ the gravitational acceleration, and $u_* = (\overline{uw}^2 + \overline{vw}^2)^{1/4}$ the friction velocity which is related to the magnitude of the mean kinematic surface stress (Wyngaard, 2010); u, v and w are the x, y and z turbulent components of the wind velocity. $1/L$ is negative for unstable regimes, positive for stable regimes and $z/L \ll 1$ for neutral regimes. Probability distributions of L^{-1} for different sites(Kelly and Gryning, 2010) show that neutral and quasi-neutral regimes ($z/L \ll 1$) occur the most often. Furthermore, quasi-neutral or weakly stable regimes, which often occur at nighttime over land, tend also to provide the largest contributions and mean sound levels at large distances (Kelly *et al.*, 2018). The neutral boundary layer can be further classified as truly and conventionally neutral(Zilitinkevich and Esau, 2002) based on the stability conditions at the top of the ABL. The stability in this region is characterized by the Brunt-Väisälä frequency N of the stable ABL-capping inversion :

$$N^2 = \frac{g}{\Theta_0}\frac{\partial \Theta}{\partial z}., \tag{3}$$

with the sign of N^2 mimicking the sign of L in terms of local stability regime . In a truly neutral boundary layer (TNBL) $N = 0$, the wind profile can be modeled using a logarithmic profile and a constant mean potential temperature Θ, hence a linearly decreasing temperature since $c = \sqrt{\gamma R T}$ (Ostashev and Wilson, 2015). In a conventionally neutral boundary layer (CNBL) $N^2 > 0$, there is entrainment from the free atmosphere aloft which produces a low level jet (LLJ). The wind profile is then characterized by a larger speed than predicted by the logarithmic profile, reaching super-geostrophic values before decreasing and converging to the geostrophic wind speed at the top of the ABL. The conventionally neutral regime is much more common than a truly neutral (idealized) regime(Zilitinkevich and Esau, 2002); thus this is the case we study in this paper. The difference in wind speed close to the ground introduces a phase error, the steepness of the wind gradient and temperature affects the height and positions of turning points and radius of curvature of the acoustic rays. The inversion at the top with the LLJ is expected to introduce reflections that will interact with the direct wave and the ground reflections.

There are different models dealing with the wind profile in such a regime (Kelly *et al.*, 2019; Liu *et al.*, 2021; Zilitinkevich and Esau, 2005). In general, all these models are accurate in the lower part of the ABL and start to lose accuracy at heights of ∼20%–70% of the ABL depth. Models with higher accuracy at the top of the ABL require parameters defined at the top of the boundary layer; due to lack of measurements at such heights, this makes them harder to use in practice. From an acoustic point of view, the effect that the accuracy of these models has on the sound field predictions on the ground are not yet known. The dynamics of the ABL and models to describe the profiles of meteorological quantities have been thoroughly investigated for decades. At the same time, many outdoor sound propagation models have been developed over the years, using different approximations and with varying degrees of accuracy. However, the effects of combining the acoustic modelling with the meteorological models and assessing the error from modelling inaccuracies has not received as much attention. This paper thus addresses the sensitivity of acoustic predictions on the ground to inaccuracies in the sound speed profile. Two basic questions thus arise:

- How does the prediction error depend on inaccuracies of the sound speed profile at the top of the boundary layer?
- Within which range are acoustic predictions reliable?

The limitations of using the logarithmic profile for sound propagation in non-neutral stability conditions are already known(Wilson *et al.*, 2008). Here, we look at a neutral case, where the logarithmic profile would be a good descriptor of the profile if one only considers surface parameters. However, we also consider the effect of the capping inversion at the top of the ABL, which causes a deviation from conventional wind and temperature profiles that, in this case, result in downward refraction and its correct modelling is crucial for long-range sound propagation (Wilson *et al.*, 2015). To our knowledge there is no study of the effect that this modelling error has on the prediction of the sound field close to the ground. The paper starts by proposing a simple analytical form for the wind and temperature profiles in a CNBL along with a definition of the vertical wavenumber, the maximum elevation angle and the corresponding turning point height in Section II. We then introduce alternative profiles to study how their differences affect the sound field on the ground in Section III. In this work, we denote the ABL depth with h', the height where the wind profile peaks with h and the width of the LLJ, i.e. the capping layer thickness, with Δh (see Figure 1). We simulate the sound fields using a MATLAB implementation of the wide angle Crank-Nicholson Parabolic Equation (CNPE)(Wilson, 2015). The results from the simulations are presented in Section IV.

II. THEORY

A. Wind profile in a CNBL

We assume here that we can approximate the profile with the LLJ (entrainment zone) typical of a CNBL by adding a correction term f to the logarithmic profile:

$$U(z) = \frac{u_{*0}}{\kappa}\left[\log\left(\frac{z}{z_0}\right) + af(z)\right], \tag{4}$$

where a is a constant that adjusts the strength of the correction. Such function allows us to control the position and the width of the LLJ. With this in mind we choose

$$f(\hat{z}, \alpha, \beta) = \frac{\hat{z}^{\alpha-1}e^{-\beta\hat{z}}\beta^{\alpha}}{\Gamma(\alpha)}, \tag{5}$$

where $\hat{z} \equiv 1 - z/h'$ is the dimensionless distance from the ABL top (distance from the start of the temperature inversion, normalized by the the ABL depth), α and β are two parameters controlling the shape of the function and Γ the Euler-Gamma function (Abramowitz and Stegun, 1964). This model is just an approximation, and it does not include the dynamics of the CNBL. For instance, a change in N or $\overline{w\theta}$ changes the size of the LLJ (Liu and Liang, 2010), its strength (Pedersen *et al.*, 2014), and shear in the ABL (Kelly *et al.*, 2019). Such effects are not explicitly modelled by (5), though it could be extended to do so. We choose this function because it also describes the probability density of a Gamma distribution. In this way we can modify the profile to either model a realistic wind profile in a CNBL or to model less realistic but illustrative edge cases (as we will do with the profiles p3 and p5 in III, see Figure 1. The parameters α and β can be derived from the meteorological quantities h and Δh using properties of the distributions such as the mode and the standard deviation, respectively. Leveraging this relation and considering the normalization employed in (5), we have:

$$\Delta\hat{h} = \frac{\sqrt{\alpha}}{\beta}, \tag{6}$$

$$\hat{h} = \frac{\alpha - 1}{\beta}, \tag{7}$$

where $\hat{h} \equiv 1 - h/h'$ is the dimensionless distance from the ABL top of the wind speed profile's peak, and $\Delta\hat{h} \equiv \Delta h/h'$ is the normalized depth of the entrainment layer. Rearranging the terms on the two equations we can express the parameters α and β as functions of micro-meteorological quantities:

$$\alpha = 1 + \hat{h}\left(\frac{\hat{h} + \sqrt{\hat{h}^2 + 4\Delta\hat{h}}}{2(\Delta\hat{h})^2}\right) \tag{8}$$

$$\beta = \frac{\hat{h} + \sqrt{\hat{h}^2 + 4\Delta\hat{h}}}{2(\Delta\hat{h})^2}. \tag{9}$$

There is no exact expression for h, where the wind speed peaks. However, it is known from Large Eddy Simulations (LES) and atmospheric literature (Kelly *et al.*, 2019; Pedersen *et al.*, 2014) that it typically occurs a little below the height where the total momentum flux reaches 5% of its value at the ground. In a CNBL we can express this height as(Zilitinkevich *et al.*, 2007)

$$h = C_h\frac{u_{*0}}{f}, \tag{10}$$

where f is the Coriolis parameter and u_{*0} is the friction velocity at the ground; here

$$C_h = C_{CN}\left(\frac{f}{N}\right)^{1/2}, \tag{11}$$

where $C_{CN} = 1.36$ and N is the Brunt-Väisälä frequency defined in Eq. (3). Θ_0 is the mean potential temperature at the ground and g is the gravitational acceleration constant.

The depth of the entrainment layer Δz has been previously investigated (Liu *et al.*, 2021). In that work, $\epsilon = \Delta z/2h'$ was found to be weakly dependent on the Zilitinkevich number $Zi \equiv N/|f|$. Furthermore, at medium- to high-latitudes such parameter can be considered constant with a value of $\epsilon = 0.12$. Assuming that h' and h are related through(Liu *et al.*, 2021)

$$h' = \frac{h}{1 - 0.005^{2/3}}, \tag{12}$$

then combining this relation with Eq. (10), the width of the LLJ Δh is then proportional to

$$\Delta h \propto 2\epsilon h' = \frac{2\epsilon}{1 - 0.05^{2/3}} C_{CN} \frac{u_{*0}}{\sqrt{fN}}. \tag{13}$$

B. Potential temperature and speed of sound profiles

Even though the temperature plays a smaller role than the wind except for very stable cases (Kelly *et al.*, 2018), we provide in this section a temperature profile consistent with a CNBL to compute the corresponding sound speed profile.

In a TNBL the potential temperature is constant, while in a CNBL it is constant until it reaches the entrainment layer (Deardorff, 1979). In this layer the temperature increases linearly with a gradient dictated by the Brunt-Väisälä frequency N in Eq. 3. Any function that is constant up to the entrainment layer and then smoothly transition to a linear increase with a slope equal to the potential temperature gradient is a suitable candidate as a profile. Here we decided to use a 'softplus' function since it fulfills the previous requirements and is also differentiable at the transition height:

$$\Theta(z) = \Theta_0 \left[1 + \frac{N^2}{g} \ln(1 + e^{z-h})\right]. \tag{14}$$

We convert the potential temperature to temperature using Eq. (2) to compute the profile of the speed of sound using (Ostashev and Wilson, 2015)

$$c^2 = \gamma R T, \tag{15}$$

where γ is the ratio of specific heats which is equal to approximately 1.4 in the atmosphere under normal condition, $R = 286.9$ J/kgK is the specific gas constant for dry air and T is the temperature in K. This expression is valid only in dry air. We account for the humidity by replacing the temperature with the virtual temperature (Wyngaard, 2010),

$$T_v = T(1 + 0.61 q_s), \tag{16}$$

where q_s is the specific humidity defined by $q_s \equiv \rho_v/\rho$ (ratio of water vapor density to total moist air density).

C. Vertical wavenumber and elevation angle in an inhomogeneous moving layer

In this chapter we calculate the highest turning point and the corresponding elevation angle given by the combination of the wind and temperature profiles. We can avoid modelling the top of the profile including the LLJ in case there is no drastic change in the elevation angle since a larger angle would lead to an increase of the downward refracted energy.

The starting point is the expression for the vertical wavenumber in a moving inhomogeneous medium. In a stratified medium, the wave-vector $\mathbf{k}$ can be expressed in terms of its horizontal (i.e., its projection on the horizontal plane) and vertical components (i.e., its projection on the vertical axis) $\mathbf{k} = (\boldsymbol{\kappa}, q)$(Ostashev and Wilson, 2015). The horizontal wavenumber stays constant along the ray path and in this work we assume the wind direction to be parallel to the propagation path and to the x-axis, so $\boldsymbol{\kappa} = k_0 cos\alpha_0 = \kappa_0$, where α_0 is the elevation angle of the direct wave, k_0 and κ_0 are the wave-number magnitude and the horizontal wave-number at ground level. In this way, the original definition of the vertical wavenumber (Eq. 3.64 in Ostashev and Wilson, 2015) can be simplified to:

$$q(z) = \left[\frac{(\omega - \kappa_0 \cdot U(z))^2}{c^2(z)} - \kappa_0^2\right]^{1/2}. \tag{17}$$

At the turning height the vertical wave number $q(z_t)$ becomes zero:

$$\left[\frac{(\omega - \kappa_0 \cdot U(z_t))^2}{c^2(z_t)} - \kappa_0^2\right]^{1/2} = 0. \tag{18}$$

Eq. (18) cannot be solved analytically in most cases. However, we can rewrite it in the form

$$U(z_t) = \frac{c_0}{\cos(\alpha_0)} - c(z_t), \tag{19}$$

where we have selected the positive branch after taking the square root in (18).

The left hand side (LHS) is the wind speed profile. The right hand side (RHS) depends on the sound speed profile, hence from the temperature profile, and the elevation angle α_0.

At $\alpha_0 = 0$, the only intersection point is zero so the turning height is also zero – the wave does not enter the moving layer. The maximum elevation angle that still produces a turning point corresponds to the case where the line representing the right part of the equation is tangent to the wind speed profile. When an LLJ is present, as it is the case in a CNBL, this point corresponds to the height where the wind speed profile reaches its maximum. In this case we can calculate this angle from the condition:

$$U_{max} = \frac{c_0}{\cos(\alpha_{0,max})} - c(h) \tag{20}$$

Hence:

$$\alpha_{0,max} = \arccos \frac{c_0}{U_{max} + c(z_{max})} \tag{21}$$

III. METHOD

The effects that a given wind profile has on the sound field are complex and difficult to tell apart. For this reason, we defined five different profiles to isolate different features and simplify the analysis of the differences in the corresponding sound fields:

- p1 No wind: The temperature is the only inhomogeneous quantity in the medium, and decreases linearly producing upward refraction in every direction.

- p2 Logarithmic: we used a simple logarithmic profile:

$$U(z) = \frac{u_{*0}}{\kappa} \log\left(\frac{z}{z_0}\right) \qquad (22)$$

- p3 CNBL profile: modelled using Eq. (4) with $a = 1.9$. α and β are obtained using Eq. (8), (9), (10) and (13) with the parameters in Table I. This profile is consistent with profiles in (Kelly *et al.*, 2019; Liu *et al.*, 2021) obtained through large eddy simulations (LES) with similar conditions.

- p4 CNBL without LLJ: this profile matches the CNBL profile (3) up to a height of 250 m, before the inversion occurs, and than evolve it linearly up to the top of the ABL. This profile allows a comparison with the logarithmic profile focusing on the different wind speed and neglecting the effects produced by the LLJ.

- p5 CNBL with stronger LLJ: also this profile matches the CNBL profile (3) up to 250 m, then it follows the profile from Eq. (4) with α and β taking 69% of their value in (3) and $a = 2.4$. This was used to ensure that the only difference with (3) was in the entrainment layer and localized to the LLJ to study the effect of different inversion strengths.

We then used Eq. (14) and (2) to compute a profile for the temperature and speed of sound. The resulting profiles are shown in Figure 1.

We then simulated the corresponding sound fields using a MATLAB implementation of the CNPE(Wilson, 2015). The simulations were performed in 1/3 of octave bands from 31.5 to 125 Hz. The resolution of the computational grid was adjusted at each frequency using the same resolution of ten points per wavelength for both the horizontal and vertical direction as recommended in the literature(Ostashev and Wilson, 2015; Salomons, 1998). The vertical resolution dz in Table I is the smallest resolution corresponding to the frequency of 125 Hz. The source was a monopole placed at $(x, z) = (0, 0)$. The position was chosen to model the typical position of a subwoofer in a open air live event and to limit the variables affecting the study of the resulting sound fields. The size of the simulation domain had a range of 5 km and height h'. We assumed a relative humidity of 30%. The humidity was used to compute the speed of sound using Eq.

TABLE I. Parameters used to compute the wind and temperature profiles. It includes the height of the ABL h' and the h computed with the rest of the parameters using Eq. (10) and (12).

Parameter	Value	Unit
N	0.01	Hz
dz	0.276	m
f	0.0001	rad/s
t_0	23	°C
u_{*0}	0.21	m/s
z_0	0.03	m
h	285	m
h'	330	m

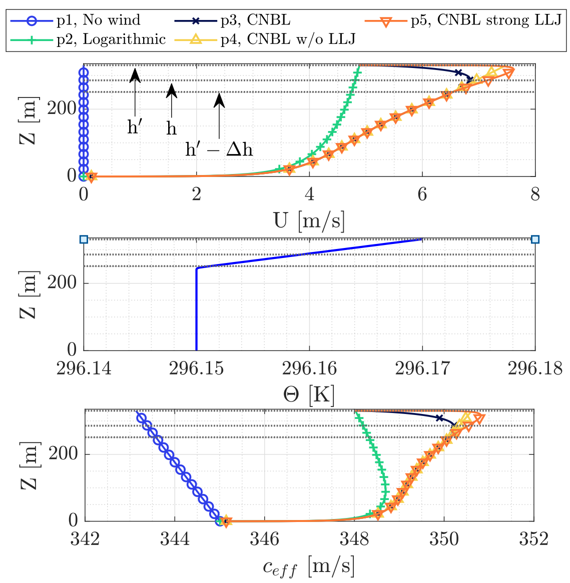

FIG. 1. The five wind profiles (top), the potential temperature profile (middle) and the resulting five effective speed of sound profiles (bottom).

(16) and (15). The sound absorption in air is calculated using humidity, temperature profile and a static pressure of 101325 Pa(Bass *et al.*, 1995). Additional parameters used to compute the ground impedance using Wilson's relaxation model(Wilson, 1993) can be found in Table II. As it can be seen from the table, we performed simulation over two type of terrain: painted concrete and grass field.

TABLE II. Parameters used to compute the ground impedance and the resulting characteristic impedance obtained using $\rho_0 = 1.2$ kg/m^3 and $c_0 = 335$ m/s at three different frequencies.

	Flow resistivity kPa s m^{-2}	Porosity	
Concrete, painted	2e5	0.4	
Grass lawn or grass field	2e2	0.515	
	Z_0 (31.5 Hz)	Z_0 (63 Hz)	Z_0 (125 Hz)
Concrete, painted	867 + 867i	613 + 613i	435 + 435i
Grass lawn or grass field	24+ 24i	17 + 16i	12 + 11i

IV. RESULTS

In this section we present the results and the differences between the sound fields obtained from the profiles in Section III. The effects produced by the LLJ are less evident when propagation takes place over painted concrete making them hard to study under this condition. A hard boundary means that ground reflections are less attenuated at each bounce than they would with a softer and porous boundary. Hence, ground reflections travel longer distances and give rise to a more dense caustic field, with more reflections interfering with each other. In this scenario, the influence of the refracted wave is harder to distinguish being masked by the additional interference produced by the ground reflections. For this reason we only present the results from propagation over grass. The results from simulations over a painted concrete ground are included as supplementary material.

We present a selection of the comparisons to simplify the analysis and to isolate and highlight the difference between the profiles:

- (p1) vs (p2): shows the effect that a height dependent wind has on the sound field on the ground.
- (p4) vs (p2): shows the speed increase in a CNBL against the traditional logarithmic profile.
- (p3) vs (p4): shows the effect of the inversion at the top of the boundary layer.
- (p5) vs (p4): shows the effect of a stronger inversion.

The similarities between the sound fields have been evaluated using the modal assurance criteria (MAC) (Allemang, 2003):

$$\mathrm{MAC} = \frac{\left|\mathbf{p_1}^{\mathrm{H}}\mathbf{p_2}\right|^2}{\left(\mathbf{p_1}^{\mathrm{H}}\mathbf{p_1}\right)\left(\mathbf{p_2}^{\mathrm{H}}\mathbf{p_2}\right)}, \tag{23}$$

where $\mathbf{p_i}$ are the vectors of complex pressure corresponding to the two sound fields under comparison (which could be interchangeably p_1 to p_5) and the superscript H indicates the hermitian transpose. The MAC provides a measure similar to coherence and ranges from 0 to 1. Another error measure used in the study is the normalized mean square error (NMSE):

$$\mathrm{NMSE} = \frac{||\mathbf{p_1} - \mathbf{p_2}||_2^2}{||\mathbf{p_1}||_2^2} \tag{24}$$

Since we are interested in a comparison of the sound fields close to the ground, we compared the sound fields within a sliding window of 5 m height and 50 m length starting from $(x, z) = (0, 0)$. We computed the MAC and NMSE inside the window and moved it in step of 25 m until reaching the end of the 5 km domain.

A. Propagation over grass

Figure 2 shows the MAC between the sound fields within a sliding window. The MAC oscillates between 0 and 1 at a rate that depends on the frequency when comparing the field obtained with the logarithmic profile and with no wind (profiles (p2) and (p1), respectively). This is due to the interference between the ground reflections and the downward refracted wavefront in case of the logarithmic profile and its absence in the case without wind. In the latter, the atmosphere is upward refracting thus the sound waves do not interact with the ground. The MAC degrades progressively when comparing the fields from the logarithmic profile (p2) and the CNBL without LLJ (p4). It still tends to have a periodic nature and it drops faster at higher frequencies. Due to the difference in wind velocity, the wavefronts resulting from the two profiles move at difference speeds. The difference in speed produce a phase difference that increases with distance. This difference increases until the two fields are out of phase before progressively reduce. The curves present peaks and dips at relatively close range that get closer to the source as the frequency increase. The region where the direct, refracted and ground wave first interact occur at different positions that are closer to the source as the wind speed and/or the frequency increases. The mismatch in speed between the two profiles cause this region to occur in slightly different positions. When the regions from both profiles fall within the same spatial window for evaluation, they produce a sudden change in the range dependent MAC. As the frequency increases the separation between these two regions gets larger producing a drop in MAC. The sound fields produced by the CNBL profile (p3) and the CNBL without LLJ (p4) have very high coherence. The LLJ has no effect on the MAC at the ground within the 5 km range in this case. The MAC between the fields corresponding to the profiles (p5) and (p4) is very different. In addition to the dip at 100 Hz and 1.25 km, the MAC starts gradually degrading beyond 2 km at every frequency, in particular at 63 Hz.

Figure 3 shows the NMSE. For profile (p1) and (p2) we see a large error associated with large oscillations and dips at frequencies above 50 Hz due to a strong interfer-

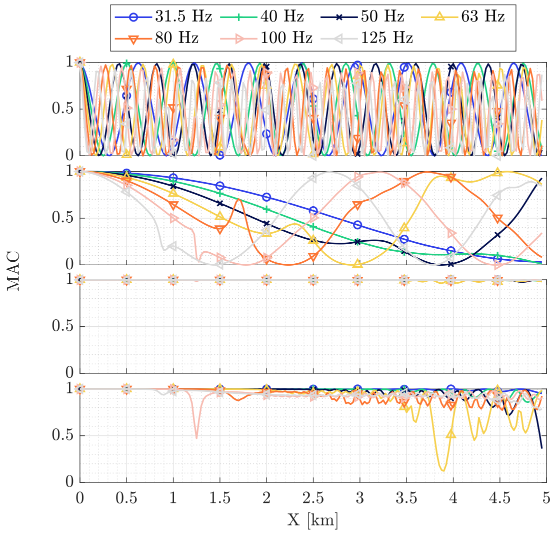

FIG. 2. MAC in a 5x50m sliding window between the sound fields generated using the profiles form Section III over grass. First row: (p1) vs (p2); second row: (p4) vs (p2); third row: (p3) vs (p4); fourth row: (p5) vs (p4)

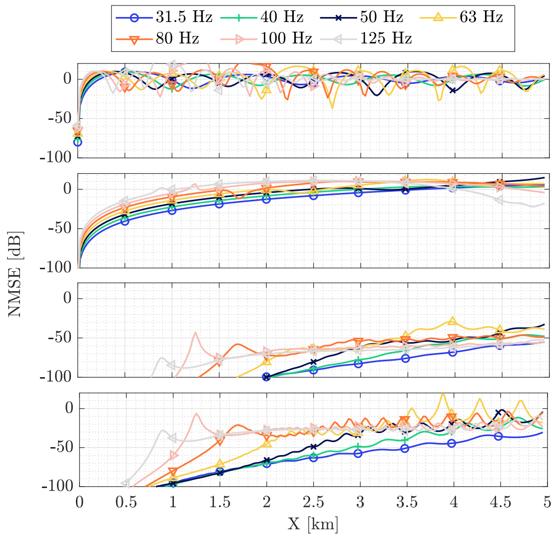

FIG. 3. NMSE in a 5x50m sliding window between the sound fields generated using the profiles form Section III over grass. First row: (p1) vs (p2); second row: (p2) vs (p4); third row: (p3) vs (p4); fourth row: (p4) vs (p5)

ence pattern that is absent in the first case. The error between profiles (p4) and (p2) increases with distance with no oscillation. The reason being the phase difference which shifts the interference pattern instead of the absence of it as in the previous case. For profiles (p3) and (p4) the error increase with distance as well but is always below -50 dB and can be ignored for any practical application. We find a similar trend between profiles (p5) and (p4) but the error is larger. In both cases we can also see large peaks hinting at an interference pattern for (p5) which is absent in (p4).

Finally, we look at the phase error in Figure 4. In this case we computed the absolute phase difference at each node in the domain and then averaged it from the ground to different heights to cover progressively taller regions. We can see how the phase error between profiles (p1) and (p2) oscillates very sharply when averaged over a few heights and becomes smoother when averaged over more nodes. In the case of profiles (p2) and (p4), the error increases with distance until the two sound fields are out of phase before decreasing again as in the MAC. It again shows that the difference between these two fields is only due to a different propagating speed. Finally, we compare the three CNBL profiles. We can see that when we add the LLJ, an additional interference pattern occurs. The stronger the LLJ the stronger the interference. The interference can be seen as ripples in the figure. The phase error increases with distance and presents periodic peaks resembling a comb filter. This shows that failing to include the LLJ can lead to large errors when propagation occurs over a soft ground.

B. Elevation angle and turning point

We can gain an insight into the differences at large distances by looking at the maximum elevation angle and highest turning points. Figure 5 shows the left and right hand side of Eq. (19) for the profiles (p2), (p3) and (p5).

The maximum elevation angles $\alpha_{0,max}$ for these three profiles ranges from 7° to 9° corresponding to the cases of (p2) and (p5), respectively. As the elevation angle grows, the turning height also increases. Using Eq. (21), we find the highest turning point for (p3) is 285 m and for (p5) is 323 m. We find numerically that the highest turning point for (p2) is 90 m. For the values of α_0 between 0 and $\alpha_{0,max}$, there are two turning point. The wave decreases exponentially above the turning height(Ostashev and Wilson, 2015). We will assume that the energy that reaches the upper turning height is small. At incidence angles larger than $\alpha_{0,max}$ the profiles do not produce any turning point.

This analysis shows that stronger jets will produce turning points at larger elevations angles. Even a small difference in the elevation angle can produce a large difference in the highest turning point affecting the accuracy of the simulation at large distances. Even though it is not shown here, the difference between (p3) and (p4) in terms of z_t are small and so is the error between the two corresponding sound field. The MAC and phase error between (p5) and (p4) are much larger instead. In this case the difference in z_t is also larger than in the previous case meaning that downward refracted waves from (p5)

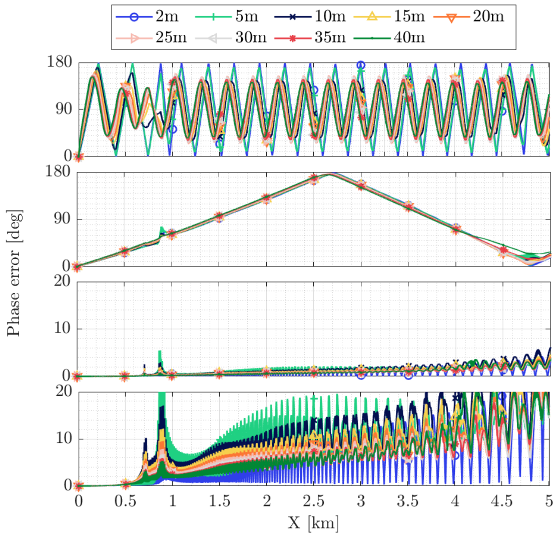

FIG. 4. Absolute phase difference between the sound fields generated using the profiles from Section III over grass. First row: (p1) vs (p2); second row: (p4) vs (p2); third row: (p3) vs (p4); fourth row: (p5) vs (p4). The scale of the y-axis in the last two plots has been changed to show the small phase error due to the exclusion of the LLJ.

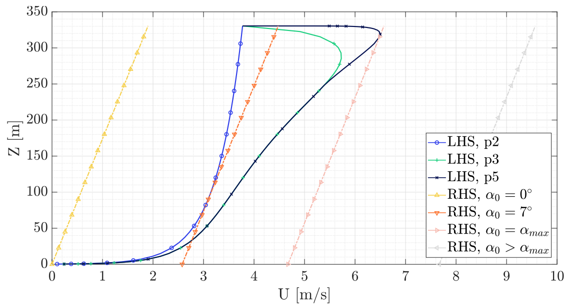

FIG. 5. The wind profiles (p2), (p3) and (p5) (LHS, solid lines) and the right hand side (RHS) of Eq. (19) (dash-dotted lines).

reaches larger distances than (p4) and keeps interacting with the ground waves.

V. DISCUSSION

The differences between profiles (p2) and (p1) show that when the wind profile is included, it creates downward refraction, as previously shown in the literature (Ostashev and Wilson, 2015; Wilson, 2003), which results in the production of an interference pattern at ground where interacts with the direct wave, the ground reflections and possibly the surface wave. The phase error has a very clear shape and periodic behavior, meaning that destructive and constructive interference occur at regular intervals. We can think of the phase error at one height as a signal with its corresponding spectrum in the spatial frequency domain. In this case it would contain a fundamental spatial frequency and odd harmonics, with a shape similar to a triangular wave in the spatial domain. Peaks and dips of the amplitude occur at different positions and spatial frequencies depending on the height. When the average spans taller portions of the domain, more amplitudes at different heights, i.e. more signals, are included. Thus, we end up with a more complex waveform as a result.

The reflections over soft ground do not propagate over larger distances. Hence, there are less reflections contributing to the caustic field which makes it weaker than it would be with a hard boundary. Due to the fewer reflections, the contributions from the top of the ABL cannot be ignored. This also mean that in this case the effect of turbulence is more relevant since it produces phase fluctuations affecting the coherence between the different propagation paths (Embleton *et al.*, 1976; Wilson *et al.*, 2008).

The logarithmic profile underestimates the wind speed in the lower portion of a CNBL and neglects the negative shear in the upper portion, which has two effects: it introduces a phase error due to the speed mismatch and underestimates the maximum elevation angle producing downward refraction. The latter also leads to underestimating the height of the highest turning point and the amount of energy refracted downwards. This introduces an error that is most noticeable at large distances where we see a more complex interference pattern as the wind speeds and strength of the inversion at the top increase.

It should be noted that these profiles are only an average property of the medium and do not exist instantaneously. Therefore, due to the limits of stationarity in the ABL, these mean profiles are valid only for time windows of up to approximately one hour (Kelly *et al.*, 2018; Wyngaard, 2010).

VI. CONCLUSIONS

Logarithmic profiles of wind speed and temperature, which arise in conditions of neutral stratification at the surface, are only appropriate in the atmospheric surface layer. However, in real ABLs, neutral surface conditions are often accompanied by stable stratification at the top of the ABL due to the capping temperature inversion, a regime called conventionally neutral. The stratification produces a jet that results in an increase in speed, which also affects lower altitudes. The logarithmic profile neglects the capping inversion, leading to underestimating the wind speed and its vertical gradient.

In this paper we propose a correction to approximate a more representative wind profile for a CNBL. Simulations performed using a wide-angle CNPE show the error introduced when a logarithmic profile is used in conventionally neutral conditions. The logarithmic profile underestimates the wind speed and its vertical gradient (shear), which introduces a phase error due especially to the lower propagation speed close to the ground. Furthermore, the lower shear also underestimates the maximum elevation angle producing downward refraction. This leads to smaller contributions at large distances where the interference between direct, ground and refracted waves is not modelled properly. This effect is more noticeable when the strength of the inversion, and so the amplitude of the LLJ, increases and when the sound wave propagates over soft ground.

For distances shorter than 2 km, for ABL depths typical in near-neutral conditions it is enough to model the speed increase without the need to include the LLJ effect. This can simplify the model required for the profile reducing the dependence on parameters defined at the top of the ABL. Beyond approximately 2 km in these commonly-occuring conditions, the effect of the LLJ starts to become noticeable and the error introduced by not modelling it progressively increases with distance.

Further studies should be conducted including the effects of the Brunt-Väisälä frequency N and the surface heat flux $Q_0 = \overline{w\theta}$. This would allow to extend the range of validity of this study to less neutral regimes; the tendency of ABL depths to be shallower in stable ABLs can also be an issue. Furthermore, the phase error between profiles with and without the capping inversion show a large difference in the interference patterns. The wind speed inversion associated with the LLJ could produce reflections, and this phenomenon should be further investigated together with the possible contributions of the surface wave to the interference pattern. Finally, further investigation should include turbulence since turbulent scattering introduce phase (as well as amplitude) fluctuations that moderate the effect of the interactions between direct, reflected and refracted waves.

SUPPLEMENTARY MATERIAL

See supplementary material at [URL will be inserted by AIP] for for the results of propagation over painted concrete and transmission losses over grass for selected cases.

ACKNOWLEDGMENTS

This research was supported by d&b audiotechnik GmbH & Co. KG.

Abdur-Rouf, K., and Shaaban, K. (**2022**). "Development of prediction models of transportation noise for roundabouts and signalized intersections," Transportation Research Part D-Transport and Environment **103**, doi: 10.1016/j.trd.2022.103174.

Abramowitz, M., and Stegun, I. A. (**1964**). *Handbook of Mathematical Functions with Formulas, Graphs, and Mathematical Tables*, ninth dover printing, tenth gpo printing ed. (Dover, New York).

Albert, D. G., and Hole, L. R. (**2001**). "Blast noise propagation above a snow cover," Journal of the Acoustical Society of America **109**(6), 2675 – 2681, doi: 10.1121/1.1360240 cited by: 10.

Allemang, R. J. (**2003**). "The modal assurance criterion - twenty years of use and abuse," Sound and Vibration **37**(8), 14–23.

Attenborough, K. (**2002**). "Sound propagation close to the ground," Annual Review of Fluid Mechanics 51–82.

Barlas, E., Zhu, W. J., Shen, W. Z., Dag, K. O., and Moriarty, P. (**2017**). "Consistent modelling of wind turbine noise propagation from source to receiver," The Journal of the Acoustical Society of America **142**(5), 3297–3310, http://dx.doi.org/10.1121/1.5012747, doi: 10.1121/1.5012747.

Bass, H. E., Sutherland, L. C., Zuckerwar, A. J., Blackstock, D. T., and Hester, D. M. (**1995**). "Atmospheric absorption of sound: Further developments," Journal of the Acoustical Society of America **97**(1), 680–683, doi: 10.1121/1.412989.

Caviedes Nozal, D., Heuchel, F. M., Agerkvist, F., and Brunskog, J. (**2019**). "The effect of atmospheric conditions on sound propagation and its impact on the outdoor sound field control," Inter-Noise 2019 Madrid - 48th International Congress and Exhibition on Noise Control Engineering .

Deardorff, J. W. (**1979**). "Prediction of Convective Mixed-Layer Entrainment for Realistic Capping Inversion Structure," Journal of the atmospheric sciences **36**, 424–436.

Embleton, T. F. W., Thiessen, G. J., and Piercy, J. E. (**1976**). "Propagation in an inversion and reflections at the ground," Journal of the Acoustical Society of America **59**(2), 278–282, doi: 10.1121/1.380883.

Heuchel, F. M., Caviedes Nozal, D., Brunskog, J., Agerkvist, F. T., and Fernandez Grande, E. (**2020**). "Large-scale outdoor sound field control," The Journal of the Acoustical Society of America **148**(4), 2392–2402, doi: 10.1121/10.0002252.

Hornikx, M., Waxler, R., and Forssén, J. (**2010**). "The extended Fourier pseudospectral time-domain method for atmospheric sound propagation," The Journal of the Acoustical Society of America **128**(4), 1632–1646, doi: 10.1121/1.3474234.

Junker, F., Gauvreau, B., Ecotiére, D., Crémézi-Charlet, C., and Blanc-Benon, P. (**2007**). "Meteorological classification for environmental acoustics - practical implications due to experimental accuracy and uncertainty," in *19th International congeess on acoustics*, September, Madrid.

Kelly, M., Barlas, E., and Sogachev, A. (**2018**). "Statistical prediction of far-field wind-turbine noise, with probabilistic characterization of atmospheric stability," Journal of Renewable and Sustainable Energy **10**(1), doi: 10.1063/1.5012899.

Kelly, M., Cersosimo, R. A., and Berg, J. (**2019**). "A universal wind profile for the inversion-capped neutral atmospheric boundary layer," Quarterly Journal of the Royal Meteorological Society **145**(720), 982–992, doi: 10.1002/qj.3472.

Kelly, M., and Gryning, S. E. (**2010**). "Long-Term Mean Wind Profiles Based on Similarity Theory," Boundary-Layer Meteorology **136**(3), 377–390, doi: 10.1007/s10546-010-9509-9.

Libianchi, P., Agerkvist, F. T., and Shabalina, E. (**2022**). "A review of techniques and challenges in outdoor sound field control," in *Proceedings of Inter·Noise 2022*, https://internoise2022.org/, 51¡sup¿st¡/sup¿ International Congress and Exposition on Noise Control Engineering, Internoise 2022 ; Conference date: 21-08-2022 Through 24-08-2022.

Liu, L., Gadde, S. N., and Stevens, R. J. A. M. (**2021**). "Geostrophic drag law for conventionally neutral atmospheric boundary layers revisited," Quarterly Journal of the Royal Meteorological Society **147**(735), 847–857, doi: 10.1002/qj.3949.

Liu, S., and Liang, X. Z. (**2010**). "Observed diurnal cycle climatology of planetary boundary layer height," Journal of Climate **23**(21), 5790–5809, doi: 10.1175/2010JCLI3552.1.

Luquet, D., Marchiano, R., and Coulouvrat, F. (**2019**). "Long range numerical simulation of acoustical shock waves in a 3d moving heterogeneous and absorbing medium," Journal of Computational Physics **379**, 237–261, doi: 10.1016/j.jcp.2018.11.041.

Ostashev, V. E., and Wilson, D. K. (**2015**). *Acoustics in Moving Inhomogeneous Media* (CRC Press), https://www.taylorfrancis.com/books/9781482266658.

Pedersen, J. G., Gryning, S. E., and Kelly, M. (**2014**). "On the Structure and Adjustment of Inversion-Capped Neutral Atmospheric Boundary-Layer Flows: Large-Eddy Simulation Study," Boundary-Layer Meteorology **153**(1), 43–62, doi: 10.1007/s10546-014-9937-z.

Raspet, R., Baird, G., and Wu, W. (**1992**). "Normal Mode Solution For Low-Frequency Sound Propagation In A Downward Refracting Atmosphere Above A Complex Impedance Plane," Journal of the Acoustical Society of America **91**(3), 1341–1352, doi: 10.1121/1.402463.

Salomons, E. M. (**1998**). "Caustic diffraction fields in a downward refracting atmosphere," The Journal of the Acoustical Society of America **104**(6), 3259–3272, doi: 10.1121/1.423966.

Stull, R. B. (**1988**). *An Introduction to Boundary Layer Meteorology* (Springer Netherlands, Dordrecht), http://link.springer.com/10.1007/978-94-009-3027-8.

Taherzadeh, S., Li, K. M., and Attenborough, K. (**1998**). "Some practical considerations for predicting outdoor sound propagation in the presence of wind and temperature gradients," Applied Acoustics **54**(1), 27–44, doi: 10.1016/S0003-682X(97)00069-8.

Tang, J., Lin, B., Hwang, J., Chen, L., Wu, B., Jian, H., Lee, Y., and Chan, T. (**2022**). "Dynamic modeling for noise mapping in urban areas," Environmental Impact Assessment Review **97**, doi: 10.1016/j.eiar.2022.106864.

Thomasson, S. I. (**1977**). "Sound propagation above a layer with a large refraction index," Journal of the Acoustical Society of America **61**(3), 659–674, doi: 10.1121/1.381352.

Van Den Berg, G. P. (**2004**). "Effects of the wind profile at night on wind turbine sound," Journal of Sound and Vibration **277**(4-5), 955–970, doi: 10.1016/j.jsv.2003.09.050.

Van Renterghem, T., Salomons, E. M., and Botteldooren, D. (**2005**). "Efficient FDTD-PE Model for sound propagation in situations with complex obstacles and wind profiles," Acta Acustica united with Acustica **91**(4), 671–679.

Wilson, D. K. (**1993**). "Relaxation-matched modeling of propagation through porous media, including fractal pore structure," Journal of the Acoustical Society of America **94**(2), 1136–1145, doi: 10.1121/1.406961.

Wilson, D. K. (**2003**). "The sound-speed gradient and refraction in the near-ground atmosphere," The Journal of the Acoustical Society of America **113**(2), 750–757, doi: 10.1121/1.1532028.

Wilson, D. K. (**2015**). "Outdoor sound propagation calculator" In: V. E. Ostashev and D. K. Wilson, Acoustics in Moving Inhomogeneous Media (second edition), Taylor & Francis.

Wilson, D. K., Lewis, M. S., Weatherly, J. W., and Andreas, E. L. (**2008**). "Dependence of predictive skill for outdoor narrowband and broadband sound levels on the atmospheric representation," Noise Control Engineering Journal **56**(6), 465–477, doi: 10.3397/1.3010733.

Wilson, D. K., Ostashev, V. E., and Pettit, C. L. (**2015**). "Sound Propagation in the Atmospheric Boundary Layer," Acoustics today **11**(2), 44–53.

Wyngaard, J. C. (**2010**). *Turbulence in the Atmosphere* (Cambridge University Press, Cambridge), http://ebooks.cambridge.org/ref/id/CBO9780511840524.

Zilitinkevich, S., Esau, I., and Baklanov, A. (**2007**). "Further comments on the equilibrium height of neutral and stable planetary boundary layers," Quarterly Journal of the Royal Meteorological Society **133**(622), 265–271, doi: 10.1002/qj.27.

Zilitinkevich, S. S., and Esau, I. N. (**2002**). "On integral measures of the neutral barotropic planetary boundary layer," Boundary-Layer Meteorology **104**(3), 371–379, doi: 10.1023/A:1016540808958.

Zilitinkevich, S. S., and Esau, I. N. (**2005**). "Resistance and heat-transfer laws for stable and neutral planetary boundary layers: Old theory advanced and re-evaluated," Quarterly Journal of the Royal Meteorological Society **131**(609), 1863–1892, doi: 10.1256/qj.04.143.

Paper E

PHASE ERROR SENSITIVITY TO THE INVERSION STRENGTH AND DEPTH OF THE BOUNDARY LAYER IN A CONVENTIONALLY NEUTRAL REGIME

Pierangelo Libianchi[1*] **Mark Kelly**[2] **Elena Shabalina**[3]
Finn Agerkvist[1] **Jonas Brunskog**[1]

[1] Acoustic Technology Group, Department of Electrical and Photonics Engineering,
Technical University of Denmark, Building 352, Ørsted Plads, DK-2800 Kongens Lyngby, Denmark
[2] Department of Wind Energy, Risø Lab/Campus,
Technical University of Denmark, Frederiksborgvej 399, DK-4000 Roskilde, Denmark
[3] Independent researcher

ABSTRACT

In outdoor sound propagation, the variation of wind speed with height plays an important role and a logarithmic profile is often assumed. This is an accurate description in a neutral boundary layer according to MOST. However, the neutral boundary layer can be either truly neutral or conventionally neutral depending on the stability condition at the top of the ABL. While the logarithmic profile is suitable in a truly neutral regime, the conventionally neutral is more commonly found. This regime is characterized by a stable stratification aloft that result in super geostrophic wind speed close to the top of the ABL and higher speed and steeper gradient close to the ground than predicted by the logarithmic profile. This work uses numerical simulations based on the Crank-Nicholson parabolic equation to derive the sensitivity of the phase to the ABL depth and inversion strength as a function of the distance from the source. The results show that a stronger inversion increases the phase differences that can be as large as 60° already at 1 km from the source. Stronger inversions and a deeper ABL produce more complex interference on the ground, showing only after approximately 2 km, that affect both phase and magnitude.

*__Corresponding author__: pielbia@dtu.dk.

Keywords: CNBL, outdoor sound propagation, inversion strength, ABL depth, logarithmic profile, phase error

1. INTRODUCTION

In the atmospheric boundary layer (ABL), the speed of sound generally depends on height. The gradient of the speed of sound defines wave phenomena in the ABL, such as refraction. Atmospheric refraction can cause sound waves from a ground source to bend back to the ground at different rates and create interference patterns with the waves travelling different paths. These effects are important for correct predictions of the sound field close to the ground.

The sound speed profile depends on the wind speed and temperature profiles in the ABL. Depending on the buoyancy at surface level, the ABL can be classified as stable, unstable and neutral. Neutral and quasi-neutral (very small buoyancy) are the most often encountered conditions [1].

In many instances the profiles are assumed to be logarithmic, based on simple similarity theory and surface-layer assumptions [2–4]. In some cases the profiles are just classified by the effect they have on sound propagation, namely upward- or downward-refracting profiles [5, 6]. According to Monin-Obukhov Similarity Theory (MOST), the logarithmic profile is suitable for neutral regimes [7]. However, Zilitinkevich and Esau [8] distinguishes between a truly and conventionally neutral ABL when considering also the stability conditions at the top of the ABL. In truly neutral conditions, well described by a logarithmic profile, the ABL is neutral both at the top and bottom. In a conventionally neutral boundary layer (CNBL), the ABL presents a stable stratification at the top, in the so called entrainment layer, that results in wind speeds larger than predicted by the logarithmic profile. Furthermore, it produces super-geostrophic wind speed close to the top of the ABL adding a characteristic "nose" to the profile that is commonly known as low-level jet (LLJ, see Figure 1). This latter condition is also the most common of the two [8]. In this paper, we focus on the wind speed in the CNBL since the effect of the stable stratification on the temperature profile is small compared to the adiabatic lapse rate. There are many formulation for the wind profile in a CNBL [9–12]. Liu and Stevens [13] provide a good description that allows to represent a range of inversion strengths and ABL heights.

An accurate description of the phase is crucial when simulating the noise emissions produced from multiple sources and for sound field control applications [14]. However, we have found no such information in the available literature. We investigated the influence that different sections of the wind profile have on the sound field at the ground for one specific ABL depth and inversion strength in a previous work [15]. In this work, we extend that study to investigate how different ABL depths and inversion strengths affect the simulated sound fields.

In this paper, we study the sensitivity of the phase error to the height of the ABL and strength of the inversion at different distances from the source.

We use numerical simulations based on the Crank Nicholson parabolic equation to simulate the sound fields produced by a simple logarithmic profile first, and then by the same profile plus a correction term suitable to a CNBL which we describe in Section 2. We then study the error introduced by neglecting this correction term by comparing the two sound fields using the Modal Assurance Criterion (MAC) and the absolute phase and magnitude errors.

2. THEORY AND METHODS

2.1 Wind profile

To model the wind profile in the CNBL, we use in this work the formulation described in Liu and Stevens [13]. In this section we briefly introduce such formulation, focusing only on the stream-wise component of the wind that is assumed to be parallel to the propagation direction of the sound waves. In this work, we are interested in the effect that the ABL depth h and the inversion strength, described by the Brunt–Väisälä frequency N, have on the prediction of the sound field close to the ground. Here, we use the common assumption that the ABL depth h is related to the height z_t, where the total shear stress reaches 5% of the surface value, through:

$$h = (1 - 0.05^{2/3}) z_t. \tag{1}$$

These two variables are included in the formulation from [13] through the inverse dimensionless boundary height $b = u_*/(fh)$ and the Zilitinkevich number $Zi = N/f$, where f is the Coriolis parameter. The friction velocity u_* in the CNBL is proportional to $h(fN)^{1/2}$ [7]. The values of all the constants used in this section are presented in Table 1.

The stream-wise component of the geostrophic wind U_g, i.e., the mean wind speed in the free atmosphere, is predicted using the geostrophic drag law:

$$\frac{\kappa U_g}{u_*} = \ln Ro_0 - A(Zi), \tag{2}$$

where $\kappa = 0.41$ is the von Kármán constant and $Ro_0 = u_*/(fz_0)$ is the surface Rossby number [16]. A is parameterized as

$$A = -A_1 m + \ln(A_0 + m) + \ln \beta, \tag{3}$$

where A_1 and A_0 are constant and m is the composite stratification parameter,

$$m = \left(1 + C_m^2 Zi^2\right)^{1/2} \beta^{-1}, \tag{4}$$

and

$$\beta = \left(C_R^{-2} + C_N^{-2} Zi\right)^{1/2}, \tag{5}$$

where C_R and C_N are constants.

The stream-wise wind component within the ABL consists of a logarithmic profile and an additional correction term:

$$\frac{\kappa U}{u_*} = \ln\left(\frac{z}{z_0}\right) + f_u(\xi, Zi), \tag{6}$$

where $\xi = z/h$ is the normalized height coordinate. The proposed expression for the correction is

$$f_u(\xi, Zi) = -a(Zi)\xi + a_\psi(Zi)\psi(\xi), \tag{7}$$

where

$$a_\psi = \frac{2-a}{1-2\epsilon}, \tag{8}$$

$$\psi = \xi - \frac{e^{\xi/\epsilon}-1}{e^{1/\epsilon}-1}, \tag{9}$$

and where ϵ relates the thickness of the entrainment layer to the boundary layer depth. Its value depends on Zi but it is possible to assume $\epsilon = 1.2$ for moderate Zi [9]. The value of $a(Zi)$ can be obtained from the continuity condition at the top of the ABL where $U(\xi = 1) = U_g$. Considering that $\psi(\xi = 1) = 0$ and combining Eq. (2) and (6) with $ln(Ro) = ln(b) + ln(h/z_0)$ at $\xi = 1$,

$$f_u(1, Zi) = \ln b - A \equiv -a(Zi). \tag{10}$$

2.2 Temperature profile

The potential temperature in a neutral boundary layer is constant across the ABL. However, in a CNBL the potential temperature increases in the entrainment layer with a slope that is proportional to inversion strength $\partial\theta/\partial z = \theta_0 N^2/g$. Any function matching this requirement could potentially be used. In this work we used the following formulation:

$$\theta(z) = \theta_0 \left[1 + \frac{N^2}{g}\ln(1 + e^{z-h(1-0.05^{2/3})})\right]. \tag{11}$$

The potential temperature can then be converted to temperature using the approximation found in [17],

$$\theta(z) = T(z) + \Gamma_{\text{dry}}(z - z_s), \tag{12}$$

where $\Gamma_{\text{dry}} = g/c_P = 9.8$ K/km is the dry air adiabatic lapse rate.

2.3 Simulations

The profiles from the previous sections were used to compute the corresponding sound fields at distances of up to 5 km using the implementation of the Crank-Nicholson parabolic equation from Wilson [18]. The constants and parameters used to compute the profiles are shown in Table 1. The source consisted of a monopole placed at $(x, y) = (0, 0)$. The simulations were performed only downwind, since this is the case where sound travels the furthest. The domain had a range of 5 km and a height ranging from 200 to 1000 m, depending on the ABL depth used in each case. A resolution of $\lambda/10$ was used in both directions. The ground was modelled as a grass field with flow resistivity σ, porosity φ and characteristic impedance calculated using Wilson's model [19] and whose values are shown in Table 1. The values of h ranged from 200 to 500 m in steps of 25 m. Also a height of 1000 m was considered as an extreme case. These values fit the distribution of the boundary layer depth found in [20]. We considered 20 values of N, equally spaced and ranging from 6 to 14 mHz, according to values found in [10]. Each combination of h and N was used to compute the correction term in Eq. (6). For each combination we computed a sound field produced by a profile using the correction term and one without, hence with a simple logarithmic profile. These pairs of sound fields were then compared to study the error introduced by using a logarithmic profile in a CNBL. We evaluated the differences between these sets of two sound fields using the MAC [21],

$$\text{MAC} = \frac{\left|\mathbf{p_{log}}^{\text{H}}\mathbf{p_{cnbl}}\right|^2}{\left(\mathbf{p_{log}}^{\text{H}}\mathbf{p_{log}}\right)\left(\mathbf{p_{cnbl}}^{\text{H}}\mathbf{p_{cnbl}}\right)}. \tag{13}$$

Further information on the nature of this error is obtained by studying the absolute phase and magnitude errors. The phase and magnitude errors were computed at each point in the domain and then averaged over the vertical coordinate up to 5 m above ground. The MAC was instead computed within regions of 50 m length and 5 m height, gradually sliding away from the source in steps of 25 m.

Table 1: Values and units of the constants and simulation parameters. The set of values for N and h are formatted as start value:step:stop value.

Parameter	Value	Unit
C_R	0.5	
C_N	1.6	
κ	1.4	
A_1	0.65	
A_0	1.3	
B_1	7	
B_0	8	
C_m	0.1	
ϵ	0.12	
f	0.0001	s^{-1}
θ_0	293	K
z_0	0.03	m
σ	200	kPasm^{-2}
φ	0.515	
N	6:0.42:14	mHz
h	200:25:500, 1000	m
$Z_{0,f=125Hz}$	12 + 11i	

3. RESULTS

This section presents the results obtained from the simulations. We show only the results at 125 Hz for space reasons and since they better show the effect of the ABL depth and inversion strength on the sound field. The same effects occur at larger distances as the frequency decreases. A subset of the profiles used to compute the sound fields are shown in Fig. 1, with and without the correction term, together with the corresponding effective speed of sound $c_{eff}(z) = c(T) + U(z)$. We then compared the sound fields resulting from these profiles with and without the correction term to asses the error introduced by using a logarithmic profiles in a CNBL.

Larger N produce larger wind speed, a steeper gradient close to the surface and a stronger inversion at the top of the boundary layer. This increases the height at which the gradient of the effective speed of sound changes sign and thus the extent of the down-refractive region of the medium. The height of the ABL has a similar effect, resulting in a larger wind speed and taller down-refracting region.

The MAC between the sound fields from these profiles and the corresponding logarithmic profile have been analyzed as a function of distance and ABL depth (Fig. 2), and inversion strength (Fig. 3). In general the two predictions diverge with distance, and the MAC drops dramatically between 1 km and 2 km. The deviation onset is closer to the source as N increases while a larger h produce more interference and larger larger spatial variations. Figure 2 shows the superposition of two patterns: one with low and another with high wavenumbers. The first occurs with any combination of N and h and is associated with the wind speed mismatch close to the ground. The ABL depth has a weaker influence on this pattern than N. However, the pattern starts slightly closer to the source as the height of the ABL increases. The high wavenumber pattern does not exist in shallow ABLs with a weak inversion. This pattern becomes more complex as the ABL depth increases. As the ABL gets taller, also the region where downward refraction occurs grows. Thus, the amount of energy refracted downwards also increases producing more complex interference at the ground.

The second pattern becomes more complex as the ABL depth and inversion strength increase. This can also be seen in Figure 3. This figure also shows two overlapping patterns as a results of different mechanisms affecting the MAC. The inversion strength N has a much larger influence on the low wavenumber pattern than h

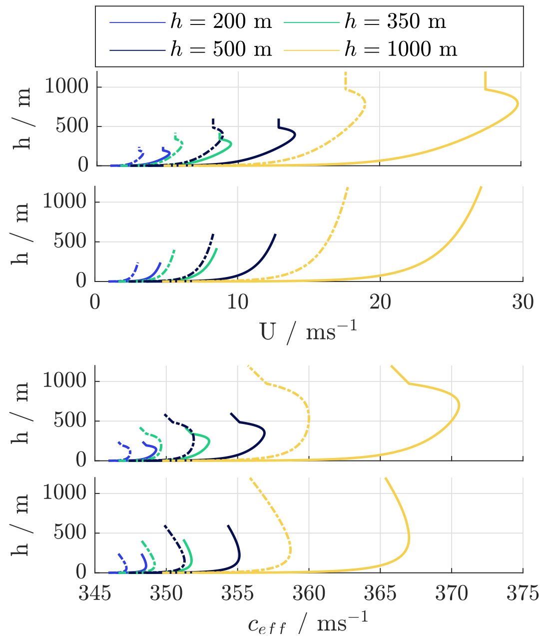

Figure 1: A subset of the profiles computed using Eq. (6). The first two plots from the top show the wind profiles with and without (logarithmic profile) the correction term, respectively. The last two plots show the corresponding profiles of the effective speed of sound. The profiles are shown for a subset of four different ABL depths (including the shallowest and the deepest) and two inversion strengths: the smallest ($N = 6$ mHz, dashed) and the largest ($N = 14$ mHz, solid).

does. The distance from the source where this pattern occurs is inversely proportional to N. The wavenumbers of this pattern are instead directly proportional to the inversion strength, i.e. as N increases the spatial variations of the pattern are larger. The inversion strength also affects the position where this second patter starts.

Figure 4 confirms that phase is the main culprit for the drop in MAC seen in the previous figures. Also here, we see the weak influence of h on the low wavenumber pattern and a larger influence on the high wavenumber one. Figure 5 shows instead how the inversion strength affects both patterns. Also this figure reflects quite well what presented in Figures 2 and 3.

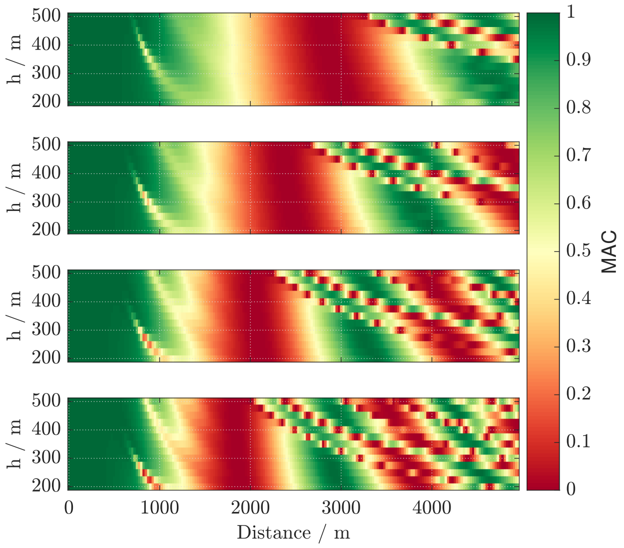

Figure 2: Four snapshots of the MAC at four different values of the inversion strength N (top to bottom): 6, 8.5, 11.5 and 14 mHz. Each plot shows the MAC as a function of distance from the source (horizontal axis) and ABL depth h up to 500 m (vertical axis).

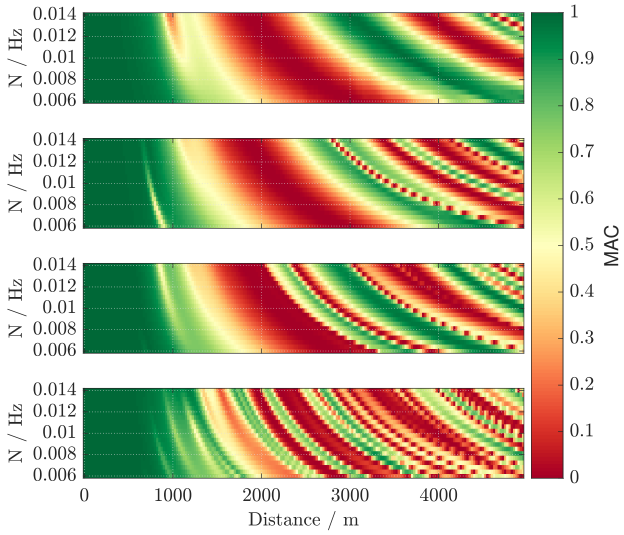

Figure 3: Four snapshots of the MAC at four different values of the ABL depth h (top to bottom): 200, 350, 500 and 1000 m. Each plot shows the MAC as a function of distance from the source (horizontal axis) and inversion strength N (vertical axis).

Figures 6 and 7 show the absolute magnitude error as a function of h and N. The magnitude error is small close to the source and resembles the pattern of the high wavenumber error found in MAC and phase. The magnitude error is relevant only where interference occurs. Before 2 km there is no interference and the magnitude of both sound fields is only affected by spherical divergence. Beyond 2 km, the direct, reflected and refracted waves interact. In this region, the discrepancy in wind speed and the amount of downward refracted energy generate different interference patterns, introducing a magnitude error. Notwithstanding the low magnitude error before 2 km, successful applications of sound field control would be limited to 1 km due to the phase error.

4. DISCUSSION

In the results we see how the magnitude error becomes relevant beyond 2 km, while the phase error can be as large as 60° at around 1 km. Beyond this distance the phase difference grows at a rate that largely depends on the inversion strength at the top of the ABL. In a sound field control application, a phase error of 60° marks the transition from noise reduction to amplification.

There are two main sources of error, visible as two different patterns. The low wavenumber pattern is the main source of error and is associated with the phase difference introduced by the wind speed mismatch close to the ground which is consistent with the findings in [15]. Without the ABL-capping inversion, the profile from Eq. 6 is equivalent to the logarithmic one. Subsequently, this pattern is only weakly affected by the ABL depth h while showing a strong dependence on inversion strength (N).

The high wavenumber pattern is instead coupled to both parameters. In general, a deeper ABL or a stronger inversion increases the height of the region where sound waves are refracted downward. As this region gets taller, the amount of downward refracted energy also increases and produces more complex interference at the ground. Since the correction term depends on both the inversion strength (stability condition given by N) and the normalized height coordinate ξ, they both affect the prediction error. Increasing N also moves this interference closer to the source. Compared to a logarithmic profile, the increase in N results in a steeper wind speed gradient around the ABL top. The steeper gradient reduces the radius of curvature of the sound rays, decreasing the dis-

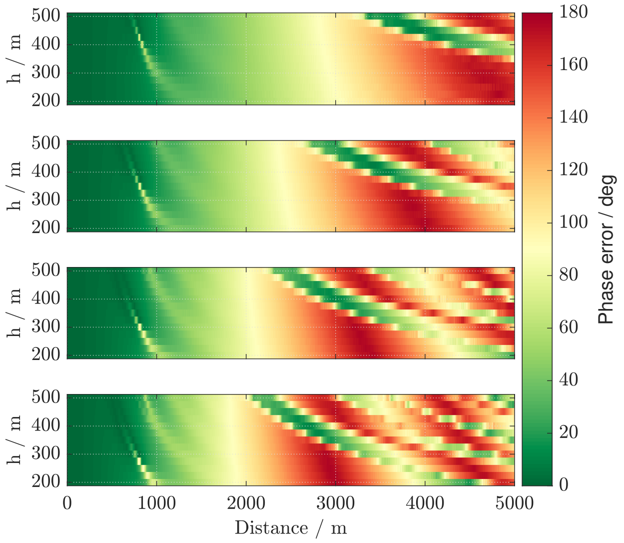

Figure 4: Four snapshots of the absolute phase error at four different values of the inversion strength N (top to bottom): 6, 8.5, 11.5 and 14 mHz. Each plot shows the absolute phase error as a function of distance from the source (horizontal axis) and ABL depth h up to 500 m (vertical axis).

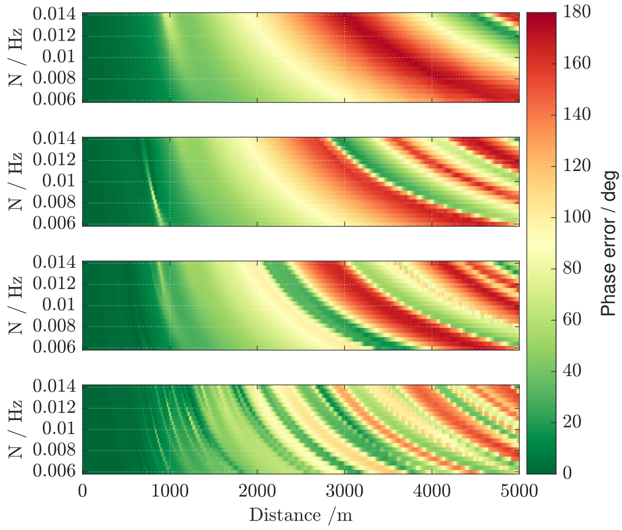

Figure 5: Four snapshots of the absolute phase error at four different values of the ABL depth h (top to bottom): 200, 350, 500 and 1000 m. Each plot shows the absolute phase error as a function of distance from the source (horizontal axis) and inversion strength N (vertical axis).

tance from the source where interference becomes significant. Furthermore, a stronger inversion produces a stronger upper-ABL jet; this increases the maximum elevation angle at the source that will result in downward refraction, when compared to a profile ignoring the ABL top.

The error introduced by using a logarithmic profile in a CNBL affects mainly the phase. The magnitude error becomes relevant beyond 2 km. From this distance, the refracted waves produce an error magnitude that is, however, confined to limited regions. On the other hand, the phase error can be as large as 45° already at 1 km and affect large portions of the domain.

The case considered here is representative for sound field control application for open air events [14,22], which often take place over grass and where sound sources are typically placed on the ground. In this study the position of the source and type of ground were chosen to limit the influence of ground reflections, to better isolate and study the influence of the propagation medium. Moving the source away from the ground produces reflections closer to the source that are not independent of the medium. A hard boundary allows such reflections to propagate over larger distances due to the reduced attenuation. In this scenario, the additional reflections produce more interference making it harder to analyze the effects produced by the medium alone and the different profiles. The resulting interference pattern is more complex and the interaction between direct and refracted wave would not be as clear.

5. CONCLUSION

In this work we analyzed the prediction error introduced by using a logarithmic profile in a CNBL, where it is not suitable due to the larger wind speed resulting from the stable stratification at the CNBL top. We described an alternative formulation for the wind and temperature profiles suited to a CNBL. This formulation is tested against a logarithmic profile by generating the two corresponding sound fields using the Crank-Nicholson parabolic equation. The two sound field are then compared through the MAC metric and in terms of the absolute phase and magnitude errors. For distances shorter than 1 km, both phase and magnitude errors are small and the two sound fields present a large spatial correlation. Beyond this distance, the prediction error appears as two overlapping patterns,

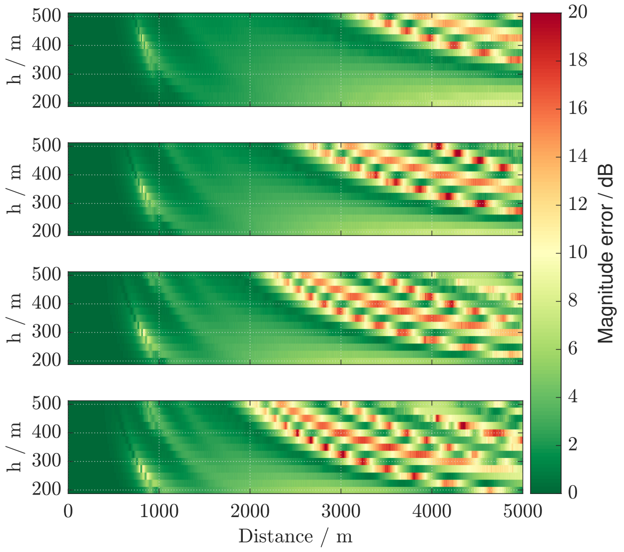

Figure 6: Four snapshots of the absolute magnitude error at four different values of the inversion strength N (top to bottom): 6, 8.5, 11.5 and 14 mHz. Each plot shows the MAC as a function of distance from the source (horizontal axis) and ABL depth h up to 500 m (vertical axis).

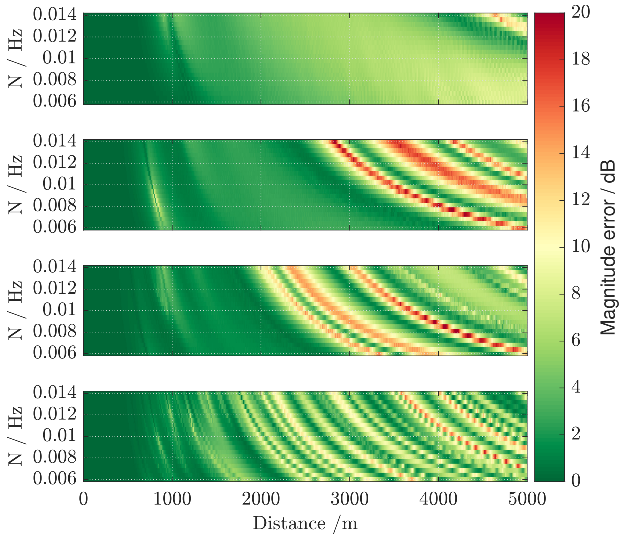

Figure 7: Four snapshots of the absolute magnitude error at four different values of the ABL depth h (top to bottom): 200, 350, 500 and 1000 m. Each plot shows the absoluite magnitude error as a function of distance from the source (horizontal axis) and inversion strength N (vertical axis).

one with low and one with high wavenumber. The former is the most important one since it affects large portions of the entire domain. It is mainly dependent on the inversion strength N and it is a results of the wind speed mismatch close to the ground. The ABL depth h has only a weak influence. The high wavenumber component instead depends on both parameters. When either of them increases, so does the error due to an increase in downward refracted energy. This increase results in more complex interactions between direct, refracted and reflected waves than with a logarithmic profile. The reason is an increase in the height of the downward refracting region due to an increase in h and an increase in the maximum turning angle due to H.

The magnitude error is relevant only in very limited regions far from the source (more than 2 km). The phase error instead is considerable at shorter distances (already at 1 km) and affects large regions of the domain. In cases where many sound sources are involved, it is crucial to limit such an error since the total sound field will not only inherit the phase error but the interaction between the sources will result in a larger magnitude error.

6. REFERENCES

[1] M. Kelly and S. E. Gryning, "Long-Term Mean Wind Profiles Based on Similarity Theory," *Boundary-Layer Meteorology*, vol. 136, no. 3, pp. 377–390, 2010.

[2] G. P. Van Den Berg, "Effects of the wind profile at night on wind turbine sound," *Journal of Sound and Vibration*, vol. 277, no. 4-5, pp. 955–970, 2004.

[3] S. Taherzadeh, K. M. Li, and K. Attenborough, "Some practical considerations for predicting outdoor sound propagation in the presence of wind and temperature gradients," *Applied Acoustics*, vol. 54, no. 1, pp. 27–44, 1998.

[4] M. Hornikx, R. Waxler, and J. Forssén, "The extended Fourier pseudospectral time-domain method for atmospheric sound propagation," *The Journal of the Acoustical Society of America*, vol. 128, no. 4, pp. 1632–1646, 2010.

[5] E. M. Salomons, "Caustic diffraction fields in a downward refracting atmosphere," *The Journal of*

the Acoustical Society of America, vol. 104, no. 6, pp. 3259–3272, 1998.

[6] F. Junker, B. Gauvreau, D. Ecotiére, C. Crémézi-Charlet, and P. Blanc-Benon, “Meteorological classification for environmental acoustics - practical implications due to experimental accuracy and uncertainty,” in *19th International congeess on acoustics*, no. September, (Madrid), 2007.

[7] J. C. Wyngaard, *Turbulence in the Atmosphere*. Cambridge: Cambridge University Press, 2010.

[8] S. S. Zilitinkevich and I. N. Esau, “On integral measures of the neutral barotropic planetary boundary layer,” *Boundary-Layer Meteorology*, vol. 104, no. 3, pp. 371–379, 2002.

[9] L. Liu, S. N. Gadde, and R. J. A. M. Stevens, “Geostrophic drag law for conventionally neutral atmospheric boundary layers revisited,” *Quarterly Journal of the Royal Meteorological Society*, vol. 147, no. 735, pp. 847–857, 2021.

[10] M. Kelly, R. A. Cersosimo, and J. Berg, “A universal wind profile for the inversion-capped neutral atmospheric boundary layer,” *Quarterly Journal of the Royal Meteorological Society*, vol. 145, no. 720, pp. 982–992, 2019.

[11] S. E. Gryning, E. Batchvarova, B. Brümmer, H. Jørgensen, and S. Larsen, “On the extension of the wind profile over homogeneous terrain beyond the surface boundary layer,” *Boundary-Layer Meteorology*, vol. 124, no. 2, pp. 251–268, 2007.

[12] S. S. Zilitinkevich and I. N. Esau, “Resistance and heat-transfer laws for stable and neutral planetary boundary layers: Old theory advanced and re-evaluated,” *Quarterly Journal of the Royal Meteorological Society*, vol. 131, no. 609, pp. 1863–1892, 2005.

[13] L. Liu and R. J. A. M. Stevens, “Vertical structure of conventionally neutral atmospheric boundary layers,” *Proceedings of the National Academy of Sciences*, vol. 119, p. e2119369119, May 2022.

[14] P. Libianchi, F. T. Agerkvist, and E. Shabalina, “A review of techniques and challenges in outdoor sound field control,” in *Proceedings of Inter·Noise 2022*, 2022. 51¡sup¿st¡/sup¿ International Congress and Exposition on Noise Control Engineering, Internoise 2022 ; Conference date: 21-08-2022 Through 24-08-2022.

[15] P. Libianchi, E. Shabalina, M. Kelly, J. Brunskog, and F. Agerkvist, “Sensitivity of the predicted acoustic pressure field to the wind and temperature profiles in a conventionally neutral boundary layer,” 2023. Under review.

[16] M. van der Laan, M. Kelly, and M. Baungaard, “A pressure-driven atmospheric boundary layer model satisfying rossby and reynolds number similarity,” *Wind Energy Science*, vol. 6, no. 3, pp. 777–790, 2021.

[17] R. B. Stull, *An Introduction to Boundary Layer Meteorology*. Dordrecht: Springer Netherlands, 1988.

[18] D. K. Wilson, “Outdoor sound propagation calculator,” 2015. In: V. E. Ostashev and D. K. Wilson, Acoustics in Moving Inhomogeneous Media (second edition), Taylor & Francis.

[19] D. K. Wilson, “Relaxation-matched modeling of propagation through porous media, including fractal pore structure,” *Journal of the Acoustical Society of America*, vol. 94, no. 2, pp. 1136–1145, 1993.

[20] S. Liu and X. Z. Liang, “Observed diurnal cycle climatology of planetary boundary layer height,” *Journal of Climate*, vol. 23, no. 21, pp. 5790–5809, 2010.

[21] R. J. Allemang, “The modal assurance criterion - twenty years of use and abuse,” *Sound and Vibration*, vol. 37, pp. 14–23, AUG 2003.

[22] P. Libianchi, J. Brunskog, F. Agerkvist, and E. Shabalina, “Active noise control at low frequencies for outdoor live music events using the conjugate gradient least square method,” *Applied Acoustics*, vol. 205, 2023.

Technical note F

A preliminary study for the use of a surrogate model in outdoor sound propagation and sound speed profile recovery

Pierangelo Libianchi[1,2] and Xenofon Karakonstantis[1]

[1]**Department of Electrical and Photonics Engineering, Technical University of Denmark, Ørsted Plads, DK-2400 Kgs. Lyngby, Denmark**
[2]**d&b audiotechnik GmbH & Co. KG, Eugen-Adolff-Straße 134, 71522 Backnang, Germany**

ABSTRACT

Obtaining acoustic transfer functions between the loudspeakers and a controlled area in outdoor environments is a tedious task, subject to many uncertainties. The speed of sound is a parameter which encompasses many of these uncertainties and often obtaining functions of acoustic significance amounts to procuring first, accurate estimates of this velocity. This report focuses on the relevance to acoustic applications where surrogate models based on neural networks have high potential for lowering the cost of computing. This report presents preliminary results obtained adapting a method first proposed in seismology with the aim of recovering velocity profiles to be used for outdoor sound propagation. The aim of this work is to adapt the original method but considering medium properties characteristic of propagation in air. A surrogate physics-informed neural network is developed to model the solution to the Helmholtz equation by first solving the forward problem of estimating the sound pressure in a prescribed medium and furthermore solve the inverse problem of estimating the sound speed profile in a inhomogeneous medium. The predictions of the pressure field in free field conditions look promising. However, the results obtained with more complex boundary conditions and the recovery of the sound speed profile are still far from the ground truth and more work is needed before this method can be considered as an alternative to traditional sound propagation models.

Keywords: PINN, Siren, Neural waveform inversion, outdoor sound propagation, sound speed profile

1 INTRODUCTION

With the advent of "physics-informed neural networks" (PINN) [1] new prospects in machine learning have surfaced, with respect to physical systems. A variety of physical problems are now being solved with surrogate neural networks, adhering to the constraints of the problem at hand. This approach can alleviate many of the pitfalls of classical numerical solutions of partial differential equations (PDEs), such as meshing complexity, inference time and epistemic uncertainty. Furthermore, these models can be used in the context of inverse problems. Even though they do not require data to learn the function space of PDEs, they can be fit against measured data to recover an unknown quantity. Such is the goal of this study, which is quite ambitious but if successful could mean significant step forward for outdoor sound propagation models in real time application scenarios.

The goal of this study is first to introduce this approach, then tackle the forward problem of simulating sound propagation through a moving inhomogeneous medium and then finally address the inverse problem of recovering properties of the medium such as the effective speed of sound from pressure measurements on the ground. This is a preliminary study that looks into adapting the technique previously used for seismology and described in [2].

Section 2 introduces the formulation of a cost function that includes the partial differential equation governing a given problem to train a neural network, hence providing knowledge of the problem. This generic approach is then applied to solve the Helmholtz equation and in a second step combined with measured data so that it can be used to infer the properties of the medium that generated said data. In Section 3, the report describes how the numerical experiments were performed with the surrogate model and the results are then presented in Section 4. The surrogate model is tested for free-field conditions first, with promising results, and then later with a more complex and realistic ground impedance boundary condition, which instead show a poor match when compared to reference solutions generated in Comsol Multiphysics. The surrogate model is then used to recover the underlying sound speed profile after providing it with measured/simulated pressure data showing that further work is required for the development of this method. These results are discussed in more detail in Section 5. Finally, Section 6 presents the conclusions drawn at the end of this preliminary study and discusses perspectives for the future.

2 THEORY

As the goal is to obtain a surrogate model that solves the Helmholtz equation and subsequently, recovers the sound speed profile for given measurements, this section aims to derive the equations that lead to these estimates.

2.1 Surrogate neural networks for solving sartial differential equations

Scientific machine learning has led to breakthroughs in surrogate models numerically approximating strenuous partial differential equations (PDEs). These surrogate models are usually a heuristically determined neural network architecture (for an example see Fig. 1). They receive a single Cartesian coordinate $\mathbf{r} = \{x, y\}$ as an input, and return the value of the function $\Phi(\mathbf{r})$ that approximates the PDE at the coordinate in a predetermined domain Ω_m. These neural networks are trained to fit the forward problem so that

$$\begin{aligned} \text{find } \Phi(\mathbf{r}) \quad & \text{s.t. } \mathscr{C}_m(\mathbf{a}(\mathbf{r}), \Phi(\mathbf{r}), \nabla\Phi(\mathbf{r}), \ldots) = 0, \\ & \forall\, \mathbf{r} \in \Omega_m, m = 1, \ldots, M, \end{aligned} \tag{1}$$

where $\mathscr{C}_m$ refers to a set of M constraints, most times in the form of the PDEs themselves. In practice, these surrogate models are simply multi-layer perceptrons (MLPs) trained with a variant of the stochastic gradient descent algorithm [1].

In a continuous space, an acoustic source can be considered as a region in the medium over which new acoustic energy is generated, in the form of a spherical wave or point source. The corresponding field in a boundless medium can be described by

$$\nabla^2 g_k(\mathbf{r} \mid \mathbf{r}_0) + k^2 g_k(\mathbf{r} \mid \mathbf{r}_0) = -\delta(\mathbf{r} - \mathbf{r}_0)\ , \tag{2}$$

where $\mathbf{r}_0$ and $\mathbf{r}$ refers to the position of the source and the positions where the sound field is evaluated respectively, $k = \frac{\omega}{c}$ is the wavenumber prescribed to the sound field and $\delta(\mathbf{r} - \mathbf{r}_0)$ is the dirac delta function. $g_k(\mathbf{r} \mid \mathbf{r}_0)$ is the Green's function.

The Green's function is the particular solution to Eq. (2) and in 2D space is given by

$$g_k(\mathbf{r}, \mathbf{r}_0) = -\frac{i}{4} H_0^{(1)}(k|\mathbf{r} - \mathbf{r}_0|), \tag{3}$$

where $H_0^{(1)}$ is a Hankel function. If the medium is bounded by surfaces, the most general solution $G_k(\mathbf{r})$ is given by the superposition of $g_k(\mathbf{r}, \mathbf{r}_0)$ and any solution $p(\mathbf{r})$ of the homogeneous Helmholtz equation $\nabla^2 p(\mathbf{r}) + k^2 p(\mathbf{r}) = 0$ [3]:

$$G_k(\mathbf{r} \mid \mathbf{r}_0) = g_k(\mathbf{r} \mid \mathbf{r}_0) + p(\mathbf{r}). \tag{4}$$

If the field is unbounded, in the limit to infinity the sound field must abide to the Sommerfeld radiation condition given by,

$$\lim_{\|\mathbf{r}-\mathbf{r}_0\| \to \infty} \|\mathbf{r} - \mathbf{r}_0\|^{\frac{D-1}{2}} \left(\frac{\partial}{\partial \|\mathbf{r} - m\mathbf{r}_0\|} p(\mathbf{r}) - jkp(\mathbf{r}) \right) = 0 \tag{5}$$

where D denotes the dimensions of the problem, which in this case is 2, so that the far pressure field is approximately locally plane. This condition ensures that there are only outgoing waves.

The surrogate model must fulfil Eqs. (2) and (4) and in most circumstances, also abide by the conditions given by Eq. (5) if free field propagation is to be assumed. This leads to

$$(\nabla^2 + k^2)\Phi(\mathbf{r}) = -G_k(\mathbf{r} \mid \mathbf{r}_0) \tag{6}$$

2.2 Boundary conditions

2.2.1 Perfectly matched layers

The Helmholtz equation has as a general solution both an outgoing and an incoming wave. Numerical methods solve differential equations in a finite domain which introduces spurious reflections. To achieve an accurate solution for free-field conditions, appropriate boundary conditions need to be defined. Eq. (5) cannot be used in this case since it is defined at infinity. A common way to deal with this problem is to use a perfectly matched layer (PML) [4]. A PML consists of an artificial absorbing layer placed around the computational domain to avoid spurious reflections from its edges by attenuating the outgoing waves and thus simulating open boundaries. In this work, the PML is implemented using a modified Helmholtz equation

$$\frac{\partial}{\partial x}\left(\frac{e_y}{e_x}\frac{\partial\Phi(\mathbf{r})}{\partial x}\right)+\frac{\partial}{\partial y}\left(\frac{e_x}{e_y}\frac{\partial\Phi(\mathbf{r})}{\partial y}\right)+e_xe_yk^2\Phi(\mathbf{r})=-G_k\left(\mathbf{r}\mid\mathbf{r}_0\right)\ , \tag{7}$$

where $\mathbf{r}=(x,y)\in\Omega, e_{r_i}=1-j\frac{\sigma_{r_i}}{\omega}, k=\omega/c$, and

$$\sigma_{r_i}=\begin{cases} a_0\omega\left(\frac{l_{r_i}}{L_{\mathrm{PML}}}\right)^2 & r_i\in\partial\Omega \\ 0 \text{ else} \end{cases} \tag{8}$$

where a_0 is the absorption coefficient, l_i is the position within the PML and L_{PML} is the extent of the PML region. Notice that outside the PML region, hence within the domain of interest, Eq. (7) reduces to the traditional Helmholtz equation.

2.2.2 Impedance condition

Alternatively, in this work, we also investigate the approximation of the radiation condition from Eq. (5) through a ρc-condition:

$$u_{\mathbf{n}}(\mathbf{r}_b)-\frac{p(\mathbf{r}_b)}{\rho c}=0 \tag{9}$$

where $u_{\mathbf{n}}(\mathbf{r}_b)$ refers to the normal component of the particle velocity at the boundary $\mathbf{r}_b$ of the domain.

Finally, in this work we also investigate the effect of the ground on sound propagation, assuming it to be locally reacting by using an impedance boundary condition:

$$u_n(\mathbf{r}_b)-\frac{p(\mathbf{r}_b)}{Z}=0 \tag{10}$$

where Z is the impedance of the ground.

3 NUMERICAL EXPERIMENTS

In this work, we study the use of a neural network to provide the surrogate model $\Phi(\mathbf{r})$ from Eq. (6). The surrogate model is used here to first solve the forward problem of predicting the sound pressure produced by an acoustic source. Secondly, the surrogate model is used to recover the sound speed profile using simulated pressure data. The two tasks used slightly different architecture and loss functions with different terms. The rest of this section describes the implementations for the two task and for the experiments undertaken with each of them.

3.1 Forward problem

In all the numerical experiments we used a fully connected network as depicted in Fig. 1. For the forward problem, the network had an input layer with 2 neurons, 3 hidden layers with 256 neurons (the figure only shows 10 of them for space reasons) and 2 neurons in the output layer. A summary of the parameters used for this problem can be found in Table 1 at the end of this section.

The input to the network are spatial coordinates $(x,y)\in\{[-25,25],[-25,25]\}$, normalised to be comprised in the interval $[-1,1]$. During training, the input is provided by drawing $(4\cdot\text{sidelength})^2$ samples from two uniform distribution in the aforementioned interval at each epoch. This input corresponds to Cartesian coordinates scaled appropriately for the neural network.

The three hidden layers use a sinusoidal activation function. Sinusoidal activation functions in neural network have shown promising results as universal approximators if initialised correctly [2]. Sinusoidal activations have been successful in modelling high frequency or periodic data, or data structures where higher order spatial derivatives are necessary, which other activation functions lack the capability to model. Benbarka et al. [5] provide more information on how fully connected networks with sinusoidal activation functions are equivalent to d-dimensional Fourier mappings, where the weights of the neurons correspond to a Fourier series.

The two neurons in the output layer have a linear activation function instead and return the real and imaginary part of the pressure at the point whose spatial coordinate have been provided at the input.

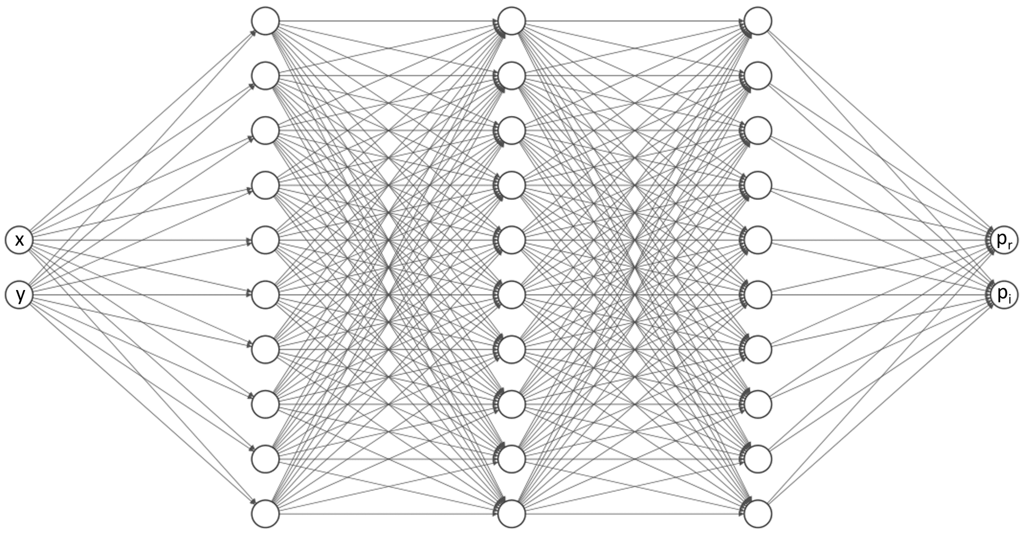

Figure 1. Architecture of the fully connected network used for the forward problem. The hidden layer show only 10 of 256 neurons for space reasons.

The cost function is what distinguishes PINN from traditional neural networks. Usually, the loss function used to train a network poses the objective of minimizing the residual between the prediction of the network and some target data. In PINN, the loss function is made up by the PDE for which the network has to model and the boundary conditions.

In this work, for the forward problem, we perform three experiments with three different cost functions:

1. Free field with PML:

$$\mathscr{L}(\mathbf{r},\theta) = \sum_{r_i \in \Omega} ||\mathscr{L}_{\text{PDE}}(\mathbf{r_i},\theta)||_2^2 \tag{11}$$

where in this case $\mathscr{L}_{\text{PDE}}$ is Eq. (7) and θ are parameters of the network (weights and biases).

2. Free field with ρc condition:

$$\mathscr{L}(\mathbf{r},\theta) = \sum_{r_i \in \Omega \setminus \partial\Omega} ||\mathscr{L}_{\text{PDE}}(\mathbf{r_i},\theta)||_2^2 + \sum_{r_i \in \partial\Omega} ||\mathscr{L}_{\text{BC}}(\mathbf{r_i},\theta)||_2^2 \tag{12}$$

where $\mathscr{L}_{\text{PDE}}$ corresponds to Eq. (2) and is applied only to the points inside the domain. The second term on the right hand side applies to the points on the boundaries of the domain and in this case $\mathscr{L}_{\text{BC}}$ corresponds to Eq. (9). Here we chose $c = 343$ m/s and $\rho = 1.2$ kg/m^3.

3. Propagation over ground:

$$\mathscr{L}(\mathbf{r},\theta) = \sum_{r_i \in \Omega \setminus \partial\Omega} ||\mathscr{L}_{\text{PDE}}(\mathbf{r_i},\theta)||_2^2 + \sum_{r_i \in \partial\Omega_{l,t,r}} ||\mathscr{L}_{\text{BC}_1}(\mathbf{r_i},\theta)||_2^2 + \sum_{r_i \in \partial\Omega_b} ||\mathscr{L}_{\text{BC}_2}(\mathbf{r_i},\theta)||_2^2 \tag{13}$$

where also in this case $\mathscr{L}_{\text{PDE}}$ is Eq. (2). $\mathscr{L}_{\text{BC}_1}$ still corresponds to Eq. (9) but is applied only to the left, top and right boundaries. $\mathscr{L}_{\text{BC}_2}$ is applied to the points on the bottom boundary and corresponds to Eq. (10) to

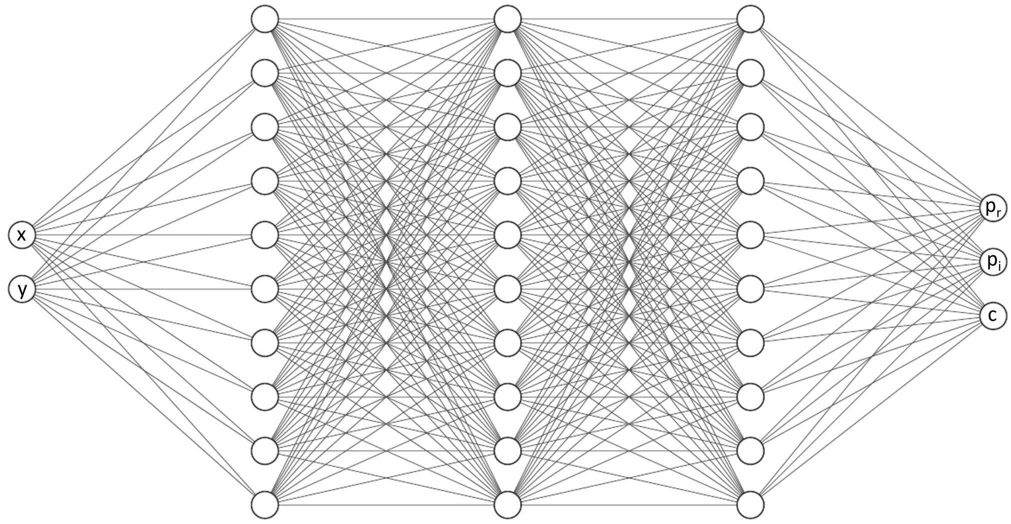

Figure 2. Architecture of the fully connected network used for the inverse problem

include the effect introduced by a grass covered ground with characteristics impedance $Z_{\text{char}} = 21 + 21i$ at 80 Hz.

The inhomogeneous term in Eq. (4) in all cases is modelled as a spatial Gaussian pulse excitation, meant to approximate the Dirac delta function of Eq. (2), and is placed at the center of the domain $(x_0, y_0) = \{0, 0\}$.

In all the experiments solving the forward problem, the medium was assumed to be homogeneous with the value of the wavenumber k fixed and given by $\omega = 2\pi f$ with $f = 80$ Hz and $c = 343$ m/s. A position dependent profile could have been used for the speed of sound but we focused on the boundary conditions and a homogeneous medium for the experiments undertaken for the forward problem.

For each numerical experiment, we set the same network hyperparameters. We use the Adam [6] algorithm for gradient descent with the default coefficients for the gradient moments (e.g. $[\beta_1, \beta_2] = [0.9, 0.999]$) and a learning rate of 0.00002. The sinusoidal activation functions are initialised according to Sitzmann et al. [2].

Table 1. Summary of the parameters used for the forward problem

Parameter	Value	Unit
f	80	Hz
a_0	5	
L_{PML}	12.5	m
Z_{char}	21+21i	
ρ	1.2	kg/m^3
c	343	m/s
x_0	0	m
y_0	0	m

3.2 Inverse problem

The surrogate model can be used also to solve the inverse problem of recovering properties of the medium such as the speed of sound [2] from pressure data that in this case has been simulated in Comsol but it could also come from measurements. For this task, both the architecture of the network and the cost function had to be modified. Fig. 2 shows the architecture of the network used for the inverse problem. For this task, the network has an additional output for the speed of sound c since it needs to be predicted by the surrogate model. A summary of the parameters used for this network can be found in Table 2 at the end of this section.

The cost function used for the inverse problem is

$$\mathscr{L}(\mathbf{r},\theta) = \sum_{\mathbf{r}_i \in \Omega} ||\mathscr{L}_{\text{PDE}}(\mathbf{r}_i,\theta)||_2^2 + \lambda \sum_{j=1}^{N} ||\mathscr{L}_{\text{data}}(\mathbf{r}_j,\theta)||_2^2 \tag{14}$$

where $\mathscr{L}_{PDE}$ corresponds to Eq. (7), λ is a weight used to balance the influence on the cost function of the PDE and the data term $\mathscr{L}_{data}$ is evaluated over N samples of either pressure or speed of sound as it will be explained in the rest of this section.

Since now c is predicted by the network and not fixed by the user in the cost function, the network needs to be pretrained to learn its value. The inversion routine then consists of two separate steps:

1. Pretraining: The surrogate model needs to be trained over an arbitrary medium, possibly resembling the one to be recovered to improve convergence and accuracy. In this step, the data term in Eq. (14) is

$$\mathscr{L}_{\text{data}}(\mathbf{r}_j,\theta) = \hat{c}(\mathbf{r}_j,\theta) - c(\mathbf{r}_j) \tag{15}$$

   where $\hat{c}$ is the network prediction, c is the speed of sound of the arbitrary medium and N is the number of samples in the batch. In this step the data term is used to minimize the residual between the speed of sound predicted by the network and the speed of sound pf the arbitrary medium so the network can learn its value. For this part of the routine, the acoustic source was placed at $(x_0,y_0) = \{-8.7,0\}$ m to increase the propagation distance between the source and the edge of the PML and more easily show the effects of the medium on the sound field.

2. Inversion: The surrogate model is used to recover the speed of sound in the medium of the target field. In this case, the data term is

$$\mathscr{L}_{\text{data}}(\mathbf{r}_j,\theta) = \hat{p}(\mathbf{r}_j,\theta) - p(\mathbf{r}_j) \tag{16}$$

   where $\hat{p}$ is the complex pressure predicted from the network, p is the complex pressure from the target field and N is the number of samples. The data term is now applied as a pressure matching term. In this way the network minimizes the residual between the prediction of the surrogate model and the target field. The speed of sound is now free from the data constraint and is updated during the minimization of the $\mathscr{L}_{PDE}$ term in the cost function.

   In this case the network was trained over five sound fields produced by acoustic sources in five different positions $(x_0,y_0) = \{-8.7,[-8.7,-4.3,0,4.3,8.7]\}$ m. This was done to improve the reconstruction of the medium during the inversion as described in [2].

The speed of sound and pressure samples used in the two steps of the inversion routine are obtained from the target field from Comsol using a latin hypercube sampling strategy.

Finally, we tried different values of the weight λ in Eq. (14) applied to the data term to study its effect on the accuracy of the solution.

Table 2. Summary of the parameters used for the inverse problem.

Parameter	Value	Unit
f	80	Hz
a_0	5	
L_{PML}	12.5	m
ρ	1.2	kg/m^3
x_0	-8.7	m
y_0	-8.7, -4.3, 0, 4.3, 8.7	m
N	30, 60	

4 RESULTS

In this section we present the predictions made by the surrogate model using different boundary conditions and for the recovery of the sound speed profile. We compare such predictions with the target fields obtained using the FEM in Comsol to validate them.

4.1 Forward problem

This section describes the problem of modelling a point source in a homogeneous medium for various boundary conditions. As previously stated, boundary conditions corresponding to ρc condition, Eq. (9), were examined, as well as a PML, Eq. (7), and further combined with a nominal ground impedance Eq. (10). All three results in this section show a phase offset due to the initial phase applied to the acoustic source.

Fig. 3 shows the comparison between the prediction made by the surrogate model against the ground truth from Comsol for the first setup where free-field radiation is modelled through the use of a PML. In this case the surrogate model generates an accurate description of the sound field that closely matches the target field from Comsol.

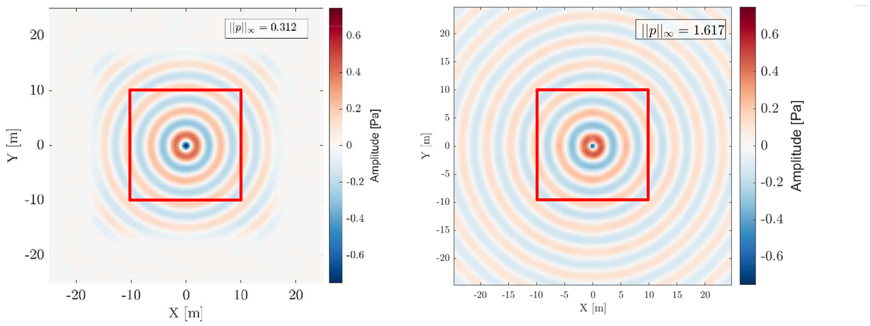

Figure 3. Real part of the pressure field using a PML as predicted by the surrogate model (left) and the target from Comsol (right). The red frame marks the edges of the region under comparison.

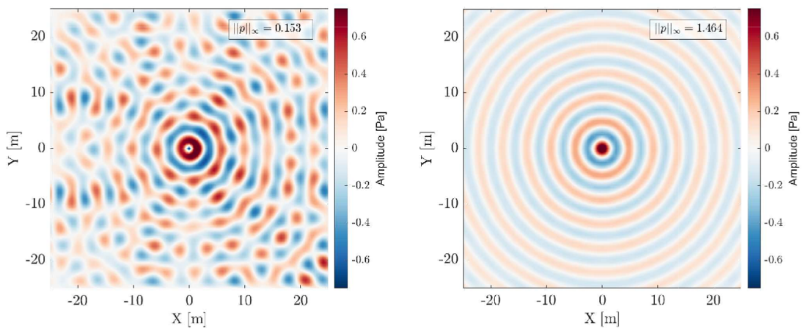

Figure 4. Real part of the pressure field using the ρc condition (left) and the target field with the same boundary condition from Comsol (right).

Fig. 4 displays the pressure field predicted by the surrogate model when applying the ρc condition. The surrogate model generates artefacts when fitting the values at the boundaries which interferes with the solution within the domain. Note that a ρc boundary condition is known to cause reflections when the incidence angle is not in the normal direction of the boundary. However, we can see from the Comsol model in the right figure that in this case this is not a large problem. The artifact reflections seen in the surrogate model on the left figure is due to other reasons. Possibly this would need heuristic tuning of loss terms for the network to properly learn the correct pressure.

As an extension, Fig. 5 displays the results when applying the ρc condition to the left, right and top boundaries, and the nominal ground impedance to the bottom boundary. Here we can see that the network is

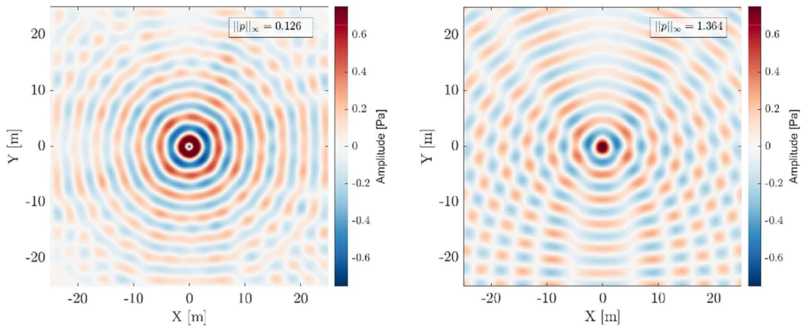

Figure 5. Real part of the pressure fields using the ρc condition with the addition of impedance condition applied to the bottom boundary (left) and target from Comsol (right).

estimating a more realistic version of the pressure as well as estimating reflections from the ground. Although we do not expect the network output to be identical to the numerical simulation on the right of Fig. 5, as the values of impedance applied are slightly different, we can see that the network is somewhat closer in approximating higher order reflections in this manner.

In summary, we can conclude that the surrogate model is most accurate at approximating a radiation source when using a PML. This motivated the choice of experiments in the following sections, where only the case with a PML has been considered. It seems as if the surrogate model has problems handling sharp shifts in the medium, such as an impedance boundary. This limitation will be evident also in the next section when dealing with a discontinuous medium.

4.2 Inverse problem

In this section we show the results of the two steps involved in the inversion problem, the pretraining and the inversion itself. The section is further split in two parts: in the first we analyze the results where the medium used for the pretraining is homogeneous and it differs from the medium in the target field; in the second, we pretrain the network using a medium that resembles the medium in the target field but not exactly. In traditional full-waveform inversion, the initial guess for the medium should somewhat resemble the one in the target field to avoid being stuck in a local minimum and cycle skipping [7]. All the plots of the sound fields have been normalised to the corresponding maximum to show the same scale.

The metric used to compare the predictions and the target field are the following:

$$\mathrm{MAC} = \frac{|\hat{\mathbf{y}}^H \mathbf{y}|^2}{(\hat{\mathbf{y}}^H \hat{\mathbf{y}})(\mathbf{y}^H \mathbf{y})} \tag{17}$$

$$\mathrm{NMSE} = \frac{1}{N} \sum_{n=1}^{N} \frac{(\hat{y_n} - y_n)^2}{y_n^2} \tag{18}$$

Where y denotes the target field variable and $\hat{y}$ the predicted variable. The MAC has only been used for the pressure field while NMSE for both the pressure field and the speed of sound.

4.2.1 Homogeneous pretraining

The medium used for the pretraining of the network in this section is shown in Fig. 6b. We used a medium with a speed of sound of 343 m/s which is the value most often used in acoustic problems. In all the cases analyzed in this section, this value was used to constrain the speed of sound during the pretraining of the network. The pressure field obtained at the end of the pretraining phase is shown in Fig. 6a. The source has been moved to the left so that the acoustic waves can travel a larger distance before reaching the PML. A longer propagation distance allows to detect the effects of an inhomogeneous medium more easily. The results obtained here are in line with the results from the previous section when a PML was also used. The sound field matches our expectations, circular wavefronts with the correct wavelength and with a gradually decreasing amplitude. These results also match the simulations from Comsol, even if they are not shown here, except for a magnitude offset as in the previous section.

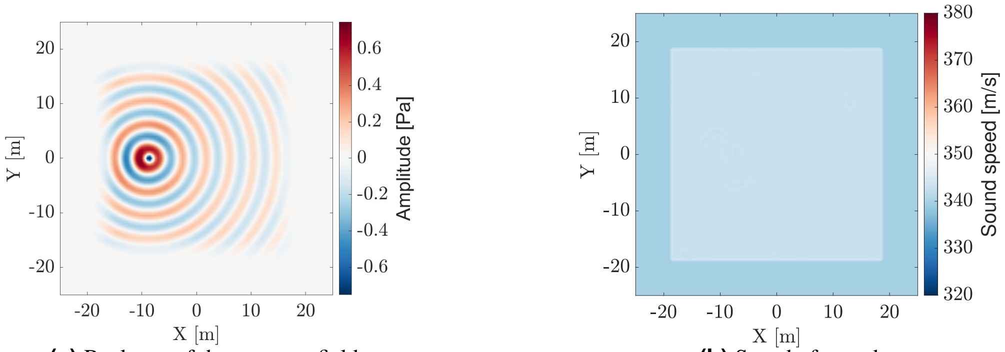

(a) Real part of the pressure field **(b)** Speed of sound

Figure 6. Output of the surrogate model after pretraining with a homogeneous medium.

This model has then been used as the starting point for the inversion phase. We have performed different numerical experiments varying the number of samples used for the data term and applying different scaling to the samples. The results of the inversion are shown in Fig. 7 and 8, for the real part of the pressure field and the speed of sound, respectively. For this experiment we used 60 samples from the target field and applied different weights to the data term. Here we show only the results with the weights λ in Eq. (14) equal to 1 and 10, as larger weights led to much worse performance. The sound fields obtained from the network show an interference pattern as one would expect from a discontinuity in the medium. However, this pattern is different from the one found in the target field where interferences occur in different locations and one can see a change in wavelength where the discontinuity occurs.

In addition, there is also an amplitude difference between the predicted and the target fields. For $\lambda = 1$, the maximum predicted pressure magnitude is 0.69 Pa versus 1.13 Pa for $\lambda = 10$ and 1.51 Pa in the target field. Furthermore, the amplitude of the pressure field decreases more slowly with distance than it should when using the smaller of the two weights. The larger of the two weights provides better predictions hinting that the optimal weight in this case lies around 10. This value gives enough weight to the data term in the loss function without overfitting the data.

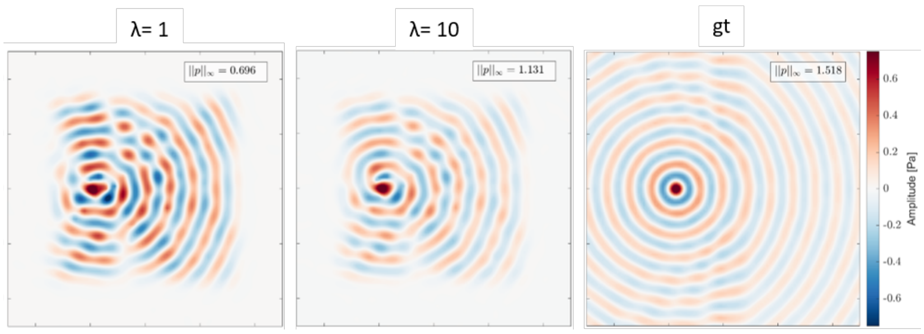

Figure 7. Real part of the pressure field after the full-waveform inversion with a vertical strip perturbation. Each column shows the solution for different weights λ applied to the data term in the loss function. Right column: target field from Comsol.

We proceeded with the full-waveform inversion routine after pretraining the network with a homogeneous speed of sound of 343 m/s. The pressure data used for the inversion was obtained from the field shown on right plot in Fig. 7 corresponding to the speed of sound field on the right of Fig. 8. The speed of sound profile recovered after the inversion is also shown in Fig. 8. The surrogate model fails to recover the speed of sound discontinuity and its correct amplitude. The network does introduce inhomogeneities in the medium, but they are distributed along the wavefronts. This could be a hint that the PDE term dominates the loss function. Further proof of it is that the wavefronts are more blurred with larger weights even though values of 100 or larger produced worse results. Thus, also for the inversion, the optimal weight lies close to 10 or between 10 and 100.

The pretrain medium and the target field might have been too different for the network to be able to recover the latter. This is further investigated in Section 4.2.2.

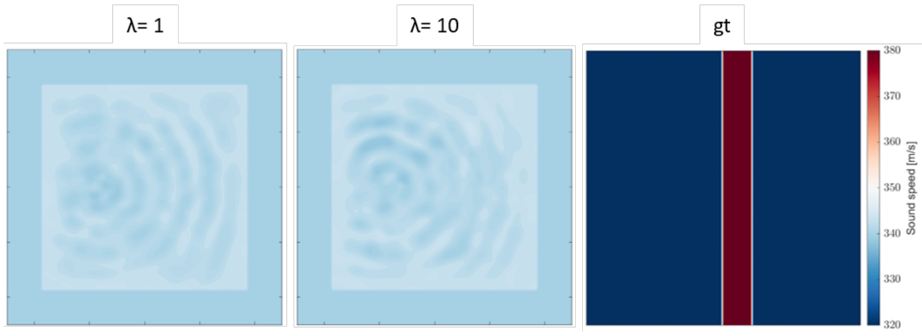

Figure 8. Speed of sound after the full-waveform inversion with a vertical strip perturbation. Each column shows the solution for different weights λ applied to the data term in the loss function. Right column: target field from Comsol.

Fig. 9 presents the convergence plots corresponding to the data term alone and to the full loss function. The data term is only relevant at the beginning of training since it makes very small contributions to the total loss after convergence. So, the data term provides an initialisation, steering the weight in a direction that minimizes the data residual but after that, only the PDE term is relevant which could explain why the wavefronts can be seen in the medium. To improve the results, the pressure samples have also been scaled in the same way as the

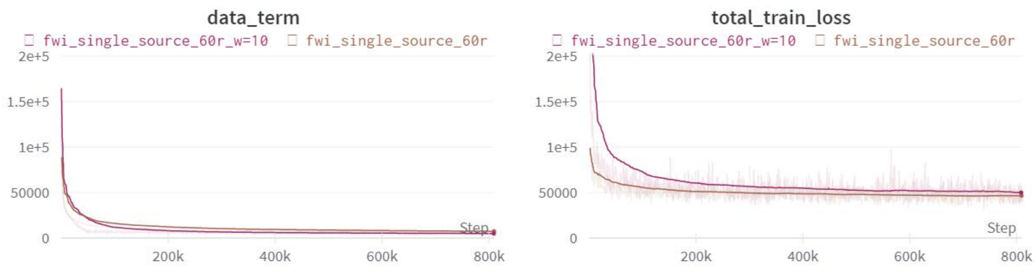

(a) Data term loss

(b) Total loss

Figure 9. Convergence plots for the inverse problem with homogeneous pretraining.

wavenumber since it is the eigenvalue of the Helmholtz equation. The results of this scaling using both 30 and 60 samples are shown in Fig. 10 in terms of their MAC and NMSE and compared with the previous experiments where the data was not scaled. This scaling actually gives worse performances according to both metrics. In these two cases, the increase of λ led to worse results in contrast with the case where the samples had not been scaled. The drop in performance is only apparent when looking at the sound field. The error related to the speed of sound is not affected by the scaling as it can be seen in Fig. 11. Other scaling strategies have been tested but only with even worse results.

4.2.2 Inhomogeneous pretraining

The first experiment has the same medium discontinuity analysed in the previous section but this time the network has been pretrained using a medium with a similar discontinuity. The width of the discontinuity in the pretraining was larger than in the target field and with slightly different values for the speed of sound, as it can be seen in Fig.

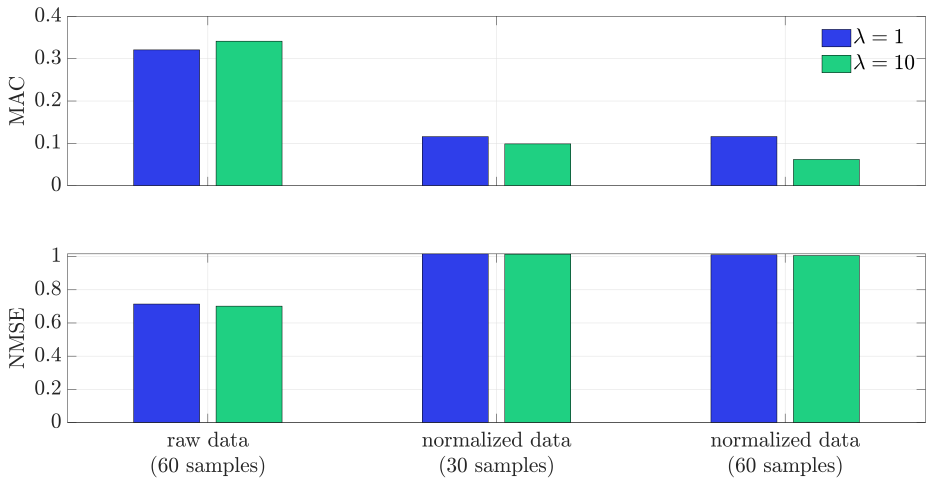

Figure 10. MAC and NMSE between the solutions from the surrogate model and Comsol for the different scaling and weighting of the data.

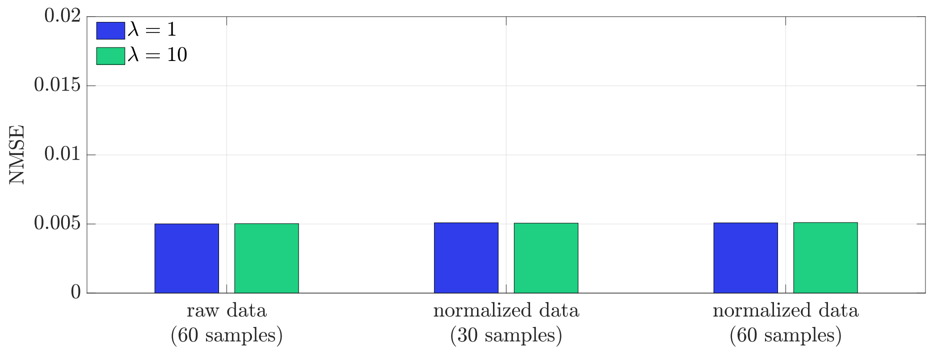

Figure 11. MAC and NMSE between the solutions from the surrogate model and Comsol for the different scaling and weights of the data.

12b. The sound field obtained after pretrain is shown in Fig. 12a and it can be seen how the surrogate model is able to resolve the sound field only on the left of the discontinuity, where the source is placed, and no propagation occurring within the discontinuity and beyond it. The discontinuity does not event results in reflections and interferences on the left side. The reason could lie in the PDE and how the problem has been formulated.

The homogeneous pretraining worked better because the Helmholtz equation is perfectly suited for such a scenario. When the discontinuity was introduced during the inversion step, the model was still able to return a continuous sound field because at the start of the inversion was already modelling the sound field over the entire domain. Also in this case the Helmholtz equation is not the best choice since when we start fitting the data the sound field is distorted and it does not resemble the target field. Given the poor results from the pretraining, any intent of solving the inverse problem was unsuccessful and the results have not been included here for clarity and brevity.

For the rest of the numerical experiments, the discontinuity in the medium has been replaced with smaller perturbations or smooth changes in the medium. The network has been pretrained using the profiles shown in Fig. 13 for a medium with a circular perturbation and a medium with a speed of sound increasing linearly with height (y). The former is a classical problem in acoustic when studying the scattering field introduced by a cylinder section on a plane and the latter is a common scenario in outdoor sound propagation with a stable atmospheric boundary layer. The gradient of the speed of sound is larger than what one would find in reality but it has been chosen so that refraction is noticeable even in a relatively small domain as the one under study here. The corresponding sound fields obtained from the pretraining are shown in Fig. 14. In this case the model can resolve the sound field over the entire domain. However, the surrogate model struggles to properly describe the sound fields. The circular perturbation (left) creates a shadow zone without the interferences from a scattered

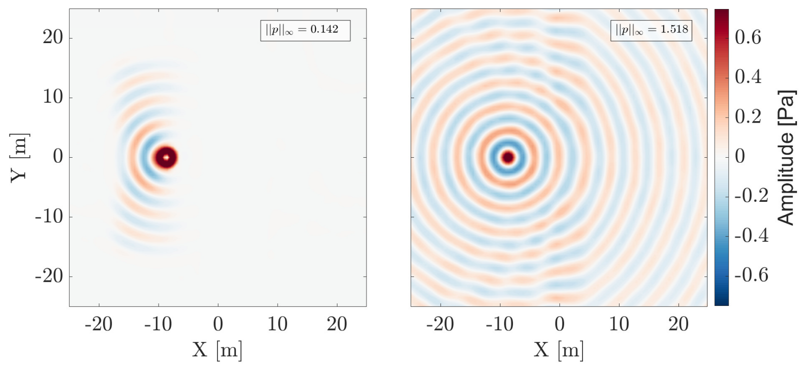

(a) Real part of the pressure field

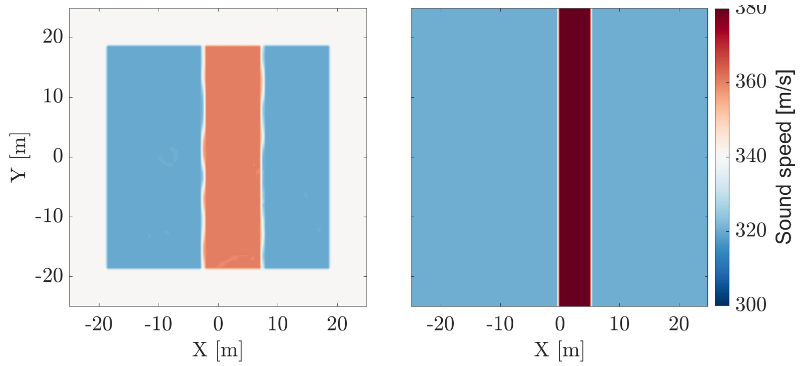

(b) Speed of sound

Figure 12. Comparison of the surrogate model after pretraining (left) with the target field from Comsol (right) using a strip perturbation.

sound field as one would expect. The linearly increasing speed of sound should introduce a lengthening of the wavelength in the direction of the increase but is nowhere to be seen in the results. Nonetheless, the models hold a description of the sound field over most of the domain and have been used to solve three different inversion problems.

In all three problems we used 60 samples from the target field. In the first problem we tried to recover a medium with a circular perturbation where the speed of sound increases from 300 m/s outside the perturbation to 380 m/s inside. The second problem is similar but instead of having a circular perturbation with sharp boundaries we used a narrow gaussian pulse. The speed of sound is also 300 m/s over most of the domain except at the center where it increases to reach a maximum of 380 m/s. The model pretrained with the circular perturbation has been used in both cases to solve the inversion problem. Finally, for the third problem we tried to recover a medium with a linear increase in the speed of sound but with a sharper gradient than the one used during pretraining. The model pretrained with the linearly increasing speed of sound has been used for this last inversion problem.

The sound fields obtained by the networks for the three problems and different weighting of the data term are shown in Fig. 15 and compared with the corresponding target field. In none of the cases the correct shape of the sound fields is recovered. In general, the wavefronts are distorted and increasing weights seems to make the reconstruction of the sound field harder. In the first two cases, i.e., the ones using perturbation, the shadow zone from pretraining is lost and new interference patterns are introduced. The case with the smaller weights has some of the interferences showing in the right directions but others are missing and the shadow zone is blurred. Larger weights provide an improvement in this sense and a maximum amplitude closer to the target field in a similar way to those we saw when using the homogeneous pretraining in the previous section. On the other hand, the wavefronts are more and more distorted as we increase the weights even though the regions where interference occurs are still visible. The fact that the sound field from pretraining provided a closer match to the target field than the sound fields after inversion might hint that the samples should have been scaled in a different way. Regarding the choice of the weights, a value between 1 and 100 should provide the best compromise between

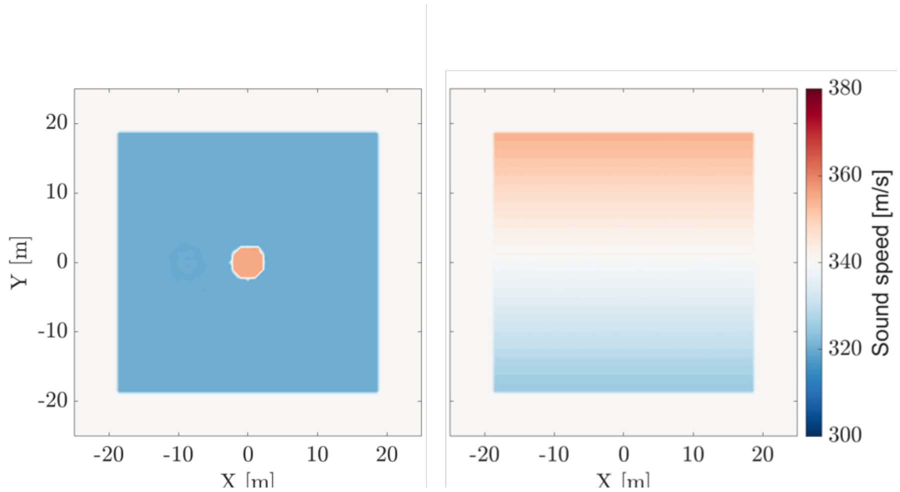

Figure 13. Speed of sound from the surrogate model after pretraining with a circular perturbation (left) and a linearly increasing speed of sound (right).

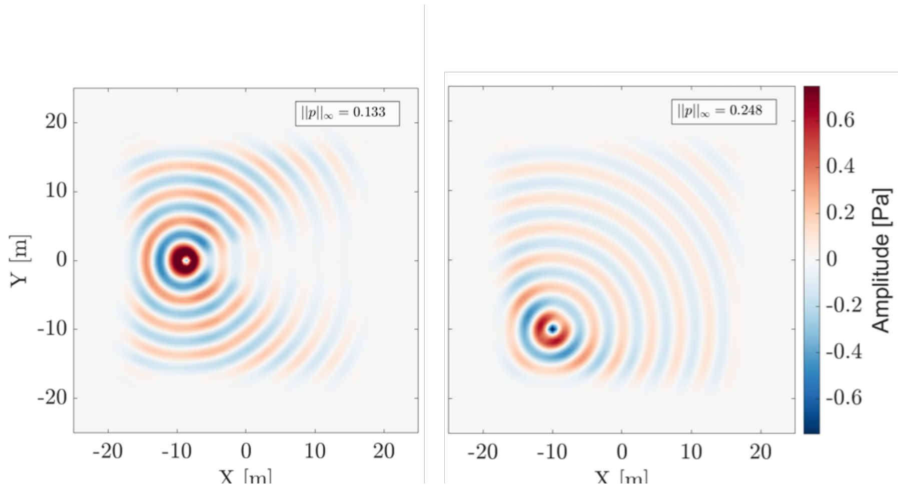

Figure 14. Real part of the pressure field from the surrogate model after pretraining using a circular perturbation (left) and a linearly increasing speed of sound (right).

reconstruction of the field and correct amplitude and rate of decay. This is consistent with the findings of the inversion with homogeneous pretraining from Section 4.2.1.

Similar conclusions can be drawn for the linearly increasing speed of sound case. Increasing weights introduce progressively larger distortion of the wavefronts. In every case, the sound field close to the source is largely distorted. The smaller weight seems to provide the best match even though is still far from correctly modelling the target field. The amplitude of the sound field and its rate of decay are different from the target field, the lengthening of the wavelength is absent and there are interferences that should not occur at all in this case.

The sound speed profiles recovered after inversion are plotted in Fig. 16. For the two cases with perturbation, we can see that with the smallest weight the network recovers an almost homogeneous medium and the perturbation that was present in the pretraining is lost. For $\lambda = 100$ we get the closest match with the target field. The network recovers a perturbation at the centre of the domain but with the wrong amplitude and further introduces new perturbations where the source is placed and where some of the samples are located. For $\lambda = 1000$ the medium shows wavefronts and large speed of sounds where the samples were located. With this weight, the network fits the data at the beginning of training, fixing the speed of sound and pressure at the position of the samples. Afterwards, the data term is not relevant anymore and the PDE term takes over. The bad balance between these two terms is probably the cause of these artefacts and wrongly placed perturbations. The

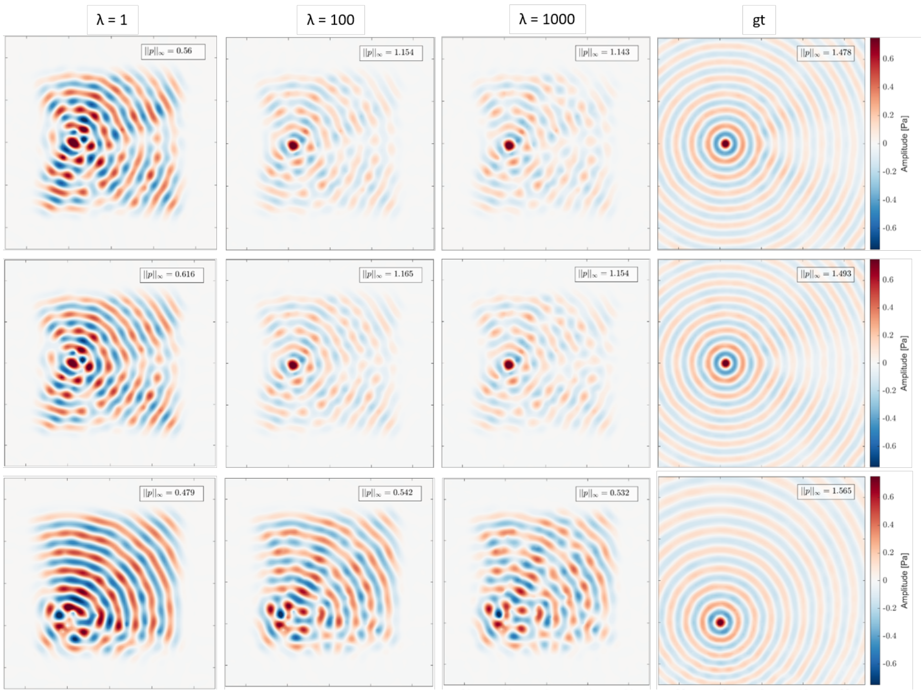

Figure 15. Real part of the pressure field after the full-waveform inversion. Top row: circular perturbation; mid row: gaussian perturbation; bottom row: linearly increasing speed of sound. Each column shows the solution for different weights λ applied to the data term in the loss function. Right column: target field from Comsol.

convergence plots in Fig. 17 confirms that the data term is only relevant at the beginning. Also in this case, a weight between 1 and 100 could provide the best balance between the PDE term and the data term.

In terms of MAC, the case with linearly increasing speed of sound provides the worst reconstruction with a value of 0.5 in the best case against 0.55 and 0.58 obtained with the circular and gaussian perturbation, respectively. However, it also shows the lowest NMSE which hints to a closer match in amplitude.

The medium with the linearly increasing speed of sound shows the lowest reconstruction error in terms of NMSE. The lowest NMSE in this case is approximately 0.004 against 0.0065 and 0.007 for the circular and gaussian perturbation, respectively. The reconstructed medium is blurred by the wavefronts introduced by the network, but the linearly increasing speed of sound is still visible underneath them. The circular and gaussian perturbation are not recovered at all and medium inhomogeneities are distributed across the domain. The different weights affect the accuracy of the reconstruction in these last two cases. The case of the linearly increasing speed of sound is unaffected. The reason for this is not clear at the time of writing.

The conclusions drawn from the previous results are tightly summarized in Figs. 18 and 19 for the pressure field and the speed of sound, respectively. These histograms show that larger weights lead to worst reconstruction of the sound field both in terms of MAC and NMSE. The problem with the gaussian pulse type perturbation gives in general the best results while the linearly increasing speed of sound provides the worst. When it comes to the speed of sound, $\lambda = 100$ provides the lowest NMSE values and $\lambda = 1$ the worst, which is consistent with what was shown in the medium and pressure field plots presented above. The different weights applied to the data term do not affect the NMSE of the speed of sound in the case of the linearly increasing speed of sound.

5 DISCUSSION

In [2] the results provided by the surrogate model are better than what found here even though also that case found a mismatch between the amplitude of the predicted pressure field and the target field.

In terms of the forward problem, the predicted pressure field matched quite well the target field from Comsol when using a PML. The impedance condition used to simulate the ground also bears some resemblance to the corresponding field simulated in Comsol even though further work is required to improve the results. The ρc condition would extend the physical domain significantly when compared to the PML. However, the pressure

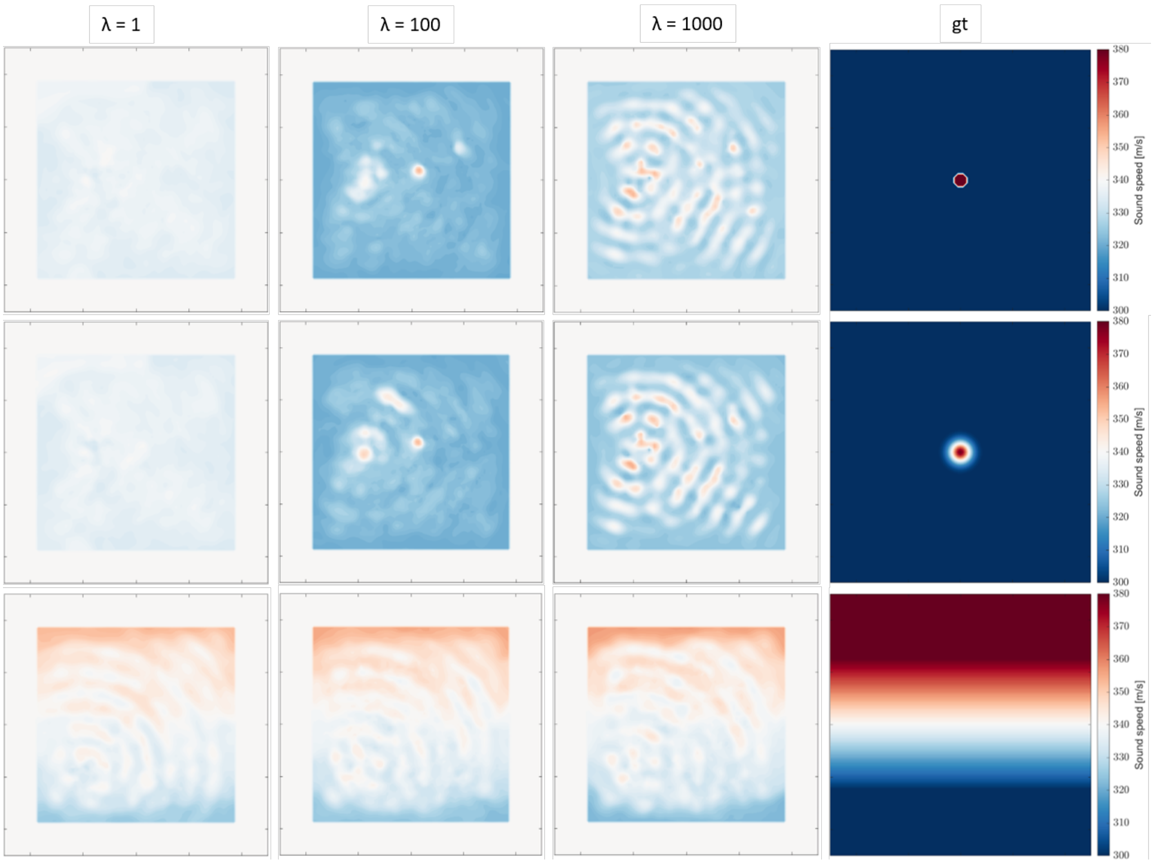

Figure 16. Speed of sound after the full-waveform inversion. Top row: circular perturbation; mid row: gaussian perturbation; bottom row: linearly increasing speed of sound. Each column shows the solution for different weights λ applied to the data term in the loss function. Right column: target field from Comsol.

field predicted with these conditions does not match the results obtained with the PML and in general the sound field characteristic of free-field conditions. Hence, the choice of the PML over the radiation conditions is a justified one.

The mismatch between the recovered sound field and medium in the inverse problem can be possibly related to a sub-optimal scaling of the samples from the target field and a loss of relevance of the data term in the loss function as the number of iterations increase. Also, different normalization strategies could be investigated. Further research should be performed to find a more suitable scaling of the pressure samples. It seems that the method is quite sensitive to the choice of the parameters. However, more experience with training of neural networks than the author had when doing this work will be required to further develop this type of network for application under study.

The computational time required by the two approaches has not been discussed for two main reasons:

- The two methods used different hardware due to the low-level implementation of the software and libraries used.
- The way the two methods work. The FEM, like other traditional numerical methods, needs to compute the solution over all the computational nodes in the domain. On the other hand, the surrogate model is grid-less and only predicting the pressure at the queried points. This means that the two methods would scale quite differently when the size of the domain increases. The application to outdoor sound propagation involves propagation distances of hundreds of meters which are too large to be dealt with the FEM and at least very demanding for other traditional methods. Furthermore, the possibility to compute the solution only at a few points is very enticing since, in most cases, one is interested in knowing the pressure at specific locations.

With this in mind, we still give some figures of the computational time. The training and pretraining of the

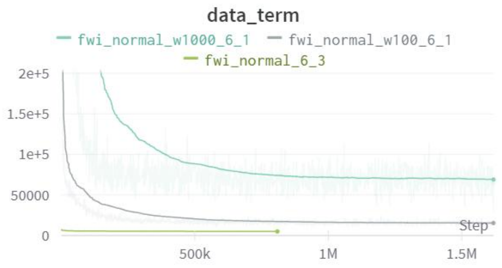

(a) Data term loss

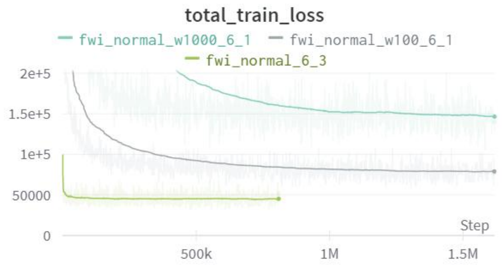

(b) Total loss

Figure 17. Convergence plots for the inverse problem with a gaussian pulse type perturbation and inhomogeneous pretraining for different weights.

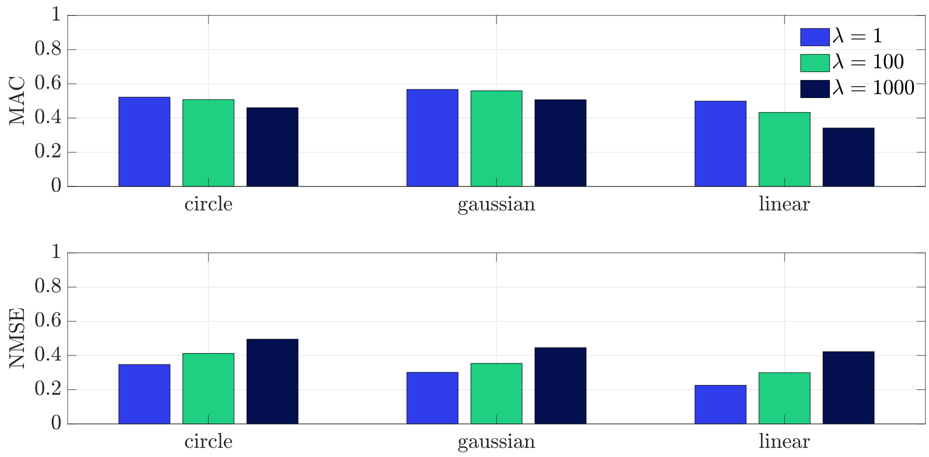

Figure 18. MAC and NMSE between the solutions from the surrogate model and Comsol for the different perturbations and weights.

network took approximately 20 hours and half of that for the inversion. After training, the network provided the sound pressure at approximately 10000 points in less than a second. The same task with the FEM took approximately 2 seconds.

More improvements could be achieved by iteratively updating the weight applied to the data term as proposed in [8]. Further work needs to be done for this approach to be considered as an alternative to more established methods such as traditional full waveform inversion. The aim is quite ambitious and it seems that more expertise on neural network training would benefit further investigation.

Finally, the surrogate model seems to have issues when dealing with sharp transition being these in the medium or in the boundary conditions.

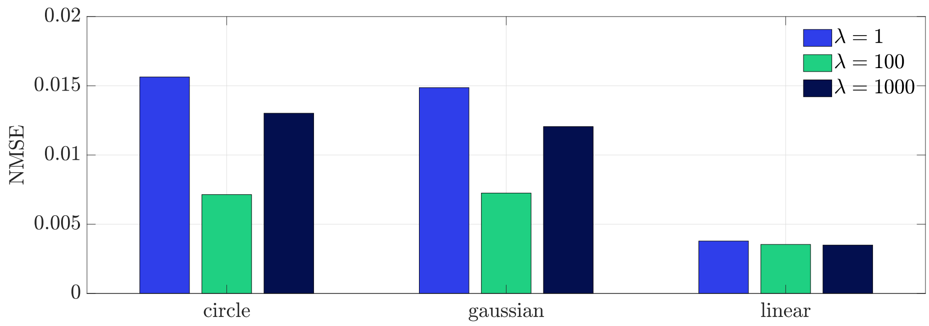

Figure 19. NMSE between the solutions from the surrogate model and Comsol for the different perturbations and weights.

6 CONCLUSION

We explored the use of physically informed neural networks with sinusoidal activation functions to provide a surrogate model for the Helmholtz equation with different boundary conditions and medium properties. The model obtained is capable of correctly describing a simple sound field generated by a monopole with a surrounding PML. On the other hand, the model struggles with more complex and realistic boundary conditions. The ground impedance condition seems to introduce the interferences that one might expect but the pattern does not match the target field. In the case of the ρc boundary conditions, the pressure field presents circular wavefronts only close to the source and is then distorted close to the boundaries where it shows flat wavefronts.

The surrogate model has also been used to recover the underlying speed of sound of the medium from the pressure data by solving an inverse problem after being pretrained on a medium that either resembles or not the target field. In both cases the network was not able to recover the sound field or the speed of sound. Some improvements have been noticed for certain perturbations and weights applied to the data term. The results have shown a relatively large sensitivity to the choice of the weight applied to the data term. Also in these cases, the error was too large to consider the results acceptable, but they can still provide insights into what could be done for improvement even though further research is needed.

While this investigation did not achieve similar performance as reported in literature, it remains a relevant and promising research path to pursue as the benefits for real time application in outdoor sound field control would be significant.

REFERENCES

[1] M. Raissi, P. Perdikaris, and G. E. Karniadakis, "Physics-informed neural networks: A deep learning framework for solving forward and inverse problems involving nonlinear partial differential equations," *Journal of Computational physics*, vol. 378, pp. 686–707, 2019.

[2] V. Sitzmann, J. Martel, A. Bergman, D. Lindell, and G. Wetzstein, "Implicit neural representations with periodic activation functions," *Advances in Neural Information Processing Systems*, vol. 33, pp. 7462–7473, 2020.

[3] P. Morse and K. Ingard, *Theoretical acoustics*, p. 320. Princeton, New Jersey: Princeton University Press, 1986.

[4] J. P. Berenger, "A perfectly matched layer for the absorption of electromagnetic-waves," *Journal of computational physics*, vol. 114, pp. 185–200, OCT 1994.

[5] N. Benbarka, T. Höfer, A. Zell, *et al.*, "Seeing implicit neural representations as fourier series," in *Proceedings of the IEEE/CVF Winter Conference on Applications of Computer Vision*, pp. 2041–2050, 2022.

[6] D. P. Kingma and J. Ba, "Adam: A method for stochastic optimization," *arXiv preprint arXiv:1412.6980*, 2014.

[7] H. S. Aghamiry, A. Gholami, and S. Operto, "Improving full-waveform inversion by wavefield reconstruction with the alternating direction method of multipliers," *Geophysics*, vol. 84, no. 1, pp. R139–R162, 2019.

[8] S. Wang, Y. Teng, and P. Perdikaris, "Understanding and mitigating gradient flow pathologies in physics-informed neural networks," *SIAM Journal on Scientific Computing*, vol. 43, no. 5, pp. 3055–3081, 2021.